



HAL
open science

Circuit-tunable subwavelength terahertz devices

Bruno Paulillo

► **To cite this version:**

Bruno Paulillo. Circuit-tunable subwavelength terahertz devices. Optics / Photonic. Université Paris Saclay (COmUE), 2016. English. NNT : 2016SACLS130 . tel-01544686

HAL Id: tel-01544686

<https://theses.hal.science/tel-01544686>

Submitted on 22 Jun 2017

HAL is a multi-disciplinary open access archive for the deposit and dissemination of scientific research documents, whether they are published or not. The documents may come from teaching and research institutions in France or abroad, or from public or private research centers.

L'archive ouverte pluridisciplinaire **HAL**, est destinée au dépôt et à la diffusion de documents scientifiques de niveau recherche, publiés ou non, émanant des établissements d'enseignement et de recherche français ou étrangers, des laboratoires publics ou privés.

NNT : 2016SACLS130

THESE DE DOCTORAT
DE
L'Université Paris-Saclay
PREPAREE A
L'UNIVERSITE PARIS SUD

ECOLE DOCTORALE N° 575
EOBE | Electrical, optical, bio-physics and engineering

Spécialité de doctorat: Physique

Par

M. Bruno Paulillo

Circuit-tunable subwavelength terahertz devices

Thèse présentée et soutenue à Orsay, le 21 juin 2016 :

Composition du Jury :

M., Greffet, Jean-Jacques	Professeur, IOGS – Univ. Paris Saclay	Président
M., Lampin, Jean-François	CR, IEMN – Univ. Lille 1	Rapporteur
M., Scalari, Giacomo	Lecturer, IQE – ETH Zurich	Rapporteur
M., Delga, Alexandre	CR, III-V Lab	Examineur
M., Dhillon, Sukhdeep	CR, LPA – ENS	Examineur
M., Colombelli, Raffaele	DR, C2N – Univ. Paris Saclay	Directeur de thèse
M., Degiron, Aloyse	CR, C2N – Univ. Paris Saclay	Invité

Titre : Dispositifs térahertz sub-longueur d'onde accordables par des composants discrets

Mots clés : métamatériaux, térahertz, antennes RF, confinement sub-longueur d'onde, dispositifs quantiques intersousbandes

La demande croissante en composants optoélectroniques de taille réduite, rapides, de faible puissance et à faible coût oriente la recherche vers des sources et détecteurs de radiation ayant une dimension inférieure à la longueur d'onde émise/détectée. Cette dernière est entravée par la limite de diffraction qui fixe la dimension minimale des dispositifs optiques à la moitié de la longueur d'onde de fonctionnement. A l'inverse, les dispositifs électroniques, tels que les antennes et les oscillateurs, ne sont pas limitée en taille et leur fréquence peut être accordée par des composants discrets. Par conséquent, unifier les mondes de la photonique et de l'électronique permettrait de concevoir de nouveaux dispositifs optoélectroniques sans limitation de taille imposée par la longueur d'onde et ayant des fonctionnalités empruntées aux circuits électroniques. La région spectrale idéale pour développer ce paradigme est la gamme térahertz (THz), à mi-chemin entre les domaines de l'électronique et de l'optique.

Dans la première partie de ces travaux, nous présentons de nouveaux micro-résonateurs sub-longueur d'onde en 3D qui fonctionnent comme des circuits LC microscopiques et où la fréquence de résonance peut être accordée en agissant séparément sur la région capacitive et/ou inductive. Dans la deuxième partie, nous illustrons la puissance de cette approche en réalisant de nouveaux méta-dispositifs THz passifs (polaritoniques, commutables optiquement, optiquement actifs) basés sur des composants discrets. La dernière partie de cette thèse est consacrée aux méta-dispositifs actifs. Des photodétecteurs THz à puits quantiques ayant une dimension $\approx \lambda_{\text{eff}}/10$, en configuration objet unique et réseau sont démontrées, grâce à un schéma de contact efficace et originale pour extraire (injecter) un courant depuis (dans) le cœur semi-conducteur intégré dans chaque résonateur. Enfin, une étude de faisabilité d'un laser sub-longueur d'onde aux fréquences THz est présentée.

Title : Circuit-tunable subwavelength terahertz devices

Keywords : metamaterials, terahertz, RF antennas, sub-wavelength confinement, intersubband quantum devices

The increasing need for small, fast, low-power and low-cost optoelectronic components is driving the research towards radiation sources and detectors having a dimension that is smaller than the emitted/detected wavelength. This is hampered by the optical diffraction limit which constrains the minimum dimension of optical devices at half the operating wavelength. Conversely, electronic devices, such as antennas and oscillating circuits, are not diffraction-limited in size and can be frequency tuned with lumped components. Hence, blending the worlds of photonics and electronics has the potential to enable novel optoelectronic devices with no lower size limit imposed by the wavelength and with novel functionalities borrowed from electronic circuits. The ideal spectral region to develop this paradigm is the terahertz (THz) range, halfway between the electronics and optics realms.

In the first part of this work, we present novel subwavelength 3D micro-resonators that behave as microscopic LC circuits, where the resonant frequency can be tuned acting separately on the capacitive and/or inductive regions. In the second part we illustrate the power of this concept by implementing novel lumped-elements-based passive THz meta-devices (polaritonic, optically switchable, optically active). The last part of this thesis is devoted to active meta-devices. Single-pixel and arrays of THz quantum well photodetectors featuring a $\approx \lambda_{\text{eff}}/10$ dimension are demonstrated, thanks also to an effective and original contact scheme to extract (inject) current from (into) the semiconductor core embedded by each resonator. Finally, a feasibility study of a subwavelength laser at THz frequencies is reported.

*A Chiara
che equilibra la Forza*

Acknowledgements

First and foremost I want to thank my advisor Raffaele Colombelli. It was a pleasure to pursue my PhD under his guidance and I have really learned a lot from him. His enthusiastic, creative and solution-oriented thinking was a source of inspiration for me. Most importantly, I admired his passion and integrity in science.

I am indebted to my PhD jury for the great feedback they gave on my thesis and for the far-reaching scientific discussions that followed the PhD defence.

In particular, I'd like to express my gratitude to Aloyse Degiron for the brainstorming we had over all these years, his help with simulations and his out-of-the box ideas.

During these years I was glad to meet and work in close association with the (current & former) members of the QCL team. I especially would like to thank Jean-Michel – the polariton man – who has shared with me this experience from start to finish, for his help with the THz polaritons experiments and for his advice.

I would like to express my gratitude to Stefano, who has joined the team in the crucial moment of the meta-atom QWIPs birth: his help in mastering the elusive photo-detection measures and characterizing the detectors is priceless. Moreover, he was a true support and a friend during the long months of thesis redaction.

Also, I am deeply grateful to Souad for her assistance in all kind of micro-fabrication issues, for her aid in QCLs testing and for her concern.

I'd like to thank Daniel, my PhD mate with whom I have shared all the ups and downs of the PhD student life all the way to the unusual defence organization. I wish you all the best for the future!

Special thanks to Adel, Thibault, Pierre, Yacine for the friendly atmosphere in (and outside) the lab and for their helpfulness in everything.

Thanks also to Gangyi and Elodie for the instructive discussions.

I am grateful to François Julien, for his advice and humour, and to all the people of the Nanophotonit team for all the good times spent together: Maria, Salam, Hezhi, Agnes, Vladimir and Patrick.

I take the opportunity to wish good luck to the new PhD student generation: Claire, Pierre-Baptiste, Laurent, François, Arnaud, Lu, Nan, Valerio and Martina.

All the best and many thanks to Lantian, who collaborated with me for his M2 stage doing a very nice job on the high-Q LC resonators.

I wish to acknowledge all the staff at the CTU-Minerve facility who has helped me to overcome countless obstacles in cleanroom fabrication: in particular Nathalie Isac, Jean-René Coudeville and David Bouville for their friendliness and also for all the nice moments around a coffee (and delicious foods); thanks to François Maillard and Fabien Bayle for their willingness. Moreover, I would like to show my gratitude to Stephane Guilet from LPN for IBE sessions.

This thesis would not have been possible without the high-quality samples grown by our collaborators in LPN (Grégoire Beaudoin and Isabelle Sagnes) and Leeds University (Lianhe Li, Gilles A. Davies and Edmund H. Linfield). Thank you!

I'd like to thank as well our collaborators in LPA-ENS (Sukhy Dhillon, Sarah, Hanond) and IESL-FORTH (S. Tzortzakis group) for the preliminary measures on the ultra-fast LC switches.

From IEF, I would like to thank Nicolas Zerounian, Paul Crozat, Delphine Morini and Laurent Vivien for their availability in sharing their instrumentation and expertise. I also acknowledge Guillaume Agnus, Gaële Perrusson and Arnaud Bournel for their support during my first teaching experience.

One of the enjoyable things in lab life was to have funny or active discussions during coffee breaks a/o lunch time: for this, thanks to Michele and Giovanni.

I'd like to thank Tommaso and Daniele for our scientific (and not) discussions, all the aperòs, their precious advice and friendship.

I will never forget these years thanks to the uncountable amazing people I've met here in Paris and in the conferences all around the world. Thank you all, for having enriched my life and given me new points of view.

Lastly, I would like to thank my amazing (extended) family and friends for all their affection and encouragement: it is not easy to be supportive when being hundreds of km away, but today I know that caring can be felt at a distance (the comfort of Apulia vacations helped as well!).

Particularly, to my little brother Roberto: thanks for your being so differently similar to me and for having been a perfect host at my PhD defence.

I'm immensely thankful to my parents, who have embraced lovingly my curiosity since the first time I've asked "Perché?" and who have taught me the independence of acting and thinking.

And most of all I want to thank my (future) wife Chiara. You went through the best and worst of me during these PhD years, and you were there to relieve the frustration, coach my stress management and smile proudly at my successes.

But above all things, your eyes full of love were always there to remind me, unconsciously and constantly, what life is all about.

Dispositifs térahertz sub-longueur d'onde accordables par des composants discrets

La demande croissante en composants optoélectroniques de taille réduite, rapides, de faible puissance et à faible coût oriente la recherche vers des sources et détecteurs de radiation ayant une dimension inférieure à la longueur d'onde émise/détectée. Cette dernière est entravée par la limite de diffraction qui fixe la dimension minimale des dispositifs optiques à la moitié de la longueur d'onde de fonctionnement. A l'inverse, les dispositifs électroniques, tels que les antennes et les oscillateurs, ne sont pas limitée en taille et leur fréquence peut être accordée par des composants discrets. Par conséquent, unifier les mondes de la photonique et de l'électronique permettrait de concevoir de nouveaux dispositifs optoélectroniques sans limitation de taille imposée par la longueur d'onde et ayant des fonctionnalités empruntées aux circuits électroniques. La région spectrale idéale pour développer ce paradigme est la gamme térahertz (THz), à mi-chemin entre les domaines de l'électronique et de l'optique. Aujourd'hui encore, ce domaine spectral reste fortement sous-développé, principalement à cause du manque de sources et détecteurs performants et compactes. Il est cependant en expansion rapide depuis une quinzaine d'années, grâce à l'avènement de dispositifs basés sur les transitions intersous-bandes (ISB) dans les puits quantiques à semiconducteur, à savoir le laser à cascade quantique (QCL) et le photo-détecteur infra-rouge à puits quantique (QWIP).

Dans la perspective d'unifier l'électronique et la photonique, la gamme THz est particulièrement intéressante, car les pertes ohmiques des métaux sont faibles par rapport à la gamme du proche infrarouge et du visible, et les effets liés à l'inductance cinétique des électrons peuvent être négligés. Aux fréquences THz, on peut obtenir de un confinement sub-longueur d'onde de la radiation sans excessives pertes et envisager des dispositifs «hybrides» fonctionnant comme des circuits électroniques à composants discrets. De plus, l'expertise de l'ingénierie RF peut être empruntée pour enrichir les dispositifs THz avec des fonctionnalités aujourd'hui inaccessibles avec les résonateurs photoniques conventionnels.

La première partie de ces travaux porte sur la conception, simulation, fabrication et caractérisation de micro-résonateurs sub-longueur d'onde en 3D pour le THz inspiré des metamatériaux et des antennes. Ce nouveau design est constitué d'une microcavité métal-semiconducteur-métal (MSM, ou patch) qui fournit une capacité, couplée à une antenne boucle inductive (schéma en FIG. 1(a)). Pour cela une technique de fabrication pour réaliser des micro-métallisations suspendues est développée. Un exemple de dispositif fabriqué est montré dans la photo MEB en FIG. 1(b).

La fabrication et la caractérisation optique en réflectivité ont été faites d'abord pour des échantillons passifs de GaAs épitaxié, ce qui permet d'étudier les modes résonantes de ces cavités en fonction des paramètres géométriques choisis.

Cet étude préliminaire est nécessaire pour pouvoir ensuite incorporer des régions actives GaAs/AlGaAs dans ces résonateurs afin de réaliser des dispositifs actifs (sources, détecteurs, LEDs polaritoniques,...) sub-longueur à la fois libérés des contraintes de taille imposées par diffraction et modulables en fréquence via les paramètres propres d'un circuit électronique.

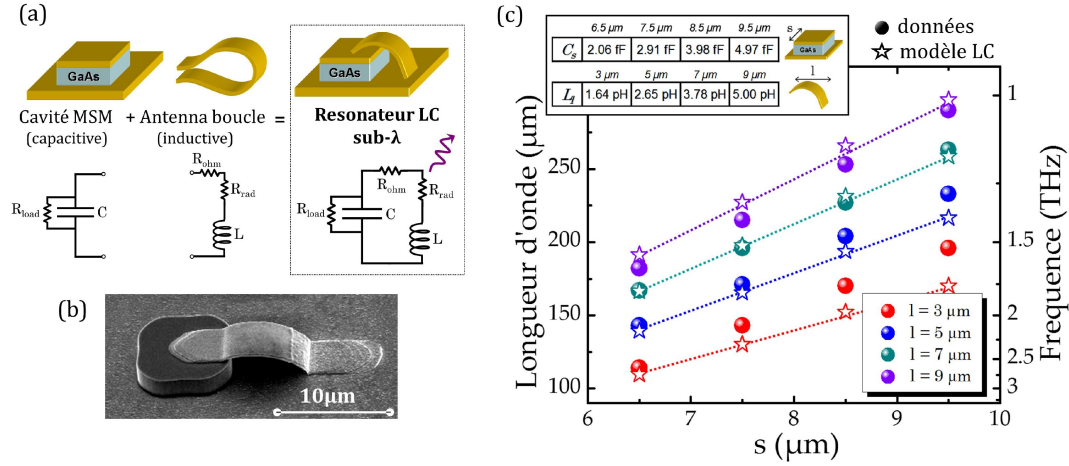


FIG. 1(a) Schéma intuitif du résonateur: une antenne boucle est connectée à une cavité MSM ; circuit LC équivalent: le patch est la section capacitive hébergeant le champ E, tandis que l'antenne est la section inductive hébergeant le champ H. L'antenne présente également une résistance radiative (R_{rad}) qui est responsable du couplage optique, une résistance ohmique (R_{ohm}) tandis que R_{load} modélise les pertes diélectriques dans le semiconducteur. (b) Image au microscope électronique à balayage (MEB) d'un dispositif réel. (c) Sphères: longueurs d'ondes expérimentales du mode LC en fonction du côté (s) du patch, pour diverses longueurs d'antenne (l). Fixée l , la tendance est linéaire, comme prévu à partir de théorie. Etoiles: résonances prédites par le modèle LC simple. Les valeurs de capacité C_s (fF) et inductance L_l (pH) obtenus à partir des échantillons des paramètres géométriques sont reportés.

On démontre que ces objets fonctionnent comme des circuits LC microscopiques, où l'on peut accorder la fréquence de résonance en changeant la géométrie de la partie capacitive ou de la partie inductive de façon indépendante (FIG. 1(c)). Un simple modèle LC à élément discrets permet de justifier les résultats expérimentaux.

On étudie ensuite le couplage optique de ces dispositifs en montrant qu'ils se comportent comme des micro-antennes magnétiques. L'impact de l'ajoute de plusieurs boucles inductives en parallèle à la cavité patch en GaAs a également été étudié du point de vue fréquentiel et optique.

Dans la deuxième partie, nous illustrons la puissance de cette approche en réalisant de nouveaux méta-dispositifs THz passifs (polaritoniques, commutables optiquement, optiquement actifs) basés sur des composants discrets.

En particulier, on montre l'application des micro-résonateurs sub-longueur d'onde précédemment développés à une étude d'électrodynamique en cavité. Pour cela, un absorbeur quantique est inséré dans le cœur du résonateur à la place du GaAs massif.

Pour cette application, un puits quantique parabolique montrant une transition intersousbande à 3.6 THz a été choisi. L'intérêt du design parabolique dans la gamme THz consiste dans le fait que l'absorption du puits est visible jusqu'à température ambiante, i.e. c'est indépendant de la distribution thermique des électrons dans l'hétérostructure. Si la transition intersousbande du puits est proche de la résonance de cavité en fréquence et largeur de raie on peut en fait accéder au régime que l'on dit de couplage fort lumière-matière, dont la signature est la naissance de nouveaux états mixtes lumière-matière, appelés *polaritons intersousbandes*. Cela demande avant tout un design judicieux pour centrer la résonance LC des résonateurs autour de la transition intersousbande du puits.

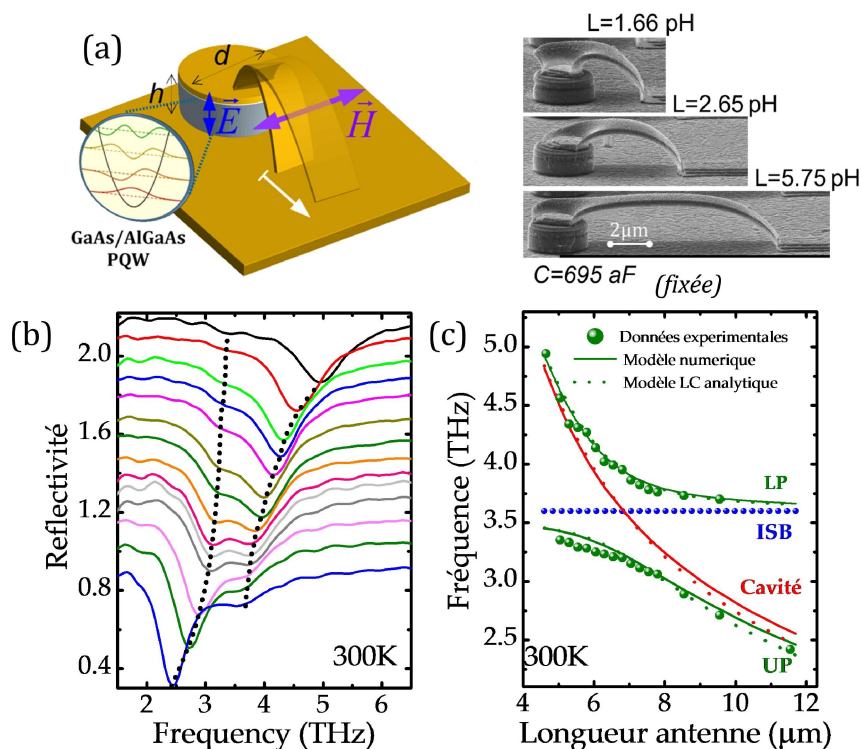


FIG. 2(a) (gauche) Schéma du résonateur LC intégrant un puits quantique parabolique comme cœur actif. L'accord en fréquence se fait (par lithographie) grâce à l'antenne externe. Les dipôles électriques et magnétiques excités par le rayonnement incident sont présentés (droite). Images MEB de trois résonateurs avec des différentes longueurs. (b) Réflectivité expérimentale des dispositifs mesuré. Les spectres sont décalés verticalement pour plus de clarté. Les lignes en pointillé permettent de suivre la position des deux états polaritoniques. (c) Minima de réflectivité en fonction de la longueur d'antenne (sphères vertes) correspondant aux fréquences des états polaritoniques. Les résonances des cavités nues calculées en utilisant le modèle électromagnétique LC (ligne rouge pleine) et le modèle analytique LC (ligne pointillé rouge) sont présentées. Les lignes vertes représentent les correspondantes fréquences polaritoniques calculées.

Le fait marquant de cette démonstration de couplage fort à température ambiante est primo la nature très sub-longueur d'onde ($\approx \lambda_{\text{eff}}/10$) du mode de cavité utilisé et secundo le fait que la modulation du couplage se fait exclusivement par un élément d'accord externe (une antenne).

Ensuite, on discute l'intégration d'un élément commutateur optique ultra-rapide au sein de la microcavité LC (collaboration avec le LPA-ENS de Paris et le IESL-FORTH de Héraklion). Cela permettrait l'étude dans le régime temporel de la dynamique d'excitation d'un mode de microcavité nue ou couplé à une transition quantique par spectroscopie pompe-sonde.

La dernière partie de cette thèse est consacrée aux méta-dispositifs actifs.

Tout d'abord on s'est adressé vers la miniaturisation des détecteurs à puits quantiques THz, exploitant la géométrie LC sub-longueur d'onde développée auparavant. Le photo-détecteur infra-rouge à puits quantique (QWIP) est un détecteur quantique exploitant une transition ISB. Dans cette structure, un puits quantique est conçu pour avoir deux niveaux électroniques confinés, le deuxième étant assez proche en énergie du continuum. Sous l'application d'un champ électrique, le niveau excité va être alors couplé (par transport tunnel) au continuum et produit un photocourant, comme dans un photoconducteur standard.

Si les détecteurs QWIPs dans le moyen infrarouge sont désormais disponibles sur le marché, cette technologie est très peu développée dans le THz, ce qui limite fortement les applications dans cette gamme spectrale. La principale difficulté des détecteurs THz est due à la faible énergie des photons (typiquement inférieure à 20 meV). Cela veut dire que le bruit lié au rayonnement thermique à température ambiante va être le principal facteur limitant la sensibilité des détecteurs. Pour cela, une extrême réduction du volume actif du détecteur pourrait être bénéfique pour abattre le bruit thermique (i.e. le courant d'obscurité) et améliorer les performances.

Dans cette partie, tout d'abord on caractérise une région active QWIP standard d'épaisseur 1.5 μm qui répond dans la bande spectrale 2-4 THz. Ensuite, on aborde le problème de l'injection électrique dans une microcavité LC (naturellement en configuration de court-circuit). Deux approches utilisant soit une isolation diélectrique, soit une ouverture d'air dans le plan de masse ont été développées. Ce dernier se révèle un schéma de contact efficace et originale pour extraire (injecter) un courant depuis (dans) le cœur semi-conducteur intégré dans chaque résonateur sub-longueur d'onde.

Suite à ce développement, des photodétecteurs THz à puits quantiques ayant une dimension $\approx \lambda_{\text{eff}}/10$, en configuration objet unique et réseau sont démontrés. FIG. 3(a-b) montre le schéma du dispositif, ainsi que une image MEB.

Dans un premier temps, les dispositifs sont caractérisés électriquement dans les deux configurations (objet unique et réseau) pour sonder l'efficacité du système d'extraction électrique développé. Un niveau très faible de courant d'obscurité (< 1 nA) circule dans le dispositif unique, ce qui est particulièrement prometteur en raison de la réduction du bruit du détecteur. Ensuite, les spectres de photocourant sous une illumination large bande sont acquis (FIG. 3(c-d)). On remarque que le cœur actif du dispositif hébergeant la structure QWIP opérant autour de 3 THz ($\lambda = 100 \mu\text{m}$), a un actif volume d'environ $\approx 20 \mu\text{m}^3$ seulement. Cela constitue la première démonstration d'un véritable *méta-atome optoélectronique* injecté électriquement.

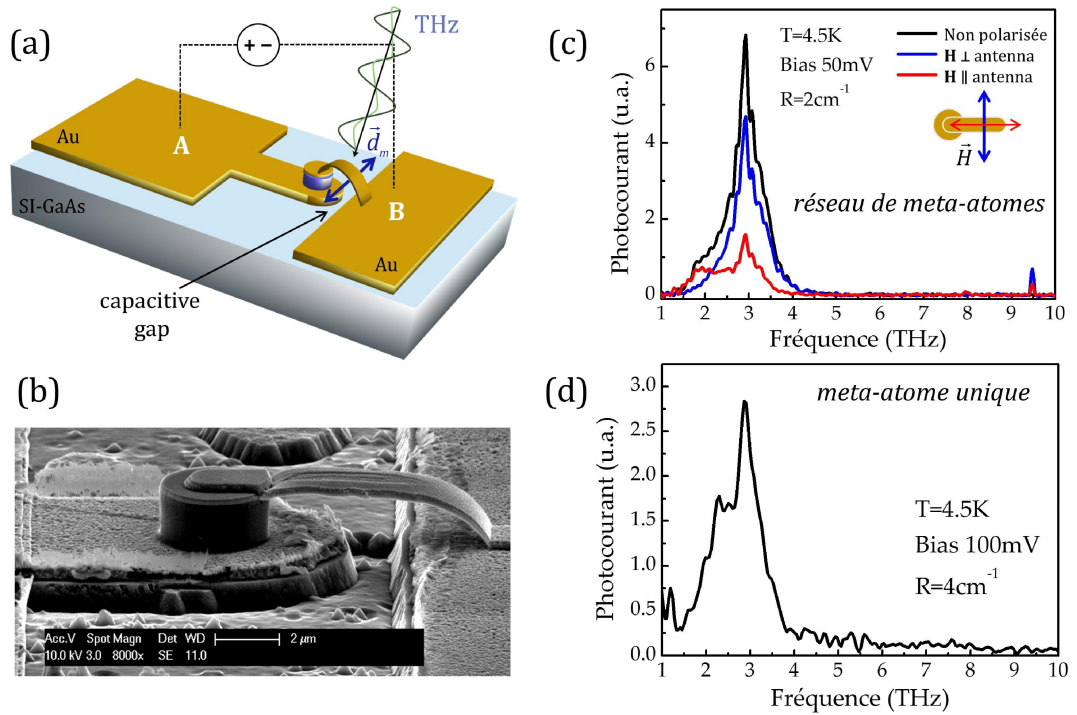


FIG. 3(a) Schéma d'un méta-atome QWIP unique avec ses contacts électriques. (b) Image MEB (détail) du dispositif. (c) Spectre de photocourant pour un réseau de méta-atomes QWIP sous illumination (incidence normale) avec un rayonnement THz non polarisée et polarisée. (d) Spectre de photocourant d'un méta-atome QWIP unique.

Enfin, une étude de faisabilité d'un laser sub-longueur d'onde aux fréquences THz est présentée. Préliminairement, des régions actives à cascade quantique (QCLs, quantum cascade lasers) performantes aux fréquences d'intérêt (≈ 3 THz) sont caractérisées et affinées pour que l'épaisseur soit compatible avec les tailles typiques des micro-résonateurs sans en dégrader trop les caractéristiques. Plusieurs régions actives ont été caractérisées et deux d'entre elles donnent des bonnes performances pour une épaisseur de $6 \mu\text{m}$.

Ensuite, une étude détaillée des pertes dans les microcavités LC a été fait par simulations aux éléments finis. En fait, contrairement au cas d'un détecteur, dans le cas d'un « nano »laser des figures de mérite tels que le facteur Q et le recouvrement électromagnétique Γ sont essentiels pour dessiner une cavité dont les pertes puissent être compensé par le gain de la région actives. A partir de cette analyse, un nouveau design de cavité pour un « nano »laser THz inspiré des cavités RF a été conçu.

L'utilisation d'une région active fine en combinaison avec un résonateur hybride optimisé devrait permettre d'obtenir un laser térahertz ultra-compact libéré de la limite de diffraction, tout en introduisant pour la première fois la possibilité d'accorder la fréquence du laser en adaptant l'impédance d'un circuit LC à composants discrets.

Contents

Introduction.....	1
1 Photonics for terahertz devices.....	5
1.1 The THz gap.....	5
1.1.1 THz sources.....	6
1.1.2 THz detectors.....	7
1.1.3 Applications of THz radiation.....	8
1.2 Intersubband transitions in semiconductor QWs.....	9
1.2.1 III-V heterostructures.....	9
1.2.2 Electron motion in a heterostructure. Quantum wells.....	10
1.2.3 Light-matter interaction in a quantum well: intersubband transitions.....	11
1.3 Optical properties of materials.....	13
1.3.1 Lorentz oscillator model.....	13
1.3.2 GaAs dielectric function.....	15
1.3.3 Gold dielectric function. Skin depth.....	16
1.3.4 Surface plasmons. Subwavelength confinement of radiation.....	18
1.3.5 Engineering the optical response: metamaterials.....	21
1.4 Photonic resonators for THz devices.....	22
1.4.1 The Helmholtz equation: electromagnetic waves.....	22
1.4.2 The parallel plate waveguide.....	24
1.4.3 TEM transmission lines.....	26
1.4.4 Transmission line resonators: the patch cavity.....	27
1.5 Subwavelength photonics: antennas and metamaterials.....	29
1.5.1 Origin of the diffraction limit.....	29
1.5.2 Maxwell and Kirchhoff.....	30
1.5.3 Antennas.....	31
1.5.4 Subwavelength antennas and resonators. Metamaterials.....	33
2 Circuit-tunable and antenna-based THz resonators.....	37
2.1 Optical properties of $\lambda/2$ patch resonators.....	37
2.1.1 FEM simulations: eigen-modes analysis, wave excitation.....	37
2.1.2 Fabrication of MSM resonators.....	41
2.1.3 Optical characterization.....	42
2.1.4 Fundamental limits of TL resonators. RLC model of a patch resonator.....	44
2.2 The lumped-element LC resonator in a nutshell.....	46
2.2.1 A capacitor's history from DC to optical frequencies.....	47
2.2.2 Loading the capacitor: the LC tank circuit.....	48
2.2.3 Energy conservation in a subwavelength mode.....	49
2.2.4 Electron kinetic inductance.....	51
2.3 Circuit-tunable THz sub- λ resonators.....	53
2.3.1 Design of lumped-elements THz resonators.....	53
2.3.3 Optical characterization: incidence angle and polarization rules for LC mode excitation.....	56
2.3.4 Circuit tuning of the resonance via L and C.....	57
2.3.5 Optical coupling of LC resonators: radiation patterns.....	59
2.3.6 Transmission-line model: antenna impedance.....	62
2.4 Adding functionalities via lumped elements.....	64
2.4.1 Suppression of magnetic coupling: the 3D eSRR.....	64
2.4.2 Inductors in parallel.....	65
2.4.3 Suspended tuning stub.....	66
3 Applications of passive resonators.....	71
3.1 Room temperature strong light-matter coupling in THz meta-atoms.....	71

3.1.1	Strong light-matter coupling.....	71
3.1.2	Intersubband polaritons	74
3.1.3	Parabolic quantum wells.....	75
3.1.4	Design and fabrication of antenna-tuned sub- λ resonators around 3.6 THz	77
3.1.5	RT strong light-matter coupling in three dimensional terahertz meta-atoms	79
3.1.6	Perspectives for cavity quantum electrodynamics in subwavelength resonators... 81	
3.2	Perspective #1: photo-induced switching of the LC resonance in a circuit-tunable resonator	83
3.2.1	Photo-switchable circuit-tunable resonators: the concept	83
3.2.2	1 st generation devices on GaAs: resonance bleaching	85
3.2.3	Towards a 2 nd generation devices.....	86
3.3	Perspective #2: optically active high-impedance surfaces.....	87
3.3.1	Engineered electromagnetic surfaces	87
3.3.2	Chiral metamaterials	88
3.3.3	Optical activity from two-inductors meta-atoms.....	89
4	THz meta-atom quantum well photodetectors.....	93
4.1	THz quantum well photodetectors.....	93
4.1.1	Long wavelength radiation detection.....	93
4.1.2	Quantum well infrared photodetectors.....	95
4.1.3	Noise in a photoconductor	97
4.1.4	Origin of the dark current in a QWIP	98
4.1.5	Detectivity and BLIP condition	100
4.1.6	THz quantum well photodetectors: state of art.....	102
4.2	THz-QWP characterization in mesa geometry.....	103
4.2.1	The 3 THz QWP structure.....	103
4.2.2	Fabrication	104
4.2.3	Experimental setup	105
4.2.4	Electrical characterization	107
4.2.5	Photodetection with a broadband source	108
4.2.6	Photodetection with a QCL source.....	109
4.3	THz meta-atom subwavelength QWPs	111
4.3.1	Motivation: reducing active volume to enhance performance	111
4.3.2	The problem of electrical injection in a split ring geometry	111
4.3.3	LC resonators with ring openings in the ground plane.....	112
4.3.4	Role of the periodic subwavelength apertures	114
4.3.5	Design and fabrication of THz meta-atom QWPs.....	115
4.3.6	Optical characterization of passive arrays.....	117
4.3.7	Electrical characterization. BLIP temperature.....	120
4.3.8	Photocurrent spectra.....	121
5	Towards the THz “nano” laser: AR size reduction and loss engineering.....	125
5.1	Laser miniaturisation.....	125
5.1.1	Round trip model for the laser threshold.....	125
5.1.2	State of art of “nano-lasers”	126
5.1.3	Lasing on a subwavelength mode comes at a price	128
5.2	Size reduction of THz QCLs active regions	129
5.2.1	Characterization of 6 μ m-thick THz QCL active regions	129
5.2.2	Conception of a lateral bottom injection scheme compatible with a split-ring geometry.....	130
5.3	Loss engineering of THz micro-resonators	131
5.3.1	Resonator Quality factor	131
5.3.2	Lossy eigenvalue analysis for Q factor calculation	132
5.3.3	Patch antennas operating around 3 THz	133
5.3.4	LC resonators operating around 1.5 THz	135
5.3.5	Design of LC resonators operating at 3 THz.....	137
5.4	Subwavelength resonator with “revolved” inductors	138
5.4.1	Revolved inductors to lower the ohmic loss	138

5.4.2	Design of “revolved inductor” resonators operating at 3 THz	140
5.4.3	Experimental results for $h_{\text{GaAs}} = 2 \mu\text{m}$	141
Conclusions and perspectives		145
Appendix A: samples growthsheet		149
Bibliography		153

Introduction

Optoelectronics, the merger of optics and electronics, is one of the most strategic and all-pervading technologies of the information age. Its applications extend throughout our everyday lives, including the fields of computing, communication, entertainment, healthcare, defence and security.

Moreover, optoelectronics provides unique tools that have had a strong impact on many scientific disciplines: for instance, ultra-fast laser spectroscopy in chemistry and laser interferometry in metrology. The recent first detection of gravitational waves in the LIGO experiment is an example of scientific breakthrough enabled by optoelectronic technology.

Widespread optoelectronic components range from flat-screen displays (TVs, computers, mobile phones ...) through the checkout bar-scanners to internet communications links. Optoelectronic industry (lasers, optical discs, image sensors, optical fibers) is a key actor of the \$1.5 trillion global information business.

In this context, the need for small, low-power and low-cost integrated optoelectronic components is driving the research towards devices that convert electrons to photons (LEDs, lasers) and vice versa (photodetectors) on a dimension that is smaller than the emitted/detected wavelength. Such tiny devices would also feature a higher operation speed, as propagation and interaction times get reduced.

Reduction of the optoelectronic devices size can only be achieved if one manage to confine both electrons and photons within the same small volume. Confinement of electrons to a few nanometers in one dimension has been achieved in the 1980s with semiconductor quantum wells (QWs); then, in the 1990s, three-dimensional confinement has been successfully implemented using quantum dots (QDs). On the other hand, the confinement of photons is more difficult due to the optical diffraction limit, which states that it is impossible to confine photons of wavelength λ in a volume smaller than $(\lambda / 2n)^3$, where n is the refractive index of the dielectric medium.

The operating wavelength limits inherently the minimum dimension of every optical device or component. Conversely, electronic devices are free from the slavery of the wavelength as their operation relies on real electronic currents. For instance, antennas are widespread devices which perform the conversion between electrical currents and electromagnetic waves. Typically employed in the radio and micro-wave bands (e.g. radio tuner, wi-fi hotspots, mobile phones), their dimension is in general not constrained by the wavelength. Similarly, electronic oscillating circuits are built with subwavelength lumped components (capacitors, inductors, resistors) and can be conveniently frequency tuned by acting separately on the geometry of each element, what is currently not possible for photonic devices such as semiconductor lasers.

This thesis is part of a far-reaching project whose goal is to develop a unified framework for photonic and electronic devices. Blending these two worlds would enable to conceive novel optoelectronic devices with no size limit imposed by the wavelength and functionalities borrowed from electronic circuits (tunability, switching, reconfiguration, ...).

Recently, spectacular advances in this direction have been reported in the research domain of *electromagnetic metamaterials*, i.e. artificial media with user-designed electromagnetic functionalities. Their striking macroscopic features (e.g. negative refraction) arise from the response of individual subwavelength resonators, called meta-atoms, which behave as miniature lumped circuits. For instance, the split-ring resonator, considered the archetypical meta-atom, implements de facto a $\approx\lambda/10$ LC circuit, as it features an inductive current-carrying metal loop and a capacitive gap where an almost uniform electric field builds. If we could fill the E-field region with an optically active medium (e.g. a detecting or lasing active region) we would obtain a hybrid “electronic-photonic” device where an optical solid-state transition is coupled to an electronic oscillator mode. In such system, the energy exchange would be mediated by a real electrical current, making the system wavelength-independent.

The ideal spectral region to develop this new paradigm is the terahertz (THz) range, halfway between the electronics and optics realms. Historically, this range is considered as a technological gap because of the lack of compact (semiconductor-based) radiation sources and detectors. Nevertheless, THz technology is important for security screening (explosives, drugs), quality control (chemical and pharmaceutical processes), healthcare (THz radiation is non-ionizing) and environmental applications. The “THz gap” has been partially filled thanks to the advent of devices based on intersubband (ISB) transitions in QWs, namely the invention (in 1994) of the mid-IR quantum cascade laser (QCL) followed in 2002 by its extension in the THz range. On the other side, at THz frequencies the quantum detector technology is greatly underdeveloped, whilst QW infrared photodetectors (QWIPs) constitute now a mature technology in the 8-12 μm wavelength range.

In the perspective of unifying electronics and photonics, the THz range is a “lucky” playground since metal ohmic losses are low compared to the near-infrared and visible ranges, and effect related to electron kinetic inductance can be neglected. At THz frequencies one can achieve sub-wavelength radiation confinement without excessive losses and envision “hybrid” devices behaving as lumped-elements circuits. Furthermore, the huge expertise of RF engineering may be borrowed to enrich THz optoelectronic devices with functionalities today unattainable with conventional photonic resonators.

Chapter 1 provides a general overview on THz technology state-of-art, some important notions about ISB transitions in semiconductor QWs and optical properties of III-V semiconductors and metals at THz frequencies. The conventional transmission-line resonators employed in THz photonics are then discussed, before introducing the optical diffraction limit and addressing the issue of subwavelength radiation confinement.

In **Chapter 2**, the modelling, fabrication and characterization of the subwavelength THz resonators conceived in this thesis will be discussed. First, the differences between the optical (microcavity) and electronic (circuital) regimes will be highlighted. For this purpose, the $\lambda/2$ patch resonator will be taken as the prototype of a purely optical cavity and compared with the lumped-elements LC circuit, which is the fundamental building block exploited later in the conception of circuit-tunable THz devices. Also, the implications of operating on sub- λ electromagnetic modes will be discussed. The core of the chapter contains a detailed experimental study of the developed 3D THz micro-resonators relying on suspended loop antennas connected to metal-semiconductor-metal micro-capacitors. It will be shown that they behave like microscopic LC circuits where the resonant frequency can be tuned acting separately on the capacitive and/or inductive regions. Moreover, we will show that they capture radiation like small loop antennas. Finally, frequency tuning via additional lumped elements and radiation pattern shaping via antenna design is demonstrated.

Chapter 3 deals with some applications of the novel lumped-elements design to realize passive meta-devices at THz frequencies.

The first part of the chapter illustrates an application to a cavity electrodynamics study: the resonators will be endowed with a THz parabolic quantum well (PQW) and their LC resonance will be tuned across the PQW ISB transition to demonstrate the strong light-matter coupling at room-temperature within an ultra-subwavelength volume. In the second part, preliminary results about the realization of optically switchable 3D metadevices and polarizing high impedance surfaces will be reported.

The core “device” results of the thesis will be presented in **Chapter 4**, where single-pixel QWIP detectors with extremely sub-wavelength dimension of the order of $\lambda_{eff}/10$ will be presented. The active core of the device hosting a GaAs/AlGaAs multi-QW structure, designed to detect radiation around 3 THz ($\lambda=100 \mu\text{m}$), has an active volume of about $20 \mu\text{m}^3$ only.

First, an effective contact scheme will be developed to extract (inject) current from (in) a subwavelength semiconductor core, without suffering from the short-circuit issue intrinsic in the split-ring geometry.

The electrical and optical characteristics of the meta-atom detectors, arranged in both single and array configurations, will be shown.

Finally, **Chapter 5** includes a (preliminary) feasibility study of a subwavelength laser at THz frequencies. In the first part of the chapter we will discuss the main issues involved in laser miniaturization and review recent advances in the field. Later, reduced-size THz QC active regions compatible with sub- λ resonators will be tested. Then, a systematic numerical study performed to engineer the losses of THz metal-semiconductor-metal small resonators will be reported. A novel design inspired from RF cavities in will be explored to realize ultra-low volume lasers in the THz range.

1 Photonics for terahertz devices

In this chapter a general overview on THz technology, intersubband transitions in semiconductor quantum wells and optical properties of materials in the THz range is provided. Then, some relevant notions about the standard transmission-line resonators employed in THz photonics are recalled. Lastly, the issue subwavelength radiation confinement below the optical diffraction limit is discussed.

1.1 The THz gap

The *terahertz* (THz) or *far-infrared* (FIR) frequency range represents a portion of the electromagnetic (EM) spectrum situated halfway between electronic technology (radio frequency, microwaves) and photonics (infrared, visible light). The boundaries of this frequency band are usually placed between 300 GHz and 30 THz, although this delimitation may change depending on the references [1]. The corresponding wavelength range goes from 1 mm to 10 μm (for that the name *submillimeter band* is also used).

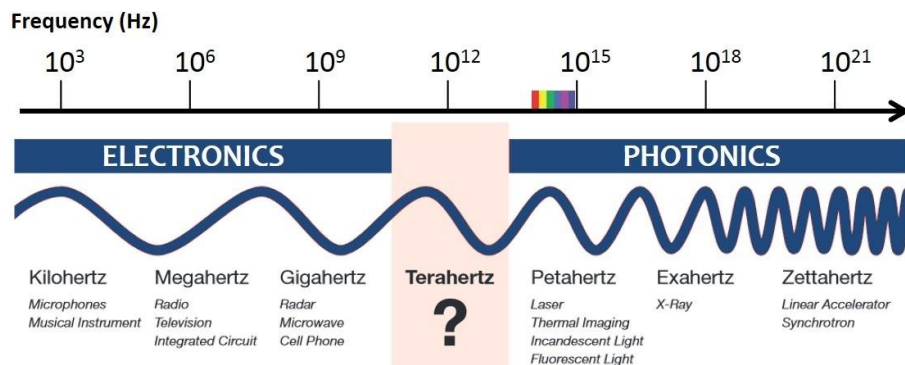


FIG. 1.1 Electromagnetic spectrum (adapted from <http://www.unbc.ca/releases/terahertz-riding-wave-future>). The “THz gap” is situated at the interface between electronics and photonics. For each frequency range major technological applications are cited.

As technology for generation, detection and manipulation of terahertz radiation is still in its infancy this frequency range is often called the “THz gap”. Though underdeveloped, this band has a tremendous potential both in terms of practical applications (medical imaging, security, manufacturing) and fundamental applications (spectroscopy, astronomy). The field of terahertz-related research and technology has seen a continuously growing trend in the last years (see FIG. 1.2), but despite the research effort the key issue to address remains the development of compact and performing THz sources and detectors.

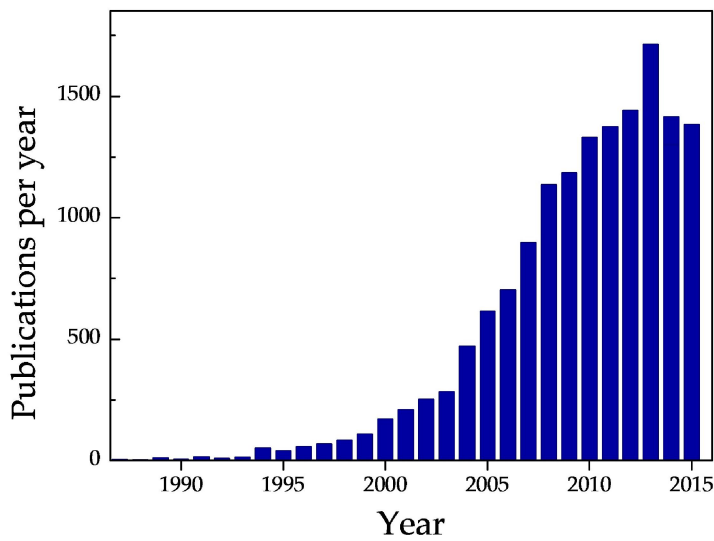


FIG. 1.2 Number of publications having the word «terahertz» in the title (elaboration from World of Knowledge database)

1.1.1 THz sources

Three major approaches are currently employed to generate terahertz radiation. The first uses solid-state electronic devices such as transistors, Gunn oscillators and Schottky diode multipliers and is well established at low frequencies (< 1 THz). However, at high frequencies the power generated by these devices drops due to the devices RC constant. The second approach is optical THz generation using pulsed or c.w. lasers, which can occur in different ways. A first method consists in generating an ultrafast photocurrent in a photoconductive antenna evaporated onto a semiconductor (e.g. LT-GaAs) via an ultrafast optical pulse (typically a fs Ti:Sa laser is used); a THz wave is then created due to free carriers acceleration. Alternatively, THz waves are generated by nonlinear optical effects such as optical rectification, difference-frequency generation or optical parametric oscillation in materials such as GaAs, GaSe, GaP, ZnTe, CdTe and LiNbO₃. Another optical THz generation method is ambient air-plasma generation, where an intense pulsed laser induces an air plasma which emits THz radiation. More details about these techniques may be found in Refs. [1]–[3].

The third approach relies on semiconductor-based THz sources and has been enabled by recent advances in nanotechnology. The first quantum cascade laser (QCL) was developed in 1994 and had a lasing frequency of about 70 THz ($4.2 \mu\text{m}$) [4], which, after much research, was followed by a demonstration at 4.4 THz in 2002 [5]. The mid or far infrared laser emission in QCLs is achieved through the use of inter-subband transitions in a repeated stack of semiconductor multiple quantum well heterostructures. For a review of the commonly employed quantum design we refer to [6].

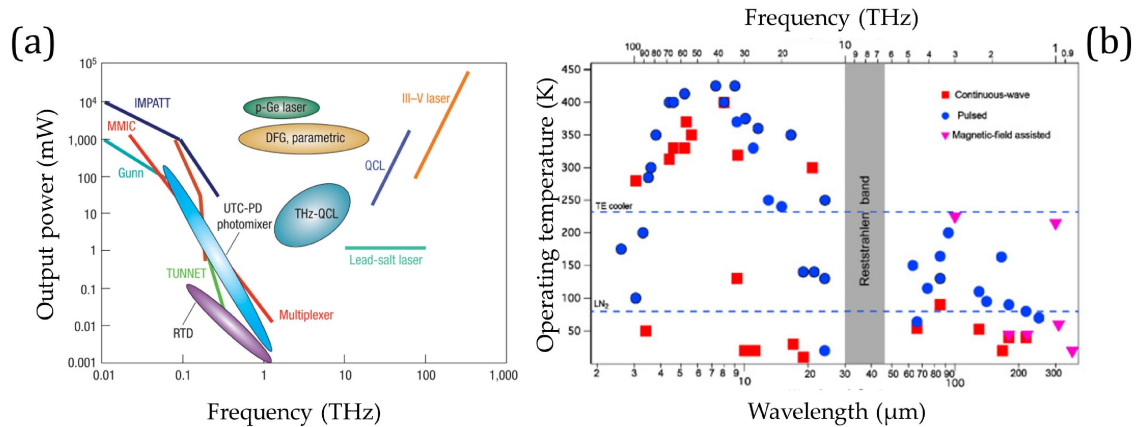


FIG. 1.3(a) State of art of THz sources (taken from [1]). (b) Spectral coverage and operating temperature of MIR and THz QCLs (taken from [7])

In the THz range, the c.w. emission power is in the tens of milliwatts as depicted in FIG. 1.3(a). At present, the spectral coverage of THz QCLs ranges from 1.2 THz to 4.9 THz (without applied magnetic field) [7]. Unfortunately THz QCLs are still limited to cryogenic operation: the highest temperature operation for a QCL in the THz frequency range is currently 199.5 K in pulsed mode [8]. To achieve room-temperature operation a new approach employs high-power two-color mid-IR QC-lasers for intracavity THz difference frequency generation where the intersubband transitions within the QC-laser material itself provide the χ^2 nonlinearity [9]. Large (but unpractical) facilities for generating high-power THz beams exist as well: the free-electron laser, which is important for fundamental science and the p-germanium laser, which can emit a peak power of 10 W in the frequency range from 1 to 4 THz.

1.1.2 THz detectors

Owing to the very low energy carried by THz photons (at room temperature: $k_B T = 25 \text{ meV}$ corresponding to $f \approx 6 \text{ THz}$) the thermal noise is the principal factor limiting the performances of THz detectors. Here we will review briefly the main available techniques to detect THz radiation following Refs.[2],[10].

The detection systems in the FIR range can be divided in *coherent detection systems*, where the signal amplitude and phase can be recovered, and *direct detection systems* which allow only to detect the signal amplitude.

A well-known coherent detection scheme is the *heterodyne detection* where THz signals are down-converted to lower frequencies ($f \approx 1\text{--}30 \text{ GHz}$) by non-linear mixing with a low frequency local oscillator and then amplified by low-noise amplifiers. To achieve efficient conversion and low noise, devices having a strong nonlinearity are employed such as Schottky barrier diodes (SBDs), superconductor-insulator-superconductor (SIS) tunnel junctions, semiconductor and superconducting hot electron bolometers (HEBs), and superlattices (SLs).

Coherent THz detection systems for time-domain spectroscopy (TDS) rely either on microstrip photoconductive antennas deposited on LT-GaAs or electro-optic crystals such as GaSe.

Direct THz detection systems include, instead, Golay cells and pyroelectric detectors (operating at room temperature), or bolometers and micro-bolometers (which employ antennas to couple power to small thermal sensing elements). These thermal detectors feature relatively long response times ($\tau \approx 10^{-2} \div 10^{-3} \text{ s}$) and modest sensitivity. The typical *noise equivalent power* (NEP) value for uncooled detectors is $\approx 10^{-10} \div 10^{-9} \text{ W} / \sqrt{\text{Hz}}$. The performances are remarkably improved using Helium-cooled bolometers (hot electron InSb, Si, Ge bolometers, extrinsic Si and Ge) with response times of $\tau \approx 10^{-6} \div 10^{-8} \text{ s}$ and $NEP \approx 10^{-13} \div 10^{-17} \text{ W} / \sqrt{\text{Hz}}$.

On the other hand, we observe that quantum THz detector technology is still greatly under-developed, as we will discuss in more details in Chapter 4.

1.1.3 Applications of THz radiation

Terahertz radiation is extremely interesting for applications as it is non-ionizing (as infrared radiation) while it can pass through non-conducting materials (as microwaves). Paper, wood, plastic, ceramics and clothing but also smoke or dust can be penetrated by T-rays whereas metal or water cannot [11].

A lot of gas molecules, such as biomolecules, explosives, narcotics, pollutants and especially water, have strong absorption lines in the terahertz range due to their rotational and vibrational modes [2].

Terahertz spectroscopy is then a powerful investigation tool in chemistry and biochemistry. In fact, intermolecular vibrations in some chemicals and organic molecules fall in the THz range enabling the study of the dynamics of large biomolecules. DNA identification and bio-sensing applications are investigated as well. [12]

Recently *THz time-domain spectroscopy* (THz-TDS) and *THz tomography* have enabled the characterization and imaging of samples that are opaque in the visible and near-infrared range.

Terahertz technology could transform the current *medical imaging* techniques which are based on X-rays as T-rays do not damage sensitively tissues and DNA. Terahertz radiation can be also used to probe the water content and density of a tissue. For instance, in this way one could detect epithelial cancers with a non-invasive and painless technology [13], [14].

Security applications are possible, since many illegal narcotics and explosives feature absorption lines in the terahertz region, whereas packaging and clothing are transparent for terahertz waves. For example, THz body scanners have been proposed to replace X-rays in security screenings to uncover hidden weapons on a person [3].

The terahertz technology has been historically very important for astronomy. It has been estimated than approximately 98% of the photons emitted since the “Big Bang” fall into the THz range. In so called *submillimetre astronomy*, researchers examine molecular clouds and dark cloud cores to understand the process of star formation from earliest collapse to stellar birth [15]. Terahertz measures on these clouds can

be used to determine chemical abundances and cooling mechanisms for the molecules which comprise them. In addition, submillimetre observations give information on the mechanisms for the formation and evolution of galaxies. The most significant limitation to the detection of astronomical emission at submillimetre wavelengths with earth-based observatories comes from atmospheric absorption, which enables detection only through discrete transparency windows. As a consequence, the challenge is building sophisticated THz space-based instruments. For a high resolution detection, highly sensitive heterodyne receivers featuring cw operation, frequency stable, narrowband and tunable are required.

Finally, the THz range is attracting increasing interest for *wireless communication* systems due to its immense available bandwidth. The channel capacity (C) of a communication link is proportional to the available bandwidth (B) as stated by Shannon's theorem $C = B \cdot \log_2(1 + SNR)$, revealing the obvious advantage of the terahertz band over the traditional microwave (MW) band for wireless applications [16], [17].

1.2 Intersubband transitions in semiconductor QWs

1.2.1 III-V heterostructures

In a pioneering work of 1970 Tsu and Esaki discovered that growing in alternation thin layers of two semiconductors with same lattice constant and different energy gap a periodic modulation of the conduction and valence bands is obtained [18]. In this so-called *heterostructure*, an artificial periodicity is superimposed to the natural periodicity of the crystal lattice which enables the control of carrier transport properties in the material. Today, thanks to the development of epitaxial growth techniques, such as molecular beam epitaxy (MBE) and metal organic chemical vapour deposition (MOCVD), it is possible to design artificial band structures to affect the motion of electrons and holes at will [19]. For instance, if a semiconductor layer of nanometric thickness is sandwiched between two layers of a high gap semiconductor, a quantum well-like potential is created blocking the carriers motion along the structure growth direction. The quantum well is only one example of *band-gap engineering* which has brought a tremendous impact in optoelectronic technology, the greatest success being the invention of the QCL in 1994 [20].

When two different semiconductors (with different energy gap and electron affinity) are brought together to form a heterostructure, at equilibrium the vacuum levels align. This means that at least one of the two band edges (conduction or valence) has to be discontinuous, according to Andersen's rule [21]. Commonly used heterostructures are of straddled type, meaning that the energy gap difference is divided in a conduction band offset ΔE_c and a valence band offset ΔE_v . Recalling that the conduction band profile represents the electron potential energy, an electron in the conduction band will see along the growth direction a succession of potential wells and barriers of height ΔE_c . In the following we will focus only on the motion of the electrons in the conduction band.

III-V semiconductors most widely employed in building heterostructures are gallium arsenide (GaAs), aluminium arsenide (AlAs) and indium arsenide (InAs) and their alloys (e.g. $\text{Al}_x\text{Ga}_{1-x}\text{As}$ where x is the Al mole fraction). To avoid mechanical stress in the formed heterostructure it is fundamental to use *lattice matched* materials.

The dominant heterostructure for THz devices is *GaAs / AlGaAs* grown on GaAs substrate having conduction band offset $\Delta E_c = 0.39\text{eV}$ and effective electron mass $m^*/m_e = 0.067$ [22].

1.2.2 Electron motion in a heterostructure. Quantum wells.

To describe the electronic motion in a heterostructure, the envelope function formalism in the Kane approximation is normally used [21], [23], [24].

The core of the envelope function approximation, which generalizes the $\vec{k} \cdot \vec{p}$ method for bulk semiconductors, is that the electronic wavefunction can be written as the product of a Bloch function of the material and an envelope function supposed slowly varying on a lattice period. In the basic case of a one-band model the electron wavefunction is

$$\psi_n(\vec{r}) = u_{\Gamma}^{B,W}(\vec{r}) \cdot f_n(\vec{r}) \quad (1.1)$$

where $u_{\Gamma}^B (u_{\Gamma}^W)$ is the conduction band wavefunction of the barrier (well) material at the Γ point of the Brillouin zone, $f_n(\vec{r})$ is the envelope function and the index n enumerates the eigenstates of the system [21].

In the Kane approximation, all the informations about the semiconductor band structure can be finally englobed in a (generally non constant) effective mass m^* while the electron motion in the artificial lattice is described by a slow-varying envelope function f_n satisfying Schrodinger's equation:

$$-\frac{\hbar^2}{2m^*} \nabla^2 f_n(\vec{r}) + V(\vec{r})f_n(\vec{r}) = E_n f_n(\vec{r}) \quad (1.2)$$

In the usual case of an epitaxial heterostructure the artificial potential is created only along the growth direction z meaning that $V(\vec{r}) = V(z)$. In this case, the electron motion is affected only in the z direction while it is free in the xy plane. Hence, equation (1.2) has solutions in the form

$$f_{n,\vec{k}_{\perp}}(\vec{r}) = \frac{1}{\sqrt{A}} e^{i\vec{k}_{\perp} \cdot \vec{r}} \varphi_n(z) \quad (1.3)$$

where $\vec{k}_{\perp} = (k_x, k_y)$ is the transverse electron wavevector and A is the sample area; equation (1.2) reduces to a 1D Schrodinger equation

$$-\frac{\hbar^2}{2m^*} \frac{d^2 \varphi_n}{dz^2} + V(z)\varphi_n(z) = E_n \varphi_n(z) \quad (1.4)$$

The electron available energy states are then

$$E_{n,\vec{k}_\perp} = E_n + \frac{\hbar^2 \vec{k}_\perp^2}{2m^*} \quad (1.5)$$

The discrete eigenvalues E_n depend on the form of the potential $V(z)$. For example, in the case of an infinite quantum well of width L we have

$$E_n = \frac{n^2 \pi^2 \hbar^2}{2m^* L^2} \quad (1.6)$$

We say that the energy states given by (1.5) are organized in *electronic subbands*: each subband comprises the electronic states corresponding to the same quantum state for the motion along z (confined) and different transverse wavevectors \vec{k}_\perp representing the free motion in the xy plane. The ensemble of the electrons populating a subband is often defined as a *two-dimensional electron gas* (2DEG).

1.2.3 Light-matter interaction in a quantum well: intersubband transitions

We consider now the optical transitions that an external EM field can induce between two quantum states $|i\rangle$ and $|f\rangle$ in a QW. The main results will be recalled here, referring to [23] for a complete description. The transition rate can be calculated from the Fermi golden rule in the dipolar approximation ($\lambda_{em} \gg \text{size QW}$) to yield

$$W_{if} = \frac{2\pi}{\hbar} \frac{e^2 E_0^2}{4m^{*2} \omega^2} \left| \langle i | \hat{e} \cdot \vec{p} | f \rangle \right|^2 \delta(E_f - E_i - \hbar\omega) \quad (1.7)$$

where a polarized plane wave in the form $\vec{E} = E_0 \hat{e} \cos(\vec{q} \cdot \vec{r} - \omega t)$ is taken. Following [21] and recalling that the states have the form (1.1) the matrix element in (1.7) can be split in two parts

$$\langle i | \hat{e} \cdot \vec{p} | f \rangle = \hat{e} \cdot \langle u_v | \vec{p} | u_{v'} \rangle \langle f_n | f_{n'} \rangle + \hat{e} \cdot \langle u_v | u_{v'} \rangle \langle f_n | \vec{p} | f_{n'} \rangle \quad (1.8)$$

where (v, v') and (n, n') denote respectively the bands and subbands initial and final states. The first term describes *interband transitions* (i.e. transitions from valence to conduction band). The second term, more interesting for us, describes *intersubband (ISB) transitions* within the same band. Expliciting the latter yields:

$$\langle f_{n,\vec{k}_\perp} | \hat{e} \cdot \vec{p} | f_{n',\vec{k}'_\perp} \rangle = \frac{1}{A} \int d\vec{r} e^{-i\vec{k}_\perp \cdot \vec{r}} \varphi_n^*(z) [e_x p_x + e_y p_y + e_z p_z] e^{+i\vec{k}'_\perp \cdot \vec{r}} \varphi_{n'}(z) \quad (1.9)$$

from which it is apparent that only the term containing e_z gives non zero contribution at finite frequency. The relevant matrix element for ISB transitions is then

$$\langle n | p_z | n' \rangle = \int dz \varphi_n^*(z) p_z \varphi_{n'}(z) \quad (1.10)$$

This result implies the well-known *polarization selection rule* of ISB transitions: optical transitions between confined states in QWs can be excited only by an electric field having a non-zero component in the heterostructure growth direction.

For this reason, photonic structures have to be used to provide a non-zero electric-field component perpendicular to the QW layers, such as diffraction gratings and antennas. For preliminary characterizations on epitaxial QW samples, a common experimental scheme is Brewster's angle transmission; unfortunately for GaAs samples this technique is suitable only for highly doped QWs, since $\theta_B = 17^\circ$ which yields a poor E_z component. For samples exhibiting weaker absorption a multipass waveguide geometry is normally employed, where the light is coupled into the sample at the edges, which are polished at a certain angle, and then undergoes several total internal reflections in the sample. The advantage of this configuration is that the reflection loss of the incident light is the same for both TM and TE polarizations, which is convenient for taking reference spectra (the TM polarization couples to the ISB transition, whereas the TE polarization doesn't).

Note: the ISB matrix element (1.10) is usually englobed in the adimensional oscillator strength which quantifies the intensity of a ISB transition

$$f_{nn'} = \frac{2m^* \omega_{n'n}}{\hbar} |\langle n|z|n' \rangle|^2 \quad (1.11)$$

Using the completeness of the eigenstates $\varphi_n(z)$ it can be shown that the following sum rule holds for the transitions departing from the n-th subband:

$$\sum_{n'} f_{nn'} = 1 \quad (1.12)$$

If we take the effective mass m^* out of the sum one can equivalently write

$$\sum_{n'} \tilde{f}_{nn'} = \frac{1}{m^*} \quad (1.13)$$

where the $\tilde{f}_{nn'}$ contains m_0 instead of m^* in the definition (1.11). Written in this fashion the sum rule highlights that the overall ISB absorption intensity scale as $1/m^*$ and is therefore dependent on the material system employed.

1.3 Optical properties of materials

1.3.1 Lorentz oscillator model

The most effective approach to describe the interaction between light and matter is the semi-classical Lorentz oscillator model. In Lorentz model the optical properties of matter arise from different types of oscillating dipoles within a medium, which are treated as damped harmonic oscillators. *Bound electrons* within the atoms are mainly responsible for properties of insulators/semiconductors at optical frequencies. Then there are *vibrational oscillators* in ionic media, resonating at lower frequencies in the infrared spectral region, and *free electron oscillators*, responsible for the optical properties of metals. Here we summarize the derivation of the main useful results of the model for our purpose, following Fox's book [25]. Consider an electronic dipole of mass m_0 and charge e elastically bound to the nucleus and be ω_0 its natural resonant frequency. The motion of the electron subject to a time-harmonic driving field is described by the following equation for the electron displacement x

$$m_0 \frac{d^2 x}{dt^2} + m_0 \gamma \frac{dx}{dt} + m_0 \omega_0^2 x = -e E_0 e^{-j\omega t} \quad (1.14)$$

where γ is the damping, ω is the angular frequency of the driving field and E_0 is its amplitude. The terms on the left-hand side represent the charge acceleration, the frictional force damping the motion and the restoring force respectively. The term on the right-hand side represents the driving force due to the AC electric field of the light wave. The forced oscillations induced by the field will be in the harmonic form $x = x_0 e^{-j\omega t}$. Substituting in (1.14) the displacement amplitude x_0 is found

$$x_0 = \frac{-e E_0 / m_0}{\omega_0^2 - \omega^2 - j\gamma\omega} \quad (1.15)$$

The displacement of the electron from its equilibrium position creates a time-varying dipole moment $p(t) = -ex(t)$ which gives a *resonant* contribution to the macroscopic polarization $P_{resonant}(t) = -Nex(t)$ where N is the number of atoms per unit volume. The electric displacement \vec{D} of the medium is related to the electric field \vec{E} through

$$\vec{D} = \epsilon_0 \vec{E} + \vec{P}_{background} + \vec{P}_{resonant} = \epsilon_0 \vec{E} + \epsilon_0 \chi \vec{E} + \vec{P}_{resonant} = \epsilon_0 \epsilon_r \vec{E} \quad (1.16)$$

where the material polarization is splitted into a non-resonant background term and the resonant term due to the oscillator. The electric susceptibility χ accounts for all other contribution to the polarization of the material. The global response of the medium is given by the dielectric function

$$\varepsilon_r(\omega) = 1 + \chi + \frac{Ne^2}{\varepsilon_0 m_0} \frac{1}{(\omega_0^2 - \omega^2 - j\gamma\omega)} \quad (1.17)$$

We can split (1.17) into its real and imaginary part

$$\varepsilon_1(\omega) = \text{Re}[\varepsilon_r(\omega)] = 1 + \chi + \frac{Ne^2}{\varepsilon_0 m_0} \frac{\omega_0^2 - \omega^2}{(\omega_0^2 - \omega^2)^2 + (\gamma\omega)^2} \quad (1.18)$$

$$\varepsilon_2(\omega) = \text{Im}[\varepsilon_r(\omega)] = \frac{Ne^2}{\varepsilon_0 m_0} \frac{\gamma\omega}{(\omega_0^2 - \omega^2)^2 + (\gamma\omega)^2} \quad (1.19)$$

We can recast (1.18) and (1.19) in a simplified form in the quasi-resonance approximation $\omega \approx \omega_0 \gg \gamma$ and introducing the low-frequency (static) and high-frequency limits for $\varepsilon_r(\omega)$

$$\varepsilon_{st} = \varepsilon_r(\omega \rightarrow 0) = 1 + \chi + \frac{Ne^2}{\varepsilon_0 m_0 \omega_0^2} \quad (1.20)$$

$$\varepsilon_\infty = \varepsilon_r(\omega \rightarrow \infty) = 1 + \chi \quad (1.21)$$

The simplified formulas for ε_1 and ε_2 as a function of the resonance detuning $\Delta\omega = \omega - \omega_0$ are

$$\varepsilon_1(\Delta\omega) = \varepsilon_\infty - (\varepsilon_{st} - \varepsilon_\infty) \frac{2\omega_0 \Delta\omega}{4(\Delta\omega)^2 + \gamma^2} \quad (1.22)$$

$$\varepsilon_2(\Delta\omega) = (\varepsilon_{st} - \varepsilon_\infty) \frac{\gamma\omega_0}{4(\Delta\omega)^2 + \gamma^2} \quad (1.23)$$

These equations describe a sharp atomic absorption line centred at ω_0 with full width at half maximum equal to γ . ε_1 and ε_2 are related to the refractive index n and the extinction coefficient κ of the medium through

$$\varepsilon_1 = n^2 - \kappa^2 \quad (1.24)$$

$$\varepsilon_2 = 2n\kappa \quad (1.25)$$

The plots of $\varepsilon_1, \varepsilon_2, n, \kappa$ for undoped GaAs are reported in FIG. 1.4. We can see that ε_2 is a strongly peaked function of ω with a maximum value at ω_0 and a full width at half maximum equal to γ . The frequency dependence of ε_1 is more complicated: approaching ω_0 from low frequency, it rises from the value ε_{st} reaching a peak at $\omega_0 - \gamma/2$, then falls sharply passing through a minimum at $\omega_0 + \gamma/2$ before rising again to the high-frequency limit ε_∞ . One important aspect of a resonant Lorentzian dipole is that the effect on the refractive index occurs over a larger frequency range

than on the absorption. In fact, the absorption dependency falls rapidly as $\sim 1/(\Delta\omega)^2$ away from resonance, meaning that there is a significant absorption only around ω_0 . On the other side, the frequency dependence of the refractive index varies more slowly as $\sim 1/\Delta\omega$: a material resonance affects the refractive index even far away from resonance.

1.3.2 GaAs dielectric function

In III-V semiconductors, like GaAs, the atoms are arranged in a zinc blende crystal structure by bonds of mainly covalent nature. The chemical bond shows a partial ionic character because the shared electrons lie slightly closer to group V atoms than to group III. This character is called *polar* to highlight that the asymmetric electron cloud creates a dipole moment that can interact with electric fields. In fact, it is known that these *covalent polar crystals* show strong absorption and reflection bands in the infrared spectral range when the frequency is close to *transverse optical* (TO) phonon modes of the crystal. The polar character of the chemical bond makes III-V semiconductors TO phonon modes IR active, a fact that strongly affects the optical response of these materials in the infrared range.

The interaction between an EM wave and TO phonons can be modelled introducing a damped TO phonon oscillator of frequency ω_{TO} in the Lorentz model, which yields a dielectric function response in the form (1.17)

$$\varepsilon_r(\omega) = 1 + \chi + \frac{Ne^2}{\varepsilon_0 m_0} \frac{1}{(\omega_{TO}^2 - \omega^2 - j\gamma_{ph}\omega)} = \varepsilon_\infty + (\varepsilon_{st} - \varepsilon_\infty) \frac{\omega_{TO}^2}{\omega_{TO}^2 - \omega^2 - j\gamma_{ph}\omega} \quad (1.26)$$

where γ_{ph} is the damping of the phonon mode. If we recall the Lyddane-Sachs-Teller relation

$$\frac{\omega_{LO}^2}{\omega_{TO}^2} = \frac{\varepsilon_{st}}{\varepsilon_\infty} \quad (1.27)$$

we can recast (1.26) in the form

$$\varepsilon_r^{ph}(\omega) = \varepsilon_\infty \left(1 + \frac{\omega_{LO}^2 - \omega_{TO}^2}{\omega_{TO}^2 - \omega^2 - j\omega\gamma_{ph}} \right) \quad (1.28)$$

The real and imaginary part of (1.28) are shown in FIG. 1.4 together with the refractive index and extinction coefficient for undoped GaAs. The model parameters are extracted from the fit with (1.28) of experimental datas [26] yielding $\varepsilon_\infty = 11.1$, $\nu_{TO} = 8.05$ THz, $\nu_{LO} = 8.75$ THz and $\gamma_{ph} = 4.07 \cdot 10^{13}$ 1/s.

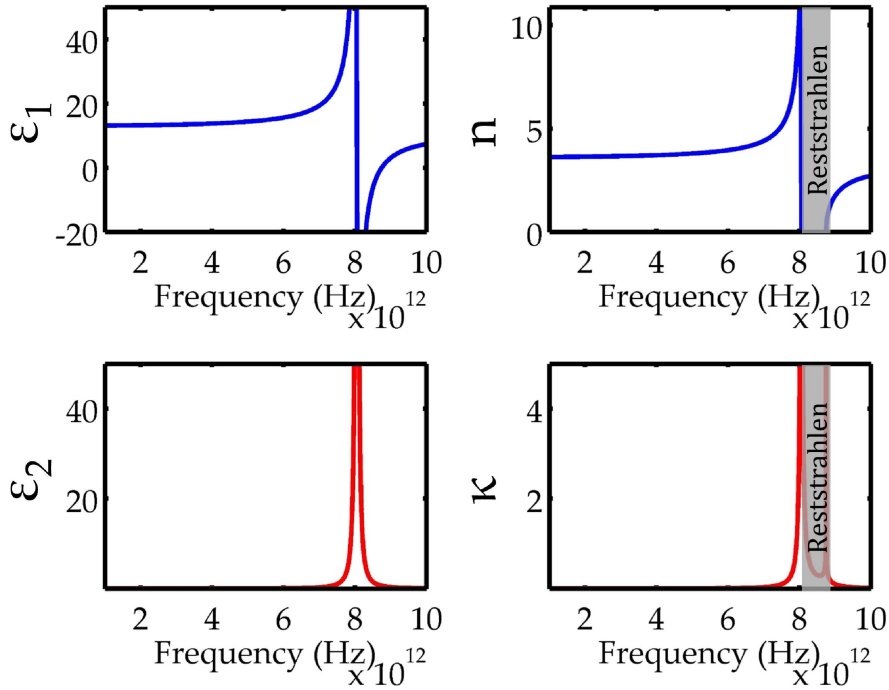


FIG. 1.4 Optical constants derived from the Lorentz model for undoped GaAs. The Reststrahlen band is delimited by the frequencies $\nu_{TO} = 8.05$ THz and $\nu_{LO} = 8.75$ THz

Note that between ν_{TO} and ν_{LO} , ϵ_r is negative and $\sqrt{\epsilon_r}$ is imaginary. In this frequency band, known as *Reststrahlen band*, light cannot propagate into the medium and is completely reflected.

1.3.3 Gold dielectric function. Skin depth.

Metals feature unique properties as electrical conductors due to their valence electrons being essentially free. Indeed, a metallic medium can be described as a *plasma* as it contains an equal number of fixed positive ions and free electrons moving in the lattice. The free electron model of metals was proposed by Drude in 1900. When an electric field is applied, the free electrons accelerate and then undergo collisions with a characteristic scattering time $\tau_{met} = 1/\gamma_{met}$. Therefore the electrical conductivity σ is limited by the scattering mechanisms.

The permittivity function of a metal can be again derived from the Lorentz dipole model where the restoring force term is now dropped as the electrons are free to move in the lattice under an applied field. This approach is known as Drude-Lorentz model as it combines the Drude free electron model of metals with the Lorentz oscillator model. The equation of motion for the displacement of a free electron of mass m_0 and charge e forced by an external AC field is then

$$m_0 \frac{d^2x}{dt^2} + m_0 \gamma_{met} \frac{dx}{dt} = -eE_0 e^{-i\omega t} \quad (1.29)$$

where γ_{met} is the metal damping, ω is the angular frequency of the incoming field, and E_0 is its amplitude. Proceeding in analogy to 1.3.1 we find for the dielectric function

$$\varepsilon_r(\omega) = 1 - \frac{Ne^2}{\varepsilon_0 m_0} \frac{1}{(\omega^2 + j\gamma_{met}\omega)} = 1 - \frac{\omega_p^2}{(\omega^2 + j\gamma_{met}\omega)} \quad (1.30)$$

where we define the *plasma frequency*

$$\omega_p = \sqrt{\frac{Ne^2}{\varepsilon_0 m_0}}. \quad (1.31)$$

We recall that the optical properties of a metal are equivalently described by the AC conductivity σ , related to ε_r by

$$\varepsilon_r(\omega) = 1 + \frac{j\sigma(\omega)}{\varepsilon_0 \omega} \quad (1.32)$$

In the top panel of FIG. 1.5 the real and imaginary parts of ε_r and σ of gold are plotted at THz frequencies. Gold will be the metal of choice in this work due to its very good conductivity and yield for long-lasting optoelectronic devices. The Drude-Lorentz model parameters for gold are obtained by fitting experimental data measured in the IR range [27]: the plasma frequency is $f_p = 2.17 \cdot 10^{15}$ Hz and the plasma damping is $\gamma_{met} = 6.48 \cdot 10^{12}$ Hz. This last value is really important because it constitutes *de facto* the separation line between the electronic and plasmonic regime as we will see in Chapter 2. In the bottom panel of FIG. 1.5 the reflectivity $R = |(n-1)/(n+1)|^2$ is plotted over a large frequency range showing how the optical properties of a metal change in the UV range, from almost perfect reflection to transparency.

In the same fashion a plasma contribution can be added in the dielectric function of a semiconductor to account for *doping*. This gives:

$$\varepsilon_r^{plasma}(\omega) = \varepsilon_\infty \left(1 - \frac{\omega_p^2}{\omega^2 + j\omega/\tau} \right) \quad (1.33)$$

with a doping-related plasma frequency

$$\omega_p = \sqrt{\frac{n_e \cdot e^2}{\varepsilon_\infty \cdot \varepsilon_0 \cdot m^*}} \quad (1.34)$$

where ε_∞ is the high-frequency dielectric constant, m^* is the effective electron or hole mass and n_e is the 3D doping in the material. The contribution (1.33) may be added to (1.28) to provide a complete dielectric function for doped GaAs in the THz range

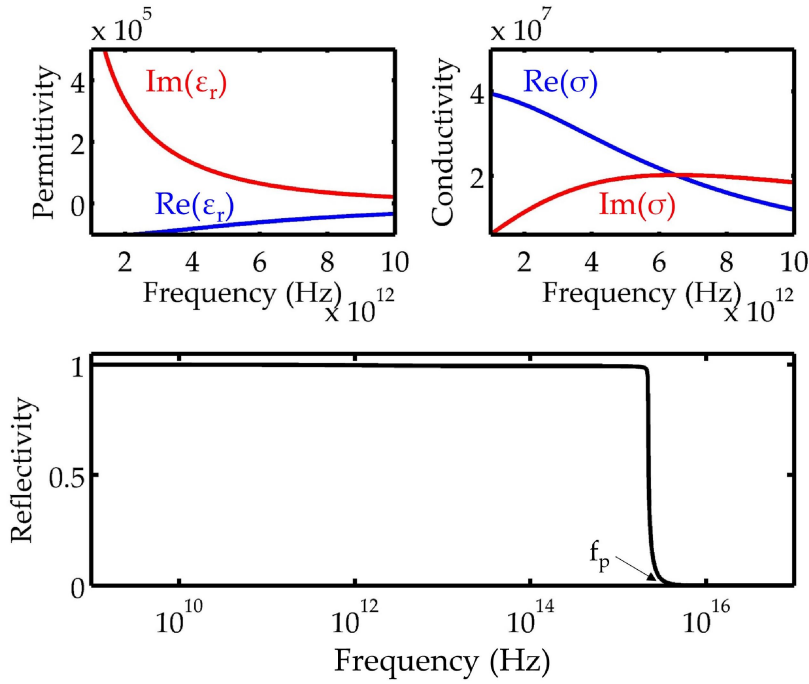


FIG. 1.5 Top: permittivity and conductivity functions for gold in the THz range; bottom: gold reflectivity up to UV range.

From (1.30) it can be shown that an AC field can penetrate only a short distance into a metal (or doped semiconductor), which is the well-known *skin effect*. The (frequency-dependent) *skin depth* is given by

$$\delta = \sqrt{\frac{2}{\sigma_0 \omega \mu_0}} \quad (1.35)$$

where σ_0 is the DC (static) metal conductivity. For example, at 3 THz the skin depth for gold is $\delta = 42$ nm knowing that $\sigma_0 = 4.1 \cdot 10^7 \text{ } \Omega^{-1} \text{m}^{-1}$.

1.3.4 Surface plasmons. Subwavelength confinement of radiation

Surface plasmons are localized electromagnetic modes localized at the interface between a metal and a dielectric. They originate from the collective oscillations of the free electron gas density in the metal as sketched in FIG. 1.6(a). The charge fluctuations in the metal generate electric field lines having both longitudinal and transverse components, meaning that plasmons can interact directly with photons. Actually, this interaction is sufficiently strong that we need to consider the photon and plasmon as a coupled system, i.e. a polariton. For that, we name more precisely these modes as surface plasmons-polaritons (SPPs). Interest in surface plasmons has increased dramatically in recent years, opening a new research field called *plasmonics*. One of the aims of the research field of plasmonics is to propagate EM waves as surface plasmon polaritons. In the following we will summarize the most important features of SPPs following Fox's book [25].

Suppose to define axes so that the plane $z=0$ corresponds to the interface, with positive and negative z corresponding to the dielectric and metal respectively. The wave is assumed to be propagating in the x direction and the electric field has components in both the x and z directions as pictured in FIG. 1.6(a). The EM field of SPPs at a dielectric-metal interface is obtained by solving Maxwell's equations in each medium with appropriate boundary conditions. First, the continuity of the tangential components of the electric and magnetic fields across the interface has to be verified. Then, the field amplitude must decay on either side when we get far from the interface.

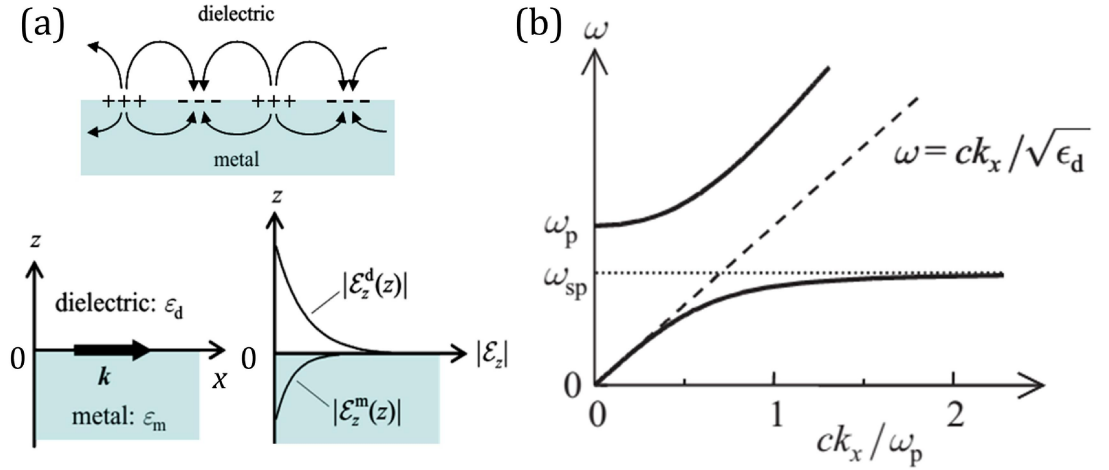


FIG. 1.6(a) Top: Sketch of plasma resonance; bottom: schematics of SPPs propagation and field penetration. (b) SPPs dispersion relation. Reproduced from Ref. [25].

The SPPs modes verifying the conditions above must have wave-vectors of magnitude (for the full calculation see [25], [28])

$$k_x = \frac{\omega\sqrt{\epsilon_d}}{c} \sqrt{\frac{\epsilon_m}{\epsilon_m + \epsilon_d}}. \quad (1.36)$$

This equation gives the dispersion relation for SPPs reported in FIG. 1.6(b). In this dispersion the relative permittivity of the dielectric ϵ_d is assumed to be real and independent of frequency while the metal permittivity ϵ_m has the form seen in (1.30). The dashed line is the light line for the propagation in the dielectric $\omega = ck_x / \sqrt{\epsilon_d}$. We are interested in the propagating modes below the plasma frequency ω_p . This branch of the dispersion curve shows that at low frequencies the SPP mode lies close to the light line and is light-like. As frequency increases, the mode moves away from the light line, gradually approaching an asymptotic limit. This occurs for $k_x \rightarrow \infty$ when the permittivities in the two media are of the same magnitude but opposite sign. The asymptotes are

$$\begin{cases} k_x \rightarrow \frac{\omega}{c} \sqrt{\epsilon_d} & \text{as } \omega \rightarrow 0 \\ k_x \rightarrow \infty & \text{as } \omega \rightarrow \omega_{sp} \end{cases} \quad (1.37)$$

where the *surface plasmon frequency* (neglecting plasma damping $\gamma_{met} = 0$) is given by

$$\omega_{sp} = \frac{\omega_p}{\sqrt{1 + \epsilon_d}} . \quad (1.38)$$

Note that the SPP dispersion lies in a region to the right of the light line (in the dielectric) where the k_x values are larger than the wave number of propagating EM waves: $k_x > \omega\sqrt{\epsilon_d}/c$. Therefore, SPPs modes are *non-radiative* (or bound) as they do not have a propagating component in the z direction (i.e. k_z is purely imaginary or evanescent). This implies that is not possible to couple light directly from the dielectric into SPP modes, since the wave vectors are not matched. In order to couple external light into a SPP mode, techniques must be used to match the incoming wavevector (e.g. gratings, prisms). Indeed, the observed drop in the reflectivity of a metallic grating when one of the diffracted orders propagates parallel to the surface has puzzled scientists for many years. This experimental evidence, known as *Wood's anomaly* [29], is now explained as due to the excitation of SPPs modes.

The most striking feature provided by surface plasmon modes is the possibility to squeeze light to subwavelength dimensions. To see this we have to consider the penetration depth into the dielectric, δ_d , or into the metal, δ_m , defined as the distance in the z direction from the interface over which the field intensity is reduced by a factor of e . From Lambert-Beer law it follows that the penetration depth is inversely proportional to the imaginary part of the z component of the wave vector $\delta = 1/2|k_z|$. It can be shown that [28]

$$\frac{\delta_m}{\delta_d} \approx \left| \frac{\epsilon_d}{\epsilon_m} \right| . \quad (1.39)$$

This means that the penetration depth in the metal is always smaller than in the dielectric. At low frequencies ($\omega \ll \omega_{sp}$) the penetration depth in the metal is much smaller than in the dielectric and is commonly approximated using the skin depth formula, whereas in the high-frequency limit with ($\omega \rightarrow \omega_{sp}$) the penetration depths in the two media become comparable.

At optical frequencies, the penetration depth in the dielectric δ_d and in the metal δ_m are respectively a few hundred and few tens of nanometres. With values of δ_m being in the sub-100nm range, SPPs modes enable the confinement of EM waves to dimensions much smaller than the wavelength of light. The subwavelength confinement provided by SPP modes thanks to the optical properties of metals has opened the realm of *nanophotonics*, which is not accessible to conventional optics due to diffraction limits.

1.3.5 Engineering the optical response: metamaterials

In this paragraph we will introduce the concept of electromagnetic metamaterial following [25]. We know that the optical properties of usual materials (dielectric, metals) are intimately related to their microscopic structure, reflected in their permittivity function ϵ_r . At the same time there are no known natural materials featuring $\mu_r \neq 1$ at infrared and optical frequencies, the natural resonances of magnetic dipoles in common media being not beyond the GHz range. For example, we saw that the presence of phonon modes in III-V semiconductors such as GaAs strongly affects the optical response in the THz range. Far from the zones where material dipoles are active, the optical constant of a transparent (dielectric) medium is real and positive. This corresponds to the first quadrant of the scheme in FIG. 1.7(a). Similarly, all the properties of metals below the plasma frequency arise from the fact that the real part of the permittivity ϵ_r is negative (while $\mu_r = 1$). This implies that the refractive index $\tilde{n} = \sqrt{\epsilon_r \mu_r}$ is purely imaginary: there are no propagating solutions in the medium and incoming waves from the air are reflected. The same would happen in a medium having $\mu_r < 0$ and $\epsilon_r > 0$. These situations occur in quadrants II and IV respectively..

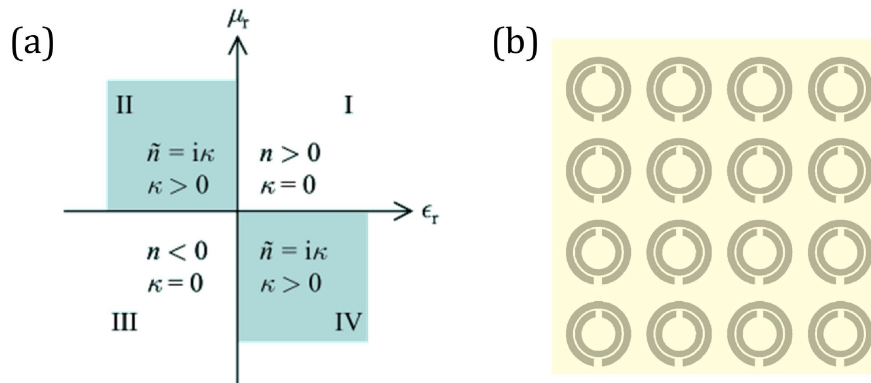


FIG. 1.7(a) Optical constants (ϵ_r, μ_r) plane. (b) Pendry's split ring resonators. From Ref. [25].

It is interesting to consider what happens in quadrant III, where both ϵ_r and μ_r are negative. This situation was first considered by Veselago in 1968, who concluded that a medium with $(\epsilon_r, \mu_r) < 0$ would be transparent, and have a *negative refractive index*. A material with $n < 0$ would show negative light refraction according to Snell's law and behave then like a perfect flat lens. We know that metals have negative values of ϵ_r at most frequencies, and so the issue is obtaining the negative value of μ_r . As said above, natural materials do not possess this property at infrared or optical frequencies. The only solution is to engineer the negative refractive index employing an artificial electromagnetic structure. Pendry was the first to propose a practical design of an artificial electromagnetic medium with a negative refractive index [30]. The breakthrough idea was to create a metallic structure acting like a magnetic dipole resonator. Inspired from small resonators already used in GHz and MHz applications, the split-ring geometry (the original design is shown in FIG. 1.7(b)) was adopted as fundamental building block for implementing $\mu_r < 0$ media. Here one can play

on the design of the elementary *split rings* (basically acting as subwavelength LC circuits) to set the overall magnetic response. The resulting “effective” medium is called a *metamaterial* due to the fact that the constituent units are smaller than the operating wavelength, but larger than the underlying atoms.

Later we will explore in detail the split-ring geometry to implement novel THz devices. However we will mainly focus on the split-ring as a single resonating object, featuring subwavelength dimensions and circuit tunability. We will just barely consider it as elementary “meta-atom” to exploit for obtaining exotic optical properties in an effective medium approach.

1.4 Photonic resonators for THz devices

1.4.1 The Helmholtz equation: electromagnetic waves.

In this paragraph we will recall the derivation of Helmholtz wave equation and its solution in free space following Pozar’s book [31].

In a source-free, linear, isotropic and homogeneous region, Maxwell’s curl equations for time-harmonic fields are

$$\begin{aligned}\vec{\nabla} \times \vec{E} &= -j\omega\mu\vec{H} \\ \vec{\nabla} \times \vec{H} &= j\omega\varepsilon\vec{E}\end{aligned}\tag{1.40}$$

We have then two equations for the two unknowns \vec{E} and \vec{H} . Taking the curl of the first equation and using the second gives

$$\vec{\nabla} \times \vec{\nabla} \times \vec{E} = -j\omega\mu\vec{\nabla} \times \vec{H} = \omega^2\mu\varepsilon\vec{E}\tag{1.41}$$

Recalling the vector identity $\vec{\nabla} \times \vec{\nabla} \times \vec{A} = \vec{\nabla}(\vec{\nabla} \cdot \vec{A}) - \nabla^2\vec{A}$ and owing to the fact that $\vec{\nabla} \cdot \vec{E} = 0$ in a source-free region we have

$$\nabla^2\vec{E} + \omega^2\mu\varepsilon\vec{E} = 0\tag{1.42}$$

This equation is known as *Helmholtz* or *wave equation*. An identical equation can be written for the magnetic field

$$\nabla^2\vec{H} + \omega^2\mu\varepsilon\vec{H} = 0\tag{1.43}$$

The *propagation constant* (aka *wave number* or *spatial frequency*) in the medium is defined as $k = \omega\sqrt{\mu\varepsilon} = nk_0$ where n is the refractive index of the medium (supposed non-magnetic) and $k_0 = \omega/c$ is the free space propagation constant. We look for solutions of Helmholtz equation in free space

$$\nabla^2\vec{E} + k_0^2\vec{E} = \frac{\partial^2\vec{E}}{\partial x^2} + \frac{\partial^2\vec{E}}{\partial y^2} + \frac{\partial^2\vec{E}}{\partial z^2} + k_0^2\vec{E} = 0\tag{1.44}$$

This wave equation holds for each cartesian component of the electric field

$$\frac{\partial^2 E_i}{\partial x^2} + \frac{\partial^2 E_i}{\partial y^2} + \frac{\partial^2 E_i}{\partial z^2} + k_0^2 E_i = 0 \quad (i=x,y,z) \quad (1.45)$$

and can be solved by the *method of separation of variables* for partial differential equations. Assuming that the solution of (1.45), say E_z can be written as a product of three functions for each of the three coordinates:

$$E_z(x, y, z) = f(x) \cdot g(y) \cdot h(z) \quad (1.46)$$

one can separate (1.45) in three ordinary 1D differential equations

$$\frac{d^2 f}{dx^2} + k_x^2 f = 0; \quad \frac{d^2 g}{dy^2} + k_y^2 g = 0; \quad \frac{d^2 h}{dz^2} + k_z^2 h = 0 \quad (1.47)$$

where three separate propagation constants have been defined, so that

$$k_x^2 + k_y^2 + k_z^2 = k_0^2 . \quad (1.48)$$

Solutions of (1.47) are *plane waves* in the forms $e^{\pm jk_x x}$, $e^{\pm jk_y y}$ and $e^{\pm jk_z z}$ respectively where by convention the – signs represent propagation in the positive x, y or z direction while the + signs propagation in the negative direction. As a matter of fact, the amount to which these various terms are excited depends on the source of the fields and the boundary conditions.

Unguided electromagnetic waves in free space (or in a bulk isotropic dielectric) can be thought as a superposition of plane waves, generally described by a 3D electric field

$$\vec{E} = \vec{E}_0 e^{-j\vec{k} \cdot \vec{r}} \quad (1.49)$$

Owing to Gauss's law in absence of charges the electric field must satisfy

$$\vec{k} \cdot \vec{E}_0 = 0 \quad (1.50)$$

meaning that the electric field amplitude vector \vec{E}_0 must be perpendicular to the direction of propagation \vec{k} . The associated magnetic field may be found from Faraday's law to give

$$\vec{H} = \frac{1}{\eta_0} \hat{n} \times \vec{E} \quad (1.51)$$

where $\eta_0 = \sqrt{\mu_0 / \epsilon_0} = 377\Omega$ is the free-space impedance.

This result shows that the magnetic field vector \vec{H} lies in a plane normal to the direction of propagation \vec{k} and is perpendicular to \vec{E} . Therefore EM radiation propagates in free space as *transverse electromagnetic (TEM)* waves.

Conversely, electromagnetic waves can be bound in one or more directions by dielectric discontinuities or conducting boundaries. This is what happens in *waveguides* (coaxial cables, optical fibers, ...) where specific boundary conditions are imposed by the guide physical structure; in this case characteristic transverse mode patterns are imposed to waves propagating at a certain frequency.

1.4.2 The parallel plate waveguide

Waveguides are structures that confine and direct electromagnetic radiation. A simple type of waveguide consists in two perfectly conducting infinite parallel plates between which EM waves are guided. We will derive the guided modes of the structure following Staelin, Morgenthaler and Kong book [32]. Suppose that the plates are separated by a distance d filled with a medium of constants (ϵ, μ) , as shown in the sketch of FIG. 1.8(a). This structure supports transverse magnetic (TM) waves ($H_x = 0, E_x \neq 0$) and transverse electric (TE) waves ($E_x = 0, H_x \neq 0$).

We first recall the behaviour of a TM wave reflected from a perfectly conducting surface located at $z=0$ (see schematics in FIG. 1.8(b)). The incident wave is described by a magnetic field in the form

$$\vec{H}_{inc} = \hat{y}H_0 e^{-jk_x x + k_z z} \quad (1.52)$$

where $k_z = k_0 \cos \theta_{inc}$ and $k_x = k_0 \sin \theta_{inc}$. Recalling that the magnetic field has to be purely tangential at a conducting boundary, the reflected wave is given by

$$\vec{H}_{ref} = \hat{y}H_0 e^{-jk_x x - k_z z} \quad (1.53)$$

assuming perfect reflection from the plate. Note that both incident and reflected waves obey the same dispersion relation

$$k_x^2 + k_z^2 = k_0^2 = \omega^2 \mu \epsilon \quad (1.54)$$

The total magnetic field is the sum of (1.52) and (1.53)

$$\vec{H} = \vec{H}_{inc} + \vec{H}_{ref} = \hat{y}2H_0 \cos(k_z z) e^{-jk_x x} \quad (1.55)$$

which gives rise to an electric field (from Ampère's law) in the form

$$\vec{E} = \frac{\vec{\nabla} \times \vec{H}}{j\omega\epsilon} = \frac{1}{j\omega\epsilon} \left(-\hat{x} \frac{\partial}{\partial z} + \hat{z} \frac{\partial}{\partial x} \right) H_y = 2\eta H_0 \left(\hat{x} \frac{k_z}{k_0} \sin(k_z z) - \hat{z} \frac{jk_x}{k_0} \cos(k_z z) \right) e^{-jk_x x} \quad (1.56)$$

We note that these electric and magnetic field do satisfy the boundary conditions that the tangential \vec{E} field and normal \vec{H} field must vanish at a conducting boundary, i.e. $E_x = E_y = H_z = 0$ at $z=0$. Moreover, these boundary conditions are also satisfied at any value $x=d$ such that $\sin(k_z d) = 0$ i.e. $k_z d = m\pi$ where m is an integer. This means that a second perfect conductor can be inserted at these special d values without disturbing the existing field. An electromagnetic TM wave can then be confined and guided in the region $0 \leq z \leq d$ between the conducting plates while \vec{E} and \vec{H} vanish outside. Each of the infinite set of TM modes is designated as TM_m where $k_z = m\pi/d$ for the m^{th} mode. In a similar way we can find that the structure supports TE modes with the same discrete set of wavenumbers. Finally, for both TM and TE waves the guidance condition is

$$k_z d = m\pi \quad (1.57)$$

where $m=0, 1, 2, \dots$ for TM modes and $m=1, 2, \dots$ for TE modes. These modes behave as standing waves in the plane transverse to the direction of propagation \hat{x} . From (1.54) the dispersion relation for the parallel-plate waveguide is

$$k_x = \sqrt{\omega^2 \mu \epsilon - (m\pi/d)^2} \quad (1.58)$$

We must highlight that the zeroth order TM_0 mode exists when $k_z = 0$ and $k_x = k_0$ from (1.54) with fields in the form

$$\begin{aligned} \vec{E} &= \hat{z} 2\eta H_0 e^{-jk_x x} \\ \vec{H} &= \hat{y} 2H_0 e^{-jk_x x} \end{aligned} \quad (1.59)$$

which are the field of a TEM wave featuring a *free space-like dispersion*.

Note that all higher order modes TM_m and TE_m become evanescent below the cut-off frequency $\omega_m = m\pi/d\sqrt{\mu\epsilon}$ while the *fundamental mode* TM_0 has no cutoff.

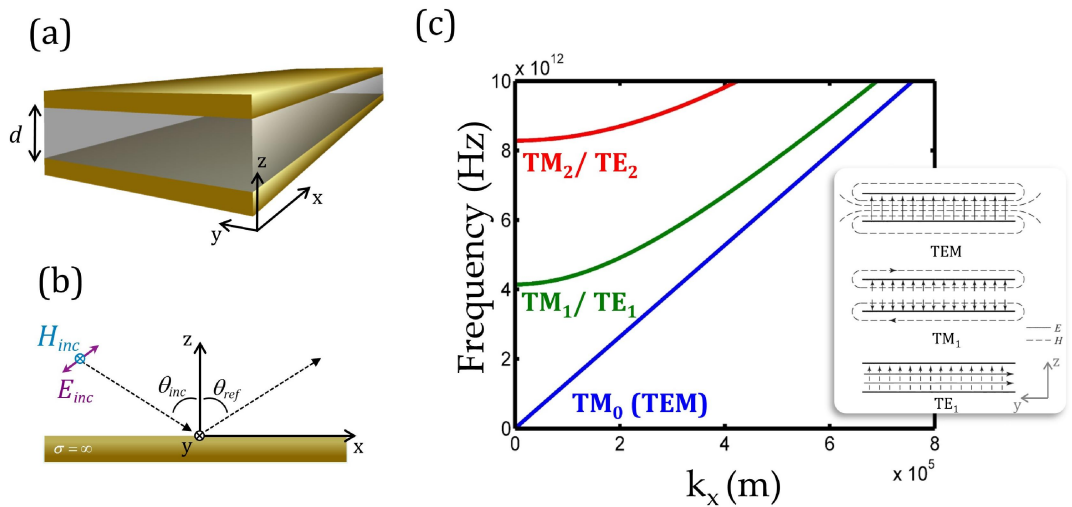


FIG. 1.8(a) Parallel plate waveguide; (b) reflection from a conducting boundary; (c) mode dispersion in a parallel plate waveguide with plates distance $d = 10\mu\text{m}$ and filled with GaAs ($\epsilon_r = 13.1$). The field lines are sketched in the inset (from Ref. [31]).

Thus the TEM mode can propagate at any frequency in the waveguide and is the only mode allowed in the structure if by design we choose an operation bandwidth such that $\omega_{op} < \pi / d\sqrt{\mu\varepsilon}$. As an example, the dispersions of modes TM_0 (TEM), TM_1/TE_1 , TM_2/TE_2 in a parallel plate waveguide having $d=10 \mu\text{m}$ and filled with GaAs ($\varepsilon_r^{GaAs} = 13.1$) are plotted in FIG. 1.8(c). This is in fact a standard waveguide employed for THz QCLs operating around 2-4 THz and having a standard thickness $\approx 10 \mu\text{m}$. From the figure it is clear that the cut-off frequency for TM_1/TE_1 propagation is above 4 THz meaning that a laser mode at 3 THz builds up in the cavity as a TEM wave.

1.4.3 TEM transmission lines

Transverse electromagnetic (TEM) waves are propagating waves having the electric and magnetic field lines restricted to directions normal (transverse) to the direction of propagation (i.e. $E_x = H_x = 0$ for propagation along \hat{x}). Plane waves in free space are an example of TEM waves. Indeed, TEM waves can propagate not only in homogeneous, unbound media but also in structures with cross-sections not varying along the direction of propagation, such as parallel plates, coaxial lines, parallel wires, and so forth. Following Ref. [32], it can be shown that in such structures a unique voltage $V(x)$ and current $I(x)$ can be defined, satisfying *transmission line* (or *telegrapher's*) *equations*

$$\begin{aligned} \frac{\partial V(x)}{\partial x} &= -j\omega L_0 I(x) \\ \frac{\partial I(x)}{\partial x} &= -j\omega C_0 V(x) \end{aligned} \quad (1.60)$$

where L_0 and C_0 are the line inductance and capacitance per unit length (assuming lossless materials). Differentiating the voltage equation and replacing $\partial I / \partial x$ one finds

$$\frac{\partial^2 V(x)}{\partial x^2} = -\omega^2 L_0 C_0 V(x) \quad (1.61)$$

which is an homogeneous wave equation for the voltage. The general solution is a plane wave $V(x) = V_0 e^{\pm jkx}$ yielding a dispersion relation

$$k^2 = \omega^2 L_0 C_0 . \quad (1.62)$$

Therefore, the velocity of voltage and current wave propagation on the line is $v = 1 / \sqrt{L_0 C_0}$ and the dispersion relation is identical to that of a uniform plane wave in an unbound medium of constants (μ, ε) where

$$L_0 C_0 = \mu \varepsilon \quad (1.63)$$

It can be shown that these results are valid for any two-conductor transmission line of arbitrary but uniform cross section. Transmission lines (TLs) such as the coaxial cable are ubiquitous in every-day life (television, data network, ...) as they enable electromagnetic signal or power propagation as TEM waves in a way mimicking free-space propagation. The main advantage of these structures is their ability to confine EM radiation at will in the plane perpendicular to the direction of propagation. In fact, a wave with any frequency can be squeezed between the two conductors in the form of a voltage (current) wave which is not affected by the line transverse size. This is the reason why all resonating structures (as we will see later) derived from the transmission line geometry, for instance metal-insulator-metal (MIM) or patch resonators provide a transverse field confinement which overcomes abundantly the diffraction limit. Nevertheless, we will see later that the lateral size of these structures is inherently limited to a minimum size of $\lambda_{\text{eff}} / 2$ due to the fact that a standing wave is built in the cavity.

1.4.4 Transmission line resonators: the patch cavity.

In waveguides and transmission lines electromagnetic waves are unbounded in at least one direction. Conversely *resonators* are structures that confine EM radiation in all dimensions so that energy is trapped in a defined volume and leaks only weakly in the external world. The typical response spectrum of a resonator is characterized by narrow frequency bands centred on discrete frequencies called *resonances* [32]. Resonators are widely employed for energy storage, frequency measurement and filtering, but also to amplify the strength of an EM field as in the case of a laser.

A resonator is easily made by terminating somehow the ends of any waveguide structure. In the case of the infinite parallel-plate line discussed above one guidance condition was found, yielding a one-dimensional standing wave pattern in the plane transverse to the direction of propagation. Therefore, for a resonator we expect three guidance conditions yielding a standing wave pattern in three dimensions. Recalling that each guidance condition constrains one component of the wave vector \vec{k} to discrete values, the three guidance conditions for a resonator will limit the dispersion to a finite set of frequencies $\omega = |\vec{k}| / \sqrt{\mu\epsilon}$ called *resonant frequencies*.

Most common resonators are obtained by closing the ends of a rectangular or circular waveguide with metal walls, forming a *cavity resonator* (e.g. the microwave oven) or by terminating both ends of a TEM transmission line, forming a *transmission line resonator*.

As an example of transmission line resonator, we will discuss the patch (aka *microstrip* or *metal-dielectric-metal*) resonator which is very interesting for applications in the THz range [33]. We consider a circular patch resonator of radius a endowing a dielectric core of height h . The modes supported by the structure can be found conveniently using the resonant cavity model described in Balanis book [34]. The cavity is composed of two perfect electric conductors at the top and bottom to represent the patch and the ground plane, and by a cylindrical perfect magnetic conductor around the circular periphery of the cavity. The dielectric material sand-

wiched between the metal layers is assumed to be truncated beyond the extent of the patch, as it is the case for dry-etched metal-semiconductor-metal (MSM) device we will deal with in the following. Normally the substrate height is small compared to the operation wavelength so the supported modes are TM^z where z is the direction perpendicular to the patch. To find them one has to solve the Helmholtz wave equation (in cylindrical coordinates) for the magnetic vector potential A_z

$$\nabla^2 A_z(\rho, \phi, z) + k^2 A_z(\rho, \phi, z) = 0 \quad (1.64)$$

As a result a discrete set of spatial frequencies is found, obeying to the relation

$$(k_\rho)^2 + (k_z)^2 = \omega^2 \mu \varepsilon \quad (1.65)$$

where

$$k_\rho = \chi'_{mn} / a \quad (m = 0, 1, 2, \dots; n = 1, 2, 3, \dots) \quad (1.66)$$

$$k_z = p\pi / h \quad (p = 0, 1, 2, \dots) \quad (1.67)$$

In (1.66) χ'_{mn} are the zeroes of the derivative of the Bessel function $J_m(x)$ and they determine the order of the resonant frequency. Then, as for typical patch resonators the dielectric height is strongly subwavelength, the fields along z are essentially constant so that $p=0$ and $k_z=0$ in (1.67). Therefore the resonant modes we are interested in are in the form TM^z_{mn0} and using (1.65) can be written as:

$$f_{mn0} = \frac{1}{2\pi\sqrt{\mu\varepsilon}} \left(\frac{\chi'_{mn}}{a} \right) = \frac{c}{2\pi\sqrt{\varepsilon_d}} \left(\frac{\chi'_{mn}}{a} \right) \quad (1.68)$$

where c is the speed of light and ε_d is the dielectric relative permittivity. The first four values of χ'_{mn} in ascending order are

$$\begin{aligned} \chi'_{11} &= 1.8412 \\ \chi'_{21} &= 3.0542 \\ \chi'_{01} &= 3.8318 \\ \chi'_{31} &= 4.2012 \end{aligned} \quad (1.69)$$

so the first four modes are the TM^z_{110} , TM^z_{210} , TM^z_{010} and TM^z_{310} .

Note that there is only one geometric degree of freedom (radius of the patch) to control the resonant frequency for a fixed dielectric material. We highlight the fact that for the fundamental TM^z_{110} the lateral cavity size (patch diameter) is $d = 2a \approx \lambda / 2\sqrt{\varepsilon_d}$ as imposed by the diffraction limit.

1.5 Subwavelength photonics: antennas and metamaterials

1.5.1 Origin of the diffraction limit

In this paragraph the origin of the diffraction limit of optical beams is described following Refs. [35], [36]. It is known from Fourier optics that an optical beam can be synthesized from a superposition of plane waves [37]. Without loss of generality we can therefore simply consider a plane wave of angular frequency ω in a uniform dielectric medium with refractive index n . The dispersion relation for such a wave is

$$|\vec{k}| = \frac{n\omega}{c} = n \frac{2\pi}{\lambda_0} \quad (1.70)$$

where $|\vec{k}| = k$ is the wavenumber in the medium, c the speed of light in vacuum and λ_0 the free space wavelength. In Cartesian coordinates, the components of the wave vector must satisfy

$$k = \sqrt{k_x^2 + k_y^2 + k_z^2} . \quad (1.71)$$

Since we are dealing with a propagating wave in the three dimensions, each component k_j must be real and satisfy $-k \leq k_j \leq k$, which means that the accessible range of spatial frequencies (in one direction) is $\Delta k_j = 2k$. According to the uncertainty relation of Fourier transforms $\Delta r_j \Delta k_j \geq \pi$ one finds that the space extent “fitting” an optical beam of spatial frequency k (i.e. free space wavelength λ_0) Δk_j has a minimum size of

$$\Delta r_j \geq \frac{\pi}{\Delta k_j} = \frac{\pi}{2k} = \frac{\lambda_0}{4n} \quad (1.72)$$

which is the well-known optical diffraction limit. Note that the same result may be obtained considering the Heisenberg’s uncertainty relation for photons $\Delta(\hbar k_j) \Delta(r_j) \geq \hbar/2$.

The diffraction limit imposes an unsurmountable limit for the confinement of an optical wave propagating in an homogeneous medium such as in conventional dielectric waveguides. This is not strictly true when an inhomogeneity in space (i.e. two media with different permittivity) is present. In fact, looking at (1.71) we note that a mathematical trick can be used to increase the wavevector component in one direction overcoming the diffraction limit. Choosing two perpendicular directions in space, e.g. x and z , we can increase one wavevector component to values beyond the total wavevector ($k_x > k$) while at the same time requiring the wavevector in the perpendicular direction to become purely imaginary ($k_z = j\kappa$) so that (1.71) is still verified. Hence, we can confine a propagating wave on a subwavelength scale but that requires the introduction of a purely imaginary wavevector component, i.e. evanescent

waves. This is what happens in surface plasmons modes described in 1.3.4. Indeed, another option to bypass the diffraction limit exists and is inspired from the world of electronic devices, as we will illustrate in the following.

1.5.2 Maxwell and Kirchhoff

It is a known fact that electronic devices are not size-constrained by the diffraction limit. For example, standard wire antennas (e.g. the vertical monopoles originally used as mobile phones antennas) are in modern smartphone replaced by folded or meandered antennas which can fit a volume of diameter much smaller than the operating wavelength. It is then interesting to ask: where the boundary between electronics and optics is placed? The answer comes naturally if we recall that Kirchhoff's voltage and current laws, which are the backbones of circuit theory, are just an "approximation" of Maxwell's equations. Following Refs. [38], [39], we can show that Kirchhoff's laws can be derived from Maxwell's equations if the coupling between the \vec{E} and \vec{H} fields giving rise to the wave equation is eliminated. To see that, let's consider Maxwell's equations (differential form) in free space

$$\begin{aligned}
 \nabla \cdot \mu_0 \vec{H} &= 0 \\
 \nabla \cdot \epsilon_0 \vec{E} &= \rho \\
 \nabla \times \vec{H} &= \vec{J} + \epsilon_0 \frac{\partial \vec{E}}{\partial t} \\
 \nabla \times \vec{E} &= -\mu_0 \frac{\partial \vec{H}}{\partial t}
 \end{aligned} \tag{1.73}$$

The last two equations are especially relevant for electrodynamics: Ampère-Maxwell's law says that both conduction and displacement (capacitive) currents are source of magnetic field; Faraday's law, says that a time-varying magnetic field give rise to a spatially-varying electric field. Wave behaviour arises because of the coupling terms in these equations: a change in \vec{E} causes a change in \vec{H} , which causes a change in \vec{E} , and so forth. Note that if ϵ_0 or μ_0 were set to zero the coupling terms would vanish and the wave behaviour would disappear. The regime where Maxwell's equations are uncoupled is called *quasi-static limit* and constitutes the realm of circuit theory. For example, if we put $\mu_0 = 0$ in Faraday's law we make the \vec{E} -field irrotational, meaning that it can be expressed as the gradient of a potential. It then follows that the line integral of the \vec{E} -field (i.e. the voltage) around any closed path is zero:

$$V = \oint \vec{E} \cdot d\vec{l} = \oint (-\vec{\nabla} \phi) \cdot d\vec{l} = 0 \tag{1.74}$$

where ϕ is the well-known electrostatic potential. This equation is the field-expression of Kirchhoff's voltage law. In a similar way, if we set $\epsilon_0 = 0$ and take the divergence of both sides of Ampère-Maxwell's law we obtain:

$$\vec{\nabla} \cdot \vec{J} = \vec{\nabla} \cdot (\vec{\nabla} \times \vec{H}) = 0 \quad (1.75)$$

owing to the fact that the divergence of the curl of any vector field is always zero. The statement that the divergence of the current is zero is equivalent to Kirchhoff's current law saying that no current is created or lost at a circuit node (i.e. current conservation holds).

Recalling that the speed of light in vacuum is given by $c = 1/\sqrt{\mu_0 \epsilon_0}$ we observe that setting ϵ_0 or μ_0 to zero is equivalent to setting the speed of light to infinity. In other words, Kirchhoff's laws are valid under the hypothesis of infinitely fast propagation. This assumption is acceptable when the physical dimensions of the circuit elements are small compared to the wavelength, so that propagation effects are negligible:

$$l \ll \lambda \quad (1.76)$$

where l is the length of the circuit element and λ is the operation wavelength.

Therefore, the key difference between a circuit and a transmission line is the size of the device [31]. The physical dimensions of a circuit is normally much smaller than the operating wavelength, while a transmission line may fill a considerable fraction of a wavelength, or many wavelengths. In fact, transmission lines are called *distributed parameter networks*, because the electric and magnetic fields can vary in magnitude and phase over its length, while circuits are defined *lumped element network* because the fields do not vary appreciably over the physical dimension of the elements. In the specific case of an EM resonator (be it a resonant circuit, a cavity resonator, a Fabry-Perot resonator,...) a periodic energy exchange between the magnetic and electric fields exists. What distinguishes *photonic resonators* from *electronic resonators* is actually the current source mediating this exchange.

In electronic resonators, as seen above, propagation effects are negligible ($\partial \vec{D} / \partial t \approx 0$) and the conduction (i.e. free carrier) current \vec{J} mediates the periodic energy exchange. Conversely, photonic resonators rely on standing waves confined by metals or dielectrics and the displacement current $\partial \vec{D} / \partial t$ dominates. The fact that a photonic resonator must fit a standing wave implies that its minimal size can be no lower than $\lambda / 2n$ (n is the refractive index of the material filling the resonator) as imposed by the diffraction limit. An interesting way to beat the diffraction limit is converting a propagating EM wave in free-carrier oscillations (mimicking the operation of RF antennas, see below) and operating in the circuitual (quasi-static) regime.

1.5.3 Antennas

In this paragraph we will introduce some important concepts about antennas following Refs. [40]-[42]. An antenna can be viewed as a device that converts a guided EM wave into a free space propagating wave. Antennas are inherently bidirectional, i.e. they can be used either to emit EM waves with a well-defined radiation pattern, which can then travel over large distances, or to receive EM waves from a remote source. The peculiarity of an antenna is that it appears, on one side, as an electrical circuit element, while the other side provides an interface with a propagating plane wave.

Antennas are today ubiquitous thanks to their ability in providing an interface between guided electrical signals and wireless signals (encoded in various parameters of EM waves, such as amplitude, phase and frequency)[40]. Due to these properties, antennas have become indispensable tools in science and technology as well as in our everyday life.

An antenna operates thanks to free charges confined into a well-defined region of space: if an AC voltage is applied to the antenna, an electronic oscillation is excited yielding radiation; vice versa an EM wave reaching the antenna can excite charge oscillations to produce an AC voltage signal [40]. Well-known examples of antennas are straight or bent pieces of metal, such as TV or radio monopole antennas.

In general, the relation between free space radiation and oscillating charges can be seen recalling the wave equation (1.42) where we add the source terms:

$$\nabla^2 \vec{E} + \omega^2 \mu \epsilon \vec{E} = j\omega \mu \vec{J} + \vec{\nabla}(\rho / \epsilon) \quad (1.77)$$

This equation links the radiated electric field directly to the source. The solution can be found once boundary conditions are specified. To mimic free space, an open boundary is needed i.e. the field must be zero when the distance from the source becomes infinite. It can be shown that the solution of (1.77) in a uniform medium (ϵ, μ) is [41]

$$\vec{E}(\vec{r}) = -j\omega \mu \int_V \vec{J}(\vec{r}') \frac{e^{-jk|\vec{r}-\vec{r}'|}}{4\pi|\vec{r}-\vec{r}'|} dv' + \frac{1}{j\omega \epsilon} \vec{\nabla} \left(\vec{\nabla} \cdot \int_V \vec{J}(\vec{r}') \frac{e^{-jk|\vec{r}-\vec{r}'|}}{4\pi|\vec{r}-\vec{r}'|} dv' \right) \quad (1.78)$$

where \vec{r} is the distance vector from the origin to the observation point and \vec{r}' is from the origin to the source point. This equation says that the field radiated from the antenna can be completely reconstructed if the time-varying current \vec{J} flowing in the antenna is known. Note: only a time-varying current (i.e. oscillating charges) can generate an EM wave. Antenna design consists then in controlling the current distribution \vec{J} to obtain the desired radiated field \vec{E} [42].

The most famous example of antenna is the Hertz's dipole, which can be pictured as two metallic spheres connected by a thin wire [32], [40]. If some negative charge is initially set on one sphere while the same positive charge is set on the other one, the system will start to oscillate at a frequency $\omega_0 = 1/\sqrt{LC}$, in which L and C are the inductance and the capacitance of the system, respectively. The oscillation will be damped due to the ohmic resistance of the metal wire and also because part of the energy leaves the system as EM radiation. In fact, the charge oscillation produces a time-dependent electro-magnetic field according to Maxwell's equations. In the so-called *far-field zone* this field transforms into a plane wave which are free-space solutions of the wave equation (1.42). Note that even if we turn off the charge oscillation, the far-field waves would continue to propagate since they carry energy that is stored in the fields themselves and has been removed from the initial charge distribution. In contrast, in the *near-field zone* we find the reactive (electrostatic) field of the dipole, which returns its energy to the source after each oscillation cycle.

It is worth to note that every structure acting as “transducer” between a localized/bound electromagnetic mode and free-space EW waves is an antenna.

For instance, a non-ideal leaky cavity resonator is an antenna, though inefficient. Similarly, the patch (or microstrip) structure discussed above can be identically labelled either as resonator, cavity or antenna. A photonic crystal can be also seen as a wavelength-scale antenna and so on. Indeed, it is only a matter of language.

In RF engineering one normally designs an antenna to be highly efficient in emitting or capturing light, optimizing the radiated energy in some directions and suppressing it in others. Moreover a good matching with the loading transmission line is demanded. In general a high bandwidth and radiation efficiency is desired for an antenna, which should then behave as a low quality factor circuit. Conversely, devices providing an efficient energy storage and having only negligible radiation loss (i.e. high radiation quality factor) are more often referred as cavities or resonators.

In the following we will address the problem of miniaturizing antennas and resonators.

1.5.4 Subwavelength antennas and resonators. Metamaterials

Usually standard antennas have dimensions comparable to the wavelength. For instance, the half-wavelength dipole antenna, the prototype of wire antennas, features a total length of $\lambda/2$ and the TV/radio monopole is $\lambda/4$ long. A lot of wavelength-scale designs have been explored in the last century, so that today a large choice of antenna is available to satisfy precise requirements in terms of radiation efficiency, directionality, bandwidth and network matching. Recently, the fast growth of mobile communication systems has pushed the development of small-sized (respect to the wavelength), compact and lightweight antennas. Antennas (or resonators) are often considered to be *electrically small* when the following condition is met [42]:

$$\frac{r}{\lambda} \leq \frac{1}{2\pi} \quad (1.79)$$

where r is the radius of a sphere that just contains the antenna and λ is the wavelength.

In RF engineering, many ways have been found to reduce the size of an antenna. Some of the most common involve top loading, circuit matching, loading with a high dielectric constant material and reactive loading [42]. Nevertheless, it turns out that, despite the employed size reduction technique, all electrically small antennas feature low efficiencies and high reactances, which is why they are not popular in applications even though they are small in size.

An example of “evolution” from a conventional monopole design to an electrically small one will be discussed in 2.4.3. It will be shown that *de facto* a subwavelength antenna must behave as a lumped LC circuit with two reactive (capacitive and inductive) zones.

Historically, the need for subwavelength electromagnetic resonators arose (well before the quest for small antennas) with the first microwave tubes [28]. For instance, in the *klystron* a resonant cavity is needed to enhance the interaction of MWs with an electronic beam. The *re-entrant cavity* design, shown in Fig. 4.1, was proposed to reduce the resonator size while keeping a good resonant behaviour for using efficiently the electromagnetic power. In fact, this system supports a LC resonance because the opposing metallic grids (at the centre) provide a capacitance while the inductance is provided by the rest of the metallic cavity. Hence, there is no stationary wave bouncing between the metal walls like in a conventional cavity resonator. As in a LC circuit, the resonant frequency can be lowered by making the opposing metal surfaces closer to each other thus increasing the capacitance. A successive example of a small resonator is the *magnetron cavity* shown in FIG. 1.9(b): the current around the cavity gap plays the role of an inductor and the charge at the ends of the cavity plays the role of a capacitor. The magnetron resonance exhibits a resonance analogous to a parallel LC circuit and may be considered the ancestor of all small resonators we use today.

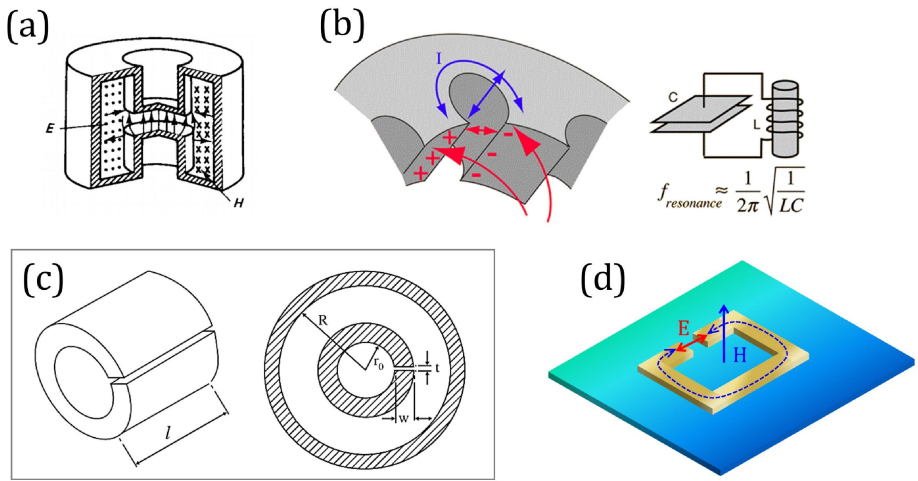


FIG. 1.9(a) Re-entrant cavity (taken from Ref. [43]). (b) Magnetron cavity (from <http://hyperphysics.phy-astr.gsu.edu/hbase/waves/magnetron.html>). (c) Split-ring resonator as modified slotted-tube (from Ref. [28]): inner core (left) and complete structure with external shield (right). (d) "Modern" planar split-ring resonator used as metamaterials building block

Later, the need for small resonators arose in the detection of nuclear magnetic resonance at MHz frequencies, where a standard cavity resonator would have been too big. A first proposed solution was the *slotted-tube resonator*, a double cylindrical structure where the inner tube is split so that the upper and lower parts can serve as a transmission line, and the outer cylinder provides a shield.

The term *split-ring resonator* was coined by Hardy and Whitehead (1981) [44] referring to a modified design of this object in which the inner ring is split. Now the inner tube is a resonator on its own, working exactly as the magnetron cavity, while the outer cylinder is for confining the magnetic field in the annular region as shown in FIG. 1.9(c). The same name was retained in the famous paper by Pendry et al. [30] where the authors foresee the potentiality of the split ring design in providing an effective negative permeability (FIG. 1.9(d)). This work inaugurated the research field of *metamaterials*. It turned out that practically all conceivable subwavelength mag-

netic resonators were capable of producing negative permeability and spectacular phenomena such as negative refraction and cloaking have since then been implemented.

From all this survey we have learnt that the key strategy to obtain a resonator smaller than the wavelength is building a lumped element LC circuit, such as the split ring resonator. Apart from the possibility to achieve device dimension well below the size imposed by the diffraction limit, the great advantage of operating in the circuitual regime is the possibility to play with lumped elements to tailor the resonator response at will. Frequency tuning, impedance matching, polarization selection and beam shaping could be easily accessible for photonic devices relying on circuit-based resonators. Building a hybrid framework between optics and electronics to build novel ultra-small and flexible THz optoelectronic devices inspired from metamaterials is the main task we will pursue in this thesis.

2 Circuit-tunable and antenna-based THz resonators

This chapter deals with the modelling, fabrication and characterization of novel 3D lumped-elements THz micro-resonators conceived in this thesis. First, simulations and measures on standard $\lambda/2$ THz patch resonators are used as benchmark to illustrate the modelling and experimental techniques employed in the following. Then, the physics of the lumped LC circuit is discussed highlighting the transition from the electrostatic to the optical regime and the implications of operating on sub-wavelength modes. A detailed experimental and theoretical study of the developed circuit-tunable resonators follows. Finally, frequency tuning via additional lumped elements and radiation pattern shaping via antenna design is demonstrated.

2.1 Optical properties of $\lambda/2$ patch resonators

In this section we will show numerical and experimental results on $\lambda/2$ metal-semiconductor-metal (MSM) patch resonators for THz applications. The optical behaviour of these objects has been briefly described in 1.4.4, and it has already been extensively studied in literature, therefore we will not detail it here. For our purpose, it constitutes a model system to introduce modelling and experimental techniques that will be used hereinafter.

2.1.1 FEM simulations: eigen-modes analysis, wave excitation

The problem of calculating the electromagnetic modes of a photonic structure can be solved analytically only for very simple systems. For most practical problems, it is necessary to resort to numerical methods for an approximate solution. The *finite element method* (FEM) is a widely used numerical method in engineering to solve boundary value problems due to its geometrical adaptability and affordable memory requirements. Here, we will sketch some important features of the method following Ref. [45]. Let's consider a generic radiator or antenna, as sketched in Figure 2.1. This object may be excited by an internal current source or by an external propagating electromagnetic wave and will radiate an electromagnetic field that is modified by its internal structure. The antenna may contain or may be embedded in anisotropic materials characterized by the permittivity and permeability tensors, $\boldsymbol{\epsilon}$ and $\boldsymbol{\mu}$.

The main objective of the FEM analysis is to investigate the resonant modes of the system, the scattering parameters, the input impedance and radiation patterns. Since the antenna radiates an electromagnetic field to infinity (or at least in a semi-space

when a ground plane is present) the problem has an unbounded solution space. To use the finite element method, this unbounded space has to be truncated into a finite space by introducing a fictitious surface S_0 to enclose the antenna. Then, to uniquely define the electromagnetic problem, one has to specify a boundary condition on S_0 making it as transparent as possible to the radiated field. Once proper boundaries are chosen, the computational domain (region where the fields are to be determined) is divided (“*meshed*”) into smaller elements. By keeping the elements small enough (a typical choice is maximum mesh element size $< \lambda_{\text{eff}}/5$), the EM field within each element can be approximated by some linear or, if necessary, higher order expansion. The collection of these elements and their associated expansion or shape function is therefore capable of modelling arbitrary field distributions.

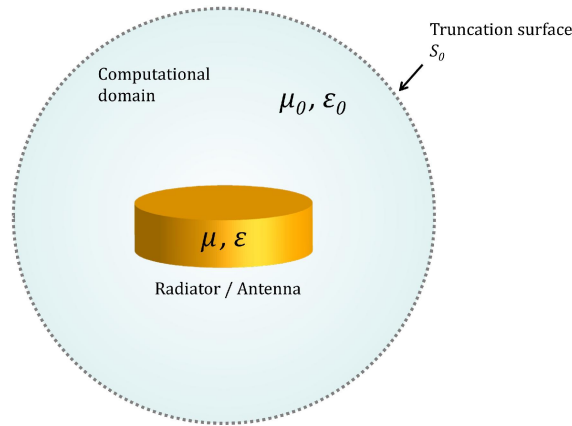


FIG. 2.1 Approximate boundary-value problem: the computational domain is truncated by an artificial surface S_0 for numerical finite element analysis. The radiator constitutive materials are modelled via their permittivity and permeability tensors.

Finally the electromagnetic problem is reduced to a matrix system with imposed boundary conditions or forced excitation (current source, incident field, etc.) and the unknown coefficients are found with the application of an iterative or direct solver.

For this work the finite element software package *COMSOL Multiphysics*® has been chosen. All the simulations presented in the manuscript are obtained using the *COMSOL RF module* which is suitable for device dimensions ranging from $d=0.1\lambda$ to $d=50\lambda$. Among the different types of studies proposed it is particularly relevant for us the *eigenvalue analysis* which provides a powerful tool for resonator design. Strictly speaking this study looks for the photonics eigenmodes of the system around a specified frequency solving Helmholtz equation (1.42). This is a linear problem whose eigenfrequencies are real if real-valued dielectric constants are provided. If the materials constitutive relations are complex valued (i.e they account for material losses) the problem becomes nonlinear (*lossy eigenvalue analysis*) and complex eigenvalues are obtained. In this case, the imaginary part represents the damping of the mode. If

properly set this analysis allows for calculation of a resonator's quality factor as it will be elucidated in Chapter 5. In FIG. 2.2 the eigenvalue analysis results for a circular patch antenna are shown. The eigenfrequencies of the two first resonant modes are $f(\text{TM}_{110})=3.24$ THz and $f(\text{TM}_{210})=5.48$ THz for a patch of $16\ \mu\text{m}$ diameter on a $2\ \mu\text{m}$ -thick GaAs slab. The materials dielectric functions are given by Lorentz model introduced in 1.3.

The metallic boundaries (patch top metal, ground plane) may be modelled as a *perfect electric conductors* (PEC, i.e. $\sigma=\infty$) when metal losses are neglected. The finite conductivity of real metals can instead be accounted by associating a complex permittivity (or, equivalently, conductivity) either to the bulk metal domains, or to metal boundaries employing the *impedance boundary condition*, which is appropriate for objects having dimensions larger than the skin depth.

The simulation domain is either a box or a hemisphere. To obtain at a first glance the modes of the resonator normally the choice of simulation boundary is not critical. Scattering or absorbing boundaries must instead be used to mimic free-space propagation and compute radiation loss.

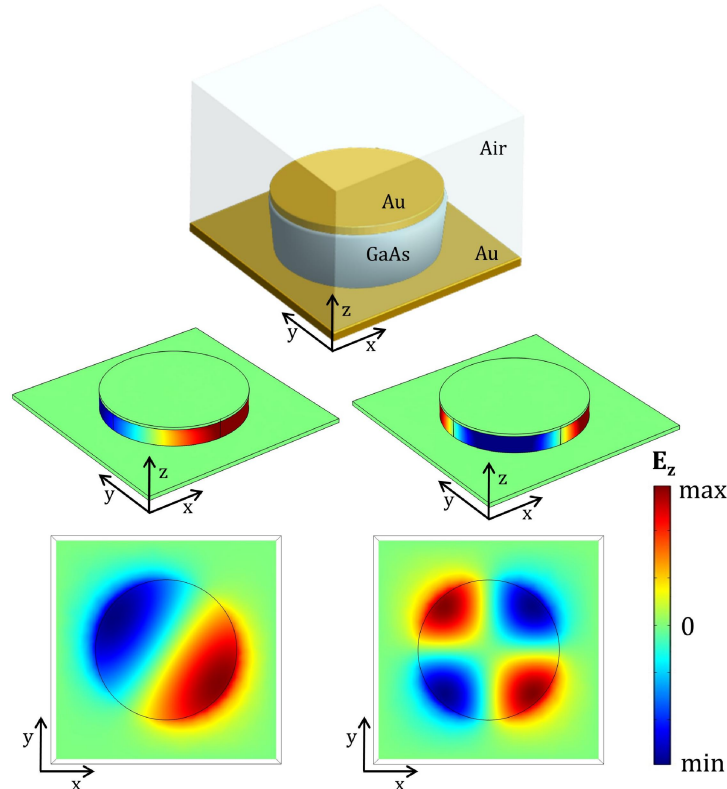


FIG. 2.2 Eigenvalue analysis for a circular patch antenna. Top: schematics of the simulation domain. Bottom: results of eigenvalues analysis; the E_z field distribution is shown for the TM_{110} and TM_{210} resonant modes in volume and in the xy plane.

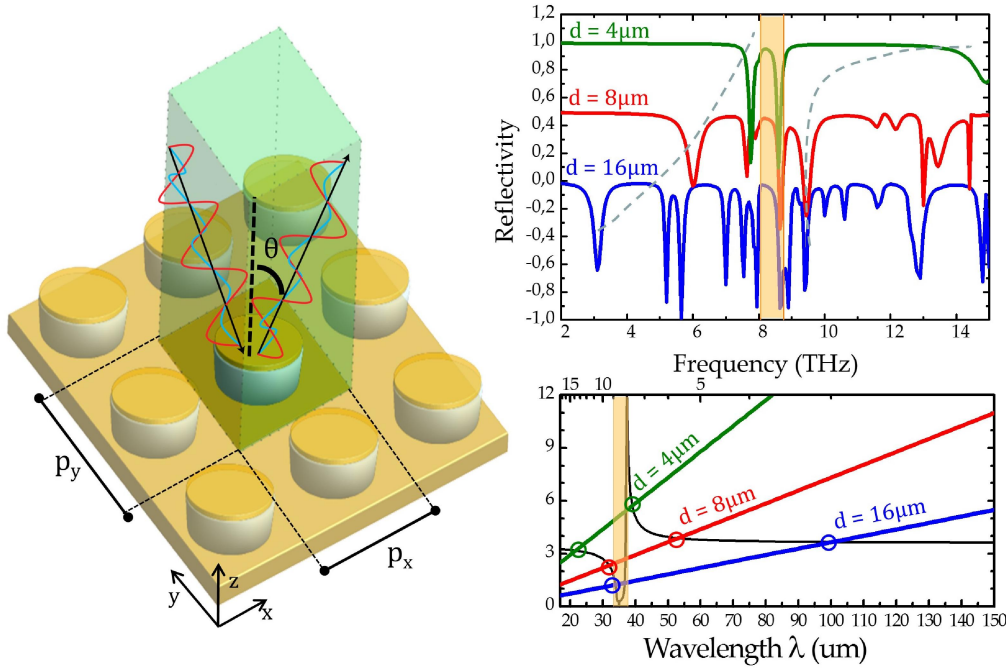


FIG. 2.3 Wave excitation analysis for a circular patch antenna. Left: schematics of the simulation domain. Scattering from an array of objects is simulated using periodic boundaries. Right, top: simulated reflectivity for circular patch antenna arrays of diameters 4, 8, 16 μm on a 2 μm GaAs slab. The yellow band delimitates GaAs Reststrahlen band. The fundamental TM_{110} mode and its “copy” beyond Reststrahlen band are highlighted by a dashed line. Right, bottom: graphical solution of equation (2.1) for the fundamental mode. Black curve shows GaAs anomalous index dispersion originating Reststrahlen effect.

Once the resonant modes of a resonator have been investigated numerically, it is possible to probe them with an external excitation, namely an impinging electromagnetic wave, similarly to what is done experimentally. In a *wave port excitation analysis* the scattering properties of an array of resonating objects can be studied. This kind of simulation is especially relevant in the THz range as its results can be directly compared to the experimental results obtained using Fourier transform infrared (FTIR) spectroscopy on arrays of real devices. A schematics of the simulation in the case of patch antennas on a ground plane is reported in FIG. 2.3: a unit cell of the array having period (p_x, p_y) is simulated and periodic boundaries on the four sidewalls are defined. Floquet periodicity is imposed on the two walls normal to the incidence plane while continuity is used on the parallel ones. A plane wave whose polarization and incidence angle can be adjusted is shined on the resonator through a periodic wave port defined on top. For a selected frequency range it is possible to compute the scattering coefficient S_{11} , and therefore the power reflectivity $R=|S_{11}|^2$.

On the top right panel of FIG. 2.3 the simulated reflectivity for circular patch antenna arrays of diameters 4, 8, 16 μm on a 2 μm GaAs slab is shown. The yellow band delimitates the GaAs Reststrahlen band. The fundamental TM_{110} mode is situated around 3 THz for the 16 μm patch and it blueshifts when the size shrinks according to equation (1.68). Note: a “copy” mode of the fundamental one appears beyond the Reststrahlen band due to the GaAs refractive index anomalous dispersion in this region, as highlighted by the dashed lines following the mode. This can be easily under-

stood using a graphical solution of the equation for the fundamental TM_{110} resonance of a circular patch [34]:

$$n(\lambda) = \frac{1.8412}{\pi d} \lambda \quad (2.1)$$

where $n(\lambda) = \sqrt{\varepsilon(\lambda)}$ is the dispersive GaAs refractive index and d is the patch diameter. For each patch dimension there are two physical modes below and above the Reststrahlen band featuring the TM_{110} field distribution.

2.1.2 Fabrication of MSM resonators

In this paragraph the fabrication of MSM patch will be discussed. The main processing steps are shown in FIG. 2.4(a). All the technological developments presented in this thesis have been carried out in Minerve-CTU facilities at IEF-Paris Sud & CNRS. GaAs passive structures were grown via MOCVD by G. Beaudoin and I. Sagnes group at LPN-CNRS (France). GaAs/AlGaAs heterostructures (PQWs, QWIPs, QCLs) were grown via MBE by E. H. Linfield group at Leeds University (UK).

First the GaAs epitaxial sample to process (grown on a GaAs substrate) is Ti/Au coated together with a second GaAs wafer holder. Then the sample carrier is glued on the holder via thermo-compressive Au-Au bonding. The GaAs substrate is removed via mechanical polishing and following selective citric acid wet etch. The $Al_{50}Ga_{50}As$ stop layer is then removed via hydrochloric and hydrofluoric acid after a plasma oxidation. Once the sample surface uncovered, a Ti/Au/Cr metal pattern is defined via standard contact photolithography and lift-off. The Cr layer is used as hard mask for chlorine-based ICP-RIE dry etch.

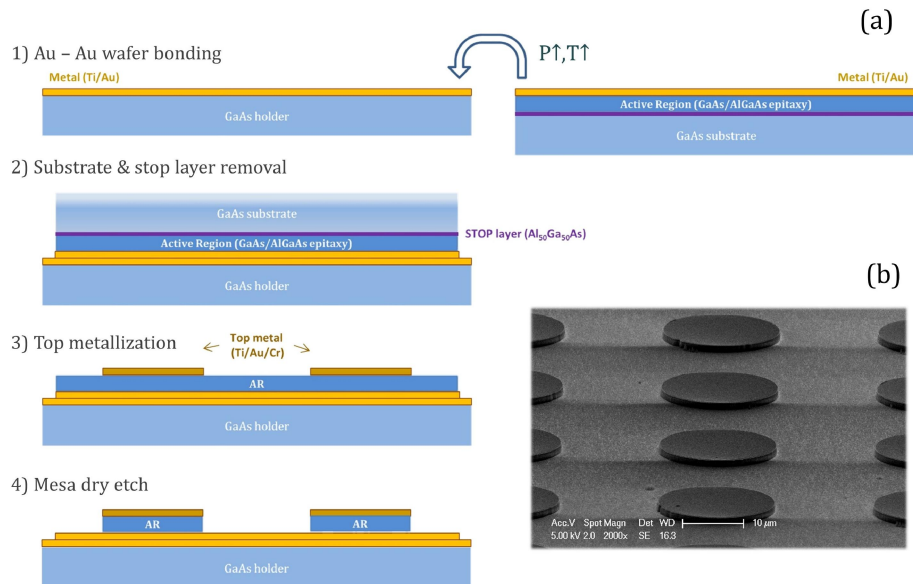


FIG. 2.4 Fabrication of MSM patch resonators in GaAs platform: 1) Au-Au wafer bonding of epitaxially grown GaAs (or GaAs/AlGaAs heterostructure) on a GaAs carrier wafer. 2) Original substrate and stop layer mechanical/chemical removal. 3) Definition of a metal etch mask. 4) Mesa ICP-RIE dry etch with a metal mask. Figure inset: SEM image of fabricated patches.

Back-end process for passive devices consists simply in sample cutting via microdicing with a diamond blade. A typical result for circular patch resonators is shown in FIG. 2.4(b).

2.1.3 Optical characterization

All spectroscopic measurements presented hereinafter are obtained with a FTIR spectrometer Bruker IFS 66/v. The instrument is sketched in FIG. 2.5. The FTIR spectrometer core is reminiscent of a Michelson interferometer: an IR beam from an internal source is split in two by a beam-splitter; one beam is back-reflected from a fixed mirror while the other one is reflected from a mobile mirror either continuously oscillating (*rapid scan modulation*) or translating in discrete positions (*step scan modulation*). The beams are then recombined at the beam splitter and focused on the sample chamber. At the sample position S the beam diameter is magnified by a factor 1.8 with respect to the beam diameter at the source (selected by a pinhole) due to internal optical components. Reflected light from the sample is then collected on an internal detector. For each spectral component the collected signal intensity will have a beating-like modulation depending on the optical path difference between the two beams. Fourier analysis allows one to recover information on the intensity of each spectral component from the collected signal (*interferogram*). The frequency spectrum is recovered by a Fourier transformation of the interferogram [46]. For THz measurements the internal source employed is either a globar (a heated SiC rod emitting black-body radiation) or a mercury-vapour lamp. The beam-splitter is a 6 μm Mylar film and the internal detector is a pyroelectric DTGS crystal. For low-noise measures a He-cooled Si bolometer can be used as external detector.

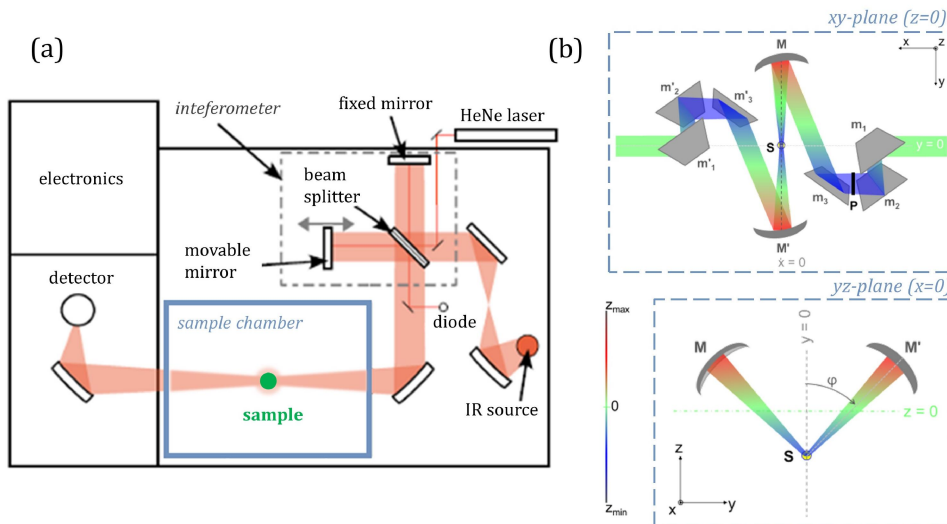


FIG. 2.5(a) Schematics (top view) of the Bruker IFS 66/v FTIR spectrometer. The interferometer (grey dashed) and sample (light blue) chamber are highlighted. A He-Ne laser beam is used for interferometer auto-alignment. (b) Schematics of reflectivity unit.

Passive metal-metal resonators can be fully characterized by reflection spectroscopy as the metallic ground plane prevents transmission of radiation. Resonator modes

appear as dips in the reflectivity (R) spectrum and sample absorptivity spectrum (A) can be recovered as $A=1-R$. In transmission line theory this is equivalent to a 1-port system where an antenna/resonator loads a transmission line representing free-space propagation (vacuum impedance is $Z_0=377\Omega$). The measure of the scattering parameter S_{11} (or equivalently of the reflection coefficient Γ) allows one to recover all the information on the load structure via its impedance Z_A . Experimentally the *absolute reflectance* R (or *reflection factor*) is measured as the ratio of the radiant intensity reflected from a sample to the radiant intensity incident on it [37]:

$$R_{abs} = \frac{I_r}{I_i} \quad (2.2)$$

In the infrared range *relative reflectivity* is commonly measured by comparison with a reference mirror, usually aluminium or gold having high and constant spectral reflectivity up to telecom wavelengths. Relative reflectance spectra shown in the following are obtained taking the ratio of the reflected radiant intensity from the sample to the reflected radiant intensity from a reference gold mirror of the same size.

$$R_{rel} = \frac{I_{sample}}{I_{ref}} \quad (2.3)$$

In order to measure R a variable angle reflection unit (Bruker A513/Q) can be inserted into the FTIR chamber. The schematics of this unit is sketched in FIG. 2.5(b). Two spherical mirrors M and M' can be rotated in the incidence plane of the setup ySz allowing one to explore incidence angles ranging from 13° to 83° . The IR radiation enters in the chamber propagating from right to left. A system of three plane mirror $m_{i=1,2,3}$ deflects incoming radiation towards M . Light is then focused at point S where the sample to analyse is placed on a micro-translation stage enabling signal maximization. The reflected light is collected from M' and again deflected towards the detector by an identical three-mirror system $m'_{i=1,2,3}$. To select the impinging polarization of THz radiation a polyethylene polarizer can be placed on M the rotating arm. A second identical polarizer may be inserted as well on M' arm to analyse the outgoing polarization. Remote control of the movable mirrors permits to operate in vacuum to suppress atmospheric water absorption lines in the THz spectra. Moreover, to avoid spurious reflections the sample is encircled with sandpaper of grit comparable with the wavelength range of interest ($\approx 100\mu\text{m}$).

Before moving on, let's consider the reflection from an ideal plane reflector of surface S as a function of incidence angle θ . The reflected radiant intensity is measured for a fixed solid angle defined by the input aperture of the detector situated at distance r from the reflector. When viewed at $\theta=0^\circ$, along the normal to the surface, a certain maximum intensity I_θ is observed.

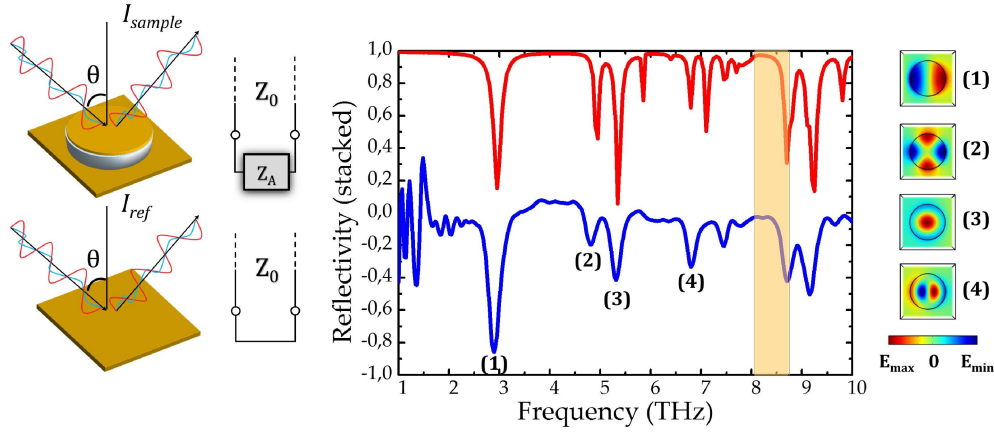


FIG. 2.6 Left panel: experiments (sketches) performed to evaluate the reflectivity according to (2.3) and their transmission line interpretation. Right panel: simulated (red) vs experimental (blue) reflectance spectra for circular patch antennas having $d=16 \mu\text{m}$ and $h_{\text{GaAs}}=2 \mu\text{m}$. Fundamental TM_{110} and high order modes below Reststrahlen band are identified with the help of FEM simulations. The E_z field profile in the xy plane at $z=h/2$ is shown.

As the aperture is moved away from the normal along the circle of radius r (in our case the collection mirror M'), the projected reflector area decreases as $S\cos(\theta)$ yielding a decreasing reflected intensity given by Lambert's cosine law [47]:

$$I(\theta) = I_0 \cos(\theta) \quad (2.4)$$

When measuring relative reflectance the incidence angle dependence disappears for the baseline but it is still relevant in evaluating the intensity of the reflectance dips in micro-resonators spectra. If we call $A(\theta) = 1 - R(\theta)$ the measured angle-resolved absorbance then the effective extinction cross section of the resonator will have the form $\sigma_{\text{ext}}(\theta) = A(\theta) \cdot \cos(\theta)$ where the corrective factor $\cos(\theta)$ accounts for the broadening of the excitation beam with the incidence angle [48].

2.1.4 Fundamental limits of TL resonators. RLC model of a patch resonator.

In paragraph 1.4.4 we saw that a circular patch resonator is inherently constrained to a minimum size of $d \approx \lambda / 2n$ due to the optical diffraction limit. This is a common feature of all TL resonators derived from TEM lines or other type of waveguides. This fundamental confinement limit can be clearly spotted by introducing an equivalent RLC model and exploiting the fundamental theorem of transmission lines given by (1.63). Indeed, the difference between TL resonators where propagation effects are relevant and lumped-elements resonators operating in the quasi-static limit (see 1.5.2) is sometimes shadowed by the ambiguous notion of LC resonance.

Consider a square MSM patch resonator of side s as the one sketched in the left panel of FIG. 2.7. Solving Helmholtz equation in analogy with 1.4.4 we find for the fundamental TM_{010}^z mode [34]:

$$f_{010} = \frac{c}{2ns} \quad (2.5)$$

where $n = \sqrt{\epsilon_d}$ is the semiconductor refractive index

In the language of optics, this mode can be understood as a Fabry-Perot resonance where the EM field bounces back and forth under the patch due to the high reflectivity at the cavity edges arising from the modal mismatch between the metal-metal and single metal regions [49].

On the other side, in TL theory a patch resonator is obtained by truncating a TEM parallel plate lines at both ends, as pictured in FIG. 2.7. In other words, this resonator consists of an open-circuited length of transmission line and it will behave like a parallel resonant circuit when its length is $\lambda/2$ [31]. Indeed, the ‘‘optical’’ description of radiation coupling into a/o out of a resonator can be framed in the TLs formalism: a resonator or, more generally, a structured surface is as a load impedance terminating a transmission line representing the free-space (see FIG. 2.6).

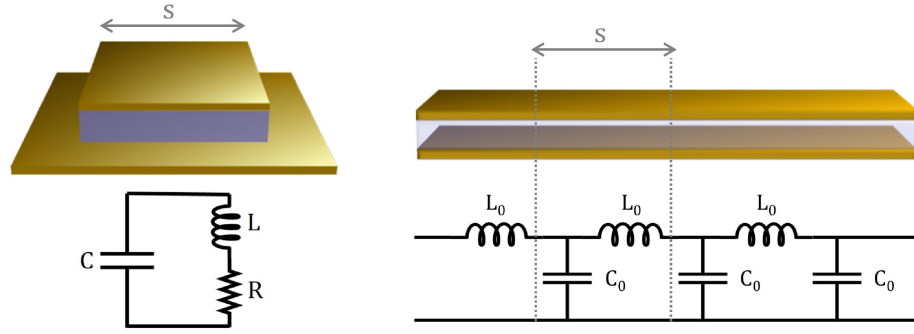


FIG. 2.7 (top) Schematics of a MSM patch resonator and a TEM parallel plate line; (bottom) equivalent circuitual picture

In this context, a lumped RLC model can always be employed to generally describe an isolate resonator mode [32]. The parallel RLC model is especially relevant for high impedance surfaces operating on a ground plane [50]. Following [51] the equivalent impedance for a patch resonator operating on the fundamental TM_{010}^z mode has the form:

$$Z = \frac{R + i\omega L}{1 - \omega^2 LC + i\omega RC} \quad (2.6)$$

Here R accounts for mode losses while C and L are respectively related to the electric and magnetic energies stored in charges/currents exchanged during oscillation at the resonant frequency $\omega_{RLC} = 1/\sqrt{LC}$.

Let’s now show that a TL-resonator is inherently limited, in one direction at least, by the diffraction limit. We saw in 1.4.3 that, for a generic TEM line fabricated using two perfect conductors and having an arbitrary cross-section not varying along the direction of propagation, the following important result yields [32]:

$$L_0 C_0 = \mu \varepsilon \quad (2.7)$$

where L_0 and C_0 are the inductance per unit length (H/m) and capacitance per unit length (F/m) of the line and (μ, ε) are the optical constants of the medium between the conductors.

In the case of a patch resonator of length s operating on the TM_{010}^z mode (2.7) may be written as:

$$\frac{LC}{s^2} = \mu_0 \varepsilon_0 \varepsilon_d = \frac{\varepsilon_r}{c^2} \quad (2.8)$$

where L and C are the lumped parameters introduced in (2.6), c is the speed of light in vacuum and ε_d is the dielectric relative permittivity assuming non-magnetic materials. Substituting (2.8) in the formula for the RLC resonance gives:

$$f_{RLC} = \frac{1}{2\pi\sqrt{LC}} = \frac{c}{2\pi ns} \quad (2.9)$$

Hence, we find again that the resonator dimension is limited to $s \approx \lambda / 2n$ as imposed by the optical diffraction limit.

Note: this limitation is valid for every TL-resonator regardless of metal patterning as long as the distance between the two conductors stays constant. Recently so-called LC electronic resonators relying on a TL geometry of constant transverse section have been used to demonstrate various applications [52], [53]. Since the geometry is a TL resonator, the aforementioned limitations apply and these devices cannot operate in a circuitual/quasi-static regime. Nevertheless, their fundamental mode can be modelled as a RLC resonance.

2.2 The lumped-element LC resonator in a nutshell

The boundary between circuit theory and transmission line theory is set by the device electrical size [31]. A TL resonator, such as a patch, is a distributed parameter network where current and voltage vary in magnitude and phase along its physical length. For such an object the size can span from half-wavelength to many wavelengths, the lower limit being set by the diffraction limit as seen above.

On the contrary electrical circuits are made with *lumped elements* having dimensions much smaller than the operating wavelength, meaning that voltages and currents do not vary appreciably over the element length. In the quasi-static limit of Maxwell's equation (see 1.5.2) the diffraction limit does not apply and *lumped elements resonators* to confine radiation on a deeply subwavelength scale can be realised.

In this context, we will see that in the THz range, one can still operate in the quasi-static limit to achieve sub-wavelength confinement and envision "hybrid" sub-lambda devices having electronic (rather than plasmonic) character. Furthermore, the huge expertise of RF engineering may be borrowed to enrich THz optoelectronic

devices with functionalities unattainable with conventional photonic resonators. In this section we start addressing this task recalling the physics of the LC tank resonator, which is the fundamental building block of every subwavelength resonator design.

2.2.1 A capacitor's history from DC to optical frequencies.

Let's discuss the behavior of an ideal capacitor as the frequency of the applied voltage sweeps from DC to AC up to quasi-optical frequencies. We will follow the dissertation by R. Feynman in Ref. [54] summarizing the main results.

We consider the capacitor shown in the left panel of FIG. 2.8. If we charge the capacitor with a DC voltage, there will be a positive charge on one plate and a negative charge on the other: the electric field will have a uniform profile between the plates.

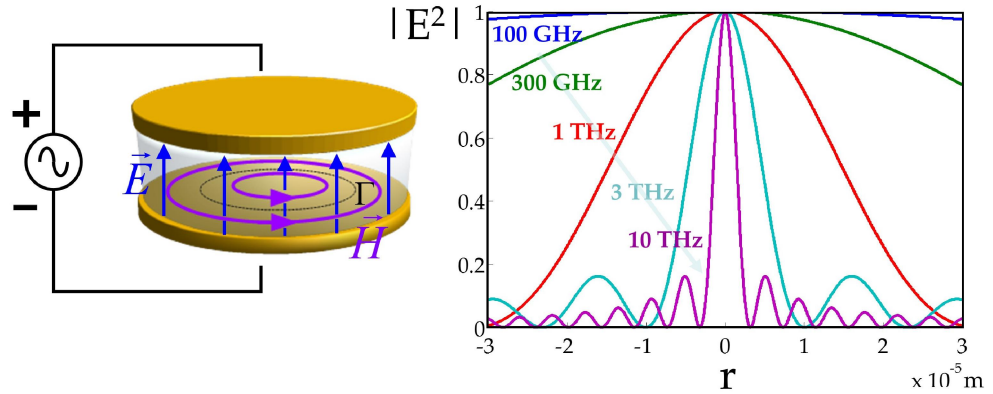


FIG. 2.8 (left) Ideal parallel plate capacitor connected to an AC generator (right). Calculated E-field profile as given by (2.13) on a $30 \mu\text{m}$ scale as a function of the AC driving frequency. The transition from the electrostatic to the microcavity regime is shown.

Moving from DC to AC bias the charges will start to swing back and forth between the plates, an oscillating electric field builds up having magnitude:

$$E = E_0 e^{i\omega t} \quad (2.10)$$

where E_0 is constant (we disregard edge effects).

Now as the electric oscillates, a time-varying flux of electric field through any closed loop Γ (as the one shown in FIG. 2.8) is created. This produces a spatially and time varying magnetic field according to Ampère's circuital law:

$$B(r) = \frac{i\omega r}{2c^2} E_0 e^{i\omega t} \quad (2.11)$$

where r is the distance from the capacitor centre. In turn, this time-varying magnetic field produces a spatially-varying correction to the electric field due to Faraday's induction law in the form:

$$E_{corr}(r) = -\frac{\omega^2 r^2}{4c^2} E_0 e^{i\omega t} \quad (2.12)$$

So the electric field is no longer uniform when an AC voltage is applied. The field intensity has a parabolic profile decreasing when moving away from the centre. Moreover, we cannot anymore assume a purely capacitive impedance for this object, as it has now a partially inductive behaviour, i.e. it stores a magnetic field. Computing the following correction to the field profile due to induction yields the exact solution:

$$E(r) = E_0 e^{i\omega t} J_0\left(\frac{\omega r}{c}\right) = E_0 e^{i\omega t} J_0(k_0 r) \quad (2.13)$$

where J_0 is the 0th-order first kind Bessel function and $k_0 = \omega/c$ is the wavenumber. This interesting result implies that if we push the driving frequency high enough, the electric field at the centre of the condenser and near the edge will point in opposite directions. As a consequence, self-sustained oscillations of the EM field can be hosted by the object: the AC capacitor transforms in a (patch) resonant cavity. This is shown in the right panel of FIG. 2.8 where electric field intensity $|E(r)|^2$ as given by (2.13) is plotted on a scale ranging from micron to tens of microns (typical size of THz devices) for different driving frequencies. The effective wavenumber $k_{eff} = n_{eff} k_0$ with $n_{eff} = 3.6$ is employed to simulate a GaAs-filled capacitor. It is apparent that up to 100 GHz the E-field profile is quasi-constant over this size and it starts bending in the sub-THz range. Above 1 THz the J_0 zeros begin to appear in this spatial range marking the transition to the microcavity regime. For instance, at around 3 THz a complete oscillation of the electric field requires 15 μm , which is the typical dimension of THz patch resonators.

2.2.2 Loading the capacitor: the LC tank circuit

We now to evaluate the feasibility of a lumped-elements LC resonator in the THz range. This implies, as already mentioned, working in the circuitual regime where the physical dimension of each lumped element is much smaller than the operation wavelength. The design, fabrication and characterization of this particular resonator will be the core of this chapter. We start here recalling the physics of the LC resonating circuit. This object is obtained loading an AC capacitor (for our purpose it will always have a dielectric-filled parallel plates geometry) with an inductor (a coil for instance) as sketched in FIG. 2.9(a). It is well known that a capacitor can store energy in the form of an electric field. Physically this energy is stored as charge separation/static voltage i.e. as *potential energy*. On the other hand an inductor can store energy in the form of a magnetic field. This energy physically manifests as motion of electrons (current) i.e. as *kinetic energy*. When connected together, these two reactive components can then store and release energy in complementary modes eventually supporting a self-sustained oscillation of frequency:

$$f_{LC} = \frac{1}{2\pi\sqrt{LC}} \quad (2.14).$$

The phases of charge oscillation in the LC circuit are sketched in FIG. 2.9(b), together with the energy oscillation diagram. Note that in the ideal lossless case the total energy is conserved and the system oscillates for an infinite time. In practice, the oscillation is always damped from parasite resistances in the circuit. The LC circuit is reminiscent of a mechanical pendulum: as the mass oscillates back and forth, potential energy transforms into kinetic energy (motion). Similarly, a pendulum's oscillation is damped due to energy dissipation related to air friction.

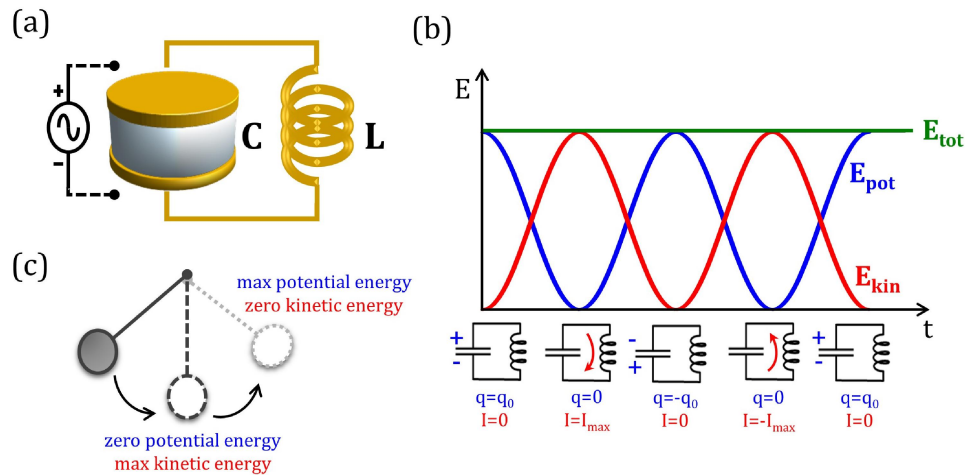


FIG. 2.9 (a) Schematics of the lumped-elements LC resonator. (b) Exchange between electrical (potential) and magnetic (kinetic) energy in LC resonance. The different oscillation phases are sketched below time axes. In the ideal (lossless) case the total energy stays constant. (c) Mechanical counterpart. Adapted from <http://www.allaboutcircuits.com/textbook/alternating-current/chpt-6/electric-pendulum>

It is remarkable that in a pendulum the period of oscillation is set only by the length of the string holding the mass, and not by the mass. In other words, the natural oscillation frequency does not depend on the amount of energy initially stored in the system. The same occurs for the LC circuit, whose oscillation frequency is only set by the geometry of the capacitor and inductor. In fact, this object is also known as *tank circuit*, since it can store electromagnetic energy oscillating at the circuit's resonant frequency regardless on the quantity of energy being stored.

2.2.3 Energy conservation in a subwavelength mode

In this paragraph we will discuss energy conservation in a truly subwavelength electromagnetic mode following approach [55]. We will also introduce the important notion of electron kinetic inductance that is useful to distinguish the boundaries of electronic, photonic and plasmonic regimes. Recall that in a generic electromagnetic mode a continuous exchange exists between the electric field energy $w_E \sim \epsilon E^2/2$ and the magnetic field energy $w_M \sim \mu H^2/2$. From Maxwell's equations it is known that the magnitude ratio between the electric and magnetic field is $H = \sqrt{\epsilon/\mu}E$ which im-

plies $w_E = w_H$. This is true for a standard photonic mode where energy is conserved during oscillation as shown in the left panel of FIG. 2.10(a). What happens if we now consider a subwavelength resonator having minimal size $d < \lambda_0 / 2n$?

To answer, we can write the electric and magnetic fields within a subwavelength cavity as $E = E_0 \sin(kz)e^{i\omega t} \approx E_0 \sin(\pi z / d)e^{i\omega t}$ and $H = H_0 \cos(kz)e^{i\omega t} \approx H_0 \cos(\pi z / d)e^{i\omega t}$ where $k = n\omega / c$. From Ampere's law, the relative magnitude of the H-field respect to the E-field is

$$H = \sqrt{\frac{\varepsilon}{\mu}} E \left(\frac{2nd}{\lambda_0} \right) \quad (2.15)$$

which gives the following for the stored magnetic energy:

$$w_M = \left(\frac{2nd}{\lambda_0} \right)^2 w_E \quad (2.16)$$

This relation shows that for a truly sub-wavelength mode the magnetic energy is much smaller than the electric energy, i.e. self-sustained oscillations are not possible as energy is not conserved [55]. This situation is sketched in the central panel of FIG. 2.10(a): when $d < \lambda_0 / 2n$ the excess of electric energy is radiated away from the mode volume as it cannot all fit in the magnetic energy. This statement expresses the diffraction limit in terms of energy conservation. The sub-lambda regime where the magnetic field is smaller than the electric field is known as *quasi-electro static regime* (QES) because, if we neglect magnetic induction $\partial H / \partial t$, it follows from Faraday's law that the electric field must be quasi-irrotational thus resembling an electrostatic field.

A way to restore energy conservation in a subwavelength mode is to add *free carriers* to the system. In this case an additional energy amount is stored as electrons kinetic energy w_K (see below) and the energy balance can be restored as $w_E = w_M + w_K$. This happens in the two situations pictured in the right panel of FIG. 2.10(a): in the first case a microscopic LC resonator is obtained combining a region storing electric field (capacitive) and another storing magnetic field, as in a split ring resonator; in the second case a plasmonic dipole nano-antenna is considered, where energy oscillation between electric and magnetic field is mediated by free carrier motion.

Note that although energy balance in a subwavelength mode can be recovered introducing free carriers, this may come at a high price in terms of mode losses. To evaluate this, we need to estimate how much energy is stored in the electron kinetic motion as compared to the energy stored in the spatial magnetic field.

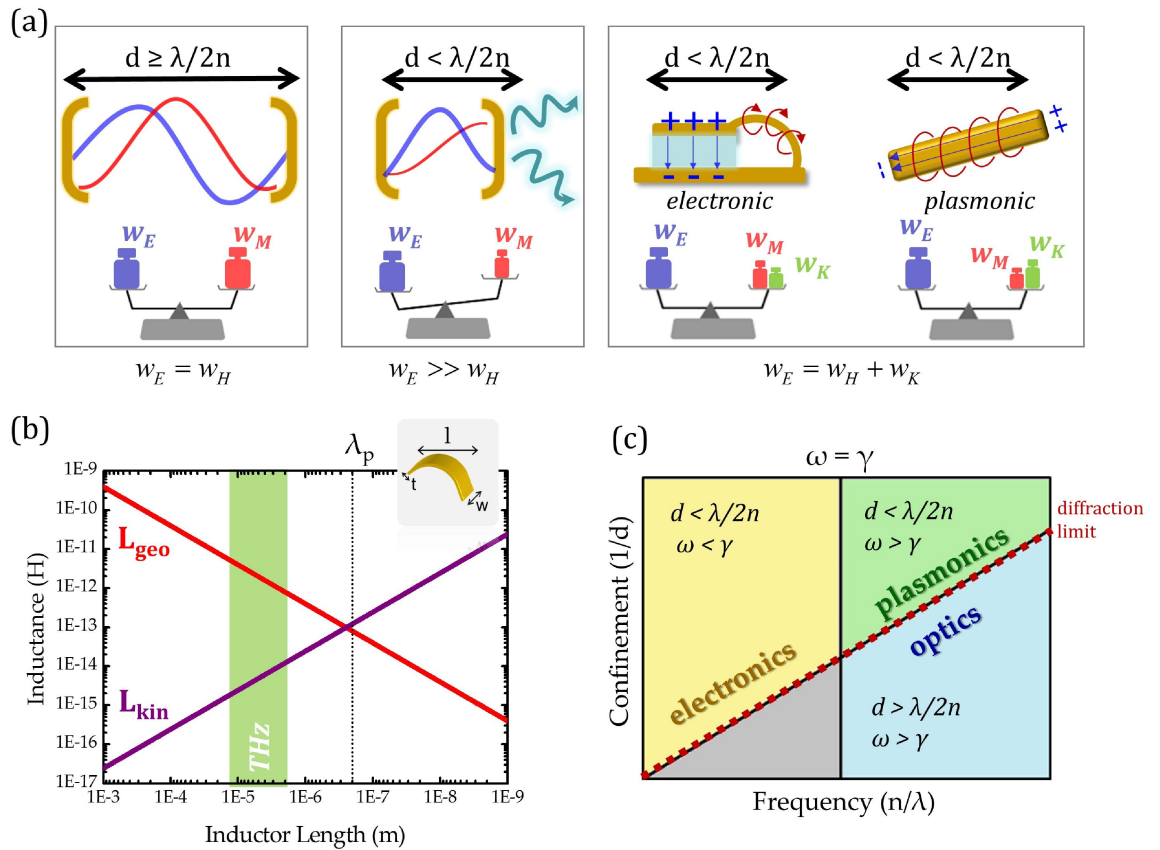


FIG. 2.10(a) Energy balance in a photonic mode (left panel) and in a sub-lambda mode (central panel). Energy conservation is restored via carrier kinetic energy for an electronic LC resonator and a plasmonic nano-antenna (right panel). (b) Geometric inductance vs kinetic inductance as a function of the inductor length. Note: the inductor aspect ratio is kept constant and $L_{kin} \approx 1/l$. The curves cross when the length is comparable to the metal plasma wavelength. THz devices are in the μm range where the kinetic inductance does not dominate yet. (c) Boundaries delimitating electronic, optical and plasmonic regimes as set by the diffraction limit and metal damping.

2.2.4 Electron kinetic inductance

Commonly, the (self)inductance of a conductor (e.g. a coil) is associated with the ability to store energy in a magnetic field and is only determined by the geometry of the conductor. At optical frequencies, however, another form of inductance comes into play, namely the *kinetic inductance*. This inductance originates from the inertia of charge carriers, that is, from their inability to immediately respond to the driving field [35].

The kinetic inductance L_{kin} of a wire of length l and transverse section A is calculated by equating the total kinetic energy of the free carriers in the wire to a form of inductive energy

$$\left(\frac{1}{2}m_e v^2\right)n_e l A = \frac{1}{2}L_{kin} I^2 \quad (2.17)$$

where m_e is the electro mass, v the electron drift velocity and n_e the electron density. Using the microscopic drift model for the electrical current in a wire of cross section A

$$I = evn_e A \quad (2.18)$$

from (2.17) we find:

$$L_{kin} = \left(\frac{m_e}{n_e} \right) \cdot \left(\frac{l}{A} \right) = \left(\frac{1}{\omega_p^2 \epsilon_0} \right) \cdot \left(\frac{l}{A} \right) \quad (2.19)$$

where the metal plasma frequency $\omega_p = \sqrt{n_e e^2 / m_e \epsilon_0}$ has been introduced.

To understand the frequency regime for which the kinetic inductance becomes relevant we must compare the standard geometric inductance L_{geo} of an inductor to the kinetic inductance calculated in (2.19). To do this, the inductance of a thin metal stripe of length l , width w and thickness t (inset of FIG. 2.10(b)) is considered; we take an aspect ratio of $l:w:t = 1:0.1:0.01$ that is comparable to the geometry of the fabricated devices that we will discuss later. The geometric inductance L_{geo} of the stripe is calculated with the formula reported in Ref.[56] for MW inductors. L_{kin} is calculated using (2.19) yielding $L_{kin} \approx l / (0.1l \times 0.01l) \approx 1/l$. FIG. 2.10(b) compares the magnitude of L_{geo} and L_{kin} as a function of l . The curves intersect when the inductor length is comparable to the metal plasma wavelength $\lambda_p = 2\pi c / \omega_p \approx 200$ nm (for Gold).

Below this boundary the largest part of the inductive energy is stored in the magnetic field and only a small fraction in electron kinetic energy. Above λ_p almost all the magnetic energy is stored in electron motion so the system loss will be dominated by metal damping.

Note that for inductors having length $1 \div 10 \mu\text{m}$ (suitable for THz micro-circuits, see later) $L_{geo} \approx$ pH and $L_{kin} \approx$ fH. This implies that metamaterials and optical antennas operating in the THz range are not dominated by kinetic effects and will have intrinsically less losses than their mid-infrared (MIR), near-infrared (NIR) and visible (VIS) counterparts.

We have now all the elements to properly distinguish the regimes of electronics, optics/photronics and plasmonics, the boundaries being defined by the diffraction limit and operating frequency with respect to metal damping. From FIG. 2.10(c) we can see that electronic devices are small compared to the operating wavelength and not dominated by metal loss (i.e. by kinetic inductance). On the other hand photonic devices are always bigger than $\lambda_{eff}/2$ but they are unaffected by metal damping as they mainly rely on displacement currents. Finally, in the plasmonic regime achieving sub-wavelength light confinement using metals at quasi-optical frequencies comes at a high price in terms of losses as kinetic inductance dominates [57].

What emerges from the above discussion is that the THz is a “lucky” range where micrometric lumped-elements not suffering from kinetic inductance effects can be realized. At THz frequencies one can therefore achieve sub-wavelength confinement

without excessive losses and envision “hybrid” sub-lambda devices having electronic (rather than plasmonic) character. Furthermore, the huge expertise of RF engineering may be borrowed to enrich THz optoelectronic devices with functionalities unattainable with conventional photonic resonators as we will show hereafter.

2.3 Circuit-tunable THz sub- λ resonators

In this section the design, fabrication and characterization of the THz sub-wavelength lumped resonators conceived in this thesis will be presented. The detailed experimental study of passive resonators is fundamental for their later exploitation for cavity electrodynamic applications (chapter 3) and integration in optoelectronic devices (chapter 4).

2.3.1 Design of lumped-elements THz resonators

The goal is to build a genuine lumped-elements THz resonator where the electric and magnetic field zones are separate in space. To this scope one can build a capacitive section hosting most of the electric field and an inductive section hosting most of the magnetic field, thus mimicking an electronic LC circuit. The electronic regime is accessible, as discussed, in the THz range and it implies that the physical dimension of each lumped element is much smaller than the operation wavelength. One possible implementation is, for example, to connect a MSM patch cavity to a loop antenna as intuitively sketched in FIG. 2.11(a).

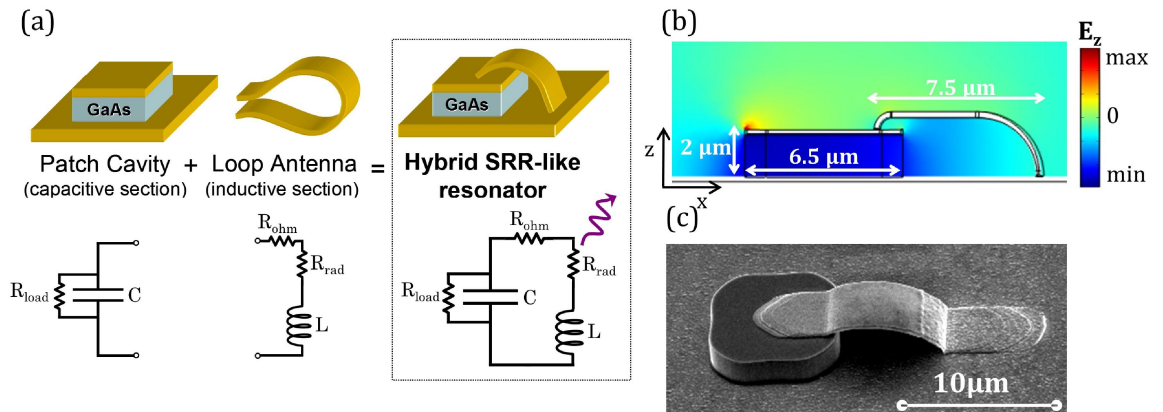


FIG. 2.11(a) Intuitive idea of the lumped-elements sub- λ resonator: a loop-antenna loads a patch cavity resulting in a “hybrid” resonator topologically analogous to a planar split ring. Equivalent LC circuit: the patch is the capacitive section hosting the E-field, while the antenna is the inductive section hosting the H-field. The antenna also features a radiative resistance (R_{rad}) which is responsible for radiation coupling and an ohmic resistance (R_{ohm}), while R_{load} in parallel to the capacitor accounts for dielectric loss. (b) FEM eigenvalue simulation of a THz LC resonator having patch side $s=6.5 \mu\text{m}$, semiconductor thickness $h=2 \mu\text{m}$ and antenna length $l=7.5 \mu\text{m}$: the E-field in the capacitor is quasi-uniform along z at the resonant frequency $f_{LC}=1.6 \text{ THz}$. (c) Scanning electronic microscope (SEM) image of a real device.

Thanks to the presence of the metallic ground plane, and exploiting the mirror symmetry, this is equivalent to fabricating just half of the antenna. This object imple-

ments a 3D topological equivalent of the 2D split ring resonator widely employed as fundamental building block of planar metamaterials. In an ideal picture, the patch cavity is a capacitive section (C) hosting the E-field while the loop antenna is an inductive section (L) hosting the H-field. Circuit analysis would yield a purely reactive impedance of the form $Z = i\omega L / (1 - \omega^2 LC)$, being the two components connected in parallel [50]. To account for radiation coupling and losses, resistances must be introduced: R_{load} accounts for the losses in the semiconductor region; R_{ohm} accounts for the losses induced by the loop and patch metal resistance; R_{rad} accounts for the radiation coupling. As a matter of fact, this hybrid resonator can be seen as a loop antenna with complex impedance $Z_{ant} = R_{ohm} + R_{rad} + i\omega L$, connected to a capacitive load formed by the two metallic plates with complex impedance $Z_{load} = R_{load} / (1 + iR_{load}C)$. In FIG. 2.11(b) the LC mode profile for the proposed geometry obtained via FEM simulation is shown. For a square capacitor of side $s=6.5 \mu\text{m}$, semiconductor height $h=2 \mu\text{m}$ ($n=3.6$ for GaAs is considered, metals are PECs) and suspended inductor length $l=7.5 \mu\text{m}$, the LC resonance is at ≈ 1.6 THz. The colour scale represents the z-component of the E-field. Note that both the capacitor lateral size and the inductor length must be μm -sized to obtain a resonance frequency in the THz range. For comparison the SEM picture of a fabricated device is reported in FIG. 2.11(c).

2.3.2 Fabrication

The fabrication steps to define the suspended loop antennas loading standard patch resonators are detailed in the top panel of FIG. 2.12

We adapted a fabrication procedure for so-called air bridge structures, widely employed in MW technology [58]. A scaffold for sustaining the antenna is formed using a positive photoresist (Shipley S1818) as shown in FIG. 2.12(top); after lithography the resist edges are smoothed via hard baking up to 150 °C. The metal stripe constituting the antenna is then defined via photolithography and lift-off (AZ5214 image reversal photoresist is used in this step). The height of the bridge is set by the resist thickness while the width, length and position of the bridge are set by photolithography. This approach has important implications, as it permits a flexible and efficient control of the geometrical parameters which determine the circuit resonant frequency $f_{LC} = 1 / 2\pi\sqrt{LC}$. Remarkably the fabrication of the suspended antenna is completely separate from the fabrication of the capacitive patch, so one can control them independently on each other. For instance it is possible to set the resonance via the sole inductance, in complete independence from the semiconductor core size which can therefore be extremely sub-wavelength. Moreover the complete fabrication scheme is compatible with the standard process of GaAs/AlGaAs quantum-well devices (QCLs, QWIPs, ...) in metal-metal waveguides.

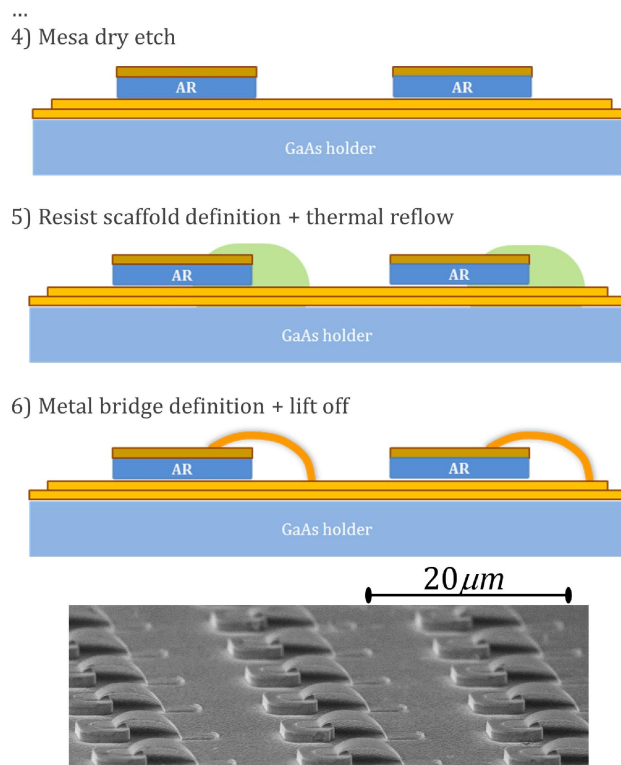


FIG. 2.12 (top) (continued from FIG. 2.4) After defining the patch by ICP etch (4) a resist scaffold is defined by photolithography and thermal reflow (5). A second photolithography allows one to deposit the metallic antenna. The scaffold resist is removed during the lift-off leaving a suspended loop antenna connecting top and bottom metal (6). (bottom) SEM picture of an array of devices.

As a first demonstration we fabricated a 4x4 matrix of resonator arrays whose specifications are reported in FIG. 2.13. The material used is undoped GaAs, grown by MOCVD, of thickness $h=2\ \mu\text{m}$. The loop antennas are made of Ti/Au and their widths and thicknesses are $4\ \mu\text{m}$ and $250\ \text{nm}$, respectively. The device density is approximately $2400\ \text{dev}/\text{mm}^2$. The guiding idea was to independently vary the inductance (via the antenna length l) or the capacitance (via the patch lateral size s) in order to precisely quantify the properties of the system. In particular, we aimed at implementing sets of *isofrequency* devices, i.e. devices with nominally identical operating frequencies, but different structural parameters. In FIG. 2.13- which also reports the *experimental* operating wavelengths/frequencies of the fundamental LC resonance - these device sets are highlighted with identical colours. This shows that L and C can be controlled in total independence, and - for a given frequency - the device geometry can be optimized to suit a specific application. For instance, capacitance dominated devices could be used for developing sub-wavelength lasers, since a large amount of gain is necessary and the optical gain is located in the active semiconductor core. On the other hand, inductance dominated devices could be useful for detectors, since the extremely small surface of the active core can lead to reduced dark currents.

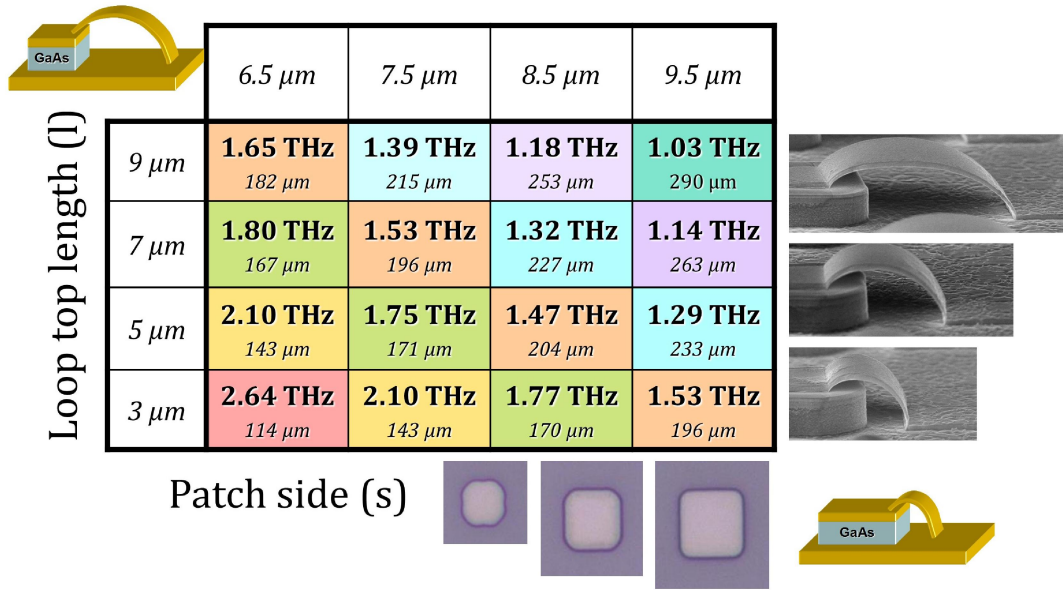


FIG. 2.13 Specifications of the fabricated devices: 16 device geometries were fabricated (a 4x4 matrix) with 4 different patch side s , and 4 different loop antenna size l . The GaAs thickness t is kept constant at 2 μm . The operating frequency (wavelength) of the fundamental LC mode of each device is reported in the corresponding matrix cell. The colours identify the nominally iso-frequency samples. Details about how the cavities were measured are given in 2.3.3

2.3.3 Optical characterization: incidence angle and polarization rules for LC mode excitation

The samples resonances have been probed by polarized, angle-resolved reflectivity measurements using the setup described in 2.1.3. A gold coated mirror of the same dimension of the samples has been used as reference to normalize the reflectivity spectra. Because the spot size S of the THz beam is much larger than the individual structures, we fabricated and characterized arrays of identical cavities that were larger than S to maximize the signal/noise ratio. The period of the arrays is largely sub-wavelength to forbid all the diffractive orders except the 0th-order reflection.

FIG. 2.14(a) summarizes the 4 independent experimental configurations (two sample orientations and two polarizations) which were explored for the characterization of the devices. FIG. 2.14(b) reports the reflectivity measurements on a typical device, for the four measurement conditions highlighted ($\theta = 45^\circ$). The resonant modes appear as sharp resonances in the reflectance spectra.

The two modes at ≈ 7 THz are the dominant $\text{TM}_{001}/\text{TM}_{010}$ modes of a standard MIM patch cavity, whose electric field z -component distribution is represented in the right inset of FIG. 2.14(b).

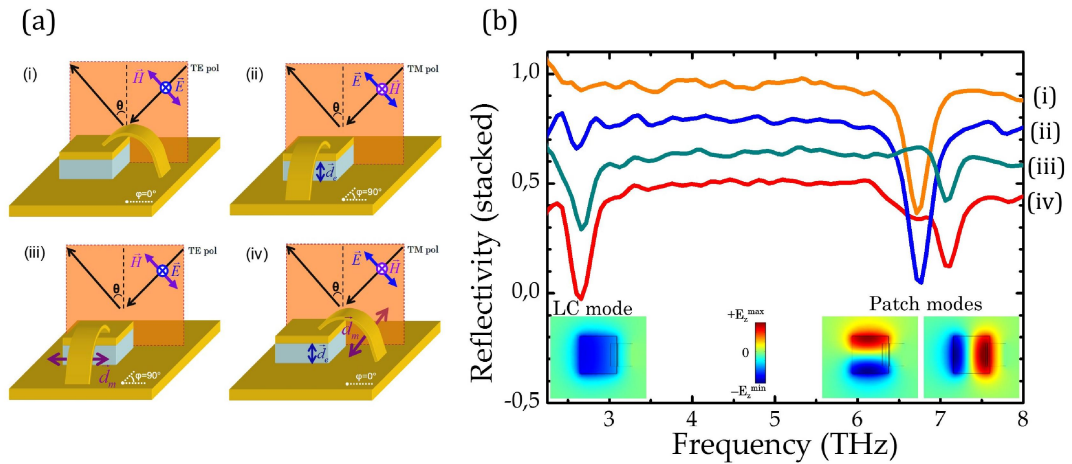


FIG. 2.14(a) Experimental configurations for device characterization. The arrangement of the E,H fields with respect to the incidence plane is highlighted for TM, TE polarizations. The twist angle φ identifies the two non-equivalent orientations of the loop antenna: $\varphi=0^\circ$ parallel to the incidence plane, $\varphi=90^\circ$ normal to the incidence plane. (b) Typical reflectivity spectrum at 45° for a device in the 4 configurations. Spectra are stacked (offset ≈ -0.2) for the sake of clarity. The top spectrum is not shifted and it shows that the background reflectivity is close to unity. The dip around $f \approx 7$ THz is the patch TM_{001}/TM_{010} mode. For configurations (ii) - (iv) the LC mode appears at ≈ 2.6 THz. The E_z field distribution at resonance in the semiconductor is shown in the insets.

The degeneracy of the two fundamental patch modes is split by the presence of the metallic bridge. The low-frequency mode at $f \approx 2.6$ THz is instead the circuitual LC mode, characterized by a (quasi) uniform AC electric field between the two metal plates. This mode exhibits the well-known coupling selection rules of split ring resonators [59], [60] as confirmed by experimental measures shown in FIG. 2.14(b). In configuration (ii) the incoming wave excites the LC resonance by inducing an AC voltage (or charge separation) over the capacitive section via the electric field normal to the metal plates (induced vertical electric dipole, d_E). In configuration (iii) a circulating AC current is instead excited in the loop antenna by the magnetic field normal to the loop plane (induced horizontal magnetic dipole moment, d_M). Both d_E and d_M are excited in configuration (iv) yielding a stronger coupling to the LC mode. No coupling to the LC mode is observed in configuration (i).

2.3.4 Circuit tuning of the resonance via L and C

In FIG. 2.15(a) the measured LC frequencies for all the fabricated devices are reported as a function of the patch side s and of the antenna length l . The operating wavelength of the devices increases linearly with the patch side s . This in agreement with the formula

$$\lambda_{LC} = \frac{2\pi}{c} \sqrt{LC} \quad (2.20)$$

since the square root of C is proportional to s . Also, for a fixed patch side, the operating wavelength increases with the inductor length again in agreement with the aforementioned formula. In all cases, the resonance frequency of the LC mode is

much lower than what is allowed by the diffraction limited patch cavity alone, $s = \lambda_{\text{eff}}/2$. The subwavelength confinement provided by this structure is typically of the order of $\lambda/10$, as for planar split-ring resonators. This design leads to extremely low effective electromagnetic volumes, also due to the very thin semiconductor core employed. For instance, the resonator with $s = 9.5 \mu\text{m}$ and $l = 9 \mu\text{m}$, exhibits a $V_{\text{eff}} = 2 \times 10^{-3} (\lambda/2 \cdot n_{\text{eff}})^3$.

A simple LC model only based on geometrical parameters is remarkably quantitative in the prediction of the resonant frequencies. This is shown in FIG. 2.15(b) where a comparison between the experimental (full dots) and the analytically calculated (open stars) operating wavelengths is reported. The capacitance C_s of the MSM patch of area S and GaAs thickness $t = 2 \mu\text{m}$ is calculated using the standard formula for the parallel plate capacitor:

$$C_s = \epsilon_0 \epsilon_r \frac{S}{h} \quad (2.21)$$

The inductance L_l of the antenna loop of length l is estimated based on the analytical formula for MW inductors [61] adapted for the THz case:

$$L_l (\text{pH}) = 0.2l \left[\ln \frac{2l}{w+t} + 0.5 + \frac{w+t}{3l} \right] \quad (2.22)$$

where the width w , thickness t and total length l of the metallic stripe are expressed in μm .

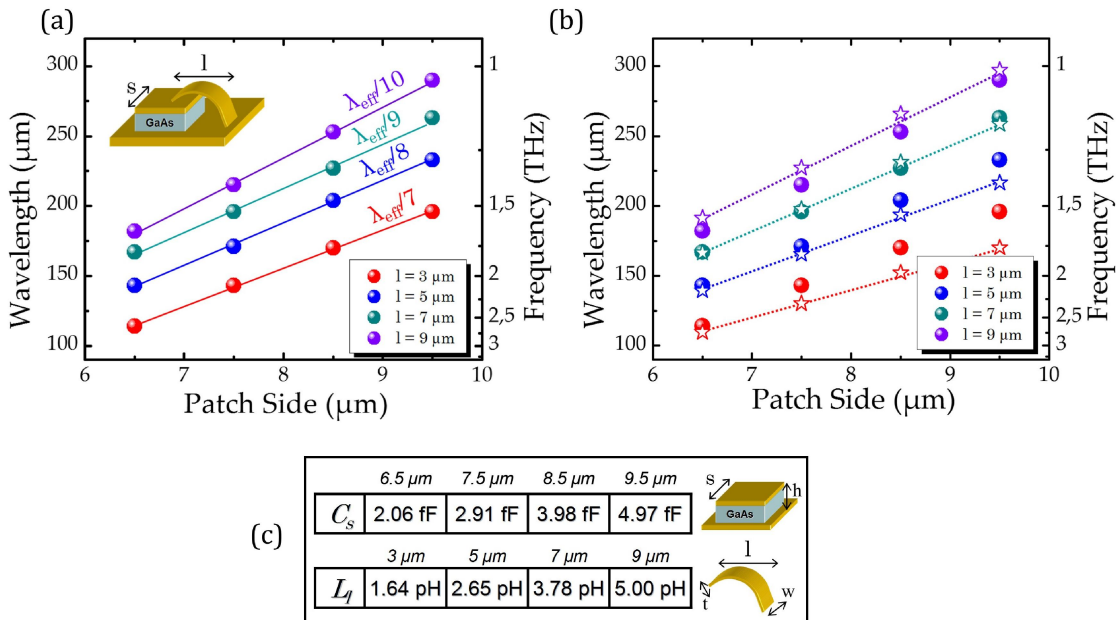


FIG. 2.15(a) Experimental wavelengths (frequencies) of the LC mode as a function of the patch side (s) for various inductor lengths (l). For a fixed loop size the trend is linear, as expected from theory. The confinement ratio in the semiconductor, λ_{eff}/s , is reported for each inductor size. (b) Resonant wavelengths (frequencies) of the LC mode obtained with a simple, parameter-free LC model (open stars) compared to the experimental data from the reflectivity measurements (full dots). (c) Values of the patch capacitance C_s (fF) and of the loop inductance L_l (pH) as obtained from the samples geometrical parameters.

The exact values of the geometrical parameters for the fabricated devices can be measured from SEM or optical microscope pictures. All the resulting values for the lumped elements are reported in FIG. 2.15(c). The agreement is very good, considering that no adjustment parameter is employed. For short values of the inductance length l a discrepancy occurs though, possibly because the loop length becomes comparable to its width. Moreover, it is more difficult to clearly separate the system into a capacitive section and an inductive one. In any case, the predictive character of this very simple LC model is an important result as it will constitute a precious tool for device design. Its accuracy may also stem from the almost complete spatial separation between the electric-field and magnetic-field regions within the device which truly behaves like a lumped-element resonator. This is a major improvement with respect to the previous implementations of the LC resonator in our team [62], [63].

2.3.5 Optical coupling of LC resonators: radiation patterns

In order to characterize the absorption properties and the quality factors of the lumped-elements resonators, reflectivity spectra for incidence angles ranging from 15° to 60° were collected for various samples. The width and depth of the reflectance dips were then estimated from Lorentz fits of the spectra around the LC resonance. The peak absorbed intensity is calculated as $A=1-R_{min}$, with R_{min} the minimum reflectivity value (reached at resonance).

We first discuss the magnetic dipole interaction. FIG. 2.16(a) reports typical angle-resolved spectra for a sample having $s=7.5 \mu\text{m}$ and $l=5 \mu\text{m}$ and for the experimental configuration (iii), as shown in the inset.

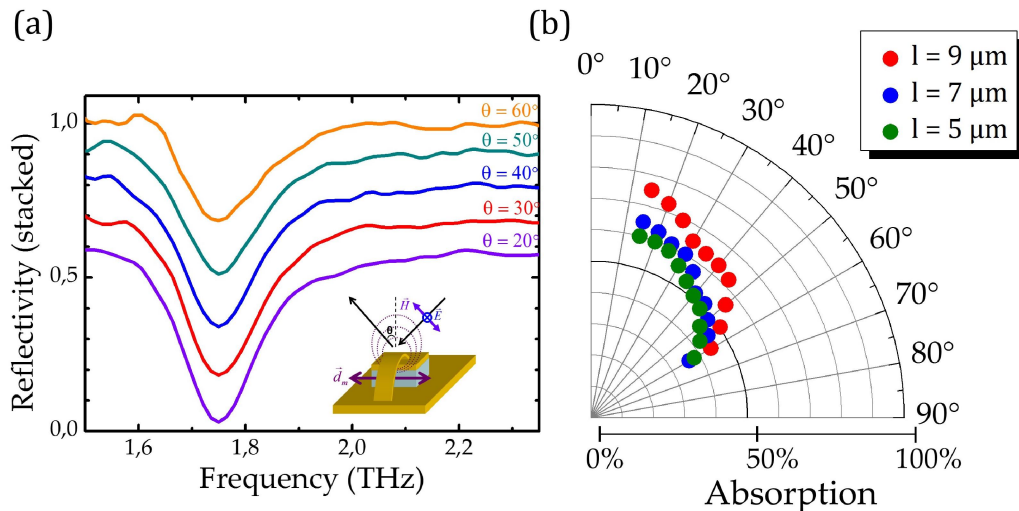


FIG. 2.16(a) Typical reflectivity spectra at different incidence angles (sample $s=7.5 \mu\text{m}$, $l=5 \mu\text{m}$) in the experimental configuration (iii) shown in the inset. Spectra are stacked (offset ≈ -0.1) for the sake of clarity. The top spectrum is not shifted and it shows that the background reflectivity is close to unity. (b) Polar plot of the absorbed intensity vs incidence angle for three devices having constant patch size ($s=7.5 \mu\text{m}$) and different loop length.

The absorption is maximal for quasi-normal incidence and it reduces at grazing angles. This behaviour is easily understood remembering that the antenna acts like an elementary inductive loop which couples to the magnetic field normal to its plane. To strengthen the conclusion, FIG. 2.16(b) plots in a polar diagram the peak absorbed intensity A as a function of the incidence angle θ for three samples having constant patch side ($s=7.5 \mu\text{m}$), but different loop lengths l . The absorption angular pattern is reminiscent of the power pattern of a small loop antenna having a null normal to the plane of the loop and a maximum along its plane [34]. The maximum measured peak absorption is $\sim 70\%$ at (quasi) normal incidence.

For a more quantitative analysis of the magnetic dipole coupling, similar polar diagrams are reported in FIG. 2.17 for the three quasi-isofrequency LC resonators operating around 1.8 THz (on the green diagonal of FIG. 2.13). FIG. 2.17(b) highlights that, at fixed operating frequency, a larger loop permits a stronger radiation coupling. A simple explanation is that the magnetic dipole moment associated to an elementary current loop is proportional to the surface enclosed by the loop itself. In RF engineering this is accounted for by the antenna radiation resistance R_{rad} which - for a small loop - is $\sim S^2/\lambda^4$ (S is the surface enclosed by the loop and λ the operating wavelength). A more insightful physical description of the free space coupling of these objects will require a detailed analysis of loss contributions (radiative, ohmic, dielectric, ...) in function of the device geometry. It is well known for example that a resonator is maximally coupled to the external world when *critical coupling* condition for losses is achieved, i.e. when the resonators are *impedance matched* to the free space. We will deal with the problem of engineering and matching losses in these antenna-based resonators in Chapter 5.

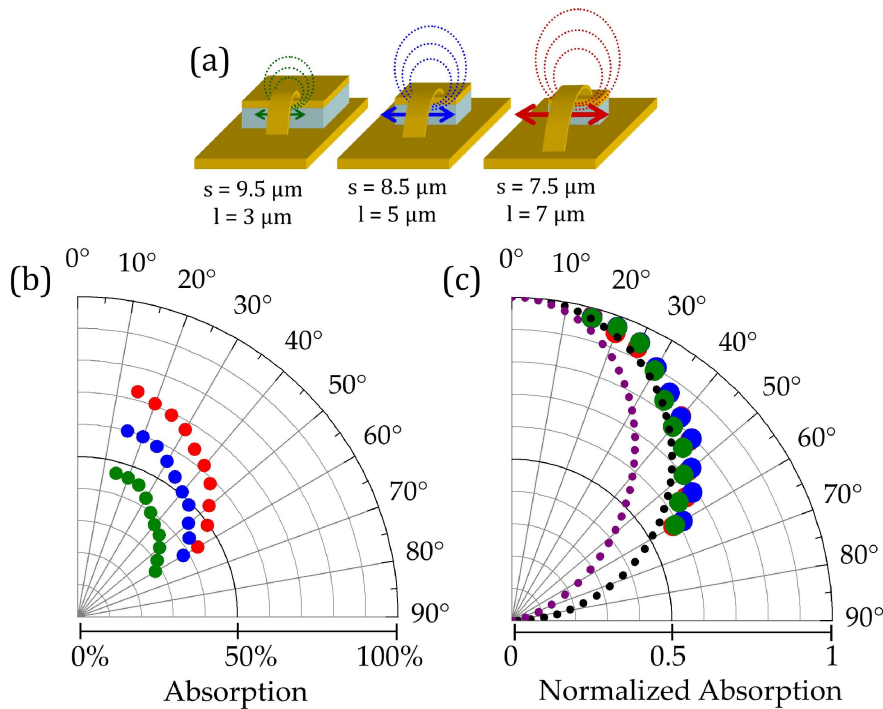


FIG. 2.17 (a) Schematics and dimensions of the *iso-frequency* resonators analyzed. (b) Polar plot of the absorption vs incidence angle. (c) Normalized absorption patterns. For comparison, a $\cos(\theta)$ fit (black dotted line) and a $\cos^2(\theta)$ fit (purple dotted line) are shown. The data clearly follow a $\cos(\theta)$ dependence.

To demonstrate that the measured absorption pattern indeed originates from the small loop antenna (or – equivalently – its magnetic dipole d_M), we plot in FIG. 2.17(c) the absorption pattern $A(\theta)$ normalized to the extrapolated maximum absorption at 0° . All the three data sets superpose and they are well fitted by a $\cos(\theta)$ function. Indeed, a $\cos^2(\theta)$ angular dependence is expected according to the well-known normalized power pattern of a small magnetic dipole. In fact, to obtain the actual absorption strength of a sub-wavelength scatterer we must compute the ratio σ/S , σ being the cross section of the object and S the area of the impinging focused (Gaussian) beam [64]. The actual scattering properties of a single LC resonator are therefore described by an effective extinction cross section of the form $\sigma_{ext}(\theta) \propto A(\theta) \cos(\theta)$ [48], where $\cos(\theta)$ accounts for the broadening of the excitation beam with the incidence angle. The measured absorption data $A(\theta) \propto \cos(\theta)$ therefore correctly lead to a cross section $\sigma_{ext}(\theta)$ with the expected dipolar dependence $\cos^2(\theta)$ [48]. We now discuss the excitation of the LC resonance through electric dipole coupling. FIG. 2.18(a) reports the angle-resolved spectra for a sample having $s=6.5 \mu\text{m}$ and $l=3 \mu\text{m}$ and for the experimental configuration (ii).

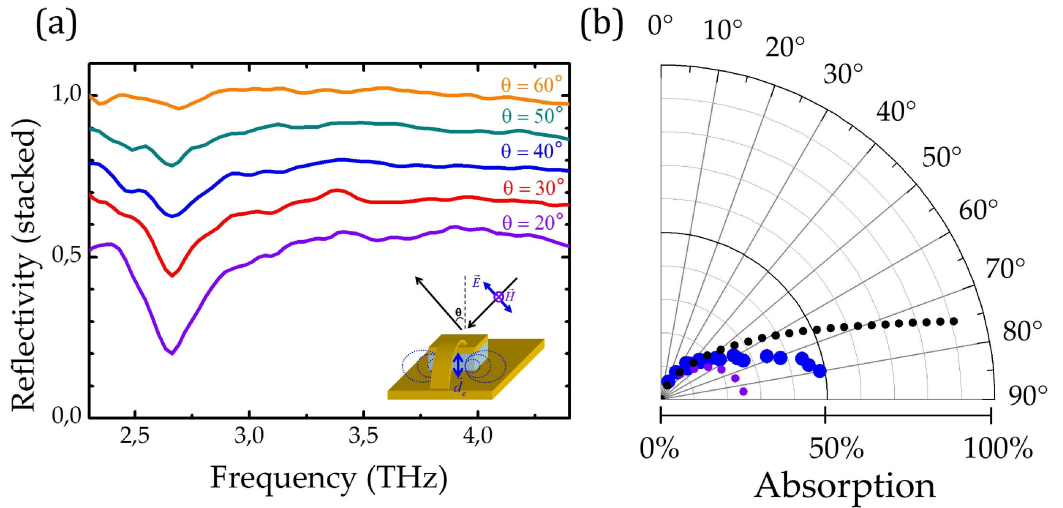


FIG. 2.18(a) Reflectivity spectra at different incidence angles (sample $s=6.5 \mu\text{m}$, $l=3 \mu\text{m}$) in the experimental configuration (ii) shown in the inset. Spectra are stacked (offset ≈ -0.1) for the sake of clarity. The top spectrum is not shifted and it shows that the background reflectivity is close to unity. (b) Polar plot of the absorbed intensity vs incidence angle. For comparison a $\approx \sin^2(x)$ (purple dotted) and a $\approx \sin^2(x)/\cos(x)$ (black dotted) are shown.

The absorption is minimal for quasi-normal incidence and grows at grazing angles (note: the angular range is here extended up to 80°). This happens because the electric field component parallel to the patch sidewalls increases with the incidence angle. This field component excites a charge oscillation at the metal plates of the patch which in turn behaves like an elementary electric dipole. The polar diagram in FIG. 2.18(b) reports the angular dependence of the absorption which is of the form $\sin^2(\theta)/\cos(\theta)$, where the factor $1/\cos(\theta)$ is introduced following the argument discussed above. The resulting cross section $\sigma_{ext}(\theta)$ yields the power dependence $\sin^2(\theta)$, as expected for a sub-wavelength electric dipole. A similar trend is observed in the experimental configuration (iv) (data not shown) where an angle-dependent

electric coupling adds to a constant magnetic coupling due to the TM incident field. An absorption larger than 90% has been measured in the latter configuration thanks to the sum of the electric and magnetic interactions.

The total quality factors (Q_{tot}) of the resonators can be extracted from the reflectivity measurements as $\omega_0/\Delta\omega$, where ω_0 is the peak absorption frequency, and $\Delta\omega$ is the FWHM. Q_{tot} is defined as $(1/Q_r+1/Q_{nr})^{-1}$, where Q_r is related to radiation loss (connected to R_r) and Q_{nr} takes into account all the other non-radiative sources of loss (semiconductor in the patch, metal in the antenna). The measured Q_{tot} for the 3 iso-frequency samples varies from 9 to 12.

2.3.6 Transmission-line model: antenna impedance

In 2.3.4 we saw that a simple calculation of the lumped parameters L and C based on geometry permits to easily design a sub-lambda resonator operating at $f = 1/2\pi\sqrt{LC}$. In a complete description loss mechanisms have to be included via the lumped resistor R in series to L accounting for radiative and non-radiative losses. In TL formalism our object is then completely characterized by its complex impedance in the form:

$$Z = \frac{R + i\omega L}{1 - \omega^2 LC + i\omega RC} \quad (2.23)$$

as already mentioned in 2.1.4. Here the parallel LC resonance model is appropriate as our resonators operate on a ground plane and the two lumped elements L and C are connected in parallel if seen from a TM-polarized field. The resistance R is related to the resonator quality factor Q_0 through the relation [51][31]:

$$Q_0 = \frac{1}{R} \sqrt{\frac{L}{C}} = \omega_0 \frac{L}{R} \quad (2.24)$$

where $\omega_0 = 1/\sqrt{LC}$.

At resonance the capacitive and inductive reactances cancel each other yielding a purely resistive impedance $Z=R$. In Chapter 5 we will discuss in detail the contribution of the different loss mechanisms to the resistance R (loss resistance, radiation resistance) i.e. to the quality factor Q of these sub-lambda resonators. This is a crucial issue in conceiving micro-cavities for lasing.

Here, to complete the description of the passive resonators, we show that the complex resonator impedance can be computed via FEM simulations. To do that an AC voltage is applied at the capacitive gap from a so called lumped port. This gap excitation techniques is not straightforward and attention should be paid if one aims at quantitative calculations (singularities in field, position of the port; see Ref.[65]). For our purpose we will limit ourselves to qualitative predictions. The main advantage with respect to eigen-frequency analysis and wave excitation is the possibility to excite a sub-lambda resonator “from within” to clearly distinguish intrinsic electro-

magnetic modes, a powerful tool available for instance in FDTD simulations which are somewhat less flexible.

In FIG. 2.19 the simulated antenna impedance (real and imaginary) for the fabricated resonator having side $s=9.5\ \mu\text{m}$ and length $l=3\ \mu\text{m}$ (right bottom corner of the matrix in FIG. 2.13) is shown. The typical resonant behaviour as expected from the RLC model is visible. At resonance the impedance is purely resistive with $Z \approx R \approx 800\ \Omega$ which is a value giving a reasonable matching with free-space (recall that the free-space impedance is $Z_0 \approx 377\ \Omega$). This is a hint about the possibility to rely the impedance of an antenna mode and the optical coupling strength [66], thus unifying the concept of optical critical coupling and antennas impedance matching. From the same FEM simulation the 3D radiation pattern can be also computed as shown in FIG. 2.19(b).

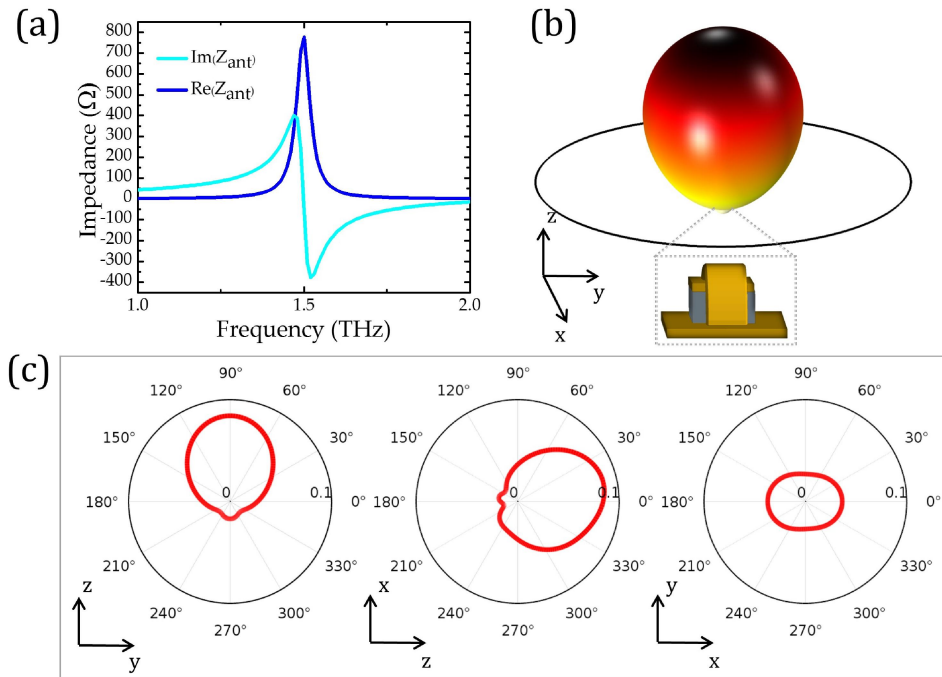


FIG. 2.19(a) Fem simulation of the antenna impedance for a 3D LC resonator having $s=9.5\ \mu\text{m}$ and $l=3\ \mu\text{m}$. The mode is excited through a lumped port (gap excitation). At resonance the impedance is purely resistive with $Z \approx R \approx 800\ \Omega$. (b) Simulated 3D radiation pattern showing the dominating magnetic dipole emission. (c) 2D radiation patterns obtained slicing the 3D pattern.

It is, as expected, reminiscent of the radiation pattern of a magnetic dipole disposed horizontally on a ground plane. The magnetic radiation is of course dominant as well known for split ring resonators. In particular the 2D pattern obtained slicing the 3D lobe along the zy plane at $x=0$ (FIG. 2.19(c)) can be compared to the experimental absorption patterns presented in FIG. 2.17.

2.4 Adding functionalities via lumped elements

In this section we will expand the circuital paradigm introduced so far giving some examples of functionalities which can be added to our circuit-tunable device using discrete elements. As a matter of fact, in order to demonstrate the results presented in the previous section we developed a powerful and flexible platform to design and fabricate 3D electronic THz micro-resonators having user-tailored properties.

2.4.1 Suppression of magnetic coupling: the 3D eSRR

An extensively studied building block for planar metamaterials is the so-called “electrically resonant” split-ring resonator (eSRR or eLC resonator) which, unlike the standard split-ring can, only be driven by an uniform electric field due to its C_{2h} symmetry [67], [68]. Exploiting the air-bridge technique we realized a 3D version of this object, as shown in FIG. 2.20(a). For the fabrication 1.5 μm thick undoped GaAs was used as dielectric core for the circular patch. In this design two inductive loops twisted at 180° are connected to the MSM capacitor.

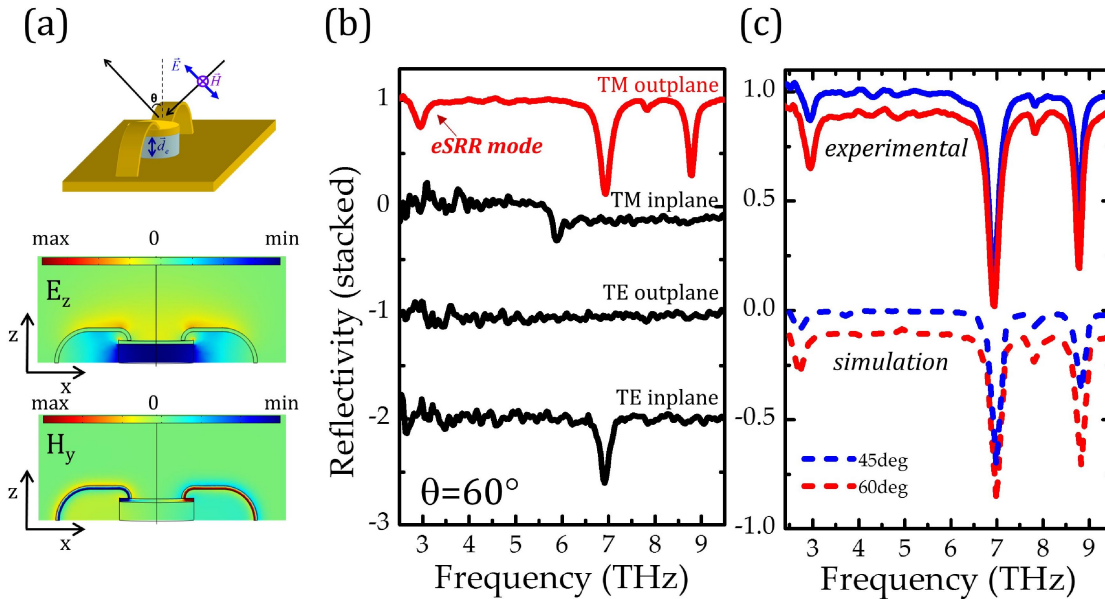


FIG. 2.20(a) The 3D eSRR concept: two lumped inductors twisted at 180° are connected to a MSM capacitor. FEM simulations: the H-field unrolling the two inductors points in opposite directions yielding two magnetic dipoles in phase opposition; a quasi-uniform E-field is excited in the patch (electric dipole). (b) Experimental spectra taken at $\theta=60^\circ$ with bolometer (red curve) and DTGS detector (black curves) for a device having $d=6 \mu\text{m}$ and $l=5.5 \mu\text{m}$. The LC mode at ≈ 3 THz is only excited in TM polarization with the antennas out of the plane of incidence. (c) Comparison between experimental spectra and simulations for $\theta=45^\circ, 60^\circ$.

From a circuital point of view, the addition of a second inductor L yields a resonance blueshift to the value $f_{LC} = \sqrt{2} / (2\pi\sqrt{LC})$, being $L/2$ the equivalent inductance of two identical inductors connected in parallel. However, due to the symmetry of this de-

sign, radiation can excite the LC mode only *via* electric dipolar coupling, as the two antenna magnetic dipoles cancel each other.

This is shown in FIG. 2.20(b) where the experimental spectra taken at $\theta=60^\circ$ are reported. The LC mode can only be excited in TM polarization when the antennas are out of the incidence plane (the configuration sketched in FIG. 2.20(a)) and it becomes more evident at grazing angles. A comparison between experimental spectra and wave propagation simulations for $\theta=45^\circ, 60^\circ$ is also reported in FIG. 2.20(c). The fundamental TM_{110} round patch mode at ≈ 7 THz is also visible just below GaAs Reststrahlen band. An interesting feature of this object is that it does not change the polarization of the incidence field. On the contrary single-SRR like media (like our single antenna 3D resonators) have magneto-electric coupling and cross-polarizing behaviour due to the lack of C_{2h} symmetry. The key message of this section is that adding more lumped elements conveniently chosen and arranged to a 3D LC resonator it is possible to modify the frequency response and the optical behaviour at once. One application of this concept will be shown in Chapter 3.

2.4.2 Inductors in parallel

Contrary to the previous paragraph here two inductors ($L_{eff}=L/3$) are connected to a patch cavity at 90° angle. While the resonant frequency is given as before as $f_{LC} = \sqrt{2} / (2\pi\sqrt{LC})$, the magnetic coupling is restored because of symmetry breaking. Furthermore a third inductor is added in parallel ($L_{eff}=L/3$) allowing a further frequency blueshift to the value $f_{LC} = \sqrt{3} / (2\pi\sqrt{LC})$.

The experimental reflectivity spectra for 2-inductors and 3-inductors resonators for various inductor lengths, but equal dimensions of the capacitive section, are shown in FIG. 2.21(a). The data are normalized to highlight the wide frequency tuning of the LC resonance with the inductance loop length. The experimental resonant frequencies are plotted in FIG. 2.21(b) as a function of the inductor length l , and the mean ratio between the LC frequencies for a 3-loop and a 2-loop device of same l is $1.28 \approx \sqrt{3}/\sqrt{2}$, in excellent agreement with the circuital law for inductors in parallel. Finally in FIG. 2.21(c) a summary on the analysed configurations for parallel inductors with their coupling rules and circuital equivalents is presented.

The important aspect emerging from these results is that a circuital approach allows one to span an extremely wide range of operating wavelengths ($70 \mu\text{m} < \lambda < 215 \mu\text{m}$ in this case) without changing the semiconductor region volume, which is in this case fixed at a lateral size of $7 \mu\text{m}$. In a hypothetical cavity electrodynamics experiment, this means keeping constant the number of active dipoles involved in the process. Or, in the case of a detector, keeping its active volume unvaried to a sub wavelength dimension irrespectively of the operating wavelength. Moreover the radiation properties (coupling, polarization) can be engineered using an external antenna and without modifying the semiconductor core.

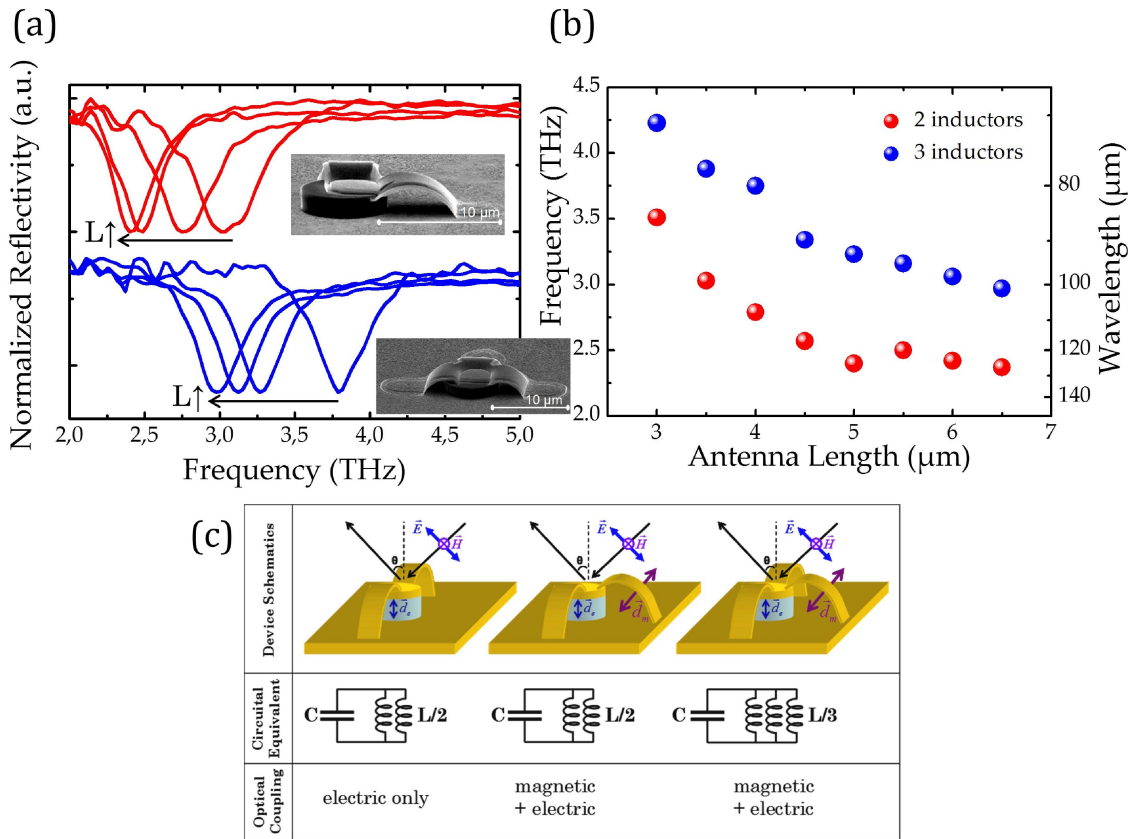


FIG. 2.21(a) Reflectivity spectra (normalized) for 2 and 3 inductor devices. Tuning of the LC resonance with inductance is shown. (b) LC frequencies (wavelengths) vs loop length for 2 and 3 inductor devices. (c) Schematics of 2 and 3 inductor devices. The experimental configuration (incidence plane, polarization) used for characterization is also sketched. Equivalent circuits and allowed optical coupling are specified.

2.4.3 Suspended tuning stub

Another useful approach to tune the LC resonance consists in endowing the resonator with a suspended tuning stub, as shown in FIG. 2.22(a). This creates a second air-filled capacitive region in parallel to the GaAs capacitor yielding an effective capacitance $C_{eff} = C_{GaAs} + C_{stub}$. Due to the low permittivity provided by air the capacitive stub allows for a fine tuning of LC resonance. This object is called *shorted folded monopole* or *F-inverted antenna (FIA)* and it's well-known in RF antenna engineering [42]. To prove this concept in the THz range a series of suspended FIAs arrays (2.5 mm x 2.5 mm, ≈ 2200 devices/mm²) has been fabricated on a 1 μm MOCVD grown GaAs slab. The fabrication scheme employed is the same described in FIG. 2.12 with the exception that a wider resist spacer is defined to create the suspended stub.

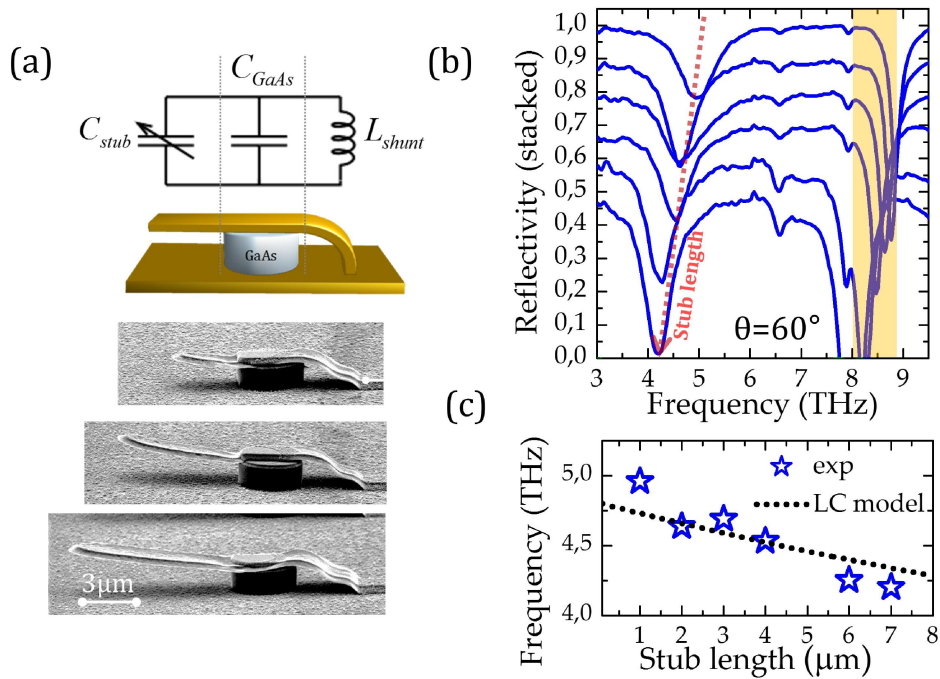


FIG. 2.22(a) Sketch of the 3D LC resonator endowed with a tuning suspended stub and its circuitual equivalent. SEM pictures of fabricated devices on a $1\mu\text{m}$ -thick GaAs slab. Patch diameter is $3\mu\text{m}$. (b) Reflectivity spectra at 60° incidence angle (TM inplane configuration) showing the LC mode redshift in function of the stub length. (c) Geometric LC model accounting for the stub capacitance vs experimental frequencies.

All the samples have constant patch diameter $d=3\mu\text{m}$, inductor length $l=4\mu\text{m}$ and width $w=3\mu\text{m}$. The stub length l_s is tuned between $1\mu\text{m}$ and $7\mu\text{m}$. In FIG. 2.22(b) the reflectivity spectra for the FIA samples is shown.

To maximize the radiation coupling TM polarized light at 60° incidence is used and the antenna is aligned in the incidence plane (configuration (iv) in FIG. 2.14(a)). As expected the LC mode gently redshifts as the metallic stub gets longer thus providing a fine tuning between 4 THz and 5 THz. The simple geometric LC model already employed in 2.3.4 can again be used to estimate the frequency redshift induced by the stub (FIG. 2.22(c)) considered that $f_{LC} = 1/2\pi\sqrt{L(C_{GaAs} + C_{stub})}$ with $C_{stub} = \epsilon_0 l_s \cdot w / h$.

At this point we can conclude the description of the 3D sub-wavelength LC resonator interpreting it from another perspective, i.e. as the extreme “compactness limit” of a monopole antenna. The derivation of the 3D lumped resonator from a standard vertical monopole antenna is shown in FIG. 2.23(a).

The quarter-wavelength monopole on a metal ground plane, invented in 1895 by radio pioneer Guglielmo Marconi, is one of the most famous RF antenna design. This object inherits its current distribution and main features from the $\lambda/2$ dipole owing to image theory but it has a lower input impedance $Z_A \approx 37\Omega$ (for a $\lambda/2$ dipole $Z_A \approx 73\Omega$). The monopole antenna is appealing for photonic applications especially because of the presence of a ground plane naturally fitting the metal-metal geometry of QW-based devices. Moreover a huge sub-lambda confinement of radiation can be achieved in a semiconductor load at the antenna gap.

A simulation of the antenna impedance for a THz $\lambda/4$ monopole of length $17\ \mu\text{m}$ resonating at $\approx 4\ \text{THz}$ is shown in the top panel of FIG. 2.23(b). The antenna is loaded by a patch of $3\ \mu\text{m}$ diameter filled with a $1\ \mu\text{m}$ -thick GaAs core. The metal stripe constituting the antenna is intentionally non-ideal (width $3\ \mu\text{m}$ and thickness $0.25\ \mu\text{m}$) to compare with typical fabricated metal stipes used as magnetic loops. The impedance shows the typical resonant behaviour around $\approx 4\ \text{THz}$ and at resonance the impedance is real and low ($Z_A \approx 30\ \Omega$). From that we can compute the reflectivity as $R = |S_{11}|^2 = |(Z_A - Z_0)^2 / (Z_A + Z_0)^2|$ (blue curve in FIG. 2.23(c)). The antenna resonance appears broad (bandwidth $\approx 1.3\ \text{THz}$) with a low Q factor ≈ 4 . At a glance the standard monopole is quite broadband and furthermore challenging to fabricate (a $\lambda/4$ monopole operating at $100\ \mu\text{m}$ would demand a $25\ \mu\text{m}$ vertical metal wire of high aspect ratio). A recent nice realization for MIR applications can be found in Ref.[69] where the resonance is narrowed exploiting antenna phasing (i.e. array periodicity effect).

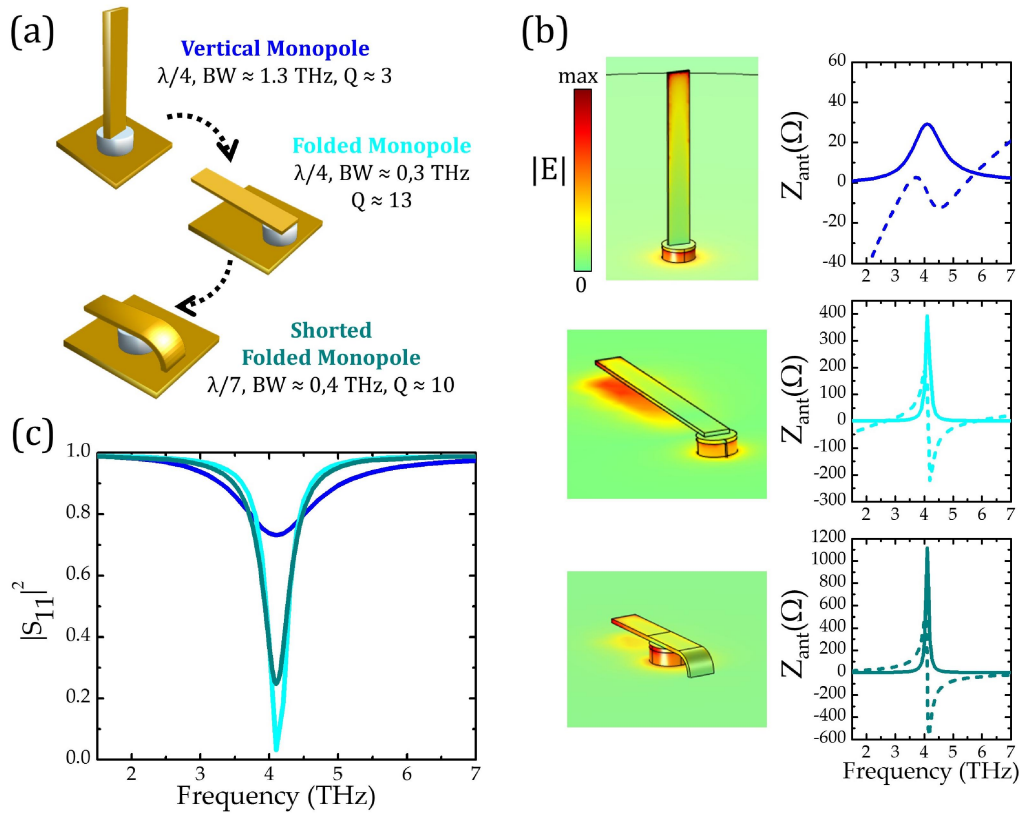


FIG. 2.23(a) Derivation of the folded monopole (L-antenna) and shorted folded monopole (F-antenna) from the vertical monopole. All the antenna are endowed with a semiconductor load (b) FEM impedance simulation: real part (continuous line) and imaginary part (dashed line). The magnitude of the electric field at the antenna is reported. (c) Simulated reflectivity $R = |S_{11}|^2$ computed from impedance for the three monopoles design.

One solution proposed in RF engineering to reduce the bandwidth consists in bending the antenna to have some of the structure parallel to the ground plane, while keeping the total length approximately around $\lambda/4$. In this configuration the contribution from the horizontal part of the structure to radiation is negligible as currents

flowing there cancel out the image currents induced in the ground. The radiation stems indeed from the small vertical part of the antenna while the total length influences the input impedance and fixes the resonant frequency. This antenna, known as *folded monopole* or *L-inverted antenna*, has narrower bandwidth with respect to the Marconi antenna i.e. higher Q factor. This is shown in FIG. 2.23(c) where the light-blue curve represents the reflectivity of a THz L-antenna obtained folding the previous 17 μm metal stub on the same load patch. Note that the mode impedance now is well matched to the vacuum impedance yielding a good optical coupling. This folded monopole would be easier to implement using standard microfabrication techniques but still would lack in compactness.

From this configuration the F-antenna discussed above is derived by shorting the monopole to the ground plane. This strategy is one example of so-called *reactive loading* [42] used in small RF antennas to reduce the antenna size with respect to the resonant wavelength. In our case the idea is to build up an inductive region where magnetic energy is stored to counterbalance the capacitive reactance associated to the folded antenna. In fact the F-antenna is way smaller than the L-antenna resonating at the same frequency. In the example of FIG. 2.23 to get a 4 THz F-antenna the suspended stub is reduced at $\approx 7 \mu\text{m}$ providing a $\lambda_{\text{eff}}/7$ confinement with a $\approx 3 \mu\text{m}$ long inductor. The price to pay for its subwavelength nature is of course a slightly larger bandwidth with respect to the previous configuration. The antenna impedance is higher than in the previous case but optical coupling remains good. In the limit where the stub length tends to zero we come back to the split-ring 3d resonator which may then be conceived as an electrically small and extremely compact version of the standard monopole antenna.

3 Applications of passive resonators

The emerging research field of metamaterial-based devices (*metadevices*) aims at exploiting the electromagnetic response of metamaterials to achieve original device functionalities. A range of functional material systems including semiconductors and liquid crystals have been integrated with metamaterial sub-wavelength building blocks leading to functionalities such as electro-optic modulation, ultrafast optical modulation, harmonic generation, and bistability [70].

Recently metasurfaces have enabled fundamental studies of cavity electrodynamics (CED) with, for example, experiments demonstrating an enhancement in the electronic dipole spontaneous decay rate in a variety of systems (e.g. quantum dots and molecules) upon combination with meta-atoms [71], [72]. In parallel, actively tunable or switchable metadevices based on electrical, mechanical or optical control of electromagnetic properties on a subwavelength scale have been realized, following the increasing request of fast information processing with light [73].

The first part of the chapter illustrates an application of the previously developed circuit-tunable meta-atoms to a CED study: the resonators are endowed with a THz parabolic quantum well (PQW) and their LC resonance is tuned across the PQW ISB transition enabling the demonstration of strong light-matter coupling at room-temperature within an ultra-subwavelength volume.

In the second part, preliminary results about the realization of optically switchable 3D metadevices and polarizing metasurfaces are presented.

3.1 Room temperature strong light-matter coupling in THz meta-atoms

3.1.1 Strong light-matter coupling

We briefly discuss the interaction between a resonant mode inside a micro-cavity and a generic two-level system (in our case it will be an ISB transition) following Fox's book [74]. The situation is shown schematically in the left part of FIG. 3.1(a). We assume that the two-level system can absorb photons from the cavity mode and also emit photons into the cavity by radiative emission. When the transition frequency ω_{21} coincides with the frequency ω_c of the cavity mode, the interaction between the two-level system and the radiation field is strongly affected, since the energy exchange is resonant. The transition frequency of the two-level system is determined by its internal structure (the QW design in the case of an ISB transition) and is considered as fixed in this analysis. The resonance condition is achieved tuning the cavi-

ty so that its frequency coincides with that of the transition. At resonance, the light-matter interaction regime is determined by three parameters:

- i. γ_c : the photon decay rate of the cavity, given by $\gamma_c = \omega_c / Q$;
- ii. γ_{21} : the transition decay rate (the FWHM of the ISB transition);
- iii. Ω : the two-level system/cavity coupling parameter.

These three parameters define characteristic time-scales for the dynamics of the system. The interaction is in the *strong coupling regime* when $\Omega > \max(\gamma_c, \gamma_{21})$. Conversely, the *weak coupling regime* is set when $\Omega < \max(\gamma_c, \gamma_{21})$ [74].

In the weak coupling regime the emission of the photon by the two-level transition is an irreversible process, but the emission rate is affected by the cavity via the Purcell factor. In the strong coupling regime, by contrast, the light-matter interaction is faster than the irreversible processes. This makes the photon emission a *reversible* process in which the photon is re-absorbed by the two-level system before it is lost from the cavity. The situation is pictorially sketched in the right panel of FIG. 3.1(a): the two-level system emits a photon into the resonant mode, which then bounces between the mirrors and is re-absorbed by the dipole faster than it is lost from the mode.

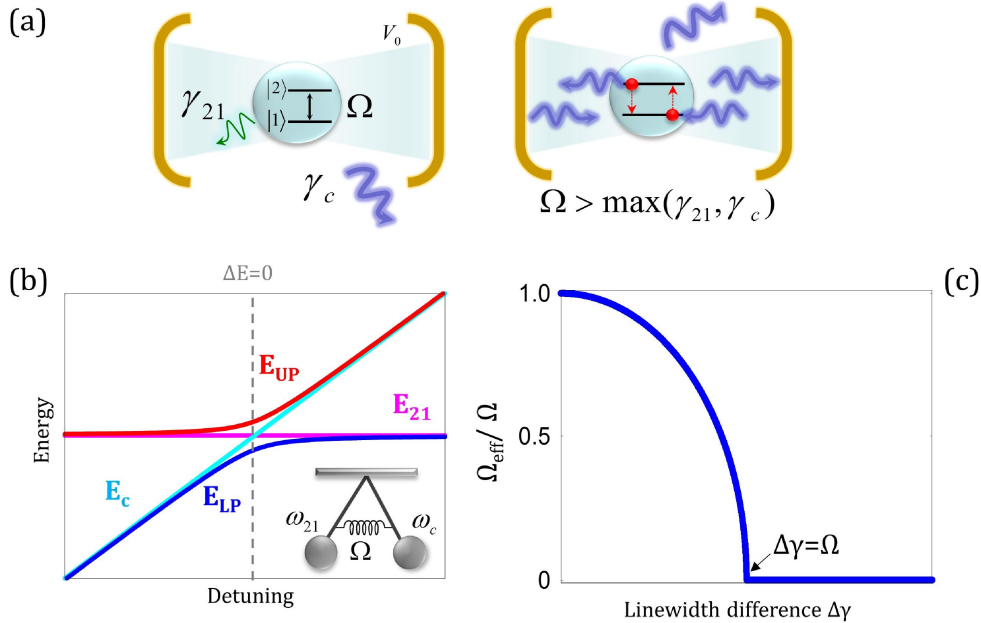


FIG. 3.1(a) Interaction of a two-level system with a microcavity mode: relevant parameters (left) and strong coupling picture (right). (b) Dispersion of polaritonic energies as a function of the detuning $\Delta E = E_c - E_{21}$; (inset) classical perspective: two oscillators of frequencies (ω_{21}, ω_c) coupled via the interaction constant Ω . (c) Effective Rabi splitting accounting linewidth broadening as given by Eq. 3.11.

The interaction between a resonant cavity mode and a two-level atom was first analysed in detail by Jaynes and Cummings in 1963 [75]. The Jaynes-Cummings model describes the interaction of a two-level atom with a single quantized mode of the radiation field. We will summarize in the following the main results of the model with-

out entering in the details of calculations. The eigenstates of the system in the strong coupling regime are derived from the complete Hamiltonian as the perturbative approach (i.e. Fermi golden rule) cannot be used. Following Ref. [76] we note the fundamental and the excited states of the two-level system $|\psi_{1,\vec{k}}\rangle$ and $|\psi_{2,\vec{k}}\rangle$ respectively, and the corresponding energies are E_1 and E_2 . The Hamiltonian describing the electronic (matter) states is then:

$$H_{mat} = E_1 |\psi_{1,\vec{k}}\rangle\langle\psi_{1,\vec{k}}| + E_2 |\psi_{2,\vec{k}}\rangle\langle\psi_{2,\vec{k}}| \quad (3.1)$$

The radiation field is described in the quantum picture by

$$H_{phot} = \hbar\omega_c \left(a^\dagger a + \frac{1}{2} \right) \quad (3.2)$$

where $\hbar\omega_c$ is the energy of a cavity photon (a monochromatic field is assumed). The interaction Hamiltonian is $H_{int} = -\vec{d} \cdot \vec{E}$ in the dipole gauge, where $\vec{d} = -e\vec{r}$ is the electric dipole operator and $\vec{E} = i\sqrt{\hbar\omega_c / 2\varepsilon_0\varepsilon_r V_0} (a - a^\dagger) \hat{\varepsilon}$ is the electric field operator (supposed homogeneous in the cavity volume V_0). In the case of a cavity mode coupled with an ISB transition, the field is assumed to be polarized along the QW growth direction ($\hat{\varepsilon} // z$). In the rotating-wave approximation the interaction Hamiltonian can be written as

$$H_{int} = -i\hbar\Omega \left(|\psi_{2,\vec{k}}\rangle\langle\psi_{1,\vec{k}}| a - |\psi_{1,\vec{k}}\rangle\langle\psi_{2,\vec{k}}| a^\dagger \right) \quad (3.3)$$

where the coupling constant for a single ISB transition is given by

$$\Omega = \sqrt{\frac{e^2 f_{12}}{4\varepsilon_0\varepsilon_r m^* V_0}} \quad (3.4).$$

It is then possible to evaluate the matrix elements of the complete Hamiltonian in the basis $\{|\psi_{1,\vec{k}}\rangle \otimes |1\rangle, |\psi_{2,\vec{k}}\rangle \otimes |0\rangle\}$ where $|n\rangle$ is the state with n photons in the cavity. This yields:

$$H_{JC} = H_{mat} + H_{phot} + H_{int} = \begin{pmatrix} \hbar\omega_c & i\hbar\Omega \\ -i\hbar\Omega & \hbar\omega_{21} \end{pmatrix} \quad (3.5)$$

which represents just a system of two oscillators of frequencies ω_c and ω_{12} coupled via the constant $\hbar\Omega$. The system eigenstates are mixed atom-photon states called *cavity polaritons* and consist of a linear superposition of the basis vectors, i.e. of an electronic excitation and a cavity photon. The polaritons energies as a function of the detuning $\Delta E = E_c - E_{21}$ are given by

$$E_{UP/LP} = \frac{1}{2} \left(E_{21} + E_c \pm \sqrt{\Delta E^2 + (2\hbar\Omega)^2} \right) \quad (3.6).$$

and they are traced in FIG. 3.1(b). Two polariton branches emerge: the high energy state is noted *upper polariton* (UP) and the low energy state *lower polariton* (LP). At zero detuning we get $E_{UP/LP} = E_{21} \pm \hbar\Omega$ giving a minimum energy splitting of $2\hbar\Omega$ (see FIG. 3.1(c)). We observe that the UP/LP polariton states are issued from the *anti-crossing* of the matter excitation energy (supposed fixed $E_{21} = \hbar\omega_{21}$) and the energy of the cavity mode E_c , which we recover as asymptotic values when we move far from resonance.

The splitting of the atom-cavity modes can be explained with a quasi-classical approach by considering the properties of two coupled classical oscillators of frequencies ω_c and ω_{21} interacting via the coupling strength Ω [77]. The frequencies of the coupled modes are given by:

$$\omega_{\pm} = (\omega_c + \omega_{21})/2 \pm \sqrt{\Omega^2 + (\omega_c - \omega_{21})^2} \quad (3.7)$$

At resonance, with $\omega = \omega_c = \omega_{21}$, this reduces to $\omega_{\pm} = \omega \pm \Omega$ in agreement with the results of the Jaynes-Cummings model above.

3.1.2 Intersubband polaritons

In the following we will consider the case of an intersubband (ISB) transition coupled to a cavity mode. The mixed light-matter states observed in the strong coupling regime are called *intersubband polaritons* and have been studied in a variety of cavity geometries [53], [78]–[80]. Studying the strong light-matter interaction employing QWs as material system is particularly interesting in the perspective of building efficient polaritonic sources such as LEDs or coherent emitters owing to the well-established III-V semiconductor technology [81].

Before moving on it should be noted that in the case of a quantum well we deal typically with an electronic population confined in 2D in the first subband and characterized by a sheet density n_{2D} . When we insert the quantum well in a cavity we have then N intersubband transitions of energy $E_{12} = \hbar\omega_{12}$ identically coupled to a cavity mode of energy E_c . It can be shown that the 2-level Jaynes-Cummings model is still valid and the Rabi splitting can be cast in the form [82]

$$\Omega_{split} = 2\Omega = \sqrt{\frac{f_{12}e^2n_{2D}}{\epsilon_0\epsilon_r m^* L_{QW}}} \cdot \sqrt{\Gamma_{opt} \cdot f_w} = \omega_p \sqrt{\Gamma_{opt} \cdot f_w} \quad (3.8)$$

where f_{12} is the oscillator strength of the ISB transition, e is the electron charge, n_{2D} is the electronic surface density, ϵ_r is the semiconductor dielectric constant, m^* is the electronic effective mass, L_{QW} is the QW width and ω_{plasma} is the plasma frequency of the electrons in the QW. Γ_{opt} is the *optical mode confinement factor* accounting for the overlap of the cavity mode with the semiconductor active region (AR) hosting the QWs

$$\Gamma_{opt} = \frac{\iiint_{AR} |E_z|^2 d\vec{r}}{\iiint_{everywhere} |E|^2 d\vec{r}} \quad (3.9).$$

f_w is a *quantum well overlap factor* quantifying the spatial coverage (in percent) of the QW layers along the heterostructure stack (i.e. where interacting electrons are actually present, for a periodic structure) [83]

$$f_w = \frac{L_{eff}}{L_b + L_w} \quad (3.10)$$

where L_{eff} is the effective quantum well length (accounting for the spatial extent of the wavefunction [84]) and L_b and L_w are the physical lengths of the barrier and well respectively.

When the linewidth broadening is relevant (broadening mechanisms in solid state systems and/or lossy resonators) phenomenologically we can account for loss mechanisms by introducing an imaginary part to each energy state. $\hbar\omega_{12}$ and $\hbar\omega_c$ are then replaced by $\hbar\omega_{12} - i\hbar\gamma_{12}$ and $\hbar\omega_c - i\hbar\gamma_c$ where γ_{12} is the FWHM of the intersubband transition and $\gamma_c = \omega_c / Q$ is the photon decay rate of the cavity. The effective Rabi splitting is thus given by

$$\Omega_{eff} = \sqrt{\Omega^2 - (\gamma_{12} - \gamma_c)^2} \approx \sqrt{\omega_p^2 \Gamma_{opt} f_w - (\gamma_{12} - \gamma_c)^2} \quad (3.11)$$

This means that the imprint of the strong-coupling regime (i.e. Rabi splitting) can be recovered in lossy systems provided that the linewidth difference does not overcome the coupling constant as shown in FIG. 3.1(d). If the losses are matched the experimental splitting reproduces exactly the coupling constant of the system as in an atomic systems where line broadening is negligible.

3.1.3 Parabolic quantum wells

The parabolic potential well is a text-book case of quantum confinement that is a direct analogy to the harmonic oscillator of classical mechanics. The eigenstates available for an electron of mass m^* trapped in a parabolic potential along the direction z are found solving Schrodinger equation

$$-\frac{\hbar^2}{2m^*} \frac{\partial^2}{\partial z^2} \psi + m^* \omega^2 \frac{z^2}{2} \psi = E\psi \quad (3.12)$$

yielding the well-known energy states ladder

$$E_n = \left(n + \frac{1}{2} \right) \hbar\omega \quad (n=0, 1, \dots) \quad (3.13)$$

We know that, thanks to band-gap engineering, user-tailorable band profiles in semiconductor heterostructures can be obtained to match various applications.

Today, semiconductor QWs featuring a parabolic potential profile (aka *parabolic quantum wells*, PQWs) are promising candidates for THz devices operating above liquid nitrogen temperature. Owing to (3.13) every transition between two adjacent energy levels contribute to the overall ISB transition at energy $\hbar\omega$, which is solely determined by the width and depth of the well. Moreover, it has been shown by Kohn that the dipole excitations in a parabolic confinement are not affected by electron-electron interactions [85]. The validity of the generalized Kohn theorem has been verified by absorption and emission spectroscopy measures on PQW systems [86]. It implies that the observable electronic resonance frequency does not blueshift with increasing doping as one would expect from depolarization effects. This feature makes PQWs attractive systems to study also the ultra-strong coupling regime [87].

In the THz range it is especially relevant that the parabolic well response is irrespective of the electron thermal distribution. For example, in a polaritonic device exploiting the intersubband excitation of a PQW one would observe strong coupling even at temperatures where the thermal energy is larger than the photon energy $kT > \hbar\omega$.

To implement a true parabolic well in the GaAs/Al_{0.15}Ga_{0.85}As system one should continuously vary the alloy component x along the growth direction (respect to the width centre) following the parabolic relation [88]

$$x(z) = x_{\min} + \frac{[z - (b - a/2)]^2 (x_{\max} - x_{\min})}{(a/2)^2} \quad (3.14)$$

where x_{\min} and x_{\max} are the limits of the alloy variation, a is the well width and b the barriers width. This would give an *analogically graded* band profile which is extremely difficult to grow. A parabolic potential can also be mimicked by *digitally grading* the band-gap, choosing an appropriate sequence of well/barrier layers on both sides of the central well. In this superlattice the “duty cycle” (i.e. fraction of the period corresponding to each of the materials) is varied as a function of the position. If the period of the superlattice is small compared to the electronic wavefunction extension, the electrons in the structure will be subject to an effective potential mimicking a PQW.

A PQW operating in the THz range has been tested in preparation for cavity electrodynamics studies in the sub- λ resonators developed previously. The PQW design is similar to that investigated in Ref. [53], offering an effective parabolic potential as shown in FIG. 3.2(a). The thick orange line highlights the effective potential, whereas the thin black line shows the actual band structure (digital alloy). The squared moduli of the eigenfunctions of the well are also reported. Note: energy eigenstates are evenly spaced as expected from a parabolic potential.

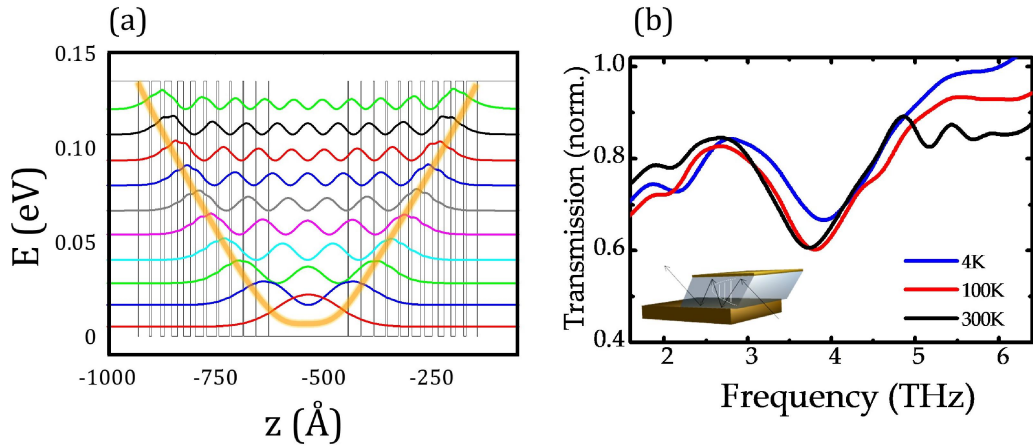


FIG. 3.2(a) Band diagram of L1006 THz PQW: real band structure of the digitally graded well (thin black line) and effective potential (orange line). The eigenstates are evenly spaced as expected from a parabolic potential. (b) Transmission spectra in multipass geometry at different temperatures.

The sample (L1006, growthsheet in Appendix A), grown by molecular beam epitaxy at Leeds University, comprises eleven repeated GaAs/Al_{0.15}Ga_{0.85}As PQWs providing a total sample thickness $h_{AR} = 1 \mu\text{m}$. The ISB transition of the sample has been measured at different temperatures using transmission spectroscopy in a multipass waveguide geometry [89]. A clear absorption peak was identified at 3.6 THz with a full-width-at-half-maximum (FWHM) of ≈ 0.9 THz (see FIG. 3.2(b)). There is no linewidth improvement with decreasing temperature, as expected from the parabolic shape of the potential.

3.1.4 Design and fabrication of antenna-tuned sub- λ resonators around 3.6 THz

Recently, some remarkable demonstrations of the strong-coupling regime between light and matter using sub-wavelength resonators and ISB transitions in semiconductor QWs have been reported. We recall that a reversible energy exchange between light and matter occurs when the interaction coupling constant (the Rabi frequency) is larger than any decay rate of the system. In this situation, new eigenmodes known as ISB polaritons emerge. The combination of metasurfaces and ISB transitions has been exploited for the demonstration of the strong coupling regime in the mid and far-IR ranges of the electromagnetic spectrum [90]–[92]

Here for the first time we demonstrate strong light-matter coupling between the fundamental mode of sub-wavelength 3D *meta-atoms* and the THz ISB transition ($f_{ISB} \approx 3.6$ THz) in the PQW characterized above.

The demonstrations of polaritonic meta-devices reported to date rely always on a planar approach. As a consequence, the tuning of the resonator frequency inherently modifies the interaction volume and the number of underlying interacting dipoles. More generally for an optoelectronic meta-device, one can envision a well-defined semiconductor spatial region in which a specific physical phenomenon takes place

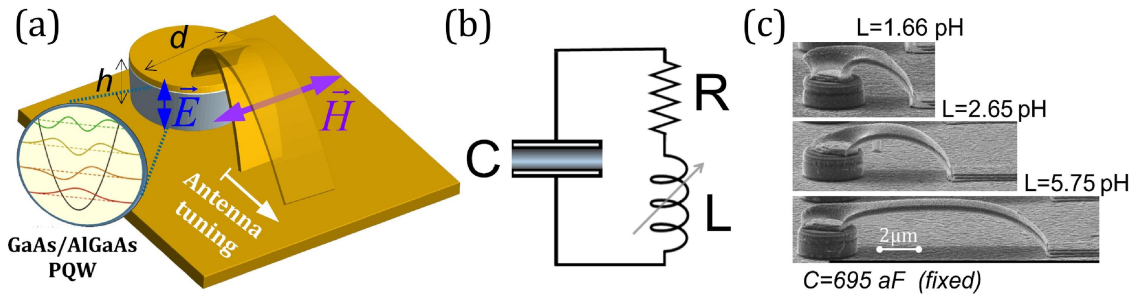


FIG. 3.3(a) (a) Schematic diagram of the lithographically-tunable LC resonator with an embedded parabolic quantum well. The electric and magnetic dipoles excited by the incoming radiation are shown. (b) Equivalent circuit. (c) SEM pictures of three resonators with different antenna lengths.

(e.g. photoluminescence, detection, lasing...), and that is combined with an external tuning circuit to adjust the resonant frequency. Indeed, this is possible adapting the design of the micro-resonators studied theoretically and experimentally in Chapter 2. In that case the lumped parameters L and C have been both varied to explore the circuital properties of these objects.

In this application, we show instead that it is possible to tune the resonant frequency of the device in and out of the ISB transition acting solely on the inductive element. The antenna, importantly, is *external* to the region where the strong light-matter interaction takes place. This permits to trace the characteristic polaritonic anti-crossing behavior as a function of the cavity-dipole frequency detuning, while keeping the volume of the capacitive active region constant across the entire set of resonant frequencies.

A schematic representation of our split-ring-like 3D meta-atom is shown in FIG. 3.3(a). The capacitive section has a fixed volume and embeds a GaAs/Al_{0.15}Ga_{0.85}As PQW (sample L1006 characterized above) as active core. The inductive loop antenna length is lithographically tuned to sweep the frequency of the fundamental LC resonance through the PQW ISB transition frequency. The equivalent circuit is sketched in FIG. 3.3(b): a lumped semiconductor-filled capacitor is connected in parallel with a tunable inductor, and a series resistor that accounts for both radiative and non-radiative losses.

The fabrication scheme follows the one described in 2.3.2. After standard Au-Au thermo-compressive wafer bonding and substrate removal, the semiconductor heterostructure was patterned into circular mesas of diameter $d = 2.7 \mu\text{m}$ by ICP-RIE etching using a Ti/Au/Cr mask. This yields a semiconductor volume of $\approx 6 \mu\text{m}^3$ for each resonator. Suspended Au loop antennas of different lengths were subsequently defined. A series of 16 samples were fabricated with antenna lengths between $4.65 \mu\text{m}$ and $11.55 \mu\text{m}$ (FIG. 3.3(c)). Using the parallel-plate capacitor formula we estimate the capacitance of each meta-atom to be $C = 695 \text{ aF}$ (using $\epsilon_r = 13.4$ for the semiconductor core [26]). The geometric inductance values range from 1.66 pH to 5.75 pH according to the formula (2.20) where the inductor width and thickness are $w = 2 \mu\text{m}$ and $t = 0.25 \mu\text{m}$, respectively. For each different antenna length, $2.5 \times 2.5 \text{ mm}^2$ arrays of meta-atoms (density $\approx 4000 \text{ devices/mm}^2$) were fabricated to maximize the

overlap with the THz beam. The period of the arrays is sub-wavelength to prevent all diffractive orders except the 0th-order reflection.

3.1.5 RT strong light-matter coupling in three dimensional terahertz meta-atoms

Recently room-temperature strong light-matter coupling between the ISB transition of a PQW and a micro-cavity mode has been reported [53], [87]. In that case microstrip planar resonators (i.e. a transmission-line geometry) are employed to demonstrate extremely low active volumes and the frequency tuning is achieved by changing the device length. Conversely our micro-resonators behave as microscopic LC circuits having separate electric-field (capacitive) and magnetic field (inductive) zones. They are $\lambda/10$ meta-atoms, achieving sub-wavelength confinement in all the three dimensions of space. Frequency sweeping around the PQW resonance is obtained with an external circuitual element (the antenna inductance).

The experimental reflectivity spectra, acquired at room temperature using a FTIR spectrometer equipped with a Globar source and a liquid-helium-cooled Si bolometer (see Chapter 2), are presented in FIG. 3.4(a) for different inductor lengths. The incoming radiation at a fixed incidence angle $\theta=60^\circ$ was TM-polarized and the antenna was placed in the incidence plane (TM inplane configuration, see FIG. 2.13) to maximize the optical coupling. The reflectivity spectrum for each sample was obtained by normalizing the sample spectrum to a reference spectrum obtained from a planar gold surface of the same area. We highlight that the parabolic well design enables the demonstration at room temperature (RT), which is important for future applications. For each sample, two minima (identified by dotted lines) are observed in the reflectivity measurements corresponding to the eigenstates of the system, the ISB polaritons.

Owing to the large number of samples, it is possible to resolve the polariton energies as a function of the frequency detuning between the cavity mode and the bare ISB transition, and an anti-crossing is observed, which is a clear signature of the strong coupling regime. The ISB polariton energies are plotted in FIG. 3.4(b) as a function of the measured total antenna length. The smallest frequency splitting (twice the Rabi frequency), measured at the anti-crossing, is equal to 0.70 THz, which represents 20% of the bare ISB transition energy.

It is then possible to compare the experimental polaritonic energies with the roots of the following secular equation, which provide the upper and lower polariton frequencies [84]:

$$\left(\omega^2 - \omega_{cav}^2\right) \times \left(\omega^2 - \omega_{12}^2\right) = \Gamma_{opt} \omega_p^2 \omega_c^2 \quad (3.15)$$

where ω_{12} is the measured ISB transition frequency, Γ_{opt} is the electromagnetic overlap, ω_p is the electronic plasma frequency in the quantum well, and ω_c is the cavity frequency (which depends on the antenna size).

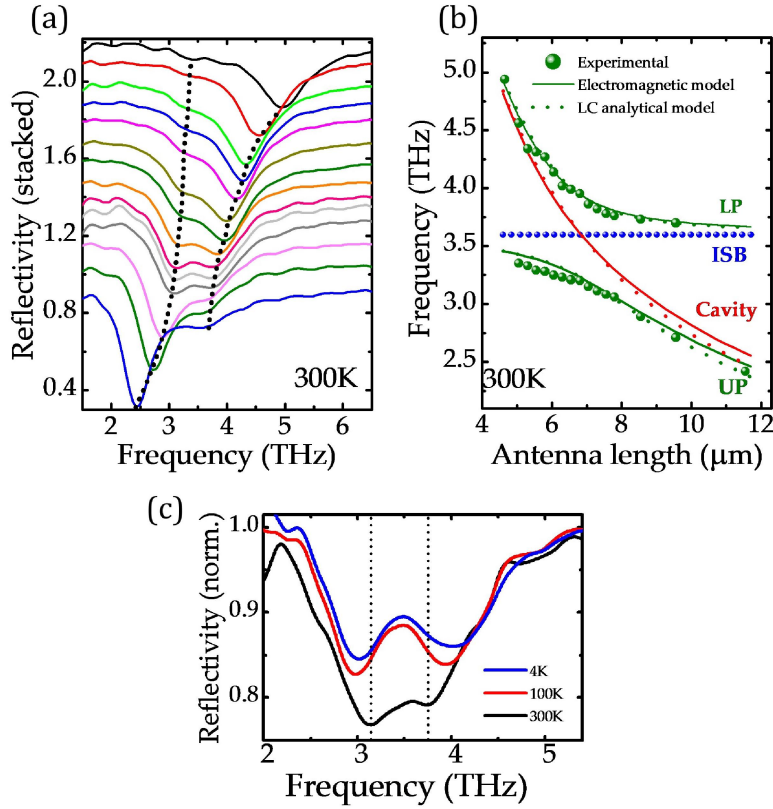


FIG. 3.4(a) Experimental reflectivity of the measured devices. The spectra are offset vertically for clarity. The dotted lines are guides to the eye and follow the position of the two polaritonic states. (b) Experimental reflectivity minima as a function of the antenna length (green full circles) corresponding to the frequencies of the polaritonic states. The calculated bare cavity resonances using the electromagnetic model (full red line) and the LC analytical model (dotted red line) are shown. The green lines represent the corresponding calculated polaritonic frequencies using equation (3.15). (c) Reflectivity spectra at different temperatures for the sample with minimum splitting, i.e. at perfect anticrossing. The Rabi splitting at 300K is 0.7 THz. It increases to 1 THz at 4K.

The bare cavity frequencies are calculated numerically using FEM simulations (COM-SOL Multiphysics) where the exact sample dimensions are used. Alternatively, the simple LC analytical model presented in 2.3.4 can be used to estimate L and C based on the sample geometry. The electromagnetic overlap (average value) is estimated from the numerical simulations to be $\Gamma_{\text{opt}} = 0.25$. The Rabi splitting being proportional to the square root of the charge density, the measured splitting yields an effective charge density of $2\text{E}11 \text{ cm}^{-2}$.

The sample with the smallest frequency splitting was further investigated as a function of temperature and the data are shown in FIG. 3.4(c). As the temperature is lowered to 4 K, the reflectivity contrast of the polaritonic branches increases, and the frequency splitting also increases up to 1 THz (28% of the bare transition). This value reflects a device at the onset of the ultra-strong coupling regime.

From the knowledge of the Rabi splitting at low temperature, which is directly related to the plasma frequency ω_p , we can infer a surface electronic density of $4.08\text{E}11 \text{ cm}^{-2}$. Doping calibrations have been performed, at low-temperature, on samples grown *before* and *after* sample L1006. They are all consistent and they provide the

value of $4.62\text{E}17\text{ cm}^{-3}$ for the sample real doping. This leads to a surface electronic density of $4.07\text{E}11\text{ cm}^{-2}$, in excellent agreement with the value inferred from the Rabi-splitting at low temperature. The observed reduction of the Rabi splitting passing from 4 K to room temperature, which can be reproduced by a reduced effective doping, is not fully understood. Temperature activated surface-depletion-effects could in principle reduce the available electronic density at RT.

3.1.6 Perspectives for cavity quantum electrodynamics in subwavelength resonators

Recently the exotic situation where only few electrons set up the strong coupling regime in a ultra-subwavelength resonator endowing an ISB transition has been investigated theoretically [93]. Furthermore, processes such as optical bistability and photon-blockade could be achievable in cavity quantum electrodynamics featuring an extremely reduced number of interaction dipoles [94]. Finally, a fascinating guess is the feasibility of the strong light-matter interaction at almost the single particle level in a solid-state system, in analogy to what is currently done in superconducting circuits [95]. The first step in this direction is of course an extreme reduction of the interaction volume that, as we will discuss, comes at a price.

Let's start with a fast calculation of the number of dipoles involved in the light-matter interaction within the meta-atoms reported above. From the knowledge of the interaction volume and the real charge density, we estimate that each resonator contains $\sim 12,000$ electrons. This is about 10 to 20 times larger than in mid-IR experiments [91].

The number of interacting dipoles could be further reduced by decreasing the active core volume (the capacitor lateral size, working with the same L1006 sample) but this would decrease the overlap factor Γ_{opt} (appearing in the Rabi splitting – Eq. (3.8)) which is already well below unity in the employed geometry.

Indeed, it is useful to determine how Γ_{opt} scales with the field confinement, since this has a direct impact on the strong coupling regime and, for very low values of Γ_{opt} , the system ultimately transitions back to weak coupling.

FIG. 3.5(a) shows the estimated Γ_{opt} for each fabricated resonator as a function of the antenna length obtained from numerical simulations. The antenna confinement factor is calculated (red full circles) conventionally to be the ratio of the free-space resonance wavelength to the diameter of the hemisphere enclosing the antenna [34]. For comparison, the confinement of the mode in the semiconductor active region (red empty circles) is calculated as the ratio of the effective wavelength in the material, $\lambda_{eff}=\lambda/n_{AR}$, to the mesa diameter.

On average the hybrid resonators provide the typical $\lambda/10$ confinement of split ring resonators and the confinement – for a fixed capacitor size – is directly dependent on the size of the inductor. On the same figure, the electromagnetic overlap is shown as a function of antenna length (blue triangles). The overlap is higher for more compact structures (shorter inductor) and does not exceed $\Gamma_{opt}=0.3$ for this cavity design.

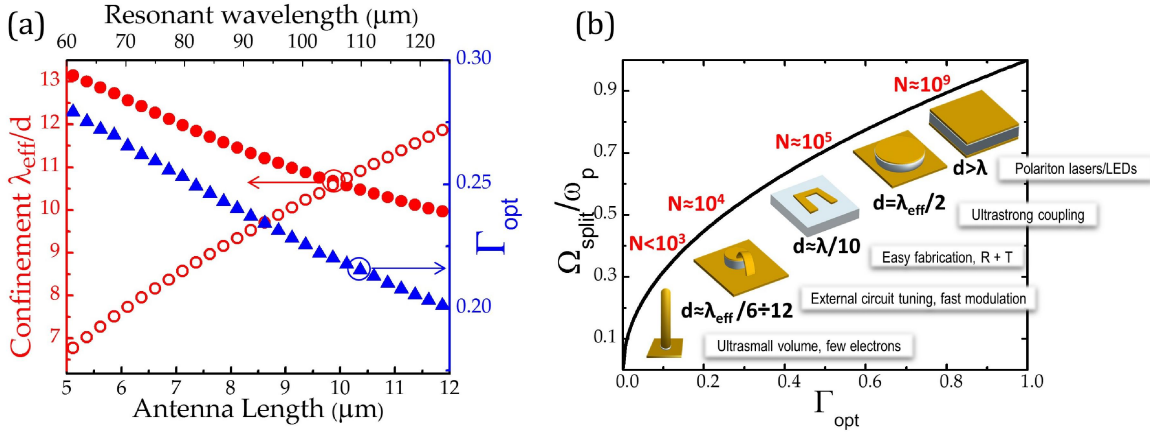


FIG. 3.5(a) Calculated confinement and electromagnetic overlap as a function of loop antenna length using FEM software. (b) Ratio of the frequency splitting to the plasma frequency as a function of the electromagnetic overlap for different resonators. For each type of resonator, the number of interacting electrons and the confinement are given qualitatively. We have also added a short description of the application that best suits each resonator architecture.

Note that a margin for improvement of the lumped 3D split-ring design exists. In fact, the Γ_{opt} stems from the geometry of the lumped capacitor and is proportional to the capacitance provided by the MSM structure. The relation between Γ_{opt} , radiative losses and capacitance will be further discussed in Chapter 5. Therefore, a higher Γ_{opt} in this structure can be achieved using high aspect ratio capacitors ($d_{patch}/h_{GaAs} \gg 1$) in order to reduce electric field fringing [13]; for example, employing an ultra-thin semiconductor core (eg. 100 nm) would yield $\Gamma_{opt} \approx 0.7$.

Nevertheless, Γ_{opt} will systematically decrease when the structure becomes more and more subwavelength. Ultimately the electromagnetic overlap achievable with wavelength-scale resonators remains unattainable with metamaterial-based resonators.

In fact, recalling the expression for the Rabi splitting $\Omega_{split} = \omega_p \sqrt{\Gamma_{opt} \cdot f_w}$, the only resonator-dependent degree of freedom is the electromagnetic overlap Γ_{opt} . As a consequence, employing sub-wavelength resonators should not bring an improvement in terms of the strength of the light-matter coupling (e.g. ultra-strong coupling) with respect to wavelength-scale structures. Even with an optimum electromagnetic overlap ($\Gamma_{opt} = 1$), the interaction strength is fixed by the plasma frequency of the ISB transition, which is directly proportional to $\sqrt{n_{2D}}$. However, extremely sub-wavelength resonators provide an opportunity to reduce the number of interacting dipoles, thus allowing the exploration of a few-electron cavity electrodynamics regime. In FIG. 3.5(b) different photonic or electronic resonators are classified as a function of their typical Γ_{opt} . The black curve shows the relative Rabi splitting achievable for a given intersubband transition (say ω_p) for each resonator design. A rough estimate of the number N of electrons involved in the light-matter coupling is provided for each resonator (the ω_p value of the PQW L1006 is used) as well as the effective subwavelength confinement. We observe that Γ_{opt} is close to unity for purely photonic resonators such as mesas [80], but is reduced to 0.5 for typical planar metamaterials on a quantum-well slab [90], [91]. Finally, for 3D structures enclosing an ultra-small semiconductor core, Γ_{opt} is normally reduced down to a few percent,

as in the case of vertical out-of-plane monopole antennas [69]. Although the reduction of the interaction active volume permits operation with progressively fewer dipoles, there is a trade-off since the reduction in confinement will be accompanied by a decrease of the frequency splitting, leading ultimately to operation in the weak coupling regime. In essence, each resonator architecture suits specific applications, as reported in the right part of FIG. 3.5(b). Large size metal-metal mesas suit the development of polariton lasers and LEDs [81]. Patch-cavities are very interesting for exploring the ultra-strong coupling regime. Planar metamaterials are easier to fabricate and permit to access both reflected *and* transmitted beams. Lumped LC resonators can present peculiar functionalities thanks to their circuital properties. For instance, since the resonance frequency is fixed by the external circuit, it can be modulated either mechanically (with MEMS) or optically as we will discuss later. Finally, a great reduction of the interacting electrons number has recently been attained using vertical monopolar antennas in the MIR range [96]. In the same demonstration, the number of resonators contributing to the strong-coupling regime has been lowered to 16, which is actually the world record in this spectral range.

3.2 Perspective #1: photo-induced switching of the LC resonance in a circuit-tunable resonator

3.2.1 Photo-switchable circuit-tunable resonators: the concept

Reconfigurable metamaterials constitutes a class of artificial materials where the intrinsic electromagnetic response can be altered in response to an external (optical, mechanical, electrical) stimulus. In particular, *photo-switchable metamaterials* have attracted a great research interest due to the possibility of controlling the electromagnetic response of a device on a much faster time scale than the one provided by other reconfiguration mechanisms such as MEMS repositioning of parts, phase-change materials or voltage-driven carrier injection [70]. Up to now, the typical photo-switchable metadvice is constituted of a planar metamaterial fabricated onto a switchable dielectric [97] or semiconductor layer whose dielectric constant can be controlled by ultrafast optical pulses [73]. The interaction of ultrafast optical pulses with planar split-ring metamaterials has been studied in Ref. [98]: the photo-excitation of carriers in a fast-response material (e.g. LT-GaAs) shunts the capacitive region of a metallic split-ring network on an picosecond scale turning off the LC resonance of the resonators.

Here we propose the integration of the photo-switch concept in the 3D micro-resonator geometry developed so far to provide a useful functionality which may open the door to different studies. This add-on would be very interesting for instance in the context of cavity electrodynamics (see 3.1.5): if an optical switching element is inserted in the antenna, then the cavity resonance frequency could be modulated on ultra-fast timescales offering the opportunity to investigate the dynamic properties of the strong coupling regime.

The proposed concept is sketched in the left panel of FIG. 3.6(a): a 3D sub- λ resonator of the type studied in Chapter 2, eventually endowed with an ISB transition, is equipped with an optical switching element controlled by an external laser pulse. The first proposed implementation of the concept is shown in the central panel: a narrow ring opening is defined in the ground plane giving access to the underlying semi-insulating GaAs substrate. The circuitual resonance of the system must now account the lumped capacitance C_{gap} provided by the ring opening (see right panel of FIG. 3.6(a)). The effective capacitance C_{eff} as seen by the inductor terminals is given by the series of the two capacitances C_{AR} and C_{gap} , i.e. $C_{eff} = C_{AR}C_{gap} / (C_{AR} + C_{gap})$ and the resonant frequency is $f_{LC} = 1 / 2\pi\sqrt{LC_{eff}}$.

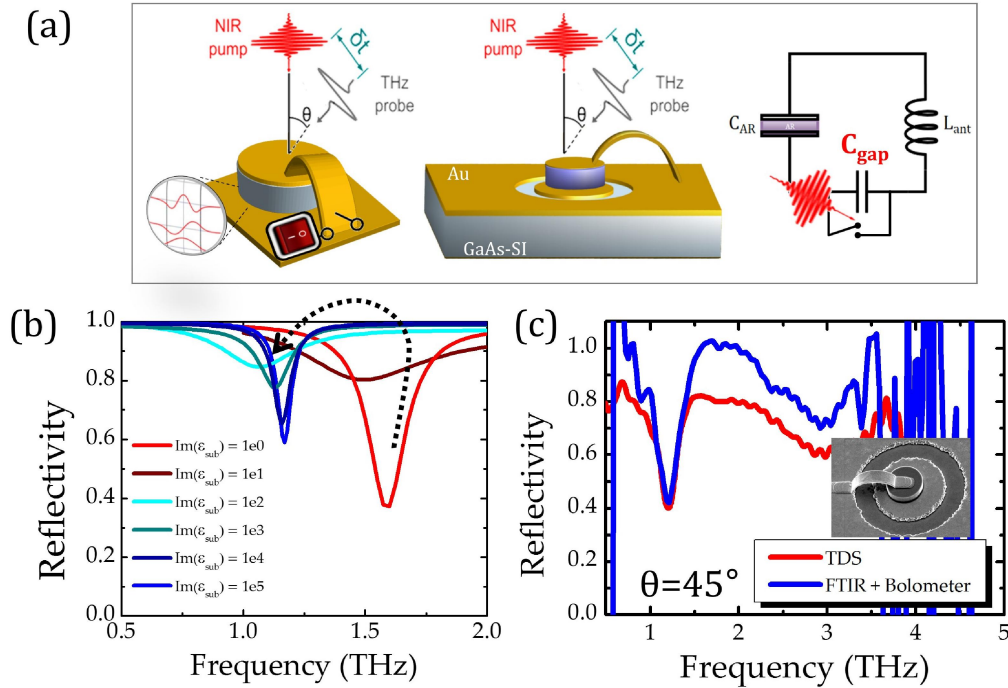


FIG. 3.6(a) Photo-switchable circuit-tunable resonators concept: (left) the LC resonance is turned on/off by an impinging laser pulse; (center) 1st proposed design featuring a ring opening in the ground plane around the patch; (right) equivalent circuit of the switchable resonator. (b) Simulated reflectivity for a resonator having $d_{patch}=7 \mu\text{m}$, $h_{AR}=1 \mu\text{m}$, $h_{gap}=3 \mu\text{m}$, $l_{ant}=9 \mu\text{m}$ for different values of substrate conductivity $\approx \text{Im}(\epsilon_{sub})$. (c) Measured reflectivity of fabricated resonators featuring a ring opening (red: THz-TDS @LPA-ENS; blue: FTIR+Bolometer @IEF). The incidence angle is 45° and the excitation configuration is TM inplane.

When a NIR optical pulse of sufficient power impinges upon the system, carriers can be photo-excited in the substrate shunting the gap capacitance. If this happens, the overall capacitance goes back to the value C_{AR} (as if no ground plane opening were present) and the system switches on a different resonant frequency $\tilde{f}_{LC} = 1 / 2\pi\sqrt{LC_{AR}}$. This situation is simulated in FIG. 3.6(b) there the reflectivity of a resonator having $d_{patch}=7 \mu\text{m}$, $h_{AR}=1 \mu\text{m}$, $h_{gap}=3 \mu\text{m}$, $l_{ant}=9 \mu\text{m}$ under normal incidence (TM inplane configuration) is simulated for different values of substrate conductivity $\approx \text{Im}(\epsilon_{sub})$. As $\text{Im}(\epsilon_{sub})$ rises from ≈ 0 (dielectric/semiconductor) to 10^5 (metal) the LC resonance passes from ≈ 1.6 THz to ≈ 1.2 THz. The observed redshift is in agreement with the observation that for two capacitor in series the relation $C_{eff} \leq (C_{AR}, C_{gap})$ holds. The

predicted “switching” between two resonant modes is similar to what observed in planar metamaterials [98].

A first generation of passive resonators featuring a 1 μm -thick undoped GaAs core and reproducing the simulated geometry have been fabricated. The fabrication scheme follows FIG. 2.4 and FIG. 2.11 with the addition of lithographic steps to define the ring opening before the antenna fabrication. After positive tone photolithography the metal ground plane is wet etched using BHF and KI solutions for Ti and Au layers respectively. The result is shown in the inset of FIG. 3.6(c). Reflectivity spectra have been acquired with a FTIR spectrometer and a liquid-He-cooled bolometer at IEF and also with a THz-TDS setup at LPA-ENS (collaboration with S. Dhillon). The LC resonance, clearly visible around ≈ 1.2 THz in both spectra, is redshifted respect to design owing to photolithography incertitude.

3.2.2 1st generation devices on GaAs: resonance bleaching

After preliminary passive characterizations THz pump and probe measurements have been performed on the fabricated sample. Two different pump-probe systems have been used for this study. Preliminary measurements have been done at the LPA-ENS laboratory using a THz pump-probe based on photoconductive antenna emitter and electro-optic detection (Pockels effect) in ZnTe [99]. A first hint on the LC resonance shunting was observed. Nevertheless, a lack of intensity on the synchronized NIR pump pulse did not allow to fully observe the expected switching mechanism.

The measurements were then conducted using a THz-TDS set-up based on an amplified Ti-Sapphire laser system at IESL-FORTH (Heraklion, Greece; collaboration with S. Tzortzakis). On one hand, such amplified system operates on a lower repetition rate and shows then a lower signal to noise ratio. On the other hand, it offers the possibility to use THz air photonic techniques where THz pulses are generated and detected using a laser-induced plasma. A larger spectral bandwidth can be covered with this technique [100]. Furthermore in such amplified laser system, the energy per pulse is so high that a larger fraction of the pulse energy can be redistributed to the NIR pump pulse used to photo-excite the sample.

Experimental spectra for different illumination intensities are shown in FIG. 3.7(a). We note that the LC resonance contrast is reduced as the NIR synchronized pump intensity increases. Nevertheless, we didn’t observe the apparition of a second resonant mode which would indicate that the system is moving on another frequency of the LC circuit, as expected from FIG. 3.6(b). Taking advantage of the larger bandwidth offered by the THz air photonic system, the behavior of the TM_{110} mode of the capacitive patch (≈ 6 THz) was also investigated. As shown on the right panel of FIG. 3.7(a), the TM_{110} mode is also switched-off.

This observation indicates that most probably not only the GaAs near the gap opening but also the one filling the capacitor is getting photo-excited under pump illumination. To confirm that, a standard LC resonator resting on a continuous ground plane (from the samples in FIG. 2.13) was probed. The same bleaching behavior of

the LC resonance and the TM_{110} mode were observed confirming that the capacitive section of GaAs semiconductor was entirely photo-activated.

For both sample the bleaching of the LC resonance is observed which means that we are actually photo-exciting carriers in the GaAs substrate and in the GaAs active core. The adopted geometry is thus not effective for selectively photo-switching the “ring-opening” capacitor. A new design of the optical switch is being explored, as shown in the following paragraph.

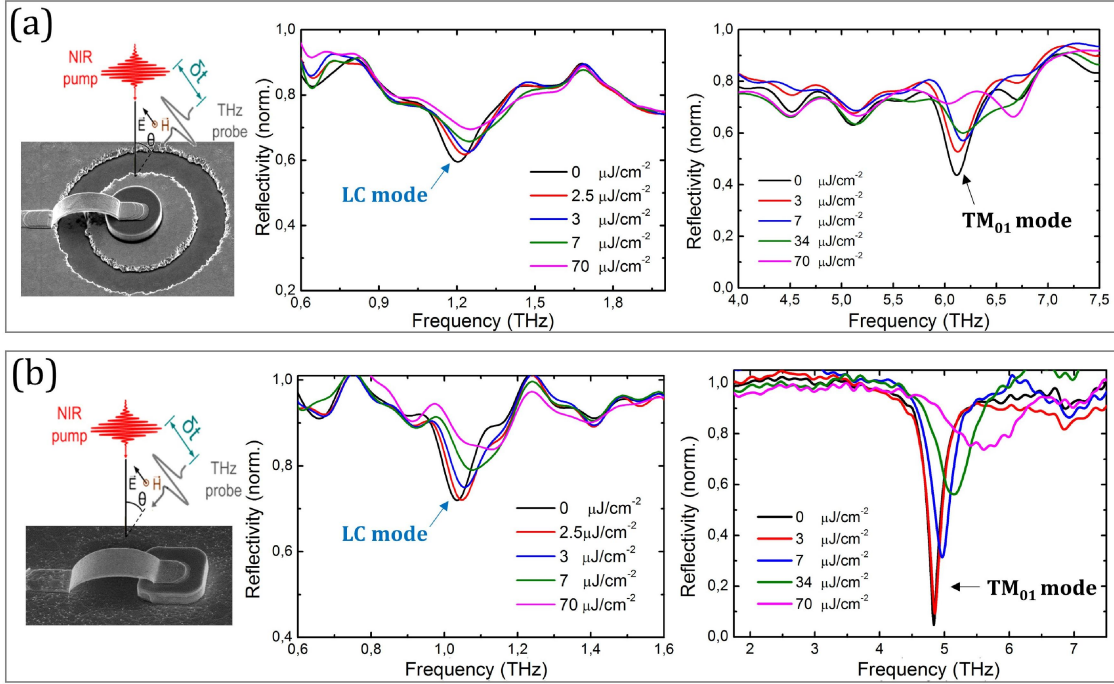


FIG. 3.7(a) Measured THz-TDS reflectivity spectra at different illumination intensities for: (a) a LC resonator featuring a ring opening in the ground plane; (b) a standard LC resonator. A sketch of the experiment is superimposed to the SEM pictures of the tested devices.

3.2.3 Towards a 2nd generation devices.

Recently amorphous Silicon (a-Si) has been successfully explored as photo-switchable material for reconfigurable nano-antennas and 3D metamaterials [101], [102]. A thin evaporated pad of a-Si could be employed as optical switching element, in alternative to the scheme discussed above. One practical advantage of this configuration is that no ground plane etch is needed, making the sample easier to fabricate and to model (it remains a 1-port system). Moreover, the very simple geometry of the capacitive pad (compared to the ring case) allows to easily estimate the switch capacitance and hence to maximize the frequency shift between the “ON” and “OFF” state. A preliminary simulation of this 2nd generation device is reported in FIG. 3.8: a small capacitive pad of a-Si is added in series to the antenna, yielding the same circuitual equivalent of FIG. 3.6(a).

The device active region features a diameter $d_{AR}=5\mu\text{m}$ and height $h_{AR}=2\mu\text{m}$, and is filled with undoped GaAs ($\epsilon_{\text{GaAs}}=13.1$). The switch pad has diameter $d_{pad}=2\mu\text{m}$, height

$h_{\text{pad}}=300$ nm and an approximated permittivity value of $\epsilon_{\text{a-Si}}=12$ for the dielectric is taken. The pad diameter is chosen so that $C_{\text{AR}} \approx C_{\text{pad}}$ to maximize the frequency shift. The “OFF” state in this example has a resonant frequency $f_{\text{OFF}} \approx 3$ THz which accounts for the series capacitance, while the “ON” i.e. photo-activated state has frequency $f_{\text{OFF}} \approx f_{\text{ON}} / \sqrt{2} = 2.1$ THz. This new structure is currently being studied in the team.

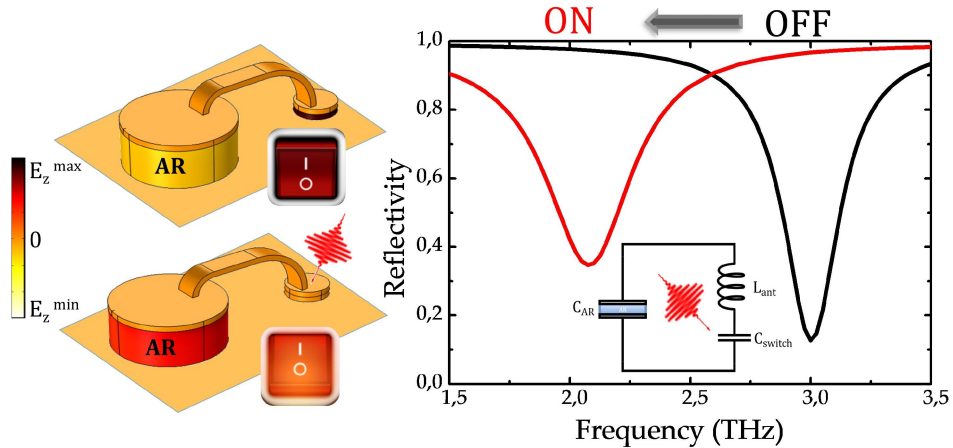


FIG. 3.8 Concept of the 2nd generation photo-switchable circuit-tunable resonators: a small capacitive pad of a-Si is added in series to the antenna. Simulated spectra for $d_{\text{AR}}=5$ μm , $h_{\text{AR}}=2$ μm , $d_{\text{switch}}=2$ μm , $h_{\text{switch}}=300$ nm, $\epsilon_{\text{a-Si}}=12$, $l_{\text{ant}}=5$ μm . The diameters are chosen so that $C_{\text{AR}} \approx C_{\text{switch}}$ to maximize the frequency shift ($f_{\text{OFF}}/f_{\text{ON}}=\sqrt{2}$)

3.3 Perspective #2: optically active high-impedance surfaces

3.3.1 Engineered electromagnetic surfaces

So far we were exclusively interested in the properties of individual subwavelength resonators, our main goal being the demonstration of an electrically-driven *optoelectronic meta-atom* (detector or source). In other words, we designed 3D THz circuit-tunable resonators by engineering the optical response of the single object and we then fabricated and characterized arrays of identical resonators featuring a subwavelength periodicity. Taking the array period $p \ll \lambda$ means keeping out all interference or *phasing* effects between neighbor objects: the optical response of the whole is the incoherent sum of the single object response. This is equivalent to state that the system behaves optically as an *effective medium*, as it is normally the case for metamaterials with user-tailored electromagnetic properties. Indeed, subwavelength-scale corrugations or elements added on a conducting plane can dramatically affect the properties of the surface, considered as a whole, from that of a standard reflector/ground plane. Such engineered electromagnetic surfaces can be designed to perform a variety of functions, for example: to change the surface impedance for one or both polarizations, to manipulate the propagation of surface waves, to control the reflection phase or to modify the radiation patterns of small antennas [103]. Moreover, by incorporating reconfigurable materials or devices (MEMS, varactor diodes) into

textured surfaces, an active control of electromagnetic radiation can be obtained to create, for instance, programmable reflectors that can steer or focus a reflected beam [104].

In 1999 D. Sievenpiper (Yablonovitch group) proposed an innovative textured surface made up of subwavelength mushroom-shaped metal protrusions in the GHz range [50], [105] (see the left panel of FIG. 3.9). The mushrooms behave as resonant parallel LC circuits and provide a high value to the surface impedance near resonance. These so called *high-impedance electromagnetic surfaces* show several interesting features. For instance, the surface reflects with a phase shift of zero (rather than π in standard conducting planes) and exhibits a surface wave bandgap, within which no bound surface waves are supported (it's like a photonic crystal for surface waves).

Coming back to our case, we notice a clear analogy between 'Sievenpiper-mushroom' structure for microwaves and the arrays of subwavelength circuit-tunable resonators for terahertz developed previously. The question is then: can we implement structured electromagnetic surfaces able to modify by design some optical properties of a THz beam impinging upon them? As a preliminary exploration of this subject, we will look at the polarization response of subwavelength 3D resonators featuring two suspended inductors disposed at an angle (see 2.4.2).

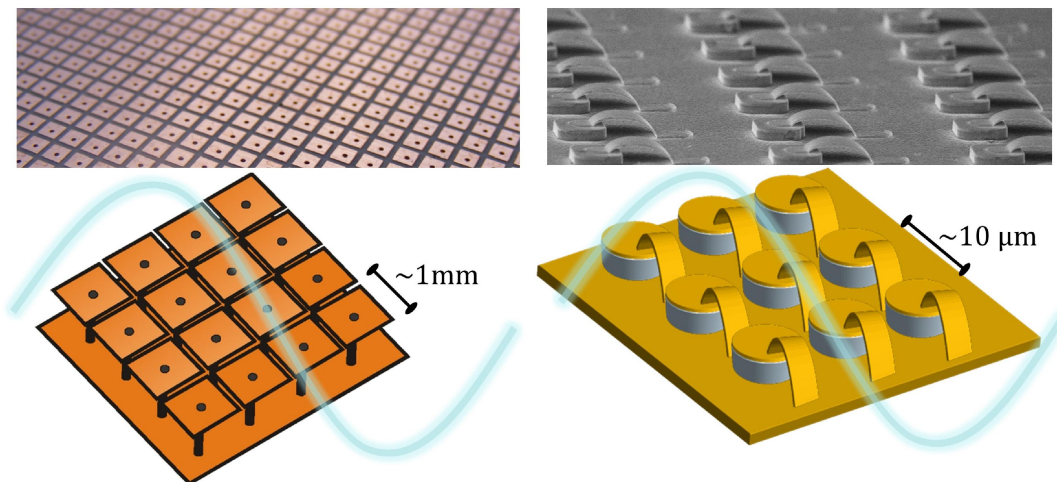


FIG. 3.9 (left) Sievenpiper-mushroom high impedance surface for the GHz range (from <http://spie.org/newsroom/1532-manipulating-microwaves-with-spoof-surface-plasmons>); (right) a subwavelength array of THz circuit-tunable resonators as a structured electromagnetic surface.

3.3.2 Chiral metamaterials

An object is defined *chiral* if it is distinguishable from (i.e. non identical to) its mirror image. In chemistry, chirality molecules having the same molecular formula but different three-dimensional orientations of the atoms in space are called *stereoisomers*.

An interesting feature of chiral materials is that they are optically active, i.e. able to rotate the plane of polarization of linearly polarized light as it travels through them [35].

Usually the optical effects observed within natural chiral media (quartz, amino acids, sugars,...) are weak. Conversely, artificial metamaterials offer the possibility to design a strong and resonant enhancement of the chiral response playing on the geometric structure of the constituting meta-atoms [106]. The chiral effect is a result of the microscopic cross coupling between electric and magnetic dipoles, which can be artificially obtained with nonplanar resonators. Giant optical activity and circular dichroism in chiral metamaterials have been demonstrated, making these materials interesting to create novel polarizing devices. Moreover, a metamaterial having a strong chirality can show a negative refractive index [107], [108].

In this context we observe that our developed 3D lumped LC resonators are an interesting playground to explore chirality-related effects. If we consider the same sub- λ resonator featuring different spatial arrangements of two identical inductors we are creating different chiral replica of the same object. We could talk about “*stereo meta-atoms*” in analogy to molecular stereoisomers. In our case the elementary components forming the meta-atom (one capacitor, two inductors) stay the same (yielding the same frequency response), while their spatial arrangement changes. The concept of stereo metamaterials inspired to stereochemistry has been introduced for the first time in Ref. [34].

3.3.3 Optical activity from two-inductors meta-atoms

In this paragraph, we investigate the polarization state of a THz beam impinging on an array of subwavelength LC resonators having two inductor in parallel, like the ones discussed in Chapter 2. To start, the far field of a single resonator consisting of a patch capacitor ($d_{patch} = 6 \mu\text{m}$, $h_{AR} = 1 \mu\text{m}$) connected to two identical inductors ($l_{tot} = 4 \mu\text{m}$) has been simulated (see 2.3.6) for several values of the relative angle between the inductors. The different angular arrangements and the simulated far fields in the horizontal plane are reported in FIG. 3.10(a). The radiation pattern is dipole-like and shows a peak emission along the bisector of the relative angle between the inductors. This can be understood considering that the overall radiated field comes from the two magnetic dipoles (inductors) arranged at a certain angle plus the electric dipole (capacitor). When the two inductors are 180° away, a purely electric dipole pattern is found, due to the suppression of magnetic radiation already discussed in 2.4.1. Note: our system is reminiscent of the V-shaped nanoresonators proposed by Capasso group to implement a phase gradient to an impinging wave; the difference here is that the electric dipole antennas are replaced by magnetic dipole antennas.

The idea is to explore if the spatial arrangement of the lumped inductors (at the single resonator level) can influence the optical response of a conducting surface structured with these objects. As a proof of concept, we take one of the samples characterized in 2.4.2 featuring two inductors arranged at 90° as shown in FIG. 3.10(b). Note that here a chirality arises from mirror symmetry breaking of the unit-cell structure

in the propagation direction. To probe the polarization state of the outgoing radiation a second polarizer is inserted at the exit of the reflectivity setup (see 2.1.3). More precisely, to measure the surface optical activity, the polarization state of the incoming beam is fixed through the first polarizer while the outgoing polarization is analyzed by rotating the second polarizer's axis with respect to the first. The analyzer rotation can be done automatically with a motorized polarizer holder (Bruker A121). A simplified sketch of the polarimetry setup is shown in FIG. 3.10(b).

To verify the operation of the setup the reflectivity from a gold mirror at $\theta=45^\circ$ incidence has been measured as a function of the analyzer angle α , where at $\alpha=0^\circ$ the analyzer and polarizer axis are aligned. The normalized intensity $I(\alpha)/I(0^\circ)$ is reported (symbols) in FIG. 3.10(c). As expected, the reflectivity drops according to Malus law [37]

$$I(\alpha) = I(0^\circ) \cos^2(\alpha) \quad (3.16)$$

Then, reflectivity spectra for the 90° -inductors sample have been acquired for α values in the $0^\circ \div 90^\circ$ range. Note: in this measure the position $\alpha=0^\circ$ corresponds to crossed polarizers; the signal baseline goes then as $I_{baseline}(\alpha) \approx \cos^2(90 - \alpha) \approx \sin^2(\alpha)$, as shown by the black line in FIG. 3.10(d). Thus the signal is very low for small α values.

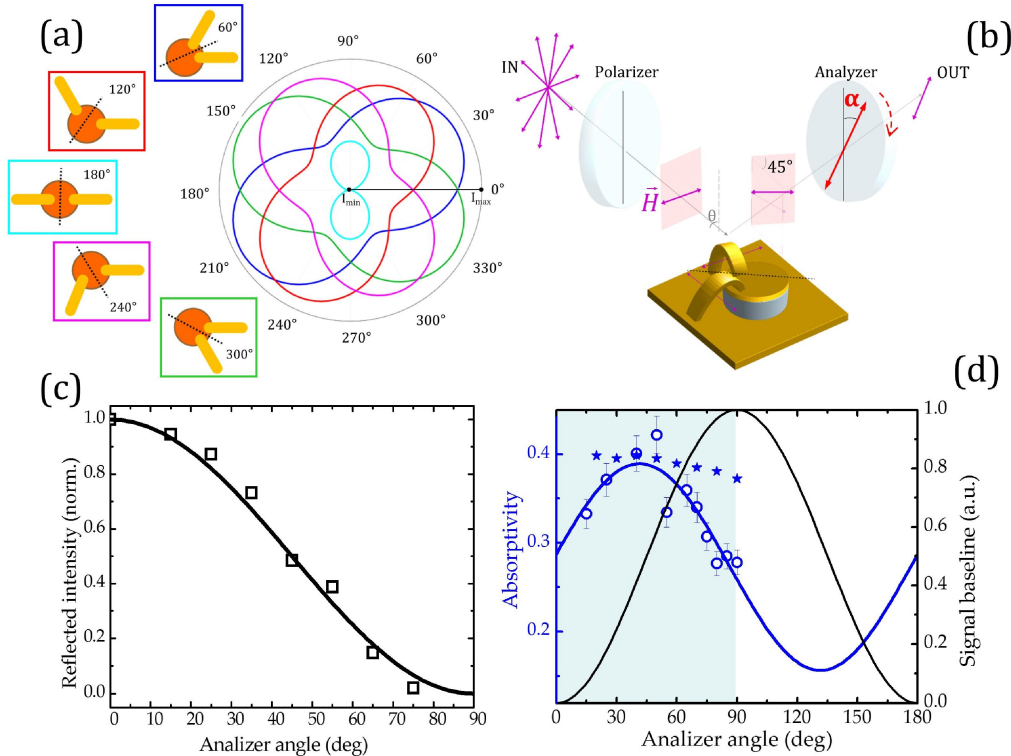


FIG. 3.10(a) Far-field simulations (horizontal plane) for 3D LC resonators featuring 2 inductors set at different angles. (b) Stokes polarimetry setup in reflection. (c) Experimental normalized reflectivity $I(\alpha)/I(0)$ from a gold mirror as a function of the analyzer angle α (symbols). The intensity drops as $\cos^2(\alpha)$ following Malus law (line). (d) Empty symbols: experimental absorptivity vs analyzer angle α for a 2-inductors sub- λ array (sample with $L=5.5 \mu\text{m}$ in REF) at LC resonance ($f_{LC}=2.4 \text{ THz}$); full line: best fit curve. Full stars: absorptivity at the TM_{110} patch resonance ($f_{patch}=7 \text{ THz}$). Black curve: signal baseline following a $\sin^2(\alpha)$ trend.

The extracted sample absorptivity ($A=1-R$) at the LC resonance ($f_{LC}=2.4$ THz) are reported in FIG. 3.10(d) as a function of the analyzer angle. The measures are quite noisy (a 10% error bar is added) both because of the poor SNR (the resonant frequency is near the DTGS detector cutoff) and the low quality of the sample. Nevertheless a maximum absorption can be distinguished around $\alpha=45^\circ$ as one would expect from the simulated far field in FIG. 3.10(a). The data points have been fitted with a curve of the form $f(\alpha)=A+B\cos^2(\alpha+C)$. The best fit parameters are $A=0.389$, $B=-0.233$, and $C=48.5$, the latter suggesting a deviation from Malus law (3.16) which is compatible with a polarization rotation of $\approx 45^\circ$; the constant contribution ($A \neq 0$) can be attributed to the electric dipole absorption.

For comparison, the absorption at the TM_{110} patch resonance ($f_{patch}=7$ THz) is also reported: the reflected intensity is (almost) independent on the analyzer angle as the radiation pattern of a patch antenna would suggest. This preliminary measure, far from being rigorous, is a first hint about the optical activity possibly shown by this kind of structured surface. A more precise study will demand a careful extrapolation of the Stokes parameter of the reflected beam as well as a new generation of high quality samples with different inductors arrangements.

As a long term perspective one could imagine to exploit the air-bridge fabrication to implement THz high-impedance surfaces showing user-tailored optical properties.

4 THz meta-atom quantum well photodetectors

The developed 3D circuit-tunable meta-atoms have proven to be appealing for meta-devices since they combine design flexibility and the possibility to shrink at will the volume of the hosted “active” semiconductor. An extreme active core reduction, together with the engineering of radiation coupling via antenna elements could, for instance, benefit the THz QW detectors technology, which is still in its infancy.

The demonstration of a first generation of THz subwavelength ($\lambda_{\text{eff}}/10$) quantum detectors operating around 3 THz and featuring an ultra-small QW active region constitutes the core of this chapter. First, we will need to develop an effective contact scheme to extract (inject) current from (in) a subwavelength semiconductor AR, bypassing the short circuit intrinsic in the split-ring geometry. Before that, the state-of-art of THz quantum well photodetectors will be presented.

4.1 THz quantum well photodetectors

4.1.1 Long wavelength radiation detection

The detection of long wavelength radiation with quantum detectors remains an open challenge in modern optoelectronics. In particular, the THz range is strongly underdeveloped in terms of photodetectors technology due to the fact that far-infrared radiation cannot be easily detected using the commonly employed techniques in the microwave and IR ranges. On one side the electronics approach is limited to sub-THz frequencies to achieve good performances (e.g. Schottky diodes). On the other side, the energy of THz photons is substantially smaller than the thermal energy ($k_B T$) at room temperature and also at liquid nitrogen temperature. Most of the commercially available THz detectors are based on *thermal sensing elements* (bolometers, pyroelectric crystals, ...) that are slow (10–400 Hz modulation frequency for Golay cells or pyroelectric detectors), yield poor performance (see D^* in FIG. 4.1(a)) and/or require deep cryogenic cooling (liquid Helium temperature for standard bolometers or lower for hot-electrons bolometers)[3]. Differently, in a *quantum (or photon) detector* the absorption of an infrared photon results directly from some specific quantum event, such an electronic inter-band transition in a semiconductor. The issue with solid-state MIR or THz detector is that a material featuring a very small bandgap must be used to get a suitable band-to-band transition. An important exploited material system is the HgCdTe alloy in which the bandgap can be tailored to yield absorp-

tion in the MIR band, providing photo-detection down to 26 μm wavelength for commercial detectors [109].

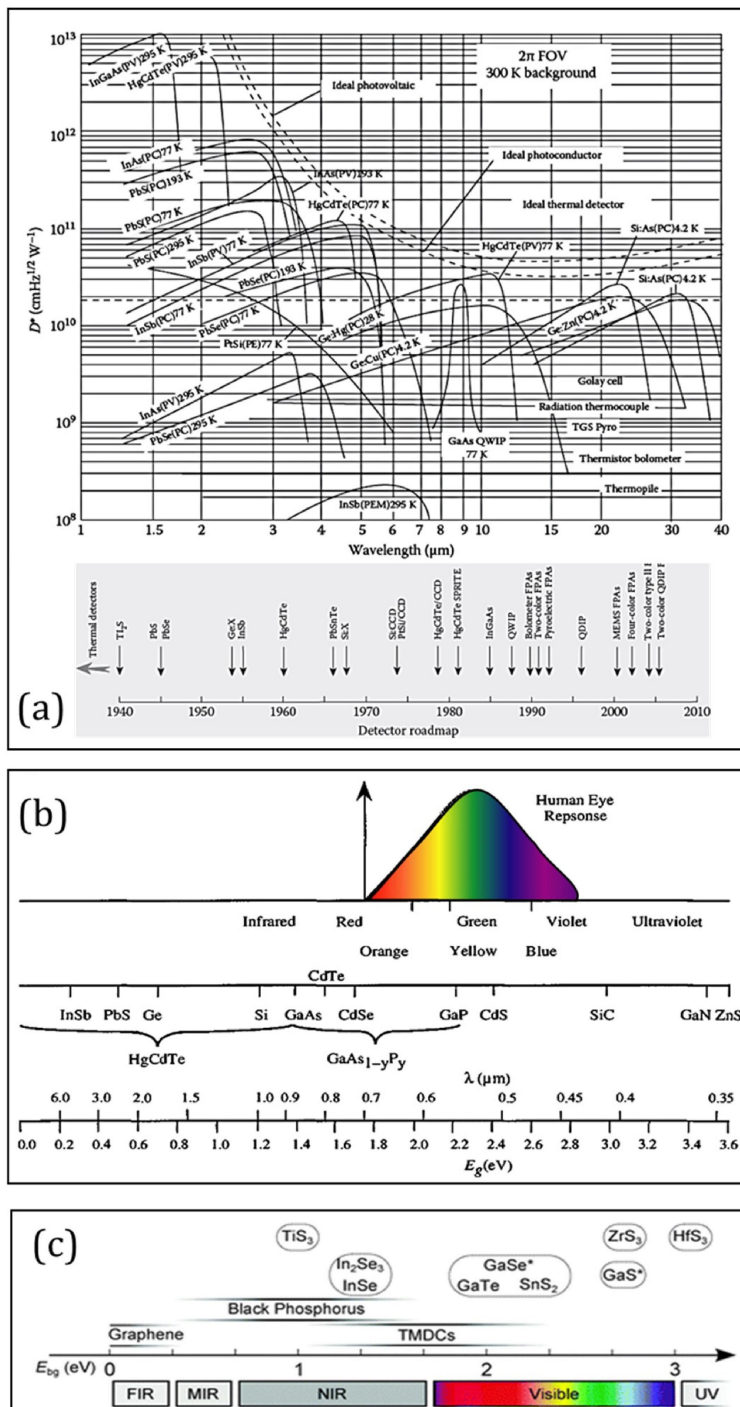


FIG. 4.1(a) Top: normalized detectivity (D^*) and spectral coverage of various commercially available IR detectors. Each detector is assumed to view an hemispherical surrounding at 300 K. Bottom: history of the development of infrared detectors (from Ref.[110]). (b) Spectral coverage of solid state band-to-band detector materials (from Ref. [17]). (c) Spectral coverage of novel 2D materials (from Ref.[111]).

To overcome the limitations due to the lack of bulk materials having sufficiently low energy gaps, band gap engineering has been used to design artificial superlattices

providing user-tailored quantum transitions in the MIR and FIR range. Detectors exploiting intersubband transitions in semiconductor quantum wells actually represent a valid solution in the 8-12 μm wavelength range, either as photoconductive detectors (quantum well infrared photodetectors, QWIPs) or photovoltaic (quantum cascade detectors, QCDs). Today QWIP cameras are commercially available in the MIR range [112].

Unfortunately, the situation is different in the THz range where the technological development is still in its infancy both in terms of quantum design and radiation coupling.

More recently two-dimensional van der Waals semiconductors have attracted attention as potential candidates for next generation optoelectronics [111]. These materials offer the possibility to modulate the bandgap as a function of the number of layers, that in turn modulates the optical absorption edge. Moreover they are almost transparent and flexible, as normally exfoliated in thin flakes for applications. In FIG. 4.1(c) the spectral coverage provided by 2D layer materials is shown. Photodetectors based on semiconducting transition metal dichalcogenides (TMDCs) cover the NIR and VIS spectral range. On the other side gapless graphene has been used to fabricate sub-THz field effect phototransistors operating at room temperature [113]. In the middle, the few-layer black phosphorus (bP) provides an intermediate bandgap between zero-bandgap graphene and large-bandgap TMDCs [114].

In this panorama, intersubband-based devices are promising candidates in the quest for high speed, high efficiency and versatile THz photo-detectors. In fact, they offer the advantages of long wavelength detection using established technologies such as the GaAs platform and fast response (i.e. high bandwidth) owing to the intrinsic short lifetime of ISB transitions. However, their operation is currently limited at very low temperature (typical background limited infrared temperatures (T_{blip}) are ≈ 15 K) which hampers practical applications.

In the following we will detail the physics and state of art of *quantum well infrared detectors* (QWIPs) in the THz range.

4.1.2 Quantum well infrared photodetectors

In this section we will cover the main physical aspects of QWIPs following Refs. [23], [112]. Consider a quantum well which is n-doped so that the ground state has a certain electronic population while the excited state is unoccupied. As discussed in Chapter 1, an ISB transition takes place when a photon with energy equal to the ISB separation impinges upon the QW. The ISB absorption process taking place between user-designed quantum states can be exploited to build a photoconductive detector only if we manage to efficiently extract an electrical signal. For this purpose the ground state should not produce an electronic current. If this condition is not satisfied, there will be a high dark current in the detector. At the same time, to efficiently extract electrons from the QW excited state, this one should be engineered near the top of the QW barrier. In this way the photo-excited electrons could be extracted by an applied electric field, as sketched in FIG. 4.2(a).

It can be shown [23] that the QW parameters (well width and Al percentage in the barrier) can be adjusted to obtain, for a desired operation wavelength, a *quasi-resonance* situation, where the first excited state lies just at the top of the well. This configuration is suitable for a QWIP detector as the oscillator strength for the optical transition is still important (being close to the case of a 1-2 bound-to-bound transition), while the promoted electron is free to propagate within the continuum. The quasi-resonance condition may be achieved over the whole far-infrared spectrum ($5 < \lambda < 100 \mu\text{m}$) with GaAs/AlGaAs QWs. Note: the growth of QWIPs operating in the THz is technologically demanding tough, as very low Al percentages have to be handled. The mid-infrared region can be as well accessed using InGaAs/AlInAs QWs.

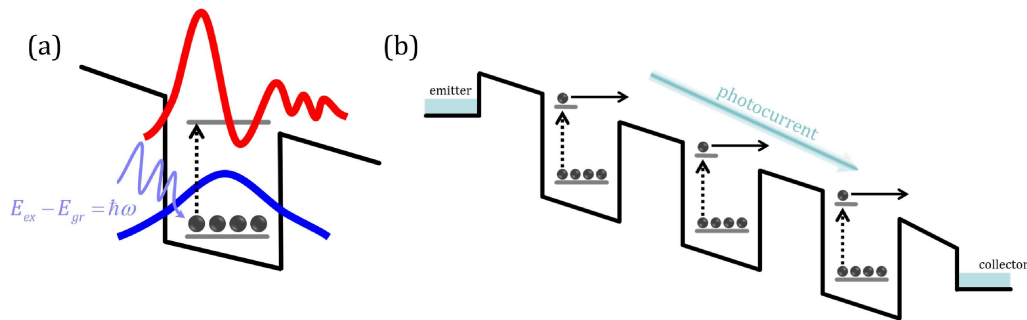


FIG. 4.2(a) Sketch of a bound-to-continuum intersubband transition in a quantum well. (b) Schematics of a QWIP under a bias: carriers in the quantum well ground state are photo-excited in the continuum and then extracted by the applied voltage yielding a detectable photocurrent.

Electrons excited into the continuum are swept out by an applied electric field leading to a photocurrent as shown in FIG. 4.2(b). The electric field E is produced by the external application of a bias voltage across two contact layers (for example highly doped n-GaAs layers). Typically, owing to the weak absorption coefficient of a single QW, a QWIP consists of a series of identical QWs (i.e. a multi-quantum well) for a total thickness of a few microns, so that an efficient light detection is achieved.

In the ideal picture when the temperature is sufficiently low and in absence of illumination, the electrons are trapped in the ground state and no current should flow in the device (in reality a non-zero dark current is always present as we will discuss later), i.e. the system behaves like an open circuit when connected to an ammeter. If then we shine radiation on the semiconductor, electrons are photoionized out of the QWs and extracted by the external electric field leading to a measurable photocurrent. We shall note here that QW detectors differ from standard photoconductive detectors because of their narrowband response arising from the bound-to-continuum nature of the involved optical transitions.

The simplest way to describe the operation of a quantum well detector is a *photoconductive model* where the impinging infrared light extracts electrons from the confined state of a quantum well rising the device conductivity. The details of the model can be found in Refs. [23], [112]. Here, we recall the expression for the *responsivity*

of a QWIP detector (i.e. the ratio of the generated photocurrent to the impinging optical power) as derived from the photoconductive model:

$$\mathfrak{R} = \frac{I_{photo}}{\hbar\omega\Phi} = \frac{e}{\hbar\omega} \eta_{1QW} G_{1QW} \quad (4.1)$$

where η_{1QW} is the *absorption quantum efficiency* of a single QW and $G_{1QW} = p_e / p_c$ is the *photoconductive gain* of a QW, given by the ratio of the emission and capture probabilities for an electron from a QW. The photoconductive gain in a QWIP may be understood as follows: to balance the loss of electrons from the QW due to photoexcitation in the continuum, electrons are injected from the top emitter contact. Since the capture probability p_c is smaller than one, extra electrons need to be injected and the total measured photocurrent can become larger than the photoemission current.

4.1.3 Noise in a photoconductor

In general, several sources of noise affect the performance of a photodetector. The physical description of noise in a QWIP being not simple, we will sketch here a general overview following Rosencher and Vinter book [23]. In every optoelectronic detector, we find an *electrical noise*, related to random fluctuations of the electrical signal (current or voltage) and a *photon noise*, created by the statistical nature of the photon arrival in the semiconductor and fluctuations of the light source.

Electrical noise sources in a detector include *Flicker noise* (aka *1/f* or *pink* noise) and *thermal (Johnson)* noise associated with photoconductor resistance. Experiments on QWIPs show that these contributions do not dominate the noise of such detectors [112], so we will neglect these terms in the following.

Noise in a photoconductor is mainly related to the statistical nature of the generation and recombination of carriers, whose number fluctuates yielding the so-called *generation–recombination noise*.

Free carrier generation processes within the detector (electrons extraction from a well in QWIP or electron-hole pairs creation in a conventional photoconductor) do not create a perfectly constant current as the exact instant of their creation is random. Current fluctuations are always present, no matter how carriers are created (photon absorption, thermal excitation) in the semiconductor.

The total current flowing in the detector is the sum of the optical signal (\bar{i}_s), the background radiation (\bar{i}_b), and the dark current (\bar{i}_d). The dark current in a generic photoconductor stems from the thermal excitation of free carriers. For long-wavelength infrared detectors, this dark current is normally the major source of noise because of the small excitation energy. For this reason, such detectors must be operated at low temperatures in order to minimize this noise (as in the case of the HgCdTe MIR detector).

The generation–recombination noise can be expressed as an amplified shot noise in the form [112], [115]:

$$\overline{i_{GR}^2} = 2eGF\Delta\nu I_{tot} = 2eGF\Delta\nu(\overline{i_S} + \overline{i_B} + \overline{i_D}) \quad (4.2)$$

where e is the elementary charge, $\Delta\nu$ is the detector bandwidth, G is the photoconductive gain and $F = \overline{\tau^2} / \overline{\tau}^2$ is the *excess noise factor* which is determined by the statistics of the carrier lifetime. For a standard photoconductor the carrier lifetime τ follows a Poisson distribution, as it is mainly determined by the carrier recombination process; this yields $F = 2$. For a multi-QW detector, if we call p_c the probability for an electron of being captured from a well, the expression for the generation-recombination noise (4.2) becomes [23]:

$$\overline{i_{GR}^2} = 2eG(2 - p_c)\Delta\nu I_{tot} \quad (4.3)$$

In the limit where $p_c \rightarrow 0$ the electron capture from a quantum well is a rare event (i.e. a Poisson process) and we come back in the photoconductor case ($F=2$). When $p_c \rightarrow 1$ the carrier is certainly captured from the consecutive well yielding $F=1$ in analogy to the case of a photodiode. In this case for a photo-generated electron the lifetime τ is given by the time employed to reach the p contact where recombination takes place. Therefore $G=1$ and $\overline{\tau^2} = \overline{\tau}^2$ hence the noise is only given by the generation process.

In Ref.[23] the simple case of a photodiode is used to derive heuristically the formula for the generation noise which can be generalized into equation (4.2).

Let's take a detector of efficiency η seeing a photon flux Φ over an integration time $T = 1/2\Delta\nu$ ($\Delta\nu$ is the detector bandwidth). A random number N of photoelectrons are created in a period T , giving an average value by $\overline{N} = \eta\Phi T$. If the fluctuation of N are poissonian, then the variance is $\sigma_N^2 = \overline{N}$. The photocurrent is given by the number of carriers created per unit time eN/T . The average value of current is then:

$$I = \overline{i} = \frac{e\overline{N}}{T} \quad (4.4)$$

and the relative variance of the photocurrent (i.e. the generation noise):

$$\overline{i_G^2} = \left(\frac{e}{T}\right)^2 \sigma_N^2 = 2e\Delta\nu I \quad (4.5)$$

4.1.4 Origin of the dark current in a QWIP

In its simplest picture a QWIP is a unipolar photoconductor consisting in the repetition of n-type (GaAs/AlGaAs) quantum wells. Photo-detection is based on photoemission of electrons from the quantum wells and current extraction from the n-type contacts on both sides of the device. Here we discuss briefly the origin of the dark current in a quantum well detector following Schneider and Liu [112]. Understanding this mechanism is crucial for design and optimization of QWIPs because dark cur-

rent represents a major contribution to the detector noise (especially at long wavelengths) and dictates the operating temperature as we will see.

Let's consider a standard QWIP as described before and suppose that the electron inter-well tunnelling is negligible (e.g. taking sufficiently thick AlGaAs barriers). In absence of external illumination, the dark current in the QWIP is controlled by (i) the flow of thermally-excited electrons above the barriers, and (ii) by the emission and capture of electrons in the wells. These two contributions to dark current are represented pictorially in FIG. 4.3.

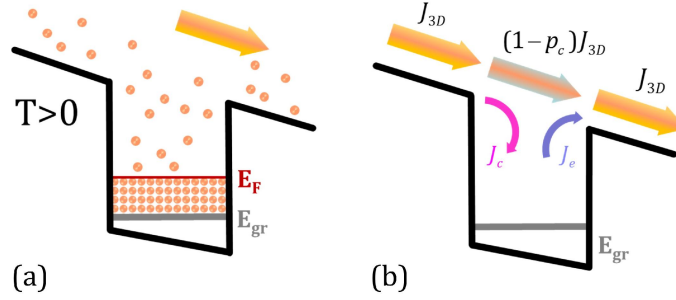


FIG. 4.3(a) Schematics of the electronic distribution in a QW at finite temperature: thermally photo-excited electrons result in a dark current. (b) Processes controlling dark current in a QWIP. Reproduced from Ref. [112]

In FIG. 4.3(a) the electron population distribution for a QWIP at finite temperature is shown. At $T=0$ K electrons occupy the ground subband in the quantum well up to the Fermi energy. When $T>0$ K electrons are not only bound in the well, but due to thermal energy a small part of them is also distributed outside of the well and on top of the barriers. This thermally-excited carriers originate the QWIP dark current.

In FIG. 4.3(b) the dark current paths are shown. Above the AlGaAs barriers, the carriers feel no confinement and the current flows in a three-dimensional fashion ($J_{dark} = J_{3D}$). On the other side, near each QW the thermal emission of electrons may occur, yielding a contribution J_e to the dark current. This current diminishes the electron density in the well and must be balanced (at the steady state) by the capture of electrons into the well ($J_e = J_c$). Note: J_e and J_{3D} are related since the dark current has to be continuous throughout the structure. Said p_c the capture probability for an electron traversing a well, one has $J_c = p_c J_{3D}$ and $J_{3D} = J_c + (1 - p_c)J_{3D}$. The dark current can be obtained calculating J_{3D} or alternatively from J_e , being $J_{dark} = J_e / p_c$.

For example, to estimate J_{dark} from J_{3D} it has been shown that a simple 3D carrier drift provides the correct order of magnitude for the dark current. In this simple model the Fermi statistics is used to evaluate the density of thermo-generated carriers above the wells and carriers drift velocity is estimated from electron mobility and applied electric field. We refer to [112] for a detailed discussion about the models for the calculation of the dark current.

In the context of this work, it is important to observe that the dark current I_{dark} is proportional to the volume V of the detector, i.e. [112]

$$I_{dark} \propto G_{th} \cdot V \quad (4.6)$$

where G_{th} is the *thermal generation rate* (the number of thermally generated electrons per time and volume). Therefore, a drastic reduction of the active semiconductor in the case of a QWIP could considerably reduce the detector noise and improve performances, as it will be discussed in 4.3.1.

4.1.5 Detectivity and BLIP condition

In this section we will derive the expressions for the two most important figures-of-merit of a QWIP, namely the detectivity (D^*) and background infrared limited performance blip temperature (T_{BLIP}).

As seen above, noise is inherently present in the photodetection mechanism. Therefore we are interested in extracting a signal (in the form of a photocurrent I_S) from a noisy background (yielding a noise current I_N) rather than in the *absolute value* of the detected signal. In other words, detecting a signal consists in obtaining the largest possible signal-to-noise ratio:

$$S / N = \frac{I_S}{I_N} \quad (4.7)$$

Generally a photocurrent signal (A) is expressed as the product of the detector response $\mathfrak{R}(A/W)$ as defined in (4.1) to the incident power $P(W)$. Recalling (4.2) the noise has the form $I_N = \sqrt{eu\Delta\nu AJ_N}$ where u is a constant accounting for the photoconductive gain G and the factor F , $\Delta\nu = 2/t_{int}$ is the bandwidth of the measurement system, A is the detector area and J_N is the noise current density. The signal-to-noise ratio is then:

$$S / N = \frac{\mathfrak{R}P_{inc}}{\sqrt{eu\Delta\nu AJ_N}} \quad (4.8)$$

The minimum detectable power is the one corresponding to a signal-to-noise ratio of 1. This quantity is referred to as the *noise equivalent power* (NEP) and its inverse gives the *detectivity* (D) of the device:

$$D = \frac{1}{NEP} = \frac{\mathfrak{R}}{\sqrt{eu\Delta\nu AJ_N}} \quad (4.9)$$

This expression for the detectivity shows that the performance of a detector depends upon the measure bandwidth and the detector surface area. To allow comparisons between different detector technologies/materials, the *normalized detectivity* D^* is introduced as:

$$D^* = \frac{\mathfrak{R}}{\sqrt{euJ_N}} = D\sqrt{\Delta\nu A} \quad (4.10)$$

D^* is the signal (per unit incident power)-to-noise ratio appropriately normalized by the detector area and the measurement electrical bandwidth and represents a good figure of merit for comparing different detectors.

It is important to highlight that the noise current density J_N has two origins:

- (i) the *dark current density* J_D which relates to conduction by free carriers in photoconductors as described in 4.1.4 and is inherent to the detector;
- (ii) the *background current density* J_B due to the fact that the detector picks up the blackbody radiation from the external environment at temperature T_B

The *BLIP* (background limited infrared performance) *regime* is defined as the regime where the dominant noise is caused by the background photons. It is always desirable to operate a detector at or under BLIP condition for maximal sensitivity. The BLIP temperature T_{BLIP} is defined as the temperature where $J_D = J_B$ and represents a good figure-of-merit for the detector noise. The definition of T_{BLIP} is sketched in FIG. 4.4(a): the red curve represents the dark current density $J_D \approx G_{th}$ increasing with the detector temperature and the blue curve gives the constant background contribution $J_B \approx e\eta\Phi_B(T_B)$ where Φ_B is the blackbody photon flux at temperature T_B . It is apparent that in the BLIP regime the maximum detectivity is limited by the background radiation.

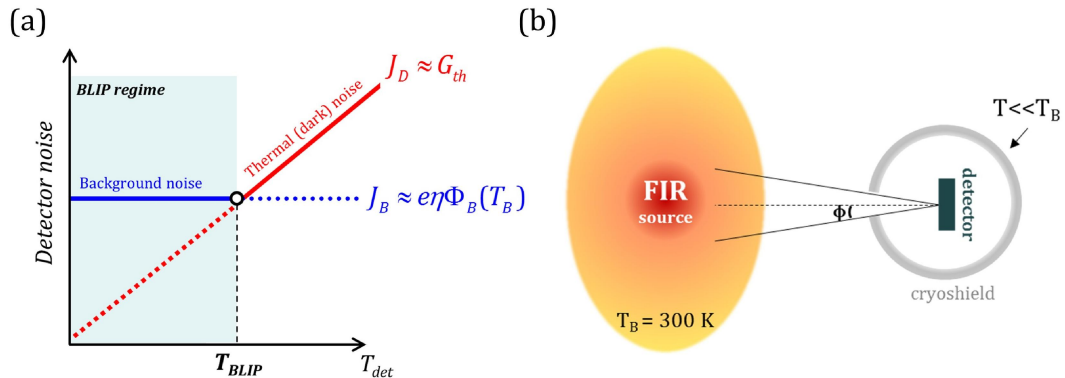


FIG. 4.4(a) Definition of BLIP regime. (b) Experimental configuration employing a QWIP: the detector views a detail against a 300 K background from an aperture yielding a finite field of view (FOV). Reproduced from Ref. [23]

In a photodetection experiment we will always deal with a detector mounted on a cryostat equipped with a cooled cryoshield featuring a finite aperture. This means that the device will detect an optical signal superimposed to a 300K thermal background filtering from the aperture (i.e. the opening is a 300K blackbody). The situation is depicted in FIG. 4.4(b). Hence, employing a cryoshield with a finite field of view (FOV) is important as the photon flux received from the 300K background decreases by $\sin^2(\phi)$ where ϕ is the acceptance angle of the aperture.

The received blackbody flux therefore diminishes as $\Phi_B^{eff} = \Phi_B \sin^2(\phi)$ and so does the background current J_B . As a consequence the detectivity in the BLIP regime can be strongly improved by limiting the detector field of view, and when giving the T_{BLIP} , the FOV is a crucial parameter.

4.1.6 THz quantum well photodetectors: state of art

THz quantum well photodetectors (THz-QWP) extend the QWIP concept in the THz range. The material system employed is the usual GaAs/AlGaAs heterostructure used for THz QCLs. In this case, the QW parameters have to be optimized for photo-detection and carrier extraction. First of all, the well width must be chosen to have the first excited state in resonance with the top of the barrier. Additionally, to operate at longer wavelengths it is crucial to reduce the absorption by free carriers and the dark current. Smaller barrier height and a lower doping density respect to standard QWIPs are therefore required. The state-of-art of THz QWPs has been summarized in 2011 [116] by J. C. Cao and H. C. Liu. Here we report some important information. In FIG. 4.5(a) the calculated parameters of Al percentage in the AlGaAs barrier (i.e. the barrier height) and well width to obtain the *quasi-resonance condition* for a given peak detection frequency (wavelength) are shown [117]. Note: very low aluminium fractions (between 0.8 and 5.4%) are required. Furthermore, the T_{BLIP} for THz detection has been calculated by equating the calculated dark current (from the 3D drift model) and the background photocurrent (FIG. 4.5(b)) in two different designs.

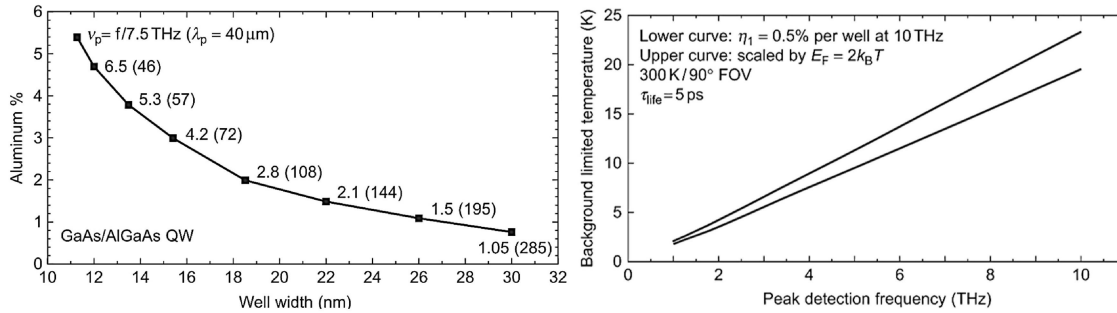


FIG. 4.5(a) Calculated Al percentage (i.e. the barrier height) and well width for the *quasi-resonance condition* at a given peak detection frequency (wavelength). (b) BLIP temperature vs detection frequency calculated for two different detector design (FOV=90°). From Ref. [117].

It has been shown, in fact, that a trade-off is necessary between maximum operating temperature and high absorption [116]. In 2004, Graf et al. demonstrated the first QW detector based on a QCL-like bandstructure and operating at ≈ 3.5 THz [118]. In the same year, Liu et al. [117] demonstrated the first THz QWP with a peak response at 7.1 THz (near the GaAs Reststrahlen-band) using a 5% Al fraction. Later a 3 THz QWP in mesa geometry (V267) has been demonstrated successfully by the same authors in [119]. The same detectors have been successively employed to demonstrate a surface detection scheme via a metal grating coupler [120]. More recently arrays of patch antennas have been used to couple THz radiation into a QWIP detector operating at ≈ 5 THz, reducing the device active core and enhancing its response [121].

4.2 THz-QWP characterization in mesa geometry

4.2.1 The 3 THz QWP structure

In this paragraph, we will report the original datas available in literature for the 3 THz QWP structure by H. C. Liu [116]. This will enable a direct comparison with the experimental measures obtained on the structure studied in this thesis which is based on the same design. The fabrication scheme and experimental photo-detection setup (similar to the ones used to measure those datas) will be described in the following paragraph.

The quantum well details of the structure V267 are reported in FIG. 4.6(a).

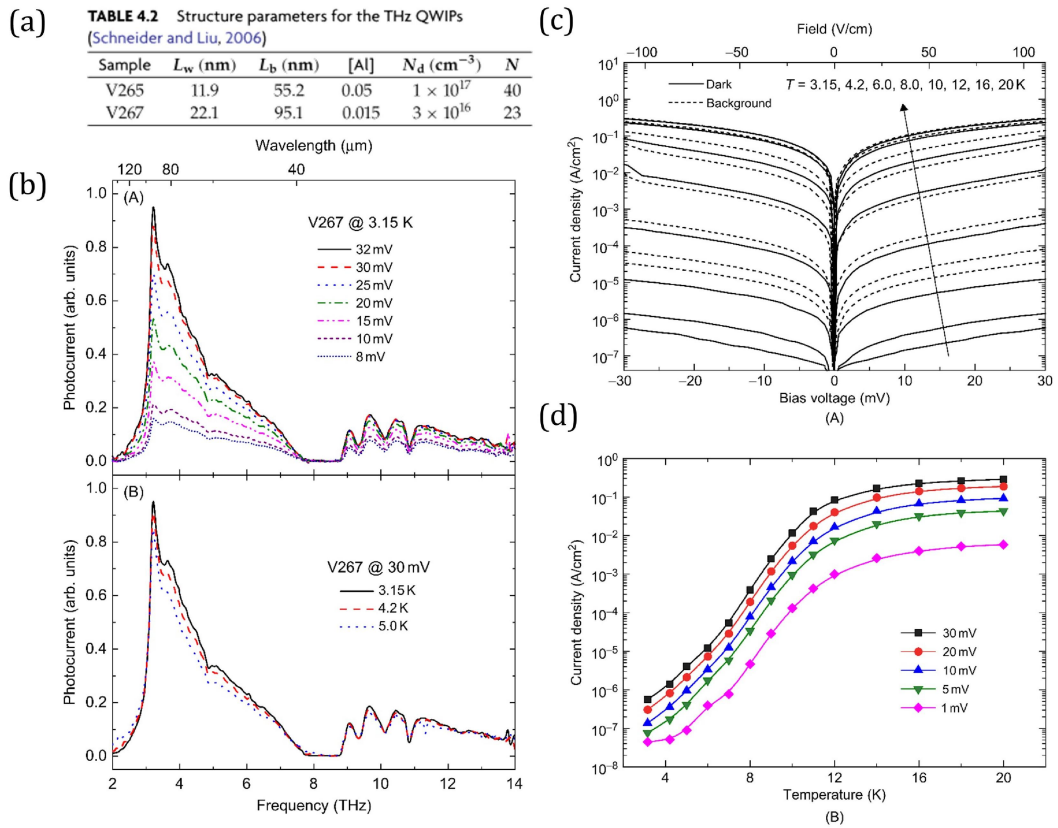


FIG. 4.6(a) Details of V267 QWP structure. (b) Experimental photocurrent spectra at different bias voltages and operating temperatures. (c) I-V curves under dark condition (solid) and under a 300-K background seen from a FOV of 90° (dash) for T varying from 3.15 to 20 K. (d) Dark current as a function the operating temperature for different bias values. The entire figure is taken from Cao and Liu review [116].

Note: the QWs are Si-doped in the centre and wide barriers are used to reduce the interwell tunnelling. The active region is sandwiched between relatively low doped top and bottom contacts ($n=1 \times 10^{17} \text{cm}^{-3}$) to reduce free carrier absorption from the contact layers. The measured photocurrent spectra of V267 at different bias voltages and operating temperature are given in FIG. 4.6(b).

From the photocurrent spectra at $T=3.15$ K we see that the device operating range is between ≈ 2.5 and 5.3 THz (peak response at 3.2 THz i.e. $93.6 \mu\text{m}$). In addition, the photocurrent spectra under 30 mV bias are measured at different operating temperatures showing a decrease in response when temperature rises. The current–voltage (I-V) curves under dark condition (solid) and under a 300 -K background seen from a FOV of 90° (dash) for temperatures varying from 3.15 to 20 K are shown in FIG. 4.6(c). It is apparent that at $T=16$ K the dark and background currents have the same order of magnitude meaning that the device is operating beyond the BLIP regime. In FIG. 4.6(d) the dark current as a function the operating temperature (I-T) is shown for different operating biases. From this graph the authors estimate that the BLIP temperature of the V267 structure is around 12 K, owing to the observation that lowering the temperature below 12 K produces a rapid decrease in dark current.

4.2.2 Fabrication

We have had a copy of V267 structure grown by MBE at Leeds University on an insulating GaAs substrate (sample L1118). The multi-quantum well consists of 11 periods (parameters given in FIG. 4.6(a)) for a total thickness of $2.5 \mu\text{m}$ which comprises a top and a (thick) bottom n-GaAs slab serving as contact layer. The detailed growth sheet of this sample (named L1118) is reported in Appendix A. A portion of the sample has been cleaved and processed with standard GaAs fabrication technology as shown in FIG. 4.7.

After cleave and cleaning, the sample is patterned in squared mesas of 1 mm or $300 \mu\text{m}$ sides. A positive tone photoresist (S1818) is used as mask for GaAs/AlGaAs wet etch with a sulfuric acid solution. The etch depth is carefully controlled during process with a mechanical profilometer in order to stop into the bottom n-GaAs slab allowing the subsequent bottom contact definition. Ni/Ge/Au/Ni/Au bottom metallization surrounding the mesas is defined via negative tone photoresist and lift-off. The evaporated layers are then annealed at 420°C for 2 min in a rapid thermal annealing (RTA) oven to create a diffused ohmic metal-semiconductor contact. Similarly, Pd/Ge is evaporated on the mesas top surface and annealed at 360°C for 5 min. Pd/Ge contact is preferred here due to its short diffusion depth (a few tens of nm) in contrast with Ni/Ge/Au/Ni/Au which diffuses farther in the semiconductor and could then damage the active region. A second top contact evaporation (Ti/Au) is performed to facilitate the application of wire bonds. Finally, the sample is back-polished and a back Ti/Au contact is evaporated to guarantee a good mechanical and thermal contact with the copper block used to mount the sample in the cryostat.

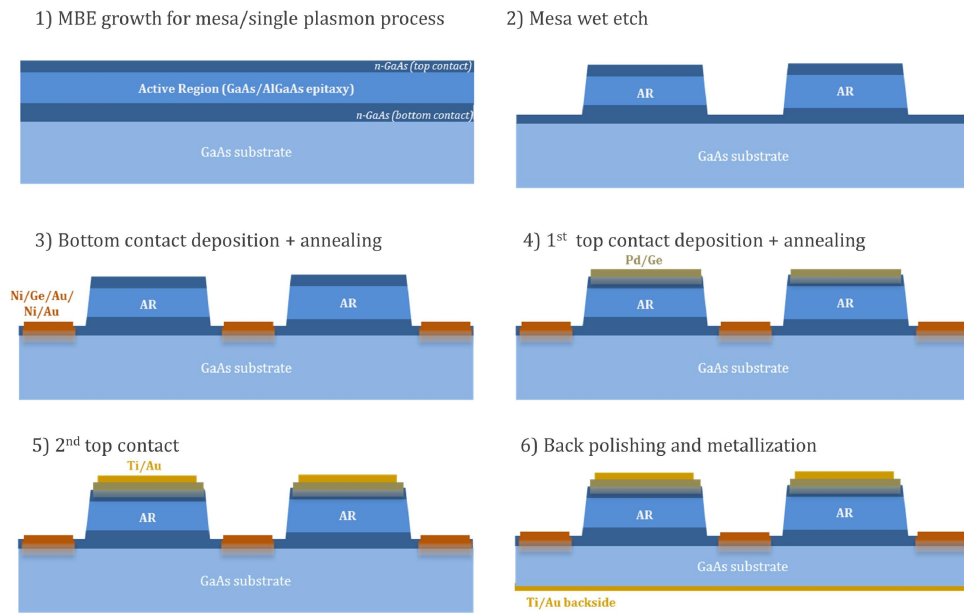


FIG. 4.7 Fabrication steps for standard THz QWP characterization in mesa geometry

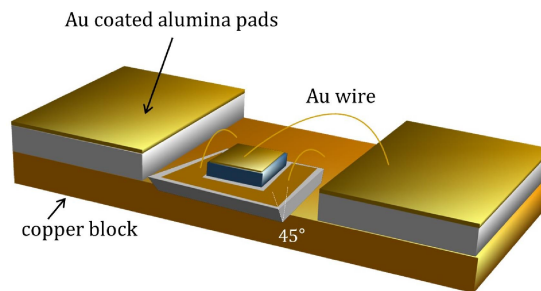


FIG. 4.8 Mounting scheme of the finalized mesa QWP.

The sample then undergoes a backend processing. First, the $\approx 1 \times 1$ cm² sample is diced into several smaller chips. Later on, one chip is selected and a 45° facet is realised by mechanical polishing on one side to couple THz radiation in the detector. The sample is then indium soldered on a copper block where gold coated alumina pads are glued as shown in FIG. 4.8(a). Finally electrical connections are realised via gold wedge bonding. In our connection scheme the top of a mesa is relied to a contact pad while the bottom is relied to the copper block.

4.2.3 Experimental setup

In this section the experimental setup employed to perform electrical and optical characterizations of the THz QWPs is described. The sample prepared as in FIG. 4.8(a) is mounted on a continuous-flow cryostat. Once the cryostat is under vacuum, it is continuously cooled by a steady flow of liquid Helium from a storage dewar.

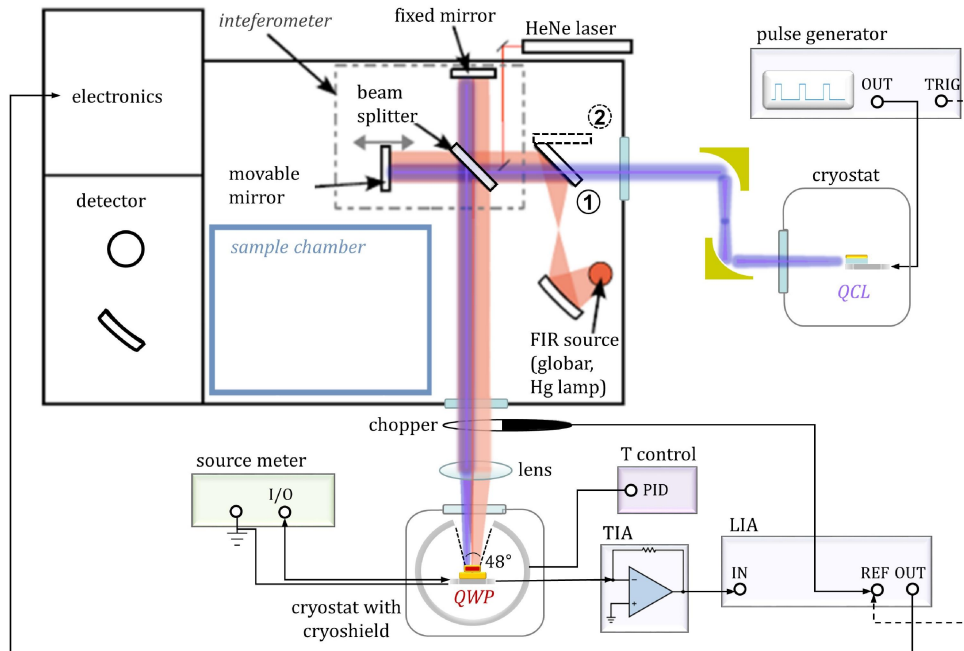


FIG. 4.9 Experimental setup for THz QWP optical and electrical characterization (top view).

Temperature control of the sample within the cryostat can be performed by controlling the flow rate of Helium into the cryostat together with a heating wire attached to a PID temperature control loop. A metal cryoshield surrounds the sample so that the detector can look at the external 300K background only from a small window, which provides a field of view $FOV = 48^\circ$.

For I-V characterizations a source meter (Keithley 2636A) is used, which provides the external bias and records the current at the same time. Photocurrent spectra can be acquired configuring the FTIR spectrometer described previously in an external detection scheme as shown in FIG. 4.9. To characterize the intrinsic response of the QWP a broadband excitation is needed. In this case, the radiation coming from an internal source (globar, Hg lamp) is sent into the interferometer (red beam in FIG. 4.9) and then outside towards the detector through a TPX window. Outside the FTIR the beam is modulated by a mechanical chopper, then focused by a TPX lens ($f=10$ cm) onto the sample (another TPX window is placed at the cryostat entry). The FTIR internal HeNe laser diode can be used to align the beam onto the sample as a strong photocurrent signal due to interband absorption in GaAs is detected. After alignment, the photocurrent signal coming from the HeNe laser can be cut inserting a high resistivity Si wafer at the FTIR output window. The photocurrent signal coming from intersubband excitation can then be amplified by a low noise trans-impedance amplifier (TIA, Stanford Research System SR570) which can also provide a DC bias to the device. Note: owing to the gain-bandwidth product of an amplifier a trade-off has to be chosen between modulation frequency and amplification. The amplified signal is then injected in a lock-in amplifier (LIA, Stanford Research System SR810) where it is filtered and sent back into the FTIR. Here an analog-to-digital converter (ADC) transforms the voltage (analog signal) corresponding to the interferogram intensity

at a given position in a digital signal which can be elaborated via computer. If the LIA is used to filter the chopped signal the FTIR acquisition has to be made in step scan modulation, which implies very long acquisition times.

A more practical option is to use the chopping + LIA configuration to align the sample, maximizing the photocurrent signal (directly read as a voltage on the LIA display). Once that has been done, the chopper is removed and the (DC) signal from the sample, amplified by the TIA, is injected directly into the FTIR. The photocurrent spectrum is then acquired with the FTIR operating in rapid scan modulation, which permit to statistically improve the SNR by averaging the measure (≈ 100) over many scans.

Alternatively, a THz QCL emitting in the QWP detection band can be employed as radiation source to probe the device. This configuration offers the advantage of enabling lock-in detection without chopper and at much higher modulation frequency (the bias modulation of the QCL, typically tens of kHz) thus improving the SNR. Moreover the brilliance of the QCL is extremely high compared to a blackbody or a discharge lamp in the THz range. In this case a THz QCL is mounted on another cryostat on the left side of the FTIR equipped with a window enabling operation with an external source. The chosen THz QCL is cooled and operated in AC mode with a pulse generator (Agilent 8114A). For normal operation a repetition rate in the tens of kHz (e.g. 33 kHz) and a duty cycle of a few percent (1-2%) is employed. The laser beam is collected by two metallic parabolic mirrors and sent into the spectrometer by switching the source selection mirror in position 2 (see the blue path in FIG. 4.9). Then the QCL beam follows the same path described before for lamp radiation. Note that in FIG. 4.9 the red and blue path are represented next to each other for clarity, while in reality the beams are almost superposed.

4.2.4 Electrical characterization

The L1118 sample processed in mesa geometry has been used as a preliminary testbed to master the standard electrical and optical measures used to characterize a THz-QWP.

Typical I-V curves for a 1 mm² mesa are shown in FIG. 4.10 for temperatures 300 K and 8 K. A drop in the measured current of more than two order of magnitude is observed when the detector is cooled. The reported current densities are compatible with the values in FIG. 4.6(c) for the original structure V267. These preliminary characterizations have been acquired under a 300 K background illumination from the cryostat window.

The curves show a (quasi)symmetric behaviour which confirms the ohmicity of the fabricated top and bottom contacts.

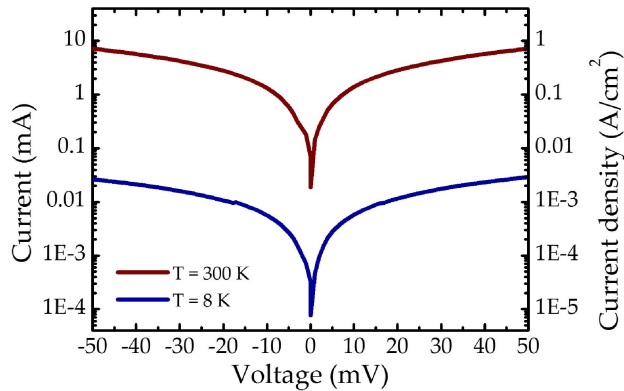


FIG. 4.10 I-V characteristics for the 1 mm² mesa THz-QWP (sample L1118) at 300 K and 8 K

4.2.5 Photodetection with a broadband source

In this section we report the standard photocurrent measures on the 1 mm² mesa THz-QWP (sample L1118) probed electrically above.

In FIG. 4.11(a) a sketch of the experimental configuration is shown: the THz beam coming from the FTIR impinges on the substrate 45° facet and it's deviated towards the sample due to the GaAs high refraction index. A bias is applied between top and bottom contact to extract the generated photocurrent. Typical measured photocurrent spectra at T=7 K as a function of the applied bias for a 1 mm side mesa are reported in FIG. 4.11(b). The spectra are acquired in step scan modulation, with unpolarised light coming from the global, chopper frequency $f_{\text{chop}} = 80$ Hz, transimpedance amplification 5 $\mu\text{A}/\text{V}$ and resolution $R = 8$ cm⁻¹. The spectral response appears very similar to the original structure V267 [119] with a detection band between 2 and 6 THz and peak response at 3.16 THz.

It has been observed that these mesa devices operate better under negative bias (best extraction is around -25 mV), while under positive bias the extracted photocurrent is lower. This slightly asymmetry may be related to an asymmetry in QWs caused by dopant segregation during growth, as observed in Ref. [119].

To verify that the detected signal originates from the ISB transition in the QWs a polarizer may be inserted on the beam path. As shown in FIG. 4.11(c) only TM polarized light is detected by the THz-QWP as well-known from the polarization rule of ISB transitions. To complete this section we show in FIG. 4.11(d) that the same photocurrent spectra may be collected equivalently, as discussed above, in rapid scan modulation without chopper nor LIA. In this case we compare the spectrum acquired with the global to a spectrum acquired with Hg lamp which has a slightly higher brilliance in the low THz band. The fact that a measurable photocurrent is observed also at zero bias confirms the asymmetry of the QWs discussed above.

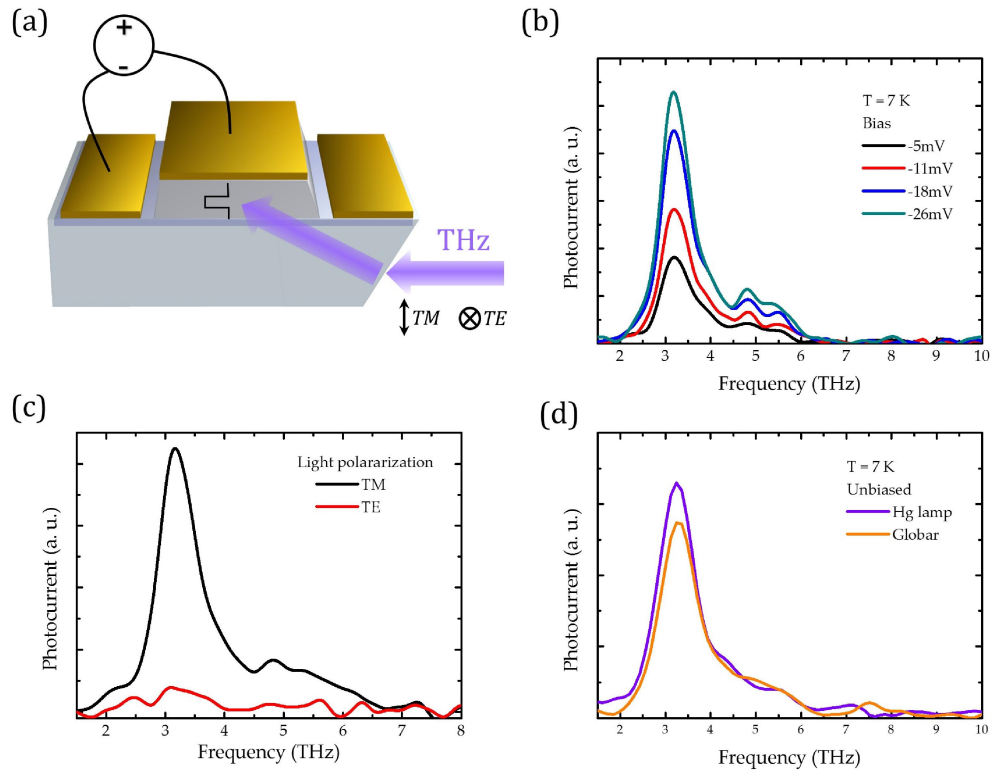


FIG. 4.11(a) Schematics of the photo-detection experiment for a mesa. A polarized may be inserted on the beam path to perform polarized measures. (b) Photocurrent spectra for a 1 mm side mesa at 7 K as a function of the applied bias. (c) Photo response in function of the beam polarization: only TM polarized light is detected from the QWs. (d) Photocurrent spectra acquired in rapid scan modulation: globar vs Hg lamp source.

4.2.6 Photodetection with a QCL source

In this paragraph we show the results obtained probing the same mesa THz-QWP detector with a home-made THz QCL source. This possibility is interesting since QWPs are superior to traditional THz detectors due to their high-speed response and compactness. The combination of THz QCLs and THz QWPs may set the basis of a THz wireless communication system. The first application of an all photonic terahertz communication link operating at 3.8 THz using a QCL and a QWP has been demonstrated by Grant et al [122].

The photocurrent spectra acquired with a 300 μm mesa detector and a 3 THz QCL source (sample L1003, design from Ref. [123]) as a function of the extraction bias are shown in FIG. 4.12(a). The QCL used is a surface emitting unphased GPH [124] operated in pulsed mode (300 ns current pulses, 2% duty cycle) at 10 K. A clear detection peak is visible at 3 THz.

The measure is acquired in rapid scan modulation with a resolution $R=1 \text{ cm}^{-1}$ and detector temperature $T_{\text{det}}=8 \text{ K}$. As discussed above, the device exhibits an asymmetric response for positive and negative bias. Most efficient photocurrent extraction is obtained at -20 mV bias. This behaviour is summarized in FIG. 4.12(b) where the peak photocurrent is plotted as a function of the bias.

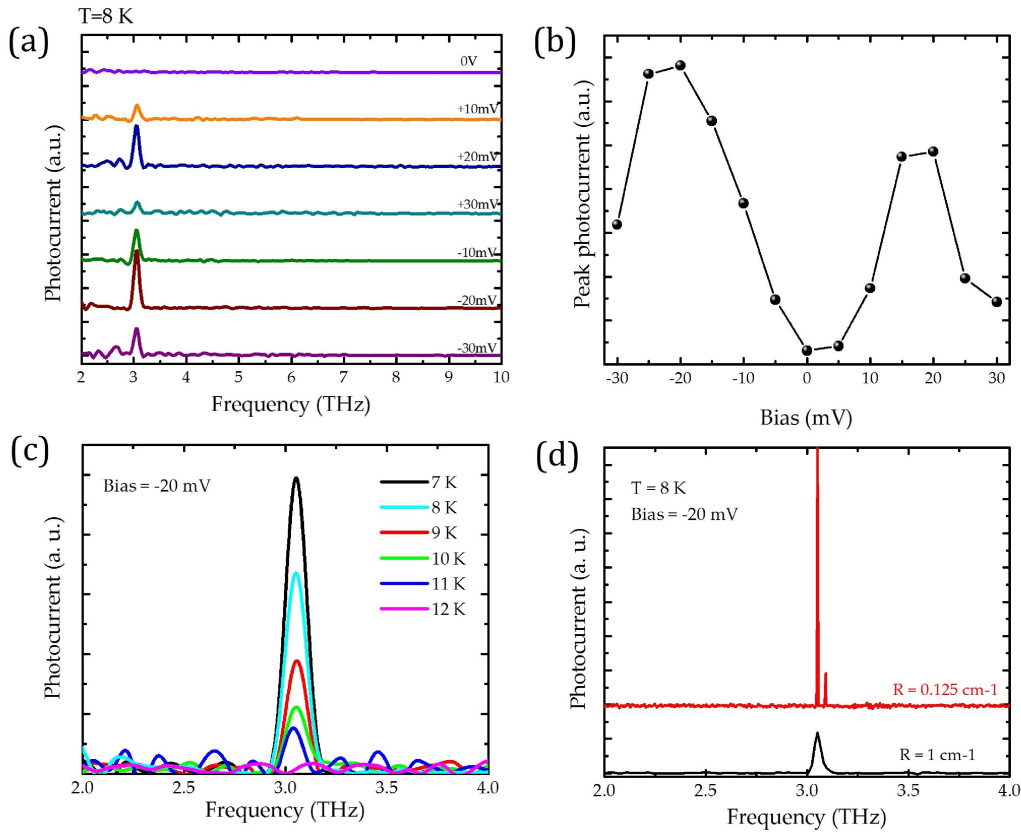


FIG. 4.12(a) Mesa THz-QWP photocurrent spectra with a 3 THz QCL source as a function of the extraction bias at $T_{\text{det}} = 8$ K. (b) Peak photocurrent vs applied bias at $T_{\text{det}} = 8$ K. (c) Photocurrent spectra as a function of detector temperature at -20 mV bias. (d) Photocurrent spectra at the maximum FTIR resolution $R = 0.125$ cm^{-1} and at $R = 1$ cm^{-1} .

In FIG. 4.12(c) the photocurrent spectra at -20 mV bias as a function of detector temperature are shown. At 12K the detector does not respond anymore due to a strong increase of the dark current which overcomes the useful signal. The device goes out of the BLIP regime, as discussed in 4.1.5. Finally in FIG. 4.12(d) we compare a low resolution ($R = 1$ cm^{-1}) spectrum to a spectrum taken with the maximum FTIR resolution $R = 0.125$ cm^{-1} where two QCL modes are resolved. This spectrum is identical to a spectrum acquired with a standard DTGS detector. THz QWPs may be then interesting for high-speed wireless communications.

4.3 THz meta-atom subwavelength QWPs

4.3.1 Motivation: reducing active volume to enhance performance

When dealing with the performances of any infrared photon detector, it can be shown that the main figure of merit is the ratio of the material absorption coefficient to the sheet thermal generation rate [125]. Roughly to obtain the highest performance one should maximize the quantity $\eta / \sqrt{(G+R)t}$ where η is the detector quantum efficiency, G and R are the sheet thermal generation and recombination rates and t is the detector thickness. One way to improve the performance of an infrared photodetector is to reduce the total amount of thermal generation within the active core by reducing its volume, which is the product of its thickness and physical area. This of course must be done without sacrificing the possibility for the device to efficiently collect the incoming radiation. The key idea is to enhance infrared absorption while reducing the active detective material size. This problem can be practically solved by embedding an ultra-small detector material into a properly designed resonator or antenna.

So far, little research effort has been devoted to improve THz QWPs performances via their miniaturization and engineering of the radiation coupling.

Borrowing concepts from the photonics world is of limited help since photonic devices rely mainly on diffractive (i.e. wavelength scale) techniques while typical QWPs active regions are deeply subwavelength (1-2 μm). In the case of standard QWIPs/QCDs coupling via a 45° polished facet into a mesa is often employed to obtain photon absorption [89]. However, this strategy is ineffective as it yields a poor overlap between the optical mode and the detector active core. Moreover, the lateral size of mesa devices is very large, yielding high dark currents.

Indeed, one challenge for THz detectors is to couple efficiently THz radiation ($\lambda \approx 100 \mu\text{m}$) into micron-size detector active cores. Antenna theory is the perfect tool for addressing this issue: antenna naturally performs a conversion between a free space electromagnetic wave and a localized electrical current. In the following, we will show that the LC geometry with a suspended loop antenna, developed so far, is suitable to implement subwavelength QWIPs featuring an ultra-small active core.

4.3.2 The problem of electrical injection in a split ring geometry

In the perspective discussed above, the closed-loop (a.k.a. split-ring) geometry presents a challenge because it's intrinsically short-circuited. Without any modification, it is therefore impossible to access the semiconductor endowing the capacitive section with a DC contact line to e.g. extract a photocurrent in the case of a subwavelength photodetector or electrically inject a subwavelength laser. To make the split-ring geometry useful for active devices one should add an independent pole insulated from the loop antenna as sketched in FIG. 4.13. In this configuration the LC reso-

nance would be slightly modified due to the capacitance of the insulating layer but the cavity mode would stay deeply subwavelength and circuit-tuneable as before.

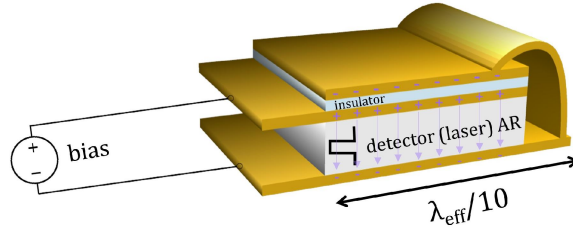


FIG. 4.13 Possible injection scheme for a split-ring-like resonator: an independent electric pole is added thanks to an insulating layer.

A drawback of this approach is the fact that the THz mode would leak out into the contact line (it is a TEM line with no cutoff, see 1.4.2) highly rising radiation loss. This problem is well-known in RF engineering where inductive chokes are for example used to block the AC signal while allowing a DC bias to pass [126]. Moreover the geometry of FIG. 4.13 is difficult to integrate with standard microfabrication of THz QWPs or QCLs. In the following an alternative strategy to implement electrical injection overcoming the short-circuit issue will be discussed and implemented. In Chapter 5 a preliminary demonstration of a contact scheme similar to the one of FIG. 4.13 to inject a THz QCL will be presented.

4.3.3 LC resonators with ring openings in the ground plane

In 3.2.1 we implemented a first generation of LC photo-activated switches. In that case the introduction of a ring opening around our lumped capacitor slightly modifies the LC resonance without fundamentally changing its properties. Here we reconsider in more detail this configuration as it naturally creates two separated metal domain that could be exploited, if conveniently modified, for electrical extraction/injection. For now, we will only explore the evolution of the LC mode as a function of the air-gap size h_{gap} . The other geometrical parameters are kept constant. The situation is sketched in FIG. 4.14(a) where the circuital scheme is also reported. As previously discussed, opening an air-gap in the ground plane introduces a supplementary capacitance which has to be considered when computing the resonant frequency. To practically open the metal ground plane an IBE etch step is added to the fabrication (see fabrication scheme in FIG. 4.17 later in this the section), as shown in the SEM picture.

In FIG. 4.14(b) the reflectivity ($R=|S_{11}|^2$), transmissivity ($T=|S_{21}|^2$) and absorptivity ($A=1-R-T$) of an array of these resonators under a normal incidence plane wave excitation (magnetic field perpendicular to the antenna plane) as a function of the gap size has been simulated via FEM simulations. The array period is $20\ \mu\text{m}$ in both directions, the patch diameter and thickness are $4\ \mu\text{m}$ and $1.5\ \mu\text{m}$ respectively, the antenna length is $7\ \mu\text{m}$. From the reflectivity one can see that the resonance redshifts and broadens while the resonance depth stays constant.

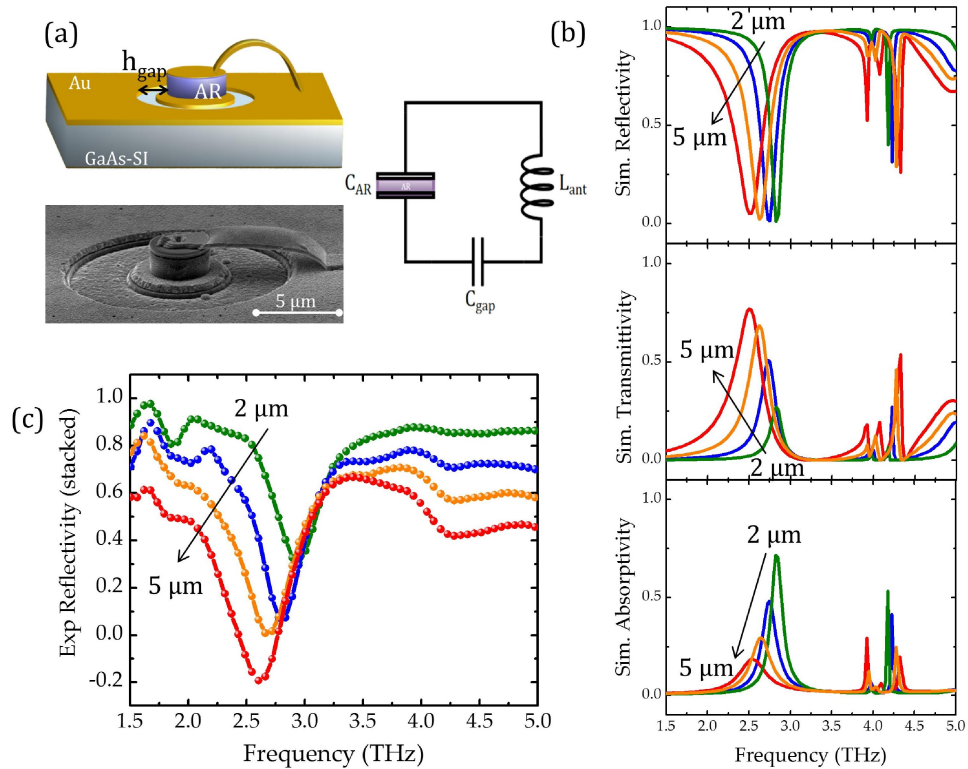


FIG. 4.14(a) Subwavelength LC resonator with a ring opening in the ground plane: schematics (top) and experimental realization (bottom). The ring opening behaves as a capacitor to be included in computing the resonant frequency. (b) Simulated reflection, transmission and absorption from a periodic array of ring LC resonators as a function of the gap size h_{gap} . (c) Measured reflectivity as a function of the gap size: the LC resonance redshifts and broadens when the gap increases.

The information grasped from the reflectivity spectra is however incomplete as we are now dealing with a 2-port system. Indeed, the system can be fully characterized only if also the transmittivity is known. From simulated transmission spectra we see that a resonant peak grows in intensity and broadens as the metal opening enlarges, the magnitude of transmission being related to the metal filling factor of the ground plane unit cell (geometric transmission). Finally, from R and T the absorptivity spectra can be computed. The resonant absorption is maximum for a narrower ring opening and it lowers by widening the gap. At the same time the resonance bandwidth broadens, moving from a simulated $Q \approx 20$ for a $2 \mu\text{m}$ gap to $Q \approx 6$ for a $5 \mu\text{m}$ gap. The predicted resonance redshift and broadening can be observed from experimental R spectra shown in FIG. 4.14(c), though the reflectivity alone is not enough to fully characterize the samples. The spectra are taken at $\theta = 15^\circ$ incidence in the same magnetic coupling configuration. So far, we can conclude that opening the metal ground plane around the subwavelength resonator slightly modifies the character of the LC resonance, which redshifts and broadens. We are moving from a 1-port to a 2-port system, still keeping the circuitual nature and subwavelength confinement within our meta-atoms.

4.3.4 Role of the periodic subwavelength apertures

Discussing the spectra in FIG. 4.14 we did not mention the origin of the resonant peaks appearing around 4.5 THz. These modes can be associated with the extraordinary optical transmission (EOT) of the subwavelength ring openings in the ground plane, also known as Wood's anomalies [127], [128]. In fact, the peak positions due to the excitation of surface modes at the metal-semiconductor interface can be estimated as $\lambda_{\max} \approx p \cdot \sqrt{\epsilon_{\text{sub}}}$ [129] yielding $\lambda_{\max} \approx 72 \mu\text{m}$ (i.e. $f_{\min} \approx 4.2 \text{ THz}$) in our example. In both simulated and experimental spectra of FIG. 4.14 the resonant LC mode appears relatively undisturbed (i.e. uncoupled) by the periodic mode. Here we want to explore the impact of the Wood's anomalies when they approach the LC resonance. Simulations as a function of the lattice period of the array have been performed for a fixed ring opening ($h_{\text{gap}} = 4 \mu\text{m}$). When the array period $p_x = p_y = p$ gets larger, the diffraction edge approaches the LC resonance eventually interacting with it. The interaction of the LC mode with the Wood's anomalies results in a Fano-like coupling which modifies the resonance shape as it is shown in FIG. 4.15(b) for 30 μm and 40 μm periods.

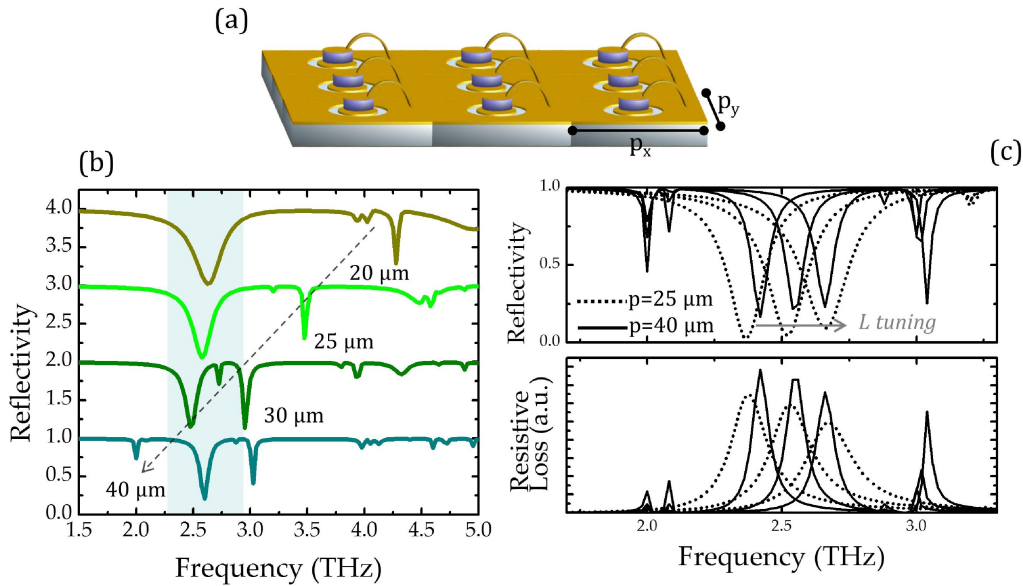


FIG. 4.15. (a) Schematics of a LC resonators array with ring ground openings. (b) Simulated reflectivity for a as a function of the array period p (square lattice). (c) LC mode tuning with the antenna length ($l_{\text{ant}} = 5, 7, 9 \mu\text{m}$) for periods $p = 25$ (dashed) and $p = 40$ (full) approaches to the LC resonance producing a Fano-like coupling.

This can be better observed in FIG. 4.15(c) where the simulated antenna tuning of the LC mode ($l_{\text{ant}} = 5, 7, 9 \mu\text{m}$) is shown for two array periods ($p = 25 \mu\text{m}$ – dotted line, $p = 40 \mu\text{m}$ – full line). For $p = 25 \mu\text{m}$ the resonances are isolated in the frequency band and Lorentz-shaped. For $p = 40 \mu\text{m}$ the tuning is “squeezed” around 2.5 THz and the resonant peaks appear narrower and Fano-shaped. In particular the shorter-antenna device (higher frequency) is clearly interacting with the periodic mode at 3 THz while the longer-antenna device (lower frequency) is interacting with the periodic mode at 2 THz. The same information obtained from reflectivity spectra can be re-

covered evaluating the resistive loss in the semiconductor active core. In conclusion, the impact of periodic modes due to the subwavelength openings in the ground plane impacts the optical response of the system, as we will see later.

4.3.5 Design and fabrication of THz meta-atom QWPs

Based on the system discussed just now, an electrical contact scheme for the sub- λ LC resonator based on subwavelength openings in the ground plane can be devised. The device concept is sketched in FIG. 4.16(a): a narrow opening in the metal ground plane is defined below the suspended antenna, in order to separate the ground metal underlying the lumped MSM capacitor from the ground metal where the antenna is attached. This creates two electrically separated domains which can be used to bias the active semiconductor that fills the capacitor and extract a photocurrent from it. Note: to ensure that the two contacts are electrically separated, an insulating substrate must be employed, e.g. semi insulating GaAs. THz radiation impinging onto the system at (quasi)normal incidence is coupled into the circuit via the excitation of the magnetic dipole moment of the suspended loop antenna.

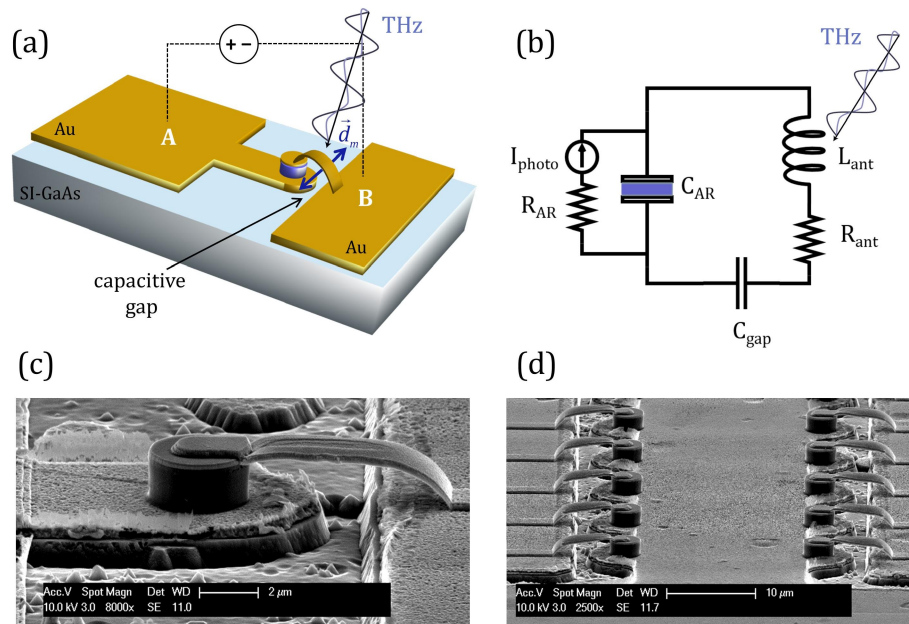


FIG. 4.16(a) Schematics of a single meta-atom THz-QWP with electric contacts. (b) Equivalent circuit: the capacitive region host a QWIP active core (represented by a photocurrent generator); the capacitance of the air gap is added in series to the AR. THz radiation is coupled via the inductive antenna. (c) SEM picture (detail) of a single QWP: a $100 \times 100 \mu\text{m}^2$ contact pad permits to wire-bond the device. (d) Array of meta-atom QWPs.

The equivalent circuit of the device is shown in FIG. 4.16(b): the QWIP active core is represented as a (photo)current generator connected, with its series resistance R_{AR} , in parallel to the MSM capacitor C_{AR} . The THz radiation is coupled into the active core through the inductive antenna L_{ant} , which as usual features a series resistance R_{ant} accounting for losses. Finally the air-gap opening in the ground plane features a capacitance C_{gap} in analogy to FIG. 4.14(a).

The ground plane patterning drawn in FIG. 4.16(a) can be modified to implement both individual detectors and arrays of devices. For the single-object configuration, the metal underlying the MSM cavity (marked A in the picture) is shaped as a single metal stripe (width $\approx 8 \mu\text{m}$) terminating on a $100 \times 100 \mu\text{m}^2$ bonding pad; conversely, in the array configuration various metal stripes (connecting tens of devices) are defined to converge to a large bonding pad.

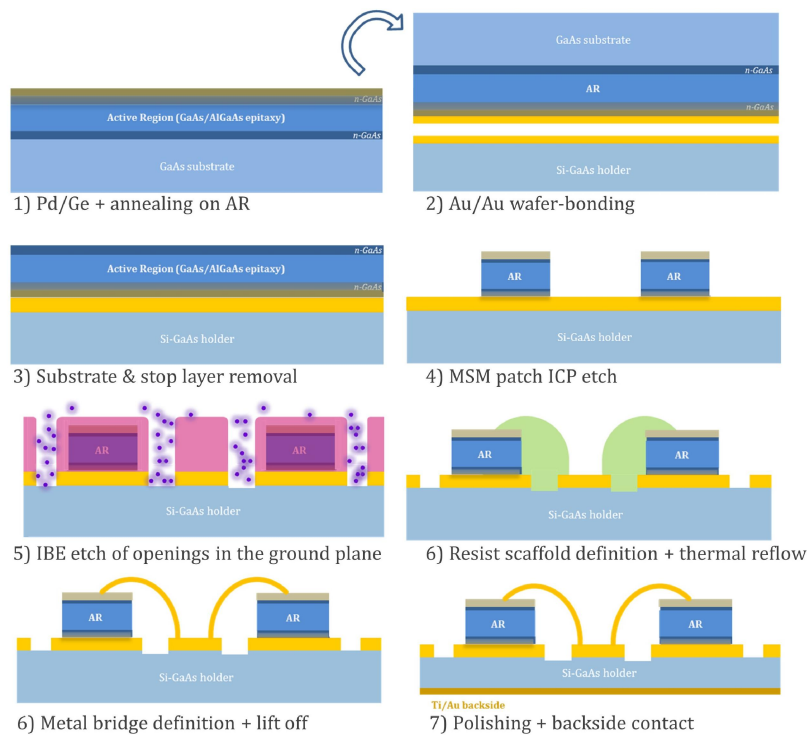


FIG. 4.17 Fabrication steps for the meta-atom THz-QWPs process

In both configurations, the metal domain where the antennas are connected (marked B in the picture) is used as a common ground for all the devices on the same chip. To optimize device packaging and create alternate A-B contact stripes in the array design neighbour rows of devices have been mirrored.

SEM pictures of typical fabricated devices in both single-object and array configurations are shown in FIG. 4.16(c-d).

The detector active region is a copy of the 3 THz QWP V267 design [119] previously tested in the mesa geometry. The new sample (L1258, growth-sheet in Appendix A) has been grown at Leeds University to be processed in metal-metal geometry and features two 100 nm n-GaAs contact layers for a total thickness of $1.58 \mu\text{m}$. The fabrication steps to obtain the final devices are summarized in FIG. 4.17.

The ground plane patterning is enabled by the insertion of an *ion beam etch* (IBE) step in the process: this technology permits to engrave the metal ground regions (and part of the underlying substrate too, see FIG. 4.16(c)) left uncovered by the photoresist mask (previously defined via lithography). All the IBE steps presented in this Chapter were realised with the help of S. Guilet at LPN-CNRS.

Note: in this first design of meta-atom QWIPs, the same narrow ($\approx 2 \mu\text{m}$) air-gap opening shown in FIG. 4.16(c) has been employed. The choice is inspired from the results reported in FIG. 4.14(a) suggesting that narrow openings have minor impact on the absorption at resonance, since less radiation is transmitted into the substrate. In terms of resonant frequency, eigenfrequency simulations reveal that the capacitance provided by such gap opening has a negligible impact on the LC resonance of the circuit, which can therefore be set, as usual, by carefully choosing C_{AR} and L_{ant} . To operate in the QWP detector band (centred around $\approx 3 \text{ THz}$, see FIG. 4.11) the capacitor diameter has been fixed at $d_{AR} = 4 \mu\text{m}$, while for the antenna top length three different values $l_{ant} = 5, 7, 9 \mu\text{m}$ have been explored.

4.3.6 Optical characterization of passive arrays

Prior to electrical and optical characterizations of the meta-atom QWIPs, large arrays ($\approx 3 \times 3 \text{ mm}^2$) of passive devices featuring the same geometric parameters have been fabricated and probed by polarized reflectivity to validate the LC design. A passive undoped GaAs sample of thickness $1.5 \mu\text{m}$ grown by MOCVD (at LPN-CNRS) has been used as active core to reproduce the geometry of the active devices.

In FIG. 4.18(a) a sketch of the experimental configuration used to excite the LC mode is provided. Note: in the array the devices are tightly packed in the y -direction ($p_y = 12 \mu\text{m}$), while they are loosely packed in the x -direction due to the contact lines. Moreover, two lattice periods exist in this direction: $p_{x1} = 30 \mu\text{m}$, for the unit cell containing only one resonator, and $p_{x2} = 60 \mu\text{m}$, for the unit cell containing two mirrored resonators. The passive reflectivity measures are performed at (quasi)normal incidence ($\theta = 15^\circ$ is the minimum allowed by our reflectivity setup), with the magnetic field orthogonal to the antennas to excite a current in the loop (see 2.3.3).

The measured reflectivity spectra (a gold mirror is used for spectra normalization) are reported in FIG. 4.18(b) for the three antenna sizes $l_{ant} = 5, 7, 9 \mu\text{m}$. A resonant mode, identifiable as the LC resonance of the system, is clearly visible around 3 THz . However, looking in detail at the band of interest (right panel) we observe that the mode tuning with the antenna length is very small, contrary to what happens for devices resting on a continuous ground plane. Moreover, the resonant dips have an asymmetric Fano-like shape. To understand the experimental findings, the situation has been reproduced by FEM simulations. In FIG. 4.18(c) the simulated reflectivity spectra of an infinite array of devices with the same specifications of the fabricated ones and excited by a polarized plane wave excitation at normal incidence) is reported. The unit cell of the simulation, shown in the inset of FIG. 4.18(c) has periods p_{x2} and p_y . Interestingly, the same experimental behaviour is found, although the simulated modes are much narrower.

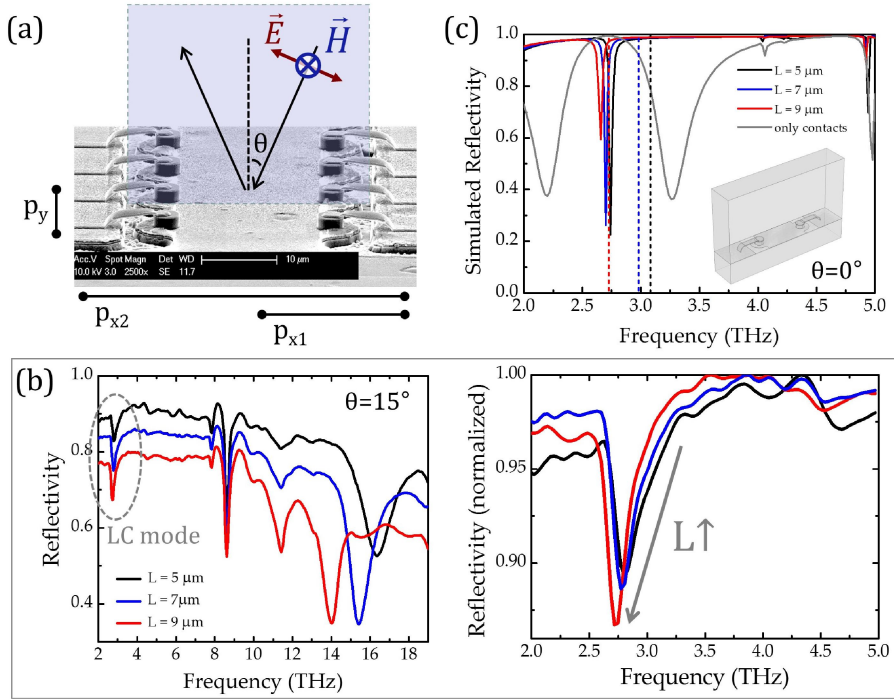


FIG. 4.18(a) Experimental excitation configuration for the LC mode. (b) Reflectivity spectra measured at 15° incidence for the three arrays with $l_{ant} = 5, 7, 9 \mu\text{m}$: (left) overview of the spectra; (right) close-up of the LC resonance identifiable slightly below 3 THz. (c) Simulated reflectivity spectra for infinite arrays with the same specifications. The reflection from the sole contact patterning is also shown. For comparison, the position of the LC mode for the three samples resting on a continuous ground plane is reported (dashed lines).

Furthermore, if the same simulation is carried out closing the ground openings the spectral position of the dips (dashed lines) is different with respect to the previous case and the usual antenna tuning is restored. The behaviour of the system in presence of ground openings can be clarified if we look at the reflectivity spectrum from the sole patterned ground, without MSM capacitor and antenna (grey line in FIG. 4.18(c)): two resonant modes are present at ≈ 2.2 THz and ≈ 3.3 THz, just above the diffraction edges of the two gratings of period p_{x2} ($\lambda_{x2} \approx n \cdot p_{x2} = 216 \mu\text{m}$) and p_{x1} ($\lambda_{x1} \approx n \cdot p_{x1} = 108 \mu\text{m}$) where $n=3.6$ is the GaAs substrate refractive index. The “anomalous” behaviour observed in the spectra of FIG. 4.18(b) can be interpreted as a result of the interaction of the LC resonant mode with the Wood’s anomalies of the two gratings [127], [130].

To further investigate the character of the LC resonance in this complex system, additional simulations have been carried out on a simpler array unit cell: the mirror symmetry along the x-direction has been dropped, and the lattice parameters are $p_x = 25 \mu\text{m}$ and $p_y = 15 \mu\text{m}$. The MSM capacitor has again $d_{AR} = 4 \mu\text{m}$ and the antenna top length is $l_{ant} = 5 \mu\text{m}$. The gold domains (top patch, antenna) are modelled with the dispersive Drude permittivity introduced in 1.3.3, the ground plane is a PEC boundary and the substrate is GaAs with permittivity given by the Lorentz model in 1.3.2. Conversely, the semiconductor filling the MSM patch is modelled with the Drude-Lorentz model (Eq.(1.33)) including a volume doping of 10^{15}cm^{-3} in order to com-

pute dissipation in the active core. The simulation domain is shown in FIG. 4.19(a) for an excitation frequency of 3.2 THz (air box not drawn). The impinging field (at normal incidence) is TM polarized to couple with the antenna magnetic dipole and excites a (quasi)uniform electric field in the MSM capacitor (the z component of the electric field is shown). Also, we observe that THz radiation is transmitted in the substrate due to the ground opening.

FIG. 4.19(b) shows the results obtained from the same simulation run in three different scenarios: (i) the LC resonator over a continuous ground plane; (ii) the experimental device system, featuring the LC resonator coupled to a ground opening; (iii) the previous configuration where the suspended antenna is removed and only the MSM capacitor is left. In the first case the usual sharp reflectivity dip corresponding to the LC mode is observed at ≈ 3.1 THz. In the second case a much smaller resonant dip is visible at ≈ 3.2 THz: this can be again identified as the LC resonance of the system (see the figure inset), modified by the presence of the openings in analogy to FIG. 4.18. Finally, when the antenna is removed no LC resonance is present and the resonant feature in the spectrum can be again identified as the Wood's anomaly of the grating of period p_x ($\lambda_x \approx n \cdot p_x = 90 \mu\text{m}$ i.e. ≈ 3.3 THz).

Moreover, if the power dissipation in the active semiconductor is computed (i.e. the resistive losses) as a function of the excitation frequency a fundamental information can be grasped: the antenna *enables the coupling* of THz radiation in the device active core. From the bottom panel of FIG. 4.19(b) it emerges that no energy is dissipated in the active semiconductor when the antenna is removed.

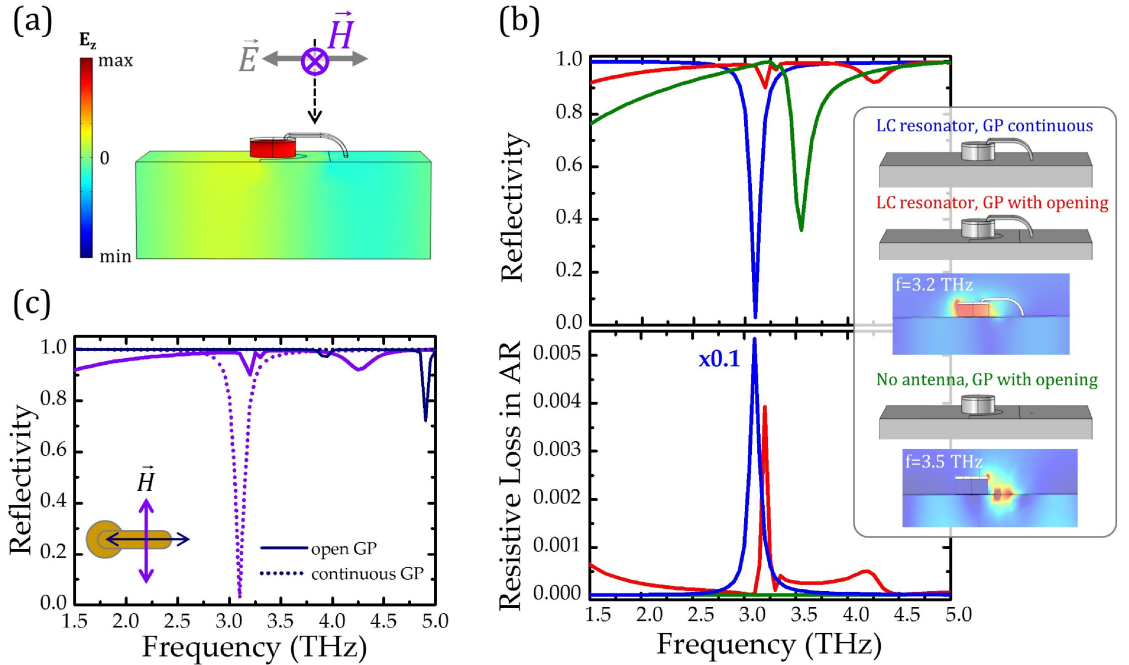


FIG. 4.19(a) Simulation domain used to investigate the resonance of a LC resonator with $d_{AR} = 4 \mu\text{m}$ and $l_{ant} = 5 \mu\text{m}$ with or without ground openings. The E_z field under excitation at $f=3.2$ THz (TM polarization, normal incidence) is shown. (b) Simulated reflectivity and AR resistive losses in the three scenarios sketched in the inset for a resonator: the antenna enables radiation coupling in the active core. (c) System probed under TM and TE polarizations: the LC resonance is only excited when the magnetic field couples to the inductive antenna.

In fact, the MSM capacitor has size much lower than the wavelength of the impinging light and no light can be coupled in it by diffraction.

It is worth noticing that the resistive loss the AR is roughly ten times higher when the ground is continuous than when the opening are introduced. Hence, the introduced electrical injection scheme based on ground openings imposes a price to pay in terms of reduced resonant absorption, since a leaky transmission channel for THz radiation is created. In FIG. 4.19(c) the LC resonance is probed in the scenarios (i) and (ii) under TM and TE polarization. As expected, in both cases, the excitation of the LC resonance around 3 THz is only possible when the magnetic field is orthogonal to the antenna. Note: in the spectrum representing the LC resonator with openings under TE excitation (blue full curve), the Wood's anomaly corresponding to the periodicity in the y-direction is visible at ≈ 5 THz ($\lambda_y \approx n \cdot p_y = 54 \mu\text{m}$).

4.3.7 Electrical characterization. BLIP temperature

After the passive study on “dummy” samples hosting a GaAs core, the active meta-atom THz-QWPs endowed with the L1258 sample have been characterized.

Current-voltage (I-V) characteristics have been measured for several meta-atom QWIPs in both single-object and array (25x12=300 devices connected in parallel) configurations. I-V curves for a representative sample featuring $l_{ant} = 5 \mu\text{m}$ are reported in FIG. 4.20 (left panel: array; right panel: single device) for different temperatures (4.5, 6, 7, 8, 9, 10, 11, 12, 15 K). As illustrated in 4.2.3, the sample is mounted on the cold finger of a continuous flow helium-filled cryostat. For dark current measures, the detector is completely surrounded by a metal cryoshield which is cooled down together with the detector. For the I-V characteristics under a 300 K background illumination, an opening is uncovered in the cryoshield which provides a 48° FOV over a calibrated 300 K blackbody placed on the cryostat window (see FIG. 4.9). Note: the I-Vs are asymmetric under forward and reverse bias because of the Schottky barrier of the top nGaAs/Ti/Au contact. The measured current densities are also reported (right axis) taking into account the effective active area of each device (for the single meta-atom $A_{single} = \pi \cdot (2\mu\text{m})^2$; for the array $A_{array} = 300 \cdot A_{single}$). Note that the LC meta-atom design permits to reduce the active semiconductor area of a factor $\approx 10^2$ for the meta-atom array and of a factor $\approx 10^4$ for the individual meta-atom. This causes a drastic reduction of the dark current, without damaging the device functionalities.

The BLIP temperature was estimated by comparing I-V curves under dark and 300 K blackbody illumination (FOV=48°). The ratio 300K blackbody-to-dark current I_{300K} / I_{dark} as a function of the applied bias and of the temperature for both the array and single devices are reported in the bottom panel of FIG. 4.20. Since T_{BLIP} is defined as the temperature at which background current equals dark current ($I_{back} = I_{dark}$), the system reaches the BLIP condition when the measured current under 300 K illumination is $I_{300K} = I_{dark} + I_{back} = 2I_{dark}$, i.e. when $I_{300K} / I_{dark} = 2$. From FIG. 4.20 we estimate $T_{BLIP} \approx 8$ K. This value is lower than the value $T_{BLIP} = 12$ K reported for the original V267 structure published in Ref.[119]. Note however that this value may be affected

from the experimental setup. For instance, the position of the thermocouple used to read the temperature on the cryostat respect to the sample can introduce a systematic error $\Delta T \approx 1-2$ K. Furthermore, the sample growth conditions can affect thermal performance. Supplementary calibrated measures have to be performed to confirm this first estimate.

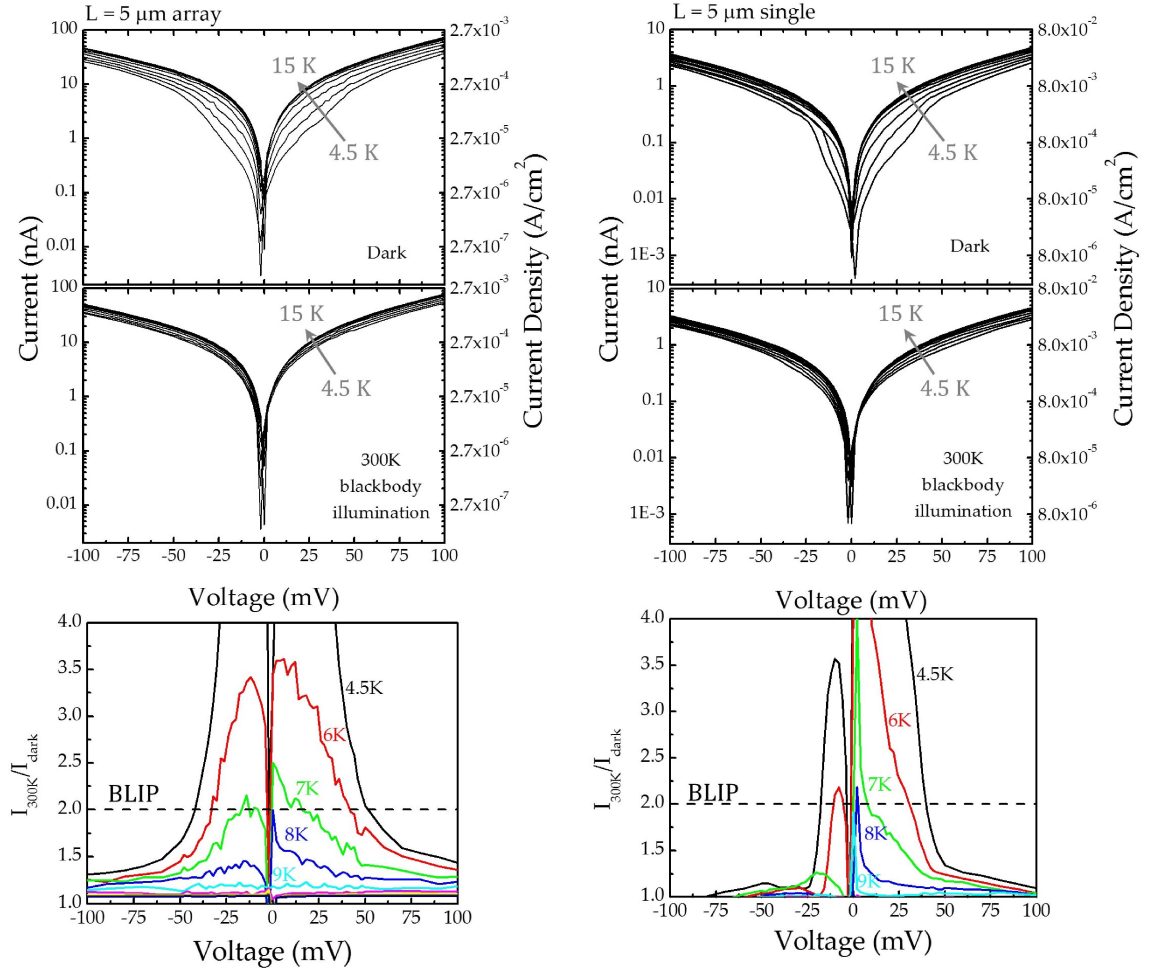


FIG. 4.20 I-V characteristics under dark and 300 K background illumination for a typical meta-atom QWP: (left) array; (right) single-object configuration. The BLIP condition is reached when the ratio $I_{back}/I_{dark} = 2$ (dashed line).

4.3.8 Photocurrent spectra

The photocurrent spectra from the meta-atom detectors have been acquired with the FTIR operated in rapid scan modulation with the setup described in 4.2.3. The Hg lamp is used as broadband source and the devices are kept at $T=4.5$ K. The array devices have been tested under 50 mV bias so that a good current level is ensured whilst operating under BLIP condition. The trans-impedance amplification for the array devices is 2 or 10 nA/V.

FIG. 4.21(a) reports the photocurrent spectra for the $l_{ant}=5$ μm array and single device tested above under normal incidence illumination. In particular, the role of the

impinging THz radiation is investigated: a sharp detection peak is observed around 3 THz for unpolarized and TM-polarized radiation, while a weak photocurrent signal is measured for TE polarized light. The TM/TE peak photocurrent ratio is ≈ 7 . Note: the spectra corresponding to TM and TE polarizations have been normalized over the response of the polyethylene polarizer.

This results confirms what expected from FIG. 4.19(c) owing to the excitation rule of the LC resonance under normal incidence. The residual TE coupling may be explained recalling that the electric dipole coupling emerges when $\theta \neq 0$ (see 2.3.5). Hence, a non-perfect sample alignment and the numerical aperture of the focusing lens ($N.A \approx 0.45$, i.e. acceptance angle $\approx 14^\circ$) can provide a non-zero TM component. Furthermore, the measured detection bandwidth is much larger (2-4 THz) than what expected from measures and simulations on passive devices discussed in paragraph 4.3.6.

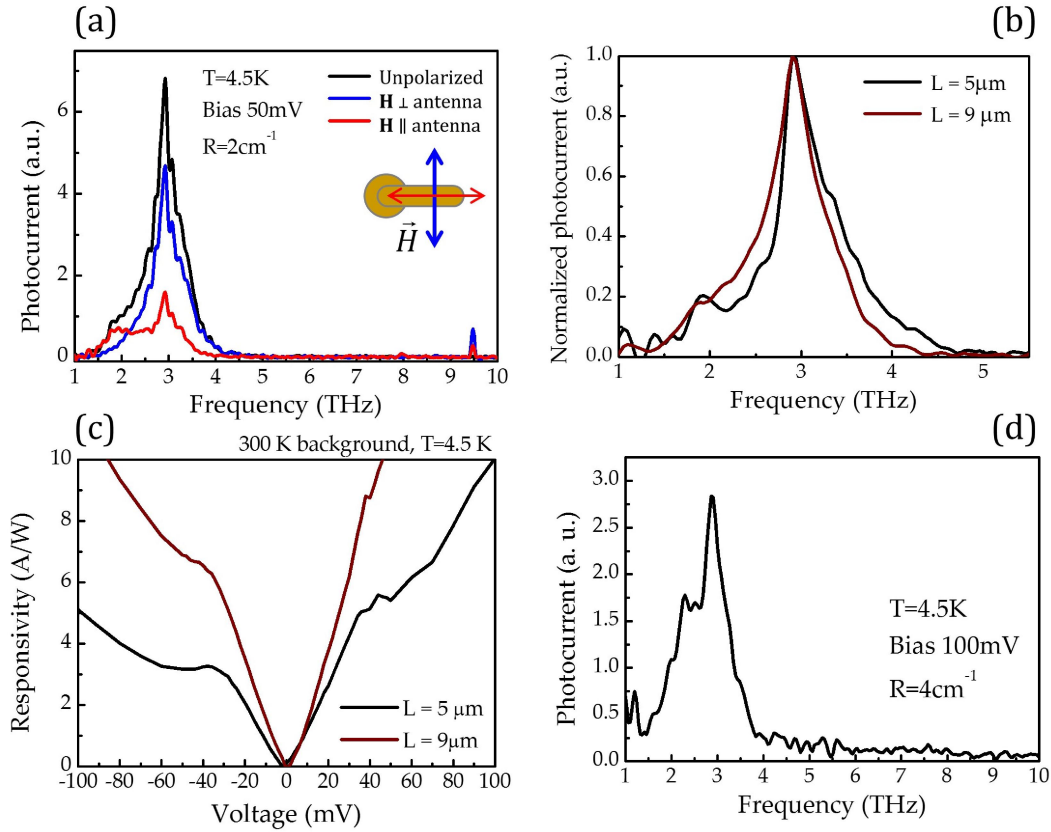


FIG. 4.21(a) Photocurrent spectra for a meta-atom QWP array ($l_{ant} = 5 \mu\text{m}$) under normal incidence illumination with unpolarised and polarized THz radiation. (b) Normalized photocurrent spectra from two arrays of different antenna lengths ($l_{ant} = 5 \mu\text{m}$ and $9 \mu\text{m}$). (c) Calculated responsivity as a function of the bias for the two arrays. (d) Photocurrent spectrum of a single QWP meta-atom with $l_{ant} = 5 \mu\text{m}$.

In FIG. 4.21(b) the (normalized) photocurrent spectra from two arrays of different antenna lengths ($l_{ant} = 5 \mu\text{m}$ and $l_{ant} = 9 \mu\text{m}$) are reported. Similarly to the reflectivity spectra of FIG. 4.18, the detection peak stays roughly in the same position, whilst the “body” of the spectrum is slightly redshifted for the device featuring the longer antennas (i.e. higher inductance). This agrees to what expected for the LC mode tuning.

In FIG. 4.21(c) the responsivity defined as the ratio of the photocurrent to the incident power $\mathfrak{R} = I_{photo} / P_{inc}$ (see definition in 4.1.2) has been calculated for the two array devices. The photocurrent is derived from the I-Vs under 300 K background illumination and dark as $I_{photo} = I_{300K} - I_{dark}$. The incident power impinging on the sample from the “hot” opening in the cryoshield has been estimated using Planck's law of black-body radiation, yielding an incident power $P_{inc} \approx 1.6$ nW.

The estimated values of responsivity ($\mathfrak{R} \approx 10$ A/W at 100 mV bias) are compatible with the reported responsivity for the original structure [119] and recent reported values for arrays of patch antennas [121]. Currently, the same sample L1258 is being processed in mesa geometry to allow a comparison with the responsivity values reported above.

Finally, in FIG. 4.21(d) a typical photocurrent spectrum for a single meta-atom QWP ($l_{ant} = 5$ μm) is reported. Here, a bias of 100 mV is used to extract a readable signal and the trans-impedance amplification is 500 pA/V. Moreover, the spectrum is averaged over 6 measures (100 scans are made for each measure) in order to improve the SNR. The same sharp resonant peak observed in the array configuration can be identified for the single-object configuration.

We have realized a THz QWP device featuring a 8×10^4 smaller active surface than a standard 1 mm² mesa, with fully preserved functionalities and ultra-small dark currents (< 1 nA). The active semiconductor core has a volume of only ≈ 20 μm^3 , which yields an effective volume $V_{eff} = 7 \times 10^{-3} (\lambda/2 \cdot n_{eff})^3$. The overall detector dimension (MSM active capacitor and coupling inductive antenna, excluded contact pads) is $\approx \lambda_{eff}/10$. To the best of our knowledge, this is the first work where active optoelectronic meta-atoms operating as electrically injected quantum detectors down to the single-object level are demonstrated.

Currently, further systematic measures are being carried out on single and array detectors to recover, for instance, the detection angular pattern. Also, the device maximum modulation speed is being investigated.

Furthermore, a new design for electric contacts is being explored to overcome the limitations in the resonance tuning due to the grating Wood's anomalies interacting with the LC mode.

On the other side, the compactness of the detector could be sacrificed to some extent in the future to improve the photon collection. Indeed, the radiation capture area (aka antenna aperture) of a subwavelength inductive loop is small if compared with standard $\lambda/2$ or bigger antennas [34]. In perspective, one could go beyond the subwavelength LC resonators explored in this thesis and try different wavelength-scale antenna geometry taking advantage of the vast experience of RF and MW engineering. In this scenario the idea is to exploit an antenna as an “extreme optical concentrator” thanks to high field enhancement attainable between two metal tips. In such hotspot an even smaller semiconductor core can be placed, as now the light capture and conversion is completely realised on the antenna body.

Well-known design such as logarithmic, spiral and bowtie antennas have already been successfully employed in the MIR and THz range to couple light within micro bolometer [131] or graphene phototransistors [132].

5 Towards the THz “nano” laser: AR size reduction and loss engineering

Since the first demonstration of semiconductor lasers, one of the main goals has been shrinking their size. Three major benefits related to small dimensions have been predicted: integration density, low power dissipation and high operational speed. Today the ultimate challenge is making lasers of size comparable with electronic devices, overcoming the restrictions imposed by the diffraction limit.

In the first part of the chapter we will discuss the main issues involved in laser miniaturization and review recent advances in the field. Later, reduced-size THz active regions are tested envisioning their integration in the sub- λ resonators developed previously. The core of the chapter deals with loss engineering of THz metal-semiconductor-metal resonators. A novel design inspired from RF cavities is explored to realize ultra-small lasers in the THz range.

5.1 Laser miniaturization

5.1.1 Round trip model for the laser threshold

In this paragraph a simplified laser model is presented to point out important physical parameters involved in the challenge of laser miniaturization [133]. Consider a laser resonator (a Fabry–Pérot cavity for the sake of simplicity) of length L , with mirror reflectivities R_1 and R_2 . Let’s call λ_0 the free-space wavelength of the propagating wave, n the modal effective index and α_w the waveguide losses. From the well-known laser round-trip model lasing sets in when the electric field amplitude at an arbitrary point in the cavity E_0 returns to its original value after a round-trip [133], [134]

$$E_0 \sqrt{R_1 R_2} e^{(G_m - \alpha_w)L} e^{i4\pi n L / \lambda_0} = E_0 \quad (5.1)$$

where G_m is the mode optical gain. Requiring the complex exponential to be one yields the condition on the cavity length

$$L = \frac{\lambda_0}{2n} m \quad (5.2)$$

where m is an integer. This condition means that only a mode featuring a whole number of half-oscillations of the electric field can be housed in the cavity. The shortest possible cavity is $\lambda_0 / 2n$ ($m=1$) as imposed by the diffraction limit for purely photonic resonators.

The condition on the field amplitude provides instead the lasing threshold. First, we relate the modal gain G_m to the material gain of the active region G_{AR} using the confinement factor Γ (defined as in Eq.(3.9)) which quantifies the fractional overlap of the laser mode volume V_0 with the volume of the active region V_{AR}

$$G_m = \Gamma G_{AR} \quad (5.3)$$

The mirror losses can be written as:

$$\alpha_m = -\frac{\ln(R_1 R_2)}{2L}. \quad (5.4)$$

We recover the laser threshold condition

$$\Gamma G_{AR} = \alpha_{tot} \quad (5.5)$$

where $\alpha_{tot} = \alpha_w + \alpha_m$ are the cavity total losses. From (5.5) we note that the relevant figure of merit to engineer a generic laser resonator is α_{tot} / Γ : the smaller this value, the easier is to achieve lasing for a given active region.

When dealing with laser miniaturization one is often interested in employing *localized modes* rather than propagating modes, as it is the case for our subwavelength THz resonators. In this case the spatial loss α_{tot} can be expressed as a function of the total quality factor Q_{tot} the cavity via the relation

$$\alpha_{tot} = \frac{2\pi n}{\lambda_0 Q_{tot}} \quad (5.6)$$

The definition of Q_{tot} and how to calculate it for a THz micro-cavity will be discussed in the next section. Note: the Γ factor, defined as an *energy confinement factor*, can be evaluated for both localized and propagating modes. Thus, the key parameters and concepts of the round-trip laser model remains generally valid and useful to compare different classes of laser resonators.

5.1.2 State of art of “nano-lasers”

As a general rule of thumb, choosing the appropriate resonator for a laser means finding a trade-off between the parameters V_{AR} , Γ and α_{tot} , which in general depends on the application. When dealing with laser miniaturization the main question is how much the device volume can be shrunk without losing the stimulated emission. Does a limit exist? If yes, it is of fundamental or practical nature?

Owing to the diffraction limit, it is impossible to confine an electromagnetic mode in a dielectric domain of volume smaller than $(\lambda / 2n)^3$.

A size reduction in (at least) one dimension is possible shifting from all-dielectric to metal-dielectric resonators. For example, in the NIR and VIS ranges, the optical field can be coupled to oscillation of free carriers in the metal: SPP modes (see 1.3.4) provide electromagnetic confinement beyond the diffraction limit. Moreover, in the MIR

and THz range the MSM geometry inspired from TEM lines naturally provides a strong vertical confinement well below the diffraction limit. Nevertheless, we saw in 2.1.4 that the lateral size of MSM patch resonators is limited to $\lambda_{eff}/2$ in at least one direction.

In the following we will review the research advances on small lasers following [133]. We recall that all the “small” or “nano” sources claimed so far have one feature in common: their critical dimension is $\lambda/2n$ in at least one dimension. In FIG. 5.1(a) the development timeline of small lasers is sketched.

The first milestone in the quest for small lasers has been the invention of the *VCSEL*, associating low material losses with very high reflectivity Bragg mirrors [135]. VCSELs cavities provide low α_{tot}/Γ thus enabling a great reduction of the active volume V_{AR} . In the 90s, *microdisk lasers* based on whispering-gallery modes on a thin semiconductor disk appeared [136]. Small current threshold have been demonstrated thanks to very high Q and small AR volumes obtainable with these devices.

Later *photonic crystals* have been explored as laser cavities. Typically 2D or 3D Bragg gratings are used to confine light in diffraction-limited volumes [137]. The great advantage of photonic crystals is the possibility to freely engineer the beam shape and the losses playing on different parameters. Q factors as high as tens of thousands have been reported for dielectric structures.

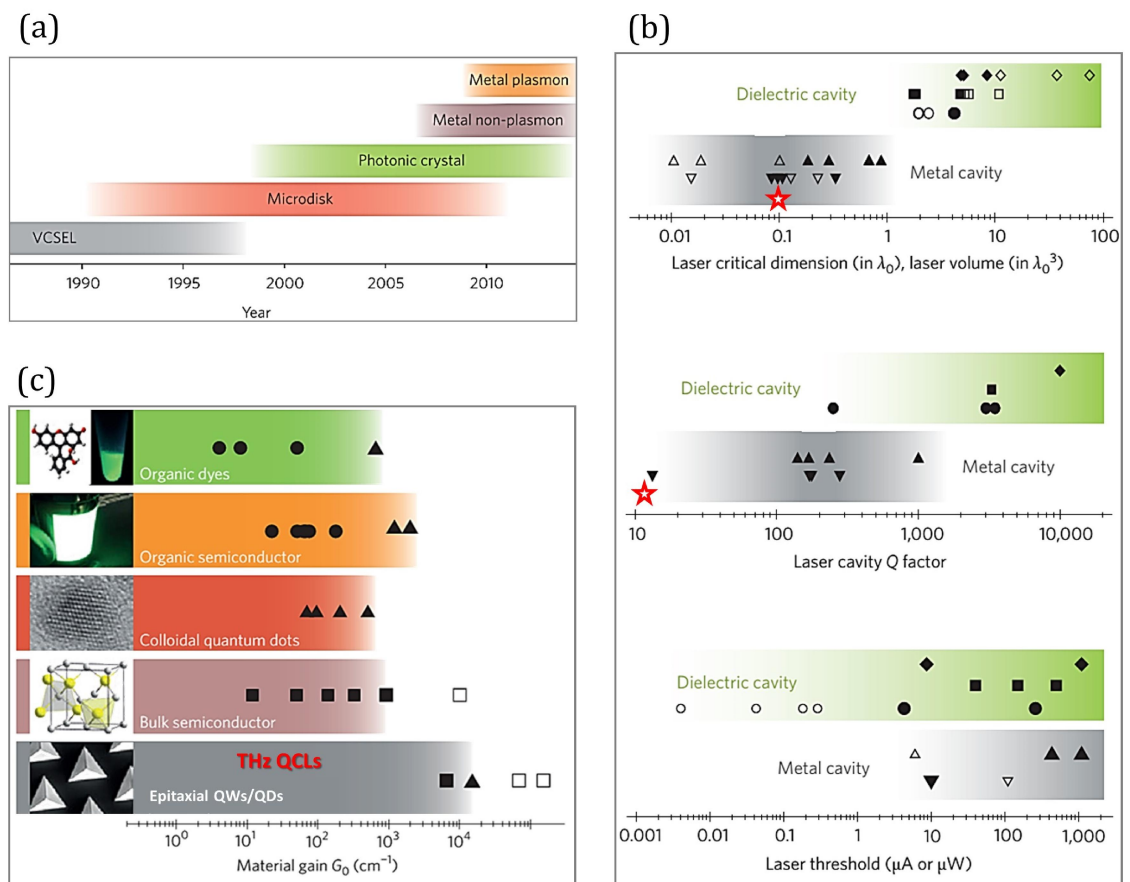


FIG. 5.1(a) Small lasers development timeline. (b) State of art of “nano” lasers classified in terms of subwavelength confinement, Q factor and laser thresholds. Red stars signal the sub- λ THz resonators developed in Chapter 2. (c) Gain provided by actually known materials. The figure is taken from Hill and Gather review [133].

In the late 2000s research has shifted towards small lasers based on *metal cavities*. Due to huge losses in metals, the achievable Q factors are dramatically reduced respect to dielectric materials, reaching the order of 100 in the best case (FIG. 5.1(b)). Despite this fact, metals are useful as they provide good heat-sinking and ease the integration of electrical contacts. In the THz range, metallic photonic crystal structures have proved successful for beam shaping and power extraction[63], [124], [138]. Micro or nano patch resonators have been widely explored as cavities for small semiconductor lasers [139], [140]. Remarkably, a microstrip geometry has been successfully exploited to demonstrate an ultra-low volume THz QCL [141]. Furthermore metal nanocavities mimicking RF resonant cavities (e.g. the microwave oven) have been exploited to enhance Γ and thus reduce V_{AR} at the price of increased metal losses. This issue is well known when comparing the 1D confinement provided by a microstrip waveguide and a single-plasmon waveguide for QCLs. Successful “nano-lasers” featuring a metal-encapsulated high-gain material in the NIR range have been reported [142], [143]. The resonant modes exploited in these structures are not, strictly speaking, plasmonic modes (“non plasmon” label in FIG. 5.1(a)) but true cavity modes where the electromagnetic field is squeezed between metallic walls. As a consequence, non-plasmon resonators are still diffraction-limited in at least one dimension.

5.1.3 Lasing on a subwavelength mode comes at a price

The first proposal of a truly subwavelength laser in three dimensions has been published in 2003 [144]. This object, called “spaser” (for *surface plasmon amplification by stimulated emission of radiation*) consists of a metallic plasmonic nanoparticle surrounded by a gain medium. Since then, research efforts have been spent to pursue this “holy grail” of plasmonics. The quest was motivated by some initial calculations predicting reasonable values for the gain needed to achieve lasing. Up to now, however, only one claim about an optically pumped spaser-like device has been reported. An electrically pumped, truly subwavelength coherent source has not been demonstrated yet.

As a matter of fact, the pursuit of a truly subwavelength coherent source must face huge metal losses and poor confinement factors, i.e. very high α_{tot} / Γ values. In particular when operating on a rigorously 3D sub- λ mode in the properly called plasmonic regime ($\omega > \gamma_{met}$, see 2.2.3), the mode damping is intrinsically dominated by the metal scattering rate ($\gamma_{tot} \approx \gamma_{met}$). This always yields $Q \approx 10$ or less independently of the resonator details. On the other side, Q factors as high as 100 have been reported for metallic cavities where at least one dimension is comparable with the wavelength (FIG. 5.1(b)). These concepts have been brilliantly explored by J. Khurgin in a series of recent papers [57], [145], [146]. It has been demonstrated, for example, that the lowest possible threshold current for a truly sub-lambda plasmonic laser ultimately depends on the free carriers scattering rate in the metal γ_m , as $I_{th} \approx e\gamma_m$. For

noble metals $\gamma_m \approx 10^{14} \text{ s}^{-1}$ which yields current densities exceeding 1 MA/cm^2 for active volumes less than $(\lambda/2n)^3$ [145]. One would then need a material gain larger than 10^5 cm^{-1} to compensate those losses. The goal seems unattainable with current laser gain materials as we can see from FIG. 5.1(c). Indeed, scepticism is growing in the scientific community about the feasibility and especially the practicality of this elusive coherent source.

In this scenario, we note that at THz frequencies electron kinetic inductance is not dominant yet (see 2.2.4). The THz range is therefore the best one to explore lasing from subwavelength modes as we operate in the electronic rather than in the plasmonic regime. As a consequence, it is possible to optimize α_{tot} / Γ in the THz regime even for a subwavelength mode, similarly to what is done in RF electronics to reduce losses in the circuitual elements due to the skin-depth effect [147]. The main limitation in the THz range seems more practical than fundamental, as one still needs a high material gain to compensate the losses. Since their first demonstration, terahertz quantum cascade lasers (THz QCLs) have improved constantly their performances but still they provide relatively low material gains if compared with materials available in other frequency domains [6], [148].

5.2 Size reduction of THz QCLs active regions

From the discussion above, the first key ingredient to realize a small laser is a performing gain material. In the THz range the best gain materials available are the epitaxial GaAs/AlGaAs heterostructures which constitute the backbone of THz QCLs. Standard THz QCL active regions (ARs) are normally $\approx 10 \text{ }\mu\text{m}$ -thick, a compromise between the number of cascading stages and growth time. Envisioning the integration of these gain media into the subwavelength resonators developed so far, a vertical size reduction is desirable. Moreover, particularly performing ARs are needed to compensate losses in small volume resonators.

5.2.1 Characterization of 6 μm -thick THz QCL active regions

Recently, a systematic study on the size reduction of THz QCLs employing metal-metal waveguides have been carried in our team [149], [150]. The strong vertical mode confinement in metal-metal waveguides permits to reduce to a minimum the AR thickness without sacrificing the confinement factor, which remains close to unity. It has been shown that it is possible to reduce the AR thickness of a THz QCL far below the effective wavelength at the price of a small increase of the threshold current density J_{th} .

For our scopes, two different THz active regions have been tested in a reduced-thickness version. An AR thickness of $6 \text{ }\mu\text{m}$ has been chosen as a compromise between vertical subwavelength confinement and number of cascade stages. The first design (sample L1032) features a bound-to-continuum transition with a one-well in-

jector, which has been proven relatively powerful [123]. The second design (sample L1187) is based on alternating photon and longitudinal optical (LO) phonon-assisted transitions between quasi-minibands, yielding low threshold current densities and low operating voltages [151]. Both samples have been grown by MBE at Leeds University, processed into standard metal-metal ridge resonators, indium soldered up onto copper mounts, wire bonded, and mounted into a cryostat for electrical and optical characterization. Devices were operated in pulsed mode at 33 kHz with 300 ns current pulses (1% duty cycle). V-J and L-J curves for two typical ridges are shown in FIG. 5.2(a). Sample L1032 exhibits $J_{th}=0.2\text{kA/cm}^2$ (at 10K) and operation above 78K while L1187 has a lower threshold $J_{th}=0.16\text{kA/cm}^2$ (at 8K) and a maximum operation temperature $T_{max} = 123\text{K}$. The emission frequency is around 2.9 THz for both devices as shown in the spectra of FIG. 5.2(b) acquired with the FTIR spectrometer using the internal DTGS detector. Remarkably, both designs do not show significant performance degradation with respect to their original counterparts ($t_{AR}\approx 10\text{ }\mu\text{m}$) and may be adequate for future integration in subwavelength resonators.

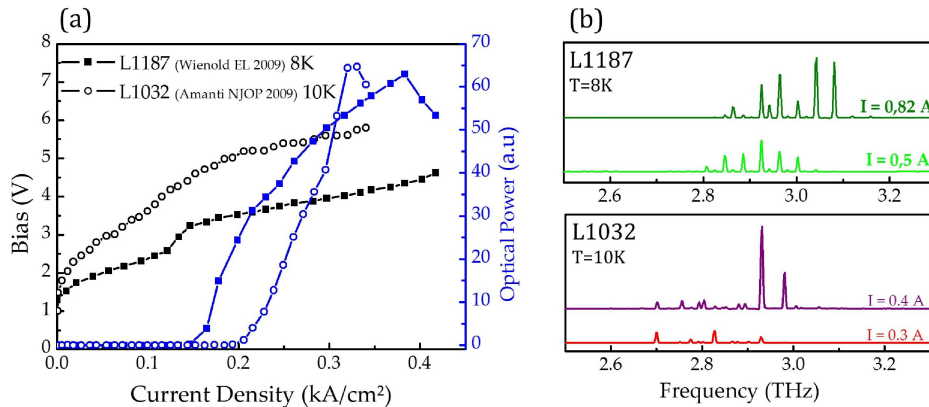


FIG. 5.2(a) V-J and L-J characteristics for L1187 and L1032 samples in standard metal-metal waveguides. (b) Emission spectra for different injected currents.

5.2.2 Conception of a lateral bottom injection scheme compatible with a split-ring geometry

The issue of electrical injection in a split-ring geometry has been already discussed in Chapter 4, where introducing small openings in the ground plane has enabled the demonstration of subwavelength QW detectors. Here an alternative injection scheme is tested to avoid the complications coming from the previous contact geometry. The concept is sketched in the top panel of FIG. 5.3(a): the active core is electrically pumped laterally, exploiting an insulating layer that separates the contact from the bottom ground plane (serving as second contact). As a preliminary demonstration, we fabricated THz ridge lasers featuring this lateral injection scheme on sample L1032. Note: an insulating layer has to be deposited on the epitaxial sample before the standard Au-Au wafer-bonding. In this demonstration a 300nm-thick SiO₂ layer grown by PECVD has been used. After substrate and stop-layer removal, the sample has been patterned by wet etching into laser ridges, carefully stopping the attack into

the bottom n-GaAs contact layer. Annealed Ni/Ge/Au/Ni/Au and non-annealed Ti/Au contacts have been defined respectively on the bottom and top surfaces. The final result is shown in the bottom panel of FIG. 5.3(a). The measured L-I-V characteristics for the new injection scheme and the standard metal-metal configuration are reported in FIG. 5.3(b). From the comparison we observe that the lateral injection scheme works properly and, importantly, does not harper nor destroy the device performances. This technology constitutes an important element to be added in the THz “nano” laser toolbox we are building.

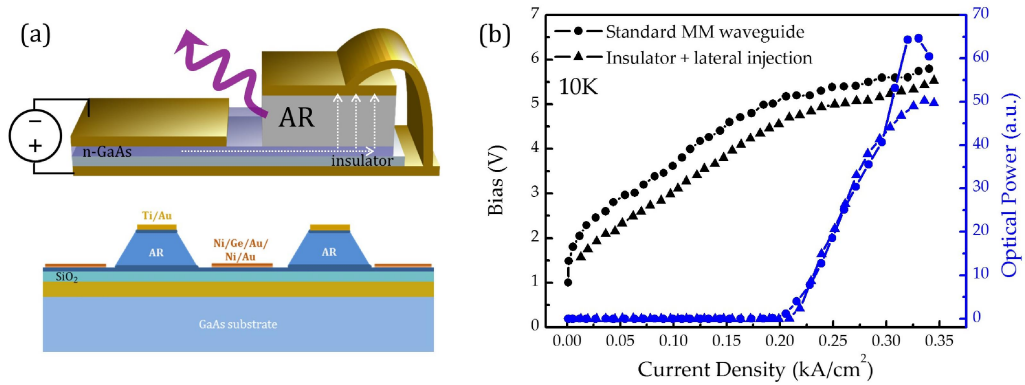


FIG. 5.3(a) Top: sketch of a subwavelength LC resonator featuring a lateral injection scheme. Bottom: fabrication scheme of THz metal-metal ridges resting on a SiO₂ insulating layer and electrically pumped from a lateral contact. (b) Comparison of L-I-V curves for a standard MM ridge and the new lateral injection scheme (sample L1032)

5.3 Loss engineering of THz micro-resonators

5.3.1 Resonator Quality factor

In a generic electronic or photonic resonator, some of the electromagnetic energy oscillating back and forth between the electric and magnetic fields is dissipated either as heat and/or as free space radiation escaping the system.

The figure of merit used to quantify the ability of a generic resonator to store energy is the quality factor (Q factor) which is defined as the ratio of the energy stored to the energy dissipated per cycle, in symbols

$$Q = \left[\frac{\omega W_{\max}}{P_d} \right]_{\omega=\omega_0} \tag{5.7}$$

where W_{\max} is the maximum (peak) energy stored and P_d is the average power dissipated at resonance.

The quality factor provides information about the loss mechanisms within a resonator or antenna. Typically we deal with radiation, ohmic (conduction) and dielectric

losses. The total quality factor is influenced by all of these contributions and is generally written as

$$\frac{1}{Q_{tot}} = \frac{1}{Q_{rad}} + \frac{1}{Q_{ohm}} + \frac{1}{Q_{diel}} \quad (5.8)$$

where Q_{tot} is the total quality factor, Q_{rad} is the quality factor due to free space radiation losses, Q_{ohm} is the quality factor due to ohmic (conduction) losses and Q_{diel} is the quality factor due to dielectric losses. The fractional bandwidth of the antenna is inversely proportional to the Q_{tot} of the antenna:

$$\frac{\Delta f}{f_0} = \frac{1}{Q_{tot}} = \gamma_{tot} \quad (5.9)$$

This formula is commonly employed to evaluate the experimental Q factor of a resonator/antenna. Experimentally one has access to the FWHM of the resonant mode (e.g. from a reflectivity spectrum) which is related to the total loss rate γ_{tot} of the cavity. Note: formula (5.9) is approximated as it does not account for the impedance mismatch between the antenna and the external transmission line to which it is connected. In other words: the system used to measure the antenna bandwidth might induce coupling losses that result in a lower Q factor [31], [34].

5.3.2 Lossy eigenvalue analysis for Q factor calculation

As discussed in Chapter 2 the primary goal of a FEM eigenfrequency analysis is to find the eigenmodes of an electromagnetic resonator solving the Helmholtz equation. These solutions are real valued when ideal (lossless) materials are used in a closed simulation domain: energy is conserved and there is no dissipation.

If the analysis involves some material loss (i.e. a nonzero imaginary part in the materials dielectric function) and/or an open boundary the calculated eigenvalues are complex numbers in the form $\tilde{\nu} = \nu + j\delta$, where ν is the eigenfrequency and δ is the mode damping. The mode quality factor (Q factor) is then defined as:

$$Q = \frac{\text{Re}(\tilde{\nu})}{2|\text{Im}(\tilde{\nu})|} = \frac{\nu}{2|\delta|} \quad (5.10)$$

The advantage of including those losses is that an analysis with proper materials modelling allows one to quantify the impact of the different loss mechanisms. In other words ohmic losses (γ_{ohm}), dielectric losses (γ_{diel}) and radiation losses (γ_{rad}) can be derived independently, contrary to what is done experimentally.

Ohmic losses can be computed with an eigenfrequency analysis where the metal domains are characterized by the complex dielectric constant introduced in 1.3.3 at the operating frequency. For gold, the Drude-Lorentz fit parameters are obtained from experimental datas of Ref.[27]. If the simulation domain is closed (for example with a

PEC boundary), energy can only be lost via resistive dissipation in the metal so the model yields the ohmic quality factor (Q_{ohm}).

Note: simulating real metal domains can be demanding in terms of computation time since a spatially fine mesh is necessary to match the metal skin depth. Luckily when the characteristic size of the metal domain (i.e. the thickness of the thinnest part of the object being simulated) is larger than the skin depth, we can assume that the currents flow on the surface only. Under this hypothesis, we can exclude the metallic domains from the calculation and use instead an *impedance boundary condition*, assuming that EM waves do not penetrate into the object and the currents flow entirely on the surface. This is a valid assumption for THz resonators: for example the skin depth of gold at 3 THz is approximately ≈ 45 nm and we normally deal with metallic layers 200-300 nm-thick.

The radiative losses can be separately computed running an identical simulation where the metal domains are modelled as ideal lossless conductors using PEC boundaries. The simulation domain is truncated with a surface mimicking an open boundary from which energy can escape as free propagating waves. *Perfectly matched layer* (PMLs) are appropriate here to mimic open boundaries. Note: for an eigenvalue analysis the wavelength dependence is dropped from the coordinate transformation defining each PML. As a consequence, one has to introduce a scaling factor of the order of the operating wavelength to make the PMLs work correctly. For THz micro-resonators operating on a ground plane, a hemi-spherical PML shell is defined to enclose the device.

Finally a simulation to compute the total quality factor (Q_{tot}) can be performed if both lossy metal domains and absorbing PML boundaries are employed.

It is therefore possible to explore a vast range of device parameters to engineer and optimize the Q factors of a resonator to match a desired application.

5.3.3 Patch antennas operating around 3 THz

To validate that FEM simulations we estimated the Q factors of a standard patch antenna, that can be used as testbed. We consider a circular patch of diameter d and thickness h . For this kind of antenna, assuming thin dielectric cores ($h \ll \lambda_0$) approximate formulas exist for the various Q factors [34]

$$Q_{rad} = \frac{2\omega\epsilon_r(d/2)^2}{hG_{rad}} \quad (5.11)$$

$$Q_{ohm} = h\sqrt{\omega\mu_0\sigma/2} = h/\delta_d \quad (5.12)$$

$$Q_{diel} = \frac{1}{\tan(\delta)} \quad (5.13)$$

where G_{rad} is the radiation conductance of the radiating slot, σ is the conductivity of the patch and ground plane metal, δ_d is the metal skin depth and $\tan(\delta)$ is the loss tangent of the dielectric core.

Note: for undoped GaAs the loss tangent is $\tan(\delta) = \text{Im}(\epsilon_d) / \text{Re}(\epsilon_d) \approx 0.0007$ at 3 THz so that the dielectric losses are, as a first approximation, negligible when interested in a preliminary resonator design.

In FIG. 5.4(a) a schematics (not to scale) of a FEM lossy eigenvalue analysis is shown. The antenna lies on a metal ground plane (not shown). The top patch metal ($h_{top}=500$ nm) and ground plane are modelled either as PEC or gold ($\epsilon_{Au} = -9.2 \cdot 10^4 - j2 \cdot 10^5$ at 3 THz [27]). The dielectric core is set as lossless GaAs with a real valued permittivity ($\epsilon_{GaAs} = 13.1$).

A first study is carried out setting the patch diameter to $d_{patch}=15 \mu\text{m}$ to operate on the fundamental TM_{110} mode around 3 THz and varying the patch thickness h . FIG. 5.4(b) summarizes the results for Q_{rad} , Q_{ohm} and Q_{tot} obtained running three distinct simulations as a function of h .

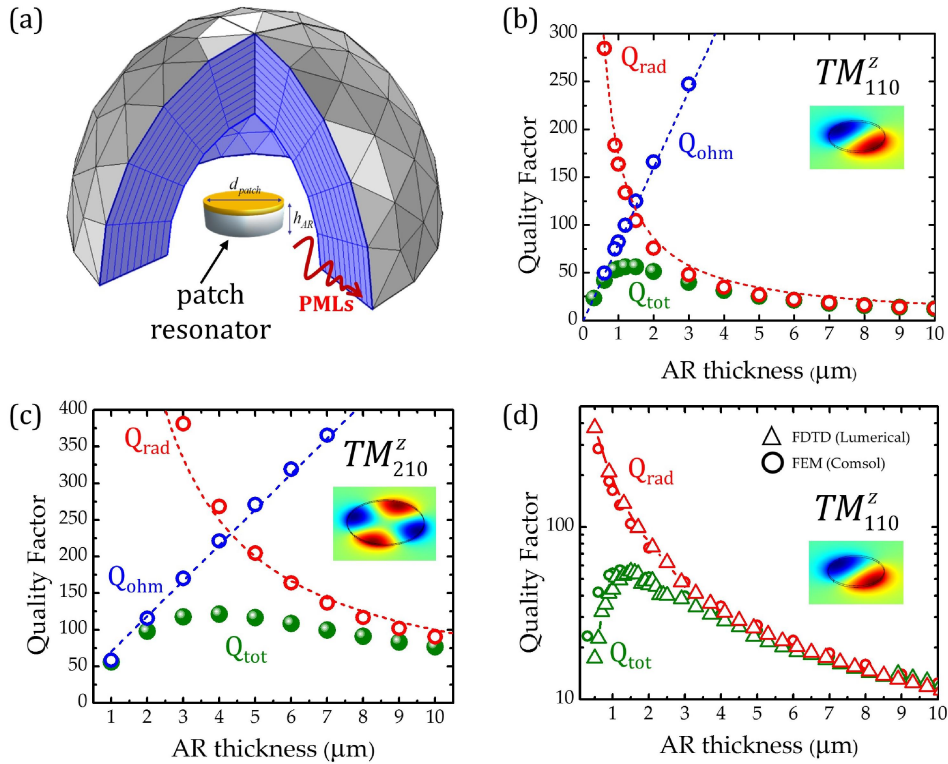


FIG. 5.4(a) Schematics of fem lossy eigenvalue analysis. (b) Q_{rad} , Q_{ohm} and Q_{tot} as a function of the AR thickness for a patch antenna operating at 3 THz on the TM_{110} mode. The best fit curves $Q_{rad}=1.73e-4/h$ (red dashed) and $Q_{ohm}=8e7/h$ (blue dashed) are reported. (c) Q_{rad} , Q_{ohm} and Q_{tot} as a function of the AR thickness for a patch antenna operating at 3 THz on the TM_{210} mode. The best fit curves $Q_{rad}=1e-3/h$ (red dashed) and $Q_{ohm}=5.2e7/h$ (blue dashed) are reported. (d) Q calculation comparison between FEM and FDTD simulations (TM_{110} mode)

As predicted by (5.11) Q_{rad} is very high when the thickness h is low (i.e. the patch aspect ratio a/h is high) and it reduces following a $\sim 1/h$ dependence. In other words: the Q_{rad} of a patch resonator is proportional to the capacitance of the metal-

insulator-metal structure (i.e. the ability in storing the electric field) as already observed in [51].

From a linear fit of $1/Q_{rad}$ and from (5.11) we can estimate a radiation conductance of $G_{rad} \approx 2.2 \cdot 10^{-3}$ S. This is in agreement with the theoretical values of G_{rad} for a circular patch reported in Ref.[34] (in our case $a/\lambda_0 \approx 0.075$ which yields $G_{th} \approx 10^{-3}$ S).

Similarly, the calculated Q_{ohm} grows linearly with h as expected from (5.12). The slope parameter yields a gold skin depth of ≈ 30 nm that is lower than the value ≈ 45 nm calculated at 3 THz from the gold permittivity. This means that the conduction losses are slightly underestimated in the model, possibly due to insufficient mesh/discretization error. Finally, the Q_{ohm} curve shows that the ohmic losses dominate for thin GaAs cores, while the radiation losses dominate when the GaAs core is thick. The total quality factor is maximum when the ohmic and radiation losses *are matched* ($Q_{ohm} = Q_{rad}$), i.e. for a GaAs thickness of $1.5 \div 2$ μm , as already elucidated in [33]. A similar numerical study for patch resonators in the GHz range carried out with HFSS software for is reported in [152].

In FIG. 5.4(c) the same Q analysis is performed for a patch resonator of diameter $d_{patch} = 30$ μm operating around 3 THz on the TM_{210} mode. The same trend described above is observed, except that the loss matching condition is shifted around $h = 4$ μm .

To further validate the FEM analysis, a comparative study of Q_{rad} and Q_{tot} calculated via FEM and FDTD (Lumerical) simulations for a 15 μm patch on a PEC ground has been performed. The results are in very good agreement as shown in FIG. 5.4(d).

In summary, lossy eigenfrequency analysis can be used to rapidly estimate the different contributions to a resonator Q factor. In particular, one can study the evolution of losses as a function of geometrical parameters. For the analysed circular patch, the results are in good agreement with theoretical calculations.

Note: we will always observe experimental quality factors that are lower than the ones derived from simulations. Indeed, the actual value of the quality factor is difficult to predict as conduction losses are often underestimated. This issue is particularly relevant in the case of devices dominated by ohmic losses, like subwavelength resonators. On one side, the optical constants employed in simulations may differ from actual values which depend strongly on the material deposition techniques. Furthermore, smooth metal domains are employed to model real evaporated metal thin films characterized by surface roughness and geometric yield limited by photolithography. Nevertheless the simulations are extremely useful to reveal how the geometry impacts the different loss channels in a device.

5.3.4 LC resonators operating around 1.5 THz

Having validated the FEM simulations as a tool for Q factors analysis, we now study the loss mechanisms in the subwavelength structures developed so far. This is a key preliminary step before addressing problems such as lasing from a subwavelength cavity where a quantitative estimate of the cavity loss is needed. We consider sub- λ LC resonators reminiscent of the ones experimentally studied in 2.3.

The evolution of the Q factors as a function of the geometry for $h_{GaAs}=2\ \mu\text{m}$ are reported in FIG. 5.5(b). Q_{rad} is very high compared to Q_{ohm} which dominates in this cavity design. Q_{tot} (which overlaps the Q_{ohm} curve in the figure) is ≈ 20 and shows a slightly growing trend when tuning from capacitance-dominated devices to inductance-dominated devices. This fact confirms the experimental findings on the iso-frequency resonators analysed in Chapter 2, where a tiny growth of Q_{tot} from 9 to 12 was measured moving along the green diagonal (bottom to top) of FIG. 2.17.

To reduce Q_{rad} in order to match Q_{ohm} , one should make the capacitor aspect ratio poor, i.e. employ thicker GaAs layers, in analogy to what observed for patch resonators (FIG. 5.4). FIG. 5.5(c) reports Q_{rad} vs h_{GaAs} for fixed d_{patch} and l_{ant} . Starting from $h_{GaAs}=6\ \mu\text{m}$ we get $Q_{rad}<100$ meaning that the radiation losses become comparable to the ohmic losses. In FIG. 5.5(d) the Q analysis for $h_{GaAs}=6\ \mu\text{m}$ is reported. Note: Q_{tot} is slightly higher than in the previous case and is still dominated by ohmic loss except for very long antenna lengths.

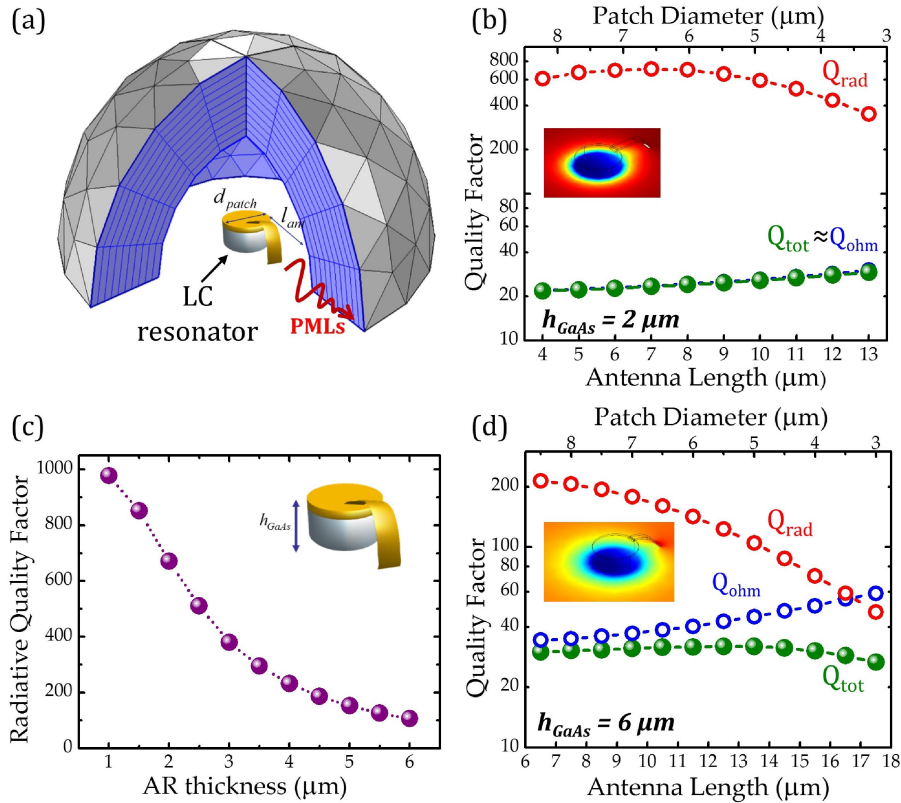


FIG. 5.5(a) Lossy eigenvalue analysis for LC resonators: patch diameter d_{patch} and antenna length l_{ant} are mutually compensated to operate around 1.5 THz (h_{GaAs} fixed). (b) Q factors as a function of (d_{patch}, l_{ant}) for $h_{GaAs}=2\ \mu\text{m}$. (c) Q_{rad} vs h_{GaAs} for fixed d_{patch} and l_{ant} . (d) Q factors as a function of (d_{patch}, l_{ant}) for $h_{GaAs}=6\ \mu\text{m}$

In the following we will focus on the design of subwavelength resonators for the two case studies $h_{GaAs}=2\ \mu\text{m}$ and $h_{GaAs}=6\ \mu\text{m}$. The first case is interesting for highly confining subwavelength structures for quantum well detectors or polaritonic meta-devices. The latter case cavity concerns the design of subwavelength THz lasers ow-

ing to the fact that the QCLs active regions can be thinned down to $6\ \mu\text{m}$ without reducing dramatically their performances.

5.3.5 Design of LC resonators operating at 3 THz

In this paragraph we will discuss the design of LC resonators operating at a specific target frequency $f_{\text{LC}}=3\ \text{THz}$ which is particularly interesting for applications. Different couples $(d_{\text{patch}}, l_{\text{ant}})$ have been found to ensure 3 THz operation for 2- μm -thick and 6- μm -thick GaAs cores. The results are shown in FIG. 5.6(a).

Note: the parameter l_{ant} used here is the antenna length as seen from the top of the device (xy-plane projection); the total antenna length (which for instance gives the inductance) is longer due to the two arcs assuring the antenna connection between the patch and the ground plane. Due to the constraints of microfabrication, patch diameters smaller than $3\ \mu\text{m}$ have not been considered. Similarly, highly bowed antenna designs ($l_{\text{ant}} < h_{\text{patch}}$) have been excluded as we shall guarantee some lateral space to insert an air-gap opening to provide DC contacts (see Chapter 4).

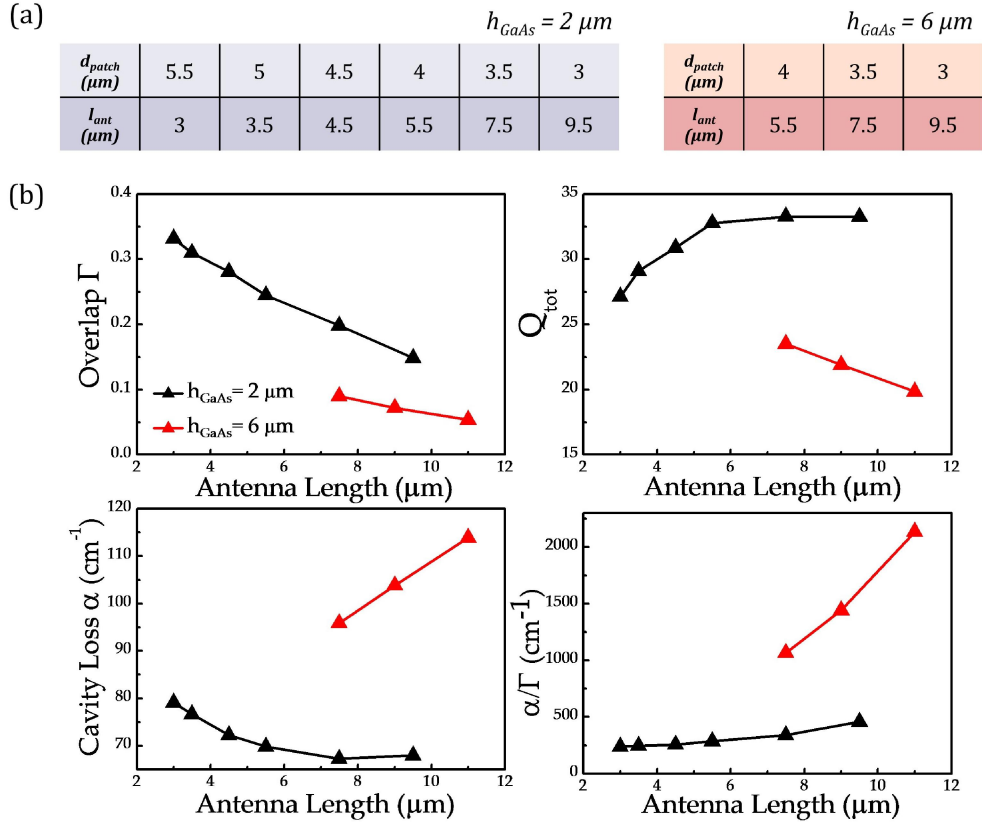


FIG. 5.6(a) Design values for iso-frequency LC resonators operating at 3 THz. (b) Calculated Q_{tot} , α , Γ and α/Γ from simulations.

The total cavity loss (α) and electromagnetic overlap (Γ) introduced in 5.1.1 have been calculated for these geometries in order to get the figure of merit α/Γ , as shown in FIG. 5.6(b). We can observe that owing to the small Q_{tot} and very weak overlap factor (even less than 10% for $h_{\text{GaAs}} = 6\ \mu\text{m}$) the predicted α/Γ values are incompatible with the material gain actually available with THz QCLs. Hence, this subwavelength

design could barely be exploited to build lasers. A strategy is needed to reduce the cavity losses and improve the mode overlap.

5.4 Subwavelength resonator with “revolved” inductors

5.4.1 Revolved inductors to lower the ohmic loss

In the previous section we learned that ohmic losses are the main responsible of the low total quality factor characterizing the subwavelength resonators developed so far. The way to rise Q_{ohm} and consequently Q_{tot} is to reduce the ohmic resistance (R_{ohm}) seen by the electrical current sustaining the LC resonance.

We recall first that in circuit theory losses are introduced by adding resistors in series or parallel to each lumped element. In our case a series resistance can be added to the resonator inductive (i.e. carrying current) section. The resonator Q factor is related to the loss resistance R via the relation

$$Q = \frac{\omega_0 L}{R} = \frac{1}{\omega_0 RC} \quad (5.14)$$

Now, to the solution to reduce ohmic loss comes simply from Ohm second law

$$R_{ohm} = \frac{l}{\sigma A} \quad (5.15)$$

where l is the conductor length, σ the material conductivity and A the conductor section. Indeed, by spreading the conduction current over a larger transverse section the resistive losses associated with our non-ideal inductor are greatly reduced. This can be realised in our design by continuously “revolving” the inductor around the patch core as shown in FIG. 5.7(a). In the frequency domain this corresponds to add continuously elementary inductors in parallel (like we did in Chapter 2 with discrete inductors) which of course produces a blueshift of the resonant frequency.

To explore if this configuration is useful to reduce conduction loss, the previously described Q analysis based on FEM simulations has been performed as a function of the revolution angle β . The patch diameter and GaAs thickness are respectively fixed at $d_{patch} = 9 \mu\text{m}$ and $h_{GaAs} = 6 \mu\text{m}$, yielding an estimated capacitance $C_{patch} \approx 1.28 \text{ fF}$. The revolved antenna/inductor has a fixed radial extension (top view) of value $l_{ant} = 7 \mu\text{m}$. FIG. 5.7(b) reports the simulation of Q_{ohm} (blue symbols) as a function of β showing, as expected, a dramatic reduction of ohmic losses. This can be further highlighted plotting the behaviour of the ohmic resistance $R_{ohm} \approx 1 / \omega_0 Q_{ohm}$ (a constant capacitance is assumed) which also accounts for the frequency shift due to the overall inductance reduction.

Moreover, closing progressively the cavity with such a metallic wall prevents energy to escape as radiation, which rises Q_{rad} as well. This is shown in FIG. 5.7(c) where the

Q_{rad} grows hugely when the cavity is quasi-closed ($\beta > 240^\circ$). The plot of the radiation resistance $R_{rad} \approx 1/\omega_0 Q_{rad}$ gives a bell-shaped curve with a maximum for pseudo-symmetric inductors and a minimum for quasi-closed geometries.

Putting together the findings about ohmic and radiative losses we get the Q_{tot} curve (FIG. 5.7(d)) where two different regions can be distinguished: the left part, corresponding to $\beta < 180^\circ$ (i.e. geometry comparable with the standard LC design), where Q_{tot} curve is stacked to a relatively low value; the right part where Q_{tot} explodes reaching simulated values above 200.

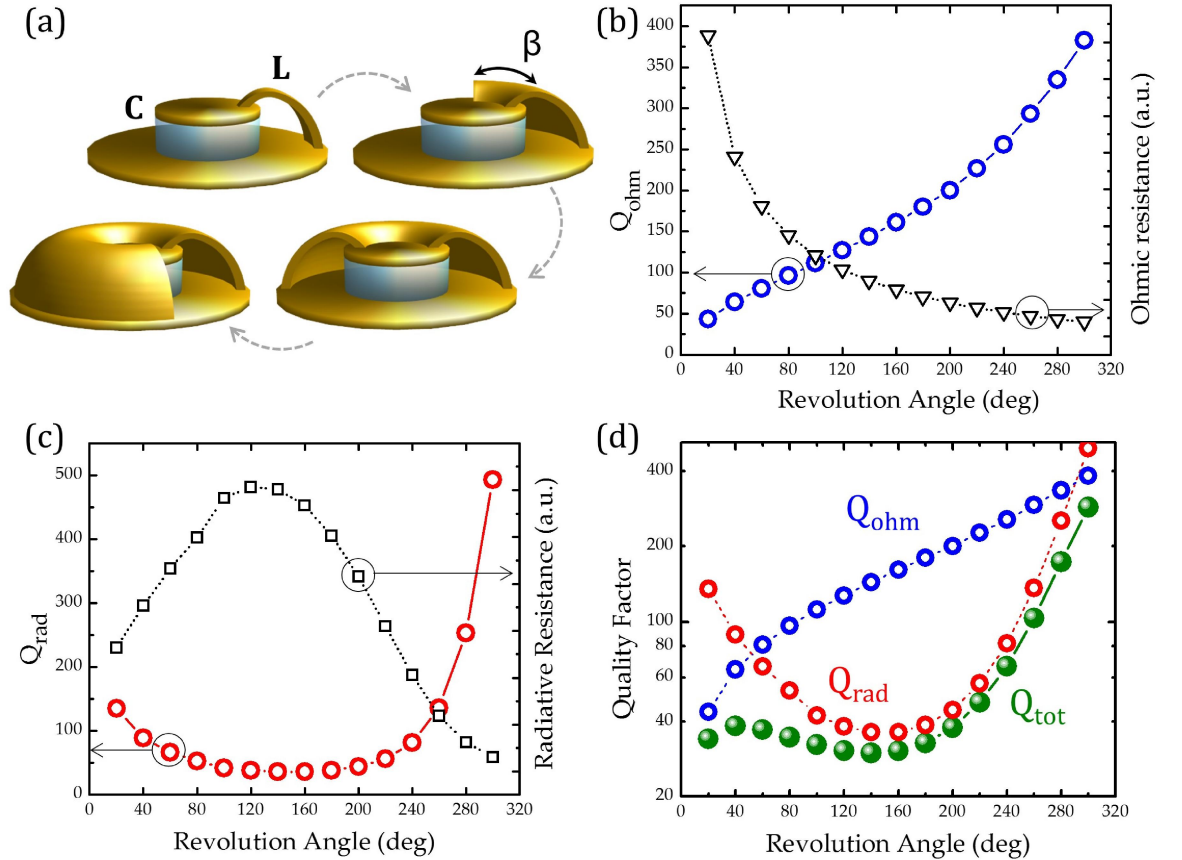


FIG. 5.7(a) Schematics of LC resonators featuring “revolved” inductors (β is the revolution angle). (b) Simulated Q_{ohm} (blue symbols) as a function of β . The trend of the resistance $R_{ohm} \approx 1/\omega_0 Q_{ohm}$ is also reported. (c) Simulated Q_{rad} (red symbols) as a function of β . The trend of the resistance $R_{rad} \approx 1/\omega_0 Q_{rad}$ is also reported. (d) Q factors as a function of the revolution angle.

As a matter of fact we are transforming our lumped-elements LC resonator into a true cavity resonator operating on its dominant TM_{010} mode [32]. This kind of resonator is highly preferred in MW domain for high-frequency applications (≥ 1 GHz) where skin-depth effects introduce large series resistance in typical inductors. The microwave cavity concept has already rescaled in the NIR range enabling a convincing demonstration of ultra-low volume lasers a discussed in 5.1.2.

The price to pay with these objects is the sacrifice, to some extent, of the extreme subwavelength confinement of the split-ring geometry ($\lambda_{eff}/10$) in favour of less confining, low loss structures. Eventually for a pseudo-closed geometry one comes back

to the diffraction-limited size ($\lambda_{\text{eff}}/2$) earning the benefits of very low cavity loss, as we are going to see.

5.4.2 Design of “revolved inductor” resonators operating at 3 THz

In this paragraph the design of iso-frequency 3 THz resonators exploiting the “revolved inductor” geometry is discussed. Proceeding in analogy to 5.3.5 the two cases $h_{\text{GaAs}}=2 \mu\text{m}$ and $h_{\text{GaAs}}=6 \mu\text{m}$ are studied. The revolved inductor radial extension is again $l_{\text{ant}}=7 \mu\text{m}$ but now the diameter d_{patch} is progressively enlarged to add more capacitance and compensate the decrease in inductance due to the revolved inductor.

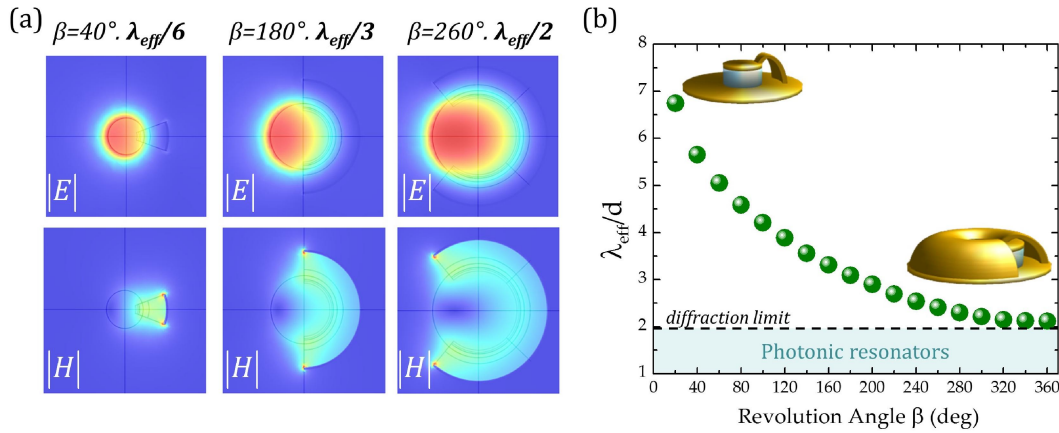


FIG. 5.8(a) Evolution of the electromagnetic field when passing from a lumped LC circuit to a cavity resonator. (b) Subwavelength parameter λ_{eff}/d as a function of the β angle for 3 THz “revolved inductor” resonators.

Before analysing the figures of merit for this design, in FIG. 5.8(a) the evolution of the electromagnetic field when transforming the LC resonator into a cavity resonator is presented for three iso-frequency resonators. The AC capacitor-like electric field is progressively squeezed towards the centre of the resonator assuming finally monopolar shape typical of the fundamental mode of a cavity. At the same time the magnetic field evolves from a spatially localized distribution to a toroidal distribution embracing the electric field. As already mentioned, this transformations implies a drop in the subwavelength confinement of the resonator. This is clearly pointed out in FIG. 5.8(b) where the subwavelength parameter λ_{eff}/d is plotted as a function of the revolution angle for a typical iso-frequency design (see FIG. 5.9). The resonator passes from a critical size which is largely subwavelength in the lumped-element (aka electrostatic) regime to a diffraction-limited size at the onset of the photonic regime.

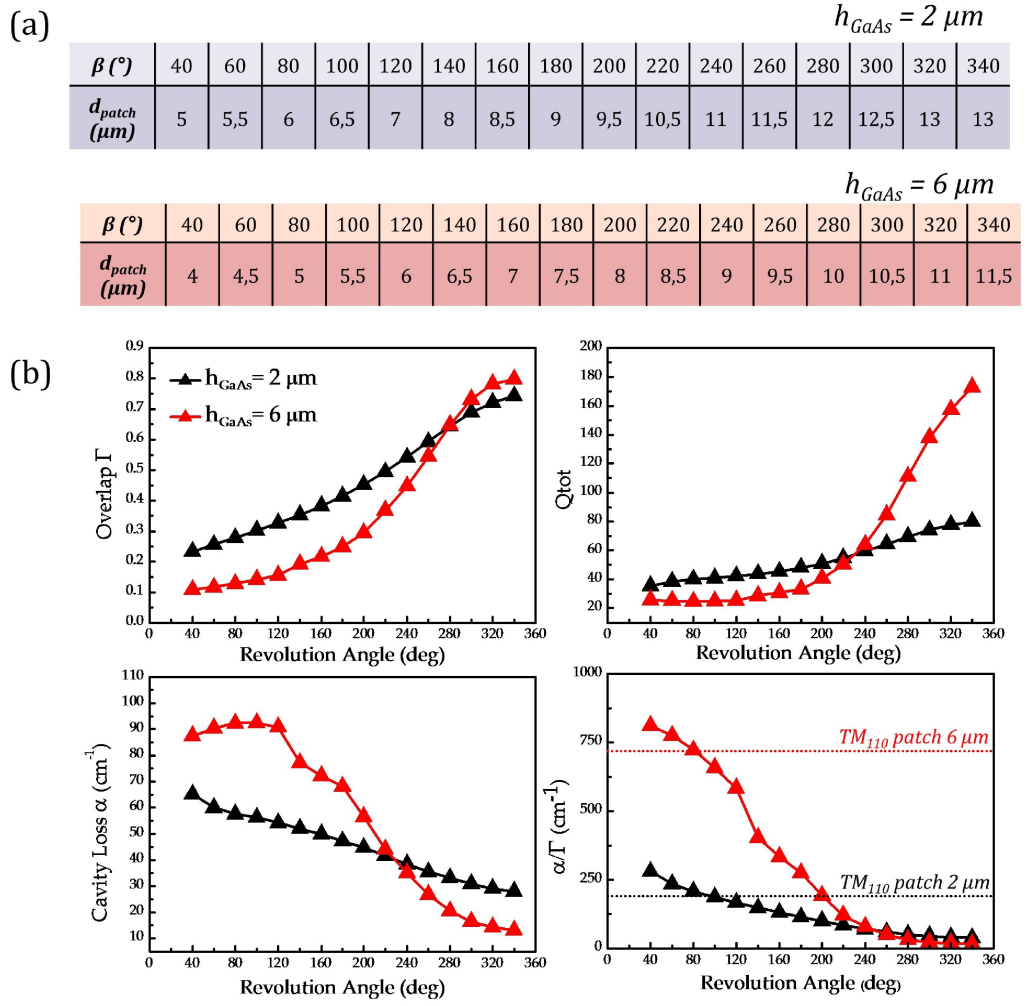


FIG. 5.9(a) Design values for iso-frequency LC resonators with “revolved inductors” operating at 3 THz. (b) Calculated Q_{tot} , α , Γ and α/Γ from simulations

In FIG. 5.9(a) the pairs $(\beta, d_{\text{patch}})$ yielding 3 THz resonance are reported for the two studied values of GaAs thickness. Again, the total Q factor (Q_{tot}), cavity loss (α), electromagnetic overlap (Γ) have been calculated to derive the figure of merit α/Γ as a function of the geometry as shown in FIG. 5.9(b). Looking at the α/Γ the advantages coming from this design emerge clearly as this parameter goes below 100 cm^{-1} for values $\beta > 240^\circ$. In particular, for $h_{\text{GaAs}} = 6 \mu\text{m}$ a quasi-closed metal cavity seems promising to build an ultra-small THz laser. This cavity resonator would in principle perform much better than its competitor patch resonator. The estimated α/Γ values for the patch resonator discussed in 5.3.3 (TM_{110} operation) are 190 cm^{-1} for the $2 \mu\text{m}$ structure and 720 cm^{-1} for the $6 \mu\text{m}$ structure. In the following the experimental realization of these resonators will be addressed.

5.4.3 Experimental results for $h_{\text{GaAs}} = 2 \mu\text{m}$

A first experimental study of the “revolved” geometry has been done for the case $h_{\text{GaAs}} = 2 \mu\text{m}$ exploiting the design parameter reported above. A $2 \mu\text{m}$ undoped GaAs sample grown by MOCVD has been used as active core. The fabrication scheme fol-

lows the one shown in FIG. 2.4 and FIG 2.11. After standard thermo-compressive wafer bonding, the sample has been patterned into patches with variable diameter d_{patch} . Then a suspended “revolved” inductor has been built similarly to the standard loop antenna case. As usual, large arrays of subwavelength period ($p_x=p_y=30\ \mu\text{m}$) have been fabricated to enable passive characterization. SEM pictures of some fabricated devices are shown in FIG. 5.10(a). Our fabrication scheme relying on suspended metal films reveals its efficacy even in building pseudo-closed cavities featuring a very narrow opening.

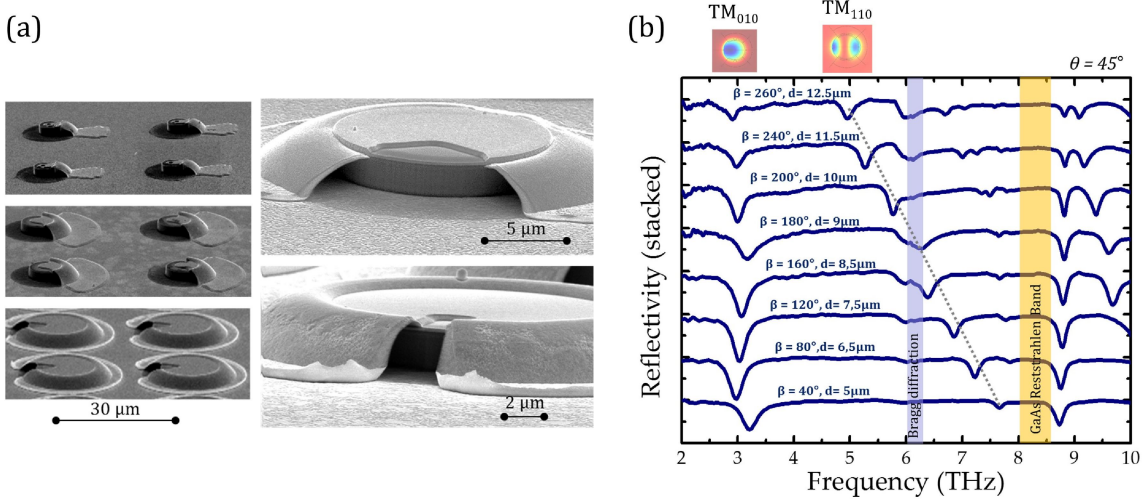


FIG. 5.10(a) SEM pictures of some fabricated “revolved inductor” resonators with a $2\ \mu\text{m}$ GaAs active core. (b) Reflectivity spectra at $\theta=45^\circ$: the resonant peak around 3 THz proves the validity of the iso-frequency design.

Reflectivity spectra have been acquired for all samples at 45° incidence in TM inplane configuration (see FIG. 2.13). For values of the β angle ranging from 40° to 260° a neat dip around 3 THz appears in the spectrum (FIG. 5.10(b)) proving the validity of the iso-frequency design. This dip is easily identified as the dominant TM_{010} of the cylindrical cavity resonator which evolves from the lumped LC mode [31]. The second dip moving in the spectra from high to low frequency (bottom to top) is the fundamental TM_{110} patch mode, approaching 3 THz as long as the patch diameter enlarges. No observable reflectivity dip has been measured instead for quasi-closed cavities (i.e. $\beta \geq 280^\circ$). Unfortunately, no appreciable improvement of the total Q factor has been measured ($Q_{\text{tot}} \approx 10$ for all devices in FIG. 5.10(b)). This may come from a poor quality of the fabricated current-carrying metal walls (especially at the edges). Note: the resonance depth as a function of β has a bell shaped form. This trend is justified when considering the mismatch between radiative and non-radiative loss in these resonators. For a 1-port system the reflectivity at resonance is given by

$$R = \left(\frac{\gamma_r - \gamma_{nr}}{\gamma_r + \gamma_{nr}} \right)^2 = \left(\frac{Q_{nr} - Q_r}{Q_r + Q_{nr}} \right)^2 \quad (5.16)$$

Hence, the reflectivity trend can be derived from the calculated radiative and ohmic (i.e. non radiative) Q factors for these design. The loss behaviour for the two cases $h_{GaAs}=2\ \mu\text{m}$ and $h_{GaAs}=6\ \mu\text{m}$ is shown in FIG. 5.11(a).

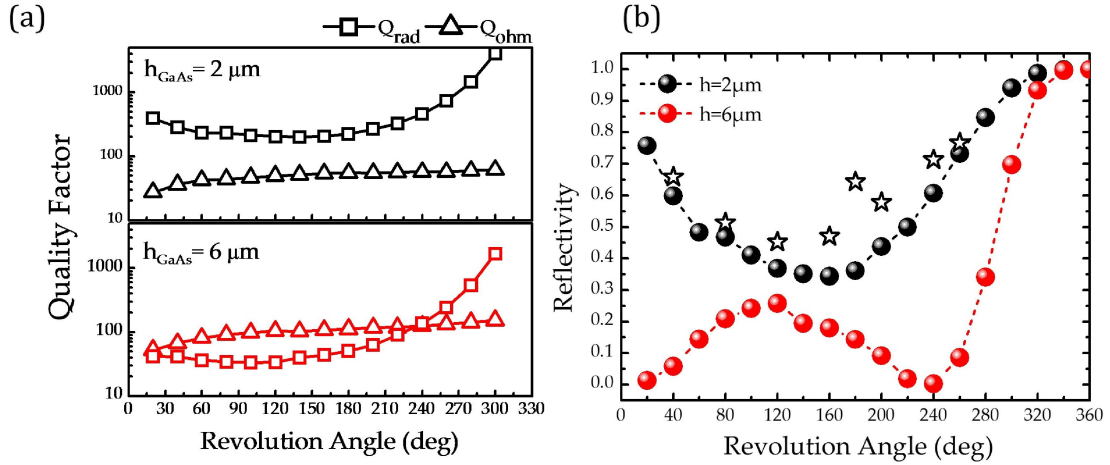


FIG. 5.11(a) Q_{rad} vs Q_{ohm} for $h_{GaAs}=2\ \mu\text{m}$ (top) and $h_{GaAs}=6\ \mu\text{m}$ (bottom). (b) Calculated reflectivity at resonance as given by (5.16) for the two structures (full circles) and experimental points for $h_{GaAs}=2\ \mu\text{m}$ (stars)

We notice that for the experimentally studied $2\ \mu\text{m}$ structure losses are never matched. The best coupling is achieved for resonator having $\beta \approx 100^\circ \div 200^\circ$ where the reflectivity (and consequently the absorption) exceeds 50% (FIG. 5.11(b)). The experimental points are in fair agreement with the simulated trend though a slightly lower contrast is measured. We note also that for $\beta > 280^\circ$ the expected resonance contrast falls below 10%, which explains probably why no resonant peak can be measured for quasi-closed geometry example. Indeed, the $6\ \mu\text{m}$ structure appears much more interesting as it presents two *critical coupling* zones where ohmic losses match radiative losses. In particular, for β values up to 300° the resonator should maintain a good coupling to the outside world while showing a steep increase in the total Q factor. The $6\ \mu\text{m}$ design will be shortly realised and studied experimentally. This design is in fact promising to be integrated with a $6\ \mu\text{m}$ -thick QCL active region to demonstrate ultra-low volume THz lasers.

Conclusions and perspectives

This thesis was framed in a wider project which aims at developing a unified framework for photonic and electronic devices. In fact, merging these two distinct worlds would establish a novel paradigm for device physics: for instance, optoelectronic devices with no size constraints imposed by the diffraction limit and currently unavailable properties could be conceived. The THz frequency range, halfway between the realms of electronic and optics, has been identified as the perfect playground to develop devices in which functionalities typical of both worlds are combined simultaneously.

The context of the work was introduced in **Chapter 1**, where a general overview on THz technology, intersubband transitions in QWs and optical properties of materials was given. Some relevant notions about the standard transmission-line resonators employed in THz photonics were also recalled. Last, the possibility to confine radiation on a subwavelength scale by operating in the quasi-static electronic regime was discussed.

In **Chapter 2** we have experimentally studied a novel design based on lumped circuit elements to build 3D subwavelength resonators operating at THz frequencies. A MSM cavity, providing capacitance, is connected to a metallic suspended loop antenna which implements an inductive region. To do this, the air-bridge technology employed in microwave circuits has been adapted to fabricate micrometric THz lumped inductors. These objects are de facto topologically equivalents of planar split-ring resonators and provide a typical subwavelength confinement of $\approx \lambda_{eff}/10$ in three dimensions. Remarkably, their resonant frequency, optical coupling, polarization and efficiency can be modified via the sole geometric design of the loop antenna and/or MSM capacitor, similarly to what is done in the RF/MW bands. Moreover, we have shown that playing with different arrangements of circuit elements one can span the whole THz range and add user-tailored functionalities.

Some applications of the novel lumped-element design have been presented in **Chapter 3** to implement passive THz meta-devices. In the first part, we have demonstrated strong light-matter coupling at room temperature within the developed 3D circuit-tunable meta-atoms. The intersubband transition of semiconductor parabolic quantum wells was strongly coupled to the confined circuitual mode of $\lambda_{eff}/10$ subwavelength resonators featuring a ultra-small active volume ($\approx 6 \mu\text{m}^3$). The cavity-matter frequency detuning was obtained via a photolithographic tuning of a suspended loop antenna, which is external to the interaction region. In the second part, preliminary results on the ultra-fast switching of the LC resonance have been reported. The first geometry explored, featuring an opening in the ground plane, has proven to be ineffective for this purpose because both the gap opening and the MSM ca-

pacitor are photo-excited by the NIR pump. A novel design featuring a tiny a-Si switch pad is currently being explored. Then, we have touched upon the possibility to realize optically active THz high-impedance surfaces exploiting chiral configurations of 3D lumped elements.

The major breakthrough of this thesis is described in **Chapter 4** where single-pixel QWIP detectors with extremely sub-wavelength dimension of $\approx \lambda_{eff}/10$ (corresponding to $\lambda_0/25$ in the detector active core) have been demonstrated. The active core of the device hosting a GaAs/AlGaAs multi-quantum-well structure designed to detect radiation around 3 THz, has an active volume of about $20 \mu\text{m}^3$ only, and the LC resonance of the resonator has been centred on the QWIP structure response band. This is the first demonstration to date of a fully functional optoelectronic meta-device operating at the single meta-atom scale.

From the electrical characterization, it emerges that a very low level of dark current (less than $\approx 1 \text{ nA}$) flows in the device. This is particularly promising in view of the reduction of the detector's noise. Moreover, such a dramatic reduction of the active region size can lead to an improvement of the THz detectors performances, in terms of operating temperature, detectivity and velocity.

The key enabling element has been the development of an effective strategy to electrically contact the devices' active core (in single and array configurations) without suffering from the short-circuit issue intrinsic in the split-ring geometry. This contact scheme, currently used for extracting the photocurrent from a sub-wavelength QWIP core, will facilitate the future implementation of individual lasing meta-atoms.

When it comes to evaluate the feasibility of a subwavelength laser, attention has to be paid to the resonator losses and electromagnetic mode overlap with the gain medium. This issue has been addressed in **Chapter 5**, where a numerical study of the quality factors and of the α/Γ parameter for the developed lumped-elements resonators has been presented. A reduction of ohmic losses is predicted when a modified LC design featuring "revolved inductors" is used. These preliminary results seem promising for the demonstration of ultra-low volume lasers in the THz range.

The demonstration of a lasing meta-atom is of course the fundamental perspective of this work. This object would arguably be the first optical oscillator tuned with an "external" circuit and would behave as a point-source of radiation with no lower size limit. Successively, such point-like lasers could be arranged in phased arrays.

For THz detectors, an important size reduction has been achieved thanks to the lumped LC geometry proposed in this thesis, yielding remarkably low dark-currents. Nevertheless, the antenna aperture (i.e the radiation capture area) of a subwavelength inductive loop is small if compared with other antenna geometries. In the future, different wavelength-scale antennas will be explored to efficiently concentrate radiation in an even smaller semiconductor detecting core.

Also, various perspectives for passive meta-devices are conceivable. In the context of cavity quantum electrodynamics, sub- λ resonators featuring an extremely

small QW core will provide an opportunity to further reduce the number of interacting dipoles, thus allowing the exploration of a few electron strong coupling regime, in which processes such as optical bistability and photon-blockade could be achievable.

Furthermore, the passive 3D lumped resonators are particularly appealing thanks to their circuital properties. For instance, since the resonance frequency is fixed by the external circuit, it can be modulated either mechanically (with a MEMS actuator) or optically. The latter option is very interesting: if an optical switching element is inserted in the antenna structure, then the resonance frequency could be modulated on ultrafast timescales offering the opportunity to investigate the dynamic properties of a bare cavity mode and/or of the strong coupling regime.

Finally, the versatile technological framework we developed is suitable for the realization of user-tailorable THz optical components: for instance, metal-dielectric high-impedance surfaces operating in reflection can be designed to absorb, filter or control the polarization state of THz radiation at will.

Appendix A: samples growthsheet

Sample L1006

THz-PQW structure (copy of APL, vol. 97, N. 19, 2010, J. Faist group)				
Total thickness = 1058 nm				
Material	[nm]	Ratio	Doping (cm ⁻³)	
GaAs	250			
AlGaAs	500	Al50Ga50As		Stop Layer
GaAs	50			
Start of 11 repeat periods				
AlGaAs	2.95	Al15Ga85As		
GaAs	0.15			
AlGaAs	2.5	Al15Ga85As		
GaAs	0.5			
AlGaAs	2.04	Al15Ga85As		
GaAs	0.96			
AlGaAs	1.67	Al15Ga85As		
GaAs	1.33			
AlGaAs	1.34	Al15Ga85As		
GaAs	1.66			
AlGaAs	1.04	Al15Ga85As		
GaAs	1.76			
GaAs	0.2		4.00E+17	
AlGaAs	0.78	Al15Ga85As		
GaAs	1.72			
GaAs	0.5		4.00E+17	
AlGaAs	0.56	Al15Ga85As		
GaAs	1.94			
GaAs	0.5		4.00E+17	
AlGaAs	0.37	Al15Ga85As		
GaAs	2.13			
GaAs	0.5		4.00E+17	
AlGaAs	0.28	Al15Ga85As		
GaAs	2.02			
GaAs	0.7		4.00E+17	
AlGaAs	0.15	Al15Ga85As		
GaAs	1.85			
GaAs	1		4.00E+17	
AlGaAs	0.15	Al15Ga85As		
GaAs	8.1			
GaAs	2		4.00E+17	
GaAs	8.1			
AlGaAs	0.15	Al15Ga85As		
GaAs	1		4.00E+17	

Appendix A: samples growthsheet

GaAs	1.85		
AlGaAs	0.15	Al15Ga85As	
GaAs	0.7		4.00E+17
GaAs	2.02		
AlGaAs	0.28	Al15Ga85As	
GaAs	0.5		4.00E+17
GaAs	2.13		
AlGaAs	0.37	Al15Ga85As	
GaAs	0.5		4.00E+17
GaAs	1.94		
AlGaAs	0.56	Al15Ga85As	
GaAs	0.5		4.00E+17
GaAs	1.72		
AlGaAs	0.78	Al15Ga85As	
GaAs	0.2		4.00E+17
GaAs	1.76		
AlGaAs	1.04	Al15Ga85As	
GaAs	1.66		
AlGaAs	1.34	Al15Ga85As	
GaAs	1.33		
AlGaAs	1.67	Al15Ga85As	
GaAs	0.96		
AlGaAs	2.04	Al15Ga85As	
GaAs	0.5		
AlGaAs	2.5	Al15Ga85As	
GaAs	0.15		
AlGaAs	14.45	Al15Ga85As	
End of repeat periods			
AlGaAs	10	Al15Ga85As	
GaAs	50		

Sample L1118

THz-QWP structure (copy of IEEE vol.32, N.5, 2011, HC Liu, V267)

Note 1: for single-plasmon / mesa process

Note 2: Alloy fraction at 1.5%!

Total thickness = 2584 nm

AR thickness = 1384 nm

Material	[nm]	Ratio	Doping (cm-3)	Doping (cm-2)
GaAs	250			
AlGaAs	300	Al50Ga50As		Stop Layer
GaAs	800		2.00E+17	
Start of 11 periods				
AlGaAs	95.1	Al1.5 Ga98.5 As		
GaAs	6.05			
GaAs	10		3.00E+16	3.00E+10
GaAs	6.05			
End of repeat periods				
AlGaAs	95.1	Al1,5 Ga98,5 As		
GaAs	400		2.00E+17	

Sample L1258

THz-QWP structure (copy of IEEE vol.32, N.5, 2011, HC Liu, V267)

Note 1: for metal-metal process

Note 2: alloy fraction at 1.5%!

Total thickness = 1584 nm

AR thickness = 1384 nm

Material	[nm]	Ratio	Doping (cm-3)	Doping (cm-2)
GaAs	250			
AlGaAs	300	Al50Ga50As		Stop Layer
GaAs	1		5.00E+18	
Start of 11 periods				
AlGaAs	95.1	Al1.5 Ga98.5 As		
GaAs	6.05			
GaAs	10		3.00E+16	3.00E+10
GaAs	6.05			
End of repeat periods				
AlGaAs	95.1	Al1,5 Ga98,5 As		
GaAs	100		2.00E+18	

Bibliography

- [1] M. Tonouchi, "Cutting-edge terahertz technology," *Nat. Photonics*, vol. 1, pp. 97–105, 2007.
- [2] P. H. Siegel, "Terahertz technology," *IEEE Trans. Microw. Theory Tech.*, vol. 50, no. 3, pp. 910–928, 2002.
- [3] C. Corsi and F. Sizov, *THz and Security Applications: Detectors, Sources and Associated Electronics for THz Applications*. Springer Netherlands, 2014.
- [4] J. Faist, F. Capasso, D. L. Sivco, C. Sirtori, A. L. Hutchinson, and A. Y. Cho, "Quantum Cascade Laser," *Science (80-.)*, vol. 264, no. 5158, pp. 553–556, 1994.
- [5] R. Köhler, A. Tredicucci, F. Beltram, H. E. Beere, E. H. Linfield, a G. Davies, D. a Ritchie, R. C. Iotti, and F. Rossi, "Terahertz semiconductor-heterostructure laser.," *Nature*, vol. 417, no. 6885, pp. 156–159, 2002.
- [6] B. S. Williams, "Terahertz quantum-cascade lasers," *Nat. Photonics*, vol. 1, no. 9, pp. 517–525, Sep. 2007.
- [7] M. S. Vitiello, G. Scalari, B. Williams, and P. De Natale, "Quantum cascade lasers : 20 years of challenges," *Opt. Express*, vol. 23, no. 4, pp. 5167–5182, 2015.
- [8] S. Fatholouloumi, E. Dupont, C. W. I. Chan, Z. R. Wasilewski, S. R. Laframboise, D. Ban, a. Mátyás, C. Jirauschek, Q. Hu, and H. C. Liu, "Terahertz quantum cascade lasers operating up to ~ 200 K with optimized oscillator strength and improved injection tunneling," *Opt. Express*, vol. 20, no. 4, p. 3866, 2012.
- [9] M. a Belkin and F. Capasso, "New frontiers in quantum cascade lasers: high performance room temperature terahertz sources," *Phys. Scr.*, vol. 90, no. 11, p. 118002, 2015.
- [10] F. Sizov and A. Rogalski, "THz detectors," *Prog. Quantum Electron.*, vol. 34, no. 5, pp. 278–347, 2010.
- [11] J. F. Federici, B. Schulkin, F. Huang, D. Gary, R. Barat, F. Oliveira, and D. Zimdars, "THz imaging and sensing for security applications—explosives, weapons and drugs," *Semicond. Sci. Technol.*, vol. 20, no. 7, pp. S266–S280, 2005.
- [12] P. Uhd Jepsen, D. G. Cooke, and M. Koch, "Terahertz spectroscopy and imaging – Modern techniques and applications," *Laser Photonics Rev.*, vol. 5, no. 1, pp. 124–166, 2011.
- [13] B. M. Fischer, M. Walther, and P. Uhd Jepsen, "Far-infrared vibrational modes of DNA components studied by terahertz time-domain spectroscopy.," *Phys. Med. Biol.*, vol. 47, no. 21, pp. 3807–3814, 2002.
- [14] E. Pickwell and V. P. Wallace, "Biomedical applications of terahertz technology," *J. Phys. D. Appl. Phys.*, vol. 39, no. 17, pp. 301–310, 2006.
- [15] T. G. Phillips and J. Keene, "Submillimeter astronomy (heterodyne spectroscopy)," *Proc. IEEE*, vol. 80, no. 11, pp. 1662–1678, 1992.
- [16] J. Federici and L. Moeller, "Review of terahertz and subterahertz wireless communications," *Journal of Applied Physics*, vol. 107, no. 11. 2010.
- [17] J. Singh, *Semiconductor Optoelectronics: Physics and Technology*. McGraw-Hill, 1995.
- [18] L. Esaki and R. Tsu, "Superlattice and Negative Differential Conductivity in Semiconductors," *IBM J. Res. Dev.*, vol. 14, no. 1, pp. 61–65, 1970.
- [19] S. M. Sze, *Semiconductor Devices: Physics and Technology*. 2006.
- [20] J. Faist, F. Capasso, D. L. Sivco, C. Sirtori, A. L. Hutchinson, and A. Y. Cho, "Quantum Cascade Laser," *Science (80-.)*, vol. 264, no. 5158, pp. 553–556, 1994.

- [21] G. Bastard, "Wave Mechanics Applied to Semiconductor Heterostructures," *Journal of Modern Optics*, vol. 38, no. 6, pp. 1211–1212, 1991.
- [22] I. Vurgaftman, J. R. Meyer, and L. R. Ram-Mohan, "Band parameters for III-V compound semiconductors and their alloys," *J. Appl. Phys.*, vol. 89, no. 11 I, pp. 5815–5875, 2001.
- [23] E. Rosencher and B. Vinter, *Optoelectronics*. Cambridge University Press, 2002.
- [24] J. Davies, *The Physics of Low-Dimensional Semiconductors*, vol. Cambridge. 1998.
- [25] M. Fox, *Optical Properties of Solids*. OUP Oxford, 2010.
- [26] E. D. Palik, *Handbook of Optical Constants of Solids II*. Academic Press, 1991.
- [27] M. A. Ordal, R. J. Bell, R. W. Alexander, L. L. Long, and M. R. Querry, "Optical properties of fourteen metals in the infrared and far infrared: Al, Co, Cu, Au, Fe, Pb, Mo, Ni, Pd, Pt, Ag, Ti, V, and W.," *Appl. Opt.*, vol. 24, no. 24, pp. 4493–4499, 1985.
- [28] L. Solymar and E. Shamonina, "Waves in metamaterials," p. 385, 2009.
- [29] W. L. Barnes, A. Dereux, and T. W. Ebbesen, "Surface plasmon subwavelength optics.," *Nature*, vol. 424, no. 6950, pp. 824–830, 2003.
- [30] J. B. Pendry, a. J. Holden, D. J. Robbins, and W. J. Stewart, "Magnetism from conductors and enhanced nonlinear phenomena," *IEEE Trans. Microw. Theory Tech.*, vol. 47, no. February 1999, pp. 2075–2084, 1999.
- [31] D. M. Pozar, *Microwave Engineering, 4th Edition*. Wiley, 2011.
- [32] D. H. Staelin, A. W. Morgenthaler, and J. A. Kong, *Electromagnetic Waves*. Prentice Hall PTR, 1994.
- [33] Y. Todorov, L. Tosetto, J. Teissier, a M. Andrews, P. Klang, R. Colombelli, I. Sagnes, G. Strasser, and C. Sirtori, "Optical properties of metal-dielectric-metal microcavities in the THz frequency range," *Opt. Express*, vol. 18, no. 13, pp. 13886–13907, 2010.
- [34] C. A. Balanis, *Antenna Theory: Analysis and Design*. Wiley, 2012.
- [35] L. Novotny and B. Hecht, *Principles of Nano-Optics*. Cambridge University Press, 2012.
- [36] S. Bozhevolnyi, *Plasmonic Nanoguides and Circuits*. Pan Stanford, 2009.
- [37] E. Hecht, *Optics*. Addison-Wesley, 2002.
- [38] T. H. Lee, *Planar Microwave Engineering: A Practical Guide to Theory, Measurement, and Circuits*, no. v. 1. Cambridge University Press, 2004.
- [39] J. D. Jackson, *Classical Electrodynamics*. Wiley, 1998.
- [40] P. Biagioni, J.-S. Huang, and B. Hecht, "Nanoantennas for visible and infrared radiation.," *Rep. Prog. Phys.*, vol. 75, no. 2, p. 024402, Mar. 2012.
- [41] R. E. Collin, "Antennas and radiowave propagation," *McGraw-Hill series in electrical engineering. Radio, television, radar, and antennas*. p. 508, 1985.
- [42] Y. Huang and K. Boyle, *Antennas: From Theory to Practice*. Wiley, 2008.
- [43] J. J. Carr, *Microwave & Wireless Communications Technology*. 1996.
- [44] W. N. Hardy and L. A. Whitehead, "Split-ring resonator for use in magnetic resonance from 200-2000 MHz," *Rev. Sci. Instrum.*, vol. 52, no. 2, pp. 213–216, 1981.
- [45] J. M. Jin and D. J. Riley, *Finite Element Analysis of Antennas and Arrays*. Wiley, 2009.
- [46] B. C. Smith, *Fundamentals of Fourier Transform Infrared Spectroscopy*. Taylor & Francis, 1995.
- [47] F. L. Pedrotti, L. M. Pedrotti, and L. S. Pedrotti, *Introduction to Optics*. Pearson Education, Limited, 2013.

- [48] P. Lunnemann, I. Sersic, and a. Koenderink, "Optical properties of two-dimensional magnetoelectric point scattering lattices," *Phys. Rev. B*, vol. 88, no. 24, p. 245109, Dec. 2013.
- [49] Y. Todorov, L. Toso, J. Teissier, a M. Andrews, P. Klang, R. Colombelli, I. Sagnes, G. Strasser, and C. Sirtori, "Optical properties of metal-dielectric-metal microcavities in the THz frequency range," *Opt. Express*, vol. 18, no. 13, pp. 13886–907, Jun. 2010.
- [50] D. Sievenpiper, R. F. J. Broas, N. G. Alexopolous, and E. Yablonovitch, "High-impedance electromagnetic surfaces with a forbidden frequency band," *IEEE Trans. Microw. Theory Tech.*, vol. 47, no. 11, pp. 2059–2074, 1999.
- [51] A. Sellier, T. V. Teperik, and A. de Lustrac, "Resonant circuit model for efficient metamaterial absorber," *Opt. Express*, vol. 21, no. S6, p. A997, 2013.
- [52] C. Walther, G. Scalari, M. I. Amanti, M. Beck, and J. Faist, "Microcavity laser oscillating in a circuit-based resonator," *Science*, vol. 327, no. 5972, pp. 1495–7, Mar. 2010.
- [53] M. Geiser, C. Walther, G. Scalari, M. Beck, M. Fischer, L. Nevou, and J. Faist, "Strong light-matter coupling at terahertz frequencies at room temperature in electronic LC resonators," *Appl. Phys. Lett.*, vol. 97, no. 19, 2010.
- [54] R. P. Feynman, F. R. P. S. M. L. R. B, R. B. Leighton, and M. Sands, *The Feynman Lectures on Physics, Desktop Edition Volume II: The New Millennium Edition*. Basic Books, 2013.
- [55] J. B. Khurgin, "How to deal with the loss in plasmonics and metamaterials," *Nat. Publ. Gr.*, vol. 10, no. 1, pp. 2–6, 2015.
- [56] K. Steinberg, M. Scheffler, and M. Dressel, "Microwave inductance of thin metal strips," *J. Appl. Phys.*, vol. 108, no. 9, p. 096102, 2010.
- [57] J. B. Khurgin and G. Sun, "Scaling of losses with size and wavelength in nanoplasmonics and metamaterials," *Appl. Phys. Lett.*, vol. 99, no. May 2015, pp. 2009–2012, 2011.
- [58] Z. Chen, a. Megrant, J. Kelly, R. Barends, J. Bochmann, Y. Chen, B. Chiaro, a. Dunsworth, E. Jeffrey, J. Y. Mutus, P. J. J. O'Malley, C. Neill, P. Roushan, D. Sank, a. Vainsencher, J. Wenner, T. C. White, a. N. Cleland, and J. M. Martinis, "Fabrication and characterization of aluminum airbridges for superconducting microwave circuits," *Appl. Phys. Lett.*, vol. 104, no. 5, p. 052602, Feb. 2014.
- [59] S. Linden, C. Enkrich, M. Wegener, J. Zhou, T. Koschny, and C. M. Soukoulis, "Magnetic response of metamaterials at 100 terahertz," *Science*, vol. 306, no. 5700, pp. 1351–3, Nov. 2004.
- [60] N. Katsarakis, T. Koschny, M. Kafesaki, E. N. Economou, and C. M. Soukoulis, "Electric coupling to the magnetic resonance of split ring resonators," *Appl. Phys. Lett.*, vol. 84, no. 15, pp. 2943–2945, 2004.
- [61] K. Steinberg, M. Scheffler, and M. Dressel, "Microwave inductance of thin metal strips," *J. Appl. Phys.*, vol. 108, no. 9, pp. 15–17, 2010.
- [62] E. Strupiechonski, G. Xu, M. Brekenfeld, Y. Todorov, N. Isac, a. M. Andrews, P. Klang, C. Sirtori, G. Strasser, a. Degiron, and R. Colombelli, "Sub-diffraction-limit semiconductor resonators operating on the fundamental magnetic resonance," *Appl. Phys. Lett.*, vol. 100, no. 13, p. 131113, 2012.
- [63] E. Strupiechonski, G. Xu, P. Cavalié, N. Isac, S. Dhillon, J. Tignon, G. Beaudoin, I. Sagnes, a. Degiron, and R. Colombelli, "Hybrid electronic-photonics subwavelength cavities operating at terahertz frequencies," *Phys. Rev. B*, vol. 87, no. 4, p. 041408, Jan. 2013.
- [64] M. Husnik, M. W. Klein, N. Feth, M. König, J. Niegemann, K. Busch, S. Linden, and M. Wegener, "Absolute extinction cross-section of individual magnetic split-ring resonators," *Nat. Photonics*, vol. 2, no. 10, pp. 614–617, Sep. 2008.
- [65] J. L. Volakis, A. Chatterjee, and L. C. Kempel, *Finite Element Method Electromagnetics: Antennas, Microwave Circuits, and Scattering Applications*. Wiley, 1998.

- [66] A. Alù and N. Engheta, "Input impedance, nanocircuit loading, and radiation tuning of optical nanoantennas," *Phys. Rev. Lett.*, vol. 101, no. 4, p. 043901, Jul. 2008.
- [67] W. Padilla, M. Aronsson, C. Highstrete, M. Lee, a. Taylor, and R. Averitt, "Electrically resonant terahertz metamaterials: Theoretical and experimental investigations," *Phys. Rev. B*, vol. 75, no. 4, p. 041102, Jan. 2007.
- [68] D. Schurig, J. J. Mock, and D. R. Smith, "Electric-field-coupled resonators for negative permittivity metamaterials," *Appl. Phys. Lett.*, vol. 88, no. 4, p. 041109, 2006.
- [69] M. Malerba, A. Alabastri, E. Miele, P. Zilio, M. Patrini, D. Bajoni, G. C. Messina, M. Dipalo, A. Toma, R. Proietti Zaccaria, and F. De Angelis, "3D vertical nanostructures for enhanced infrared plasmonics," *Sci. Rep.*, vol. 5, p. 16436, 2015.
- [70] N. I. Zheludev and Y. S. Kivshar, "From metamaterials to metadevices," *Nat. Mater.*, vol. 11, no. 11, pp. 917–24, Nov. 2012.
- [71] D. Lu, J. J. Kan, E. E. Fullerton, and Z. Liu, "Enhancing spontaneous emission rates of molecules using nanopatterned multilayer hyperbolic metamaterials," *Nat. Nanotechnol.*, vol. 9, no. 1, pp. 48–53, 2014.
- [72] K. Tanaka, E. Plum, J. Y. Ou, T. Uchino, and N. I. Zheludev, "Multifold enhancement of quantum dot luminescence in plasmonic metamaterials," *Phys. Rev. Lett.*, vol. 105, no. 22, pp. 1–4, 2010.
- [73] H.-T. Chen, J. F. O'Hara, A. K. Azad, A. J. Taylor, R. D. Averitt, D. B. Shrekenhamer, and W. J. Padilla, "Experimental demonstration of frequency-agile terahertz metamaterials," *Nat. Photonics*, vol. 2, no. 5, pp. 295–298, Apr. 2008.
- [74] M. Fox, *Quantum Optics: An Introduction: An Introduction*. OUP Oxford, 2006.
- [75] E. T. Jaynes and F. W. Cummings, "Comparison of quantum and semiclassical radiation theories with application to the beam maser," *Proc. IEEE*, vol. 51, no. 1, pp. 89–109, Jan. 1963.
- [76] A. Delteil, "Many-body enhancement of the light-matter interaction," Université Paris-Diderot - Paris VII, 2012.
- [77] L. Novotny, "Strong coupling, energy splitting, and level crossings: A classical perspective," *Am. J. Phys.*, vol. 78, no. 11, p. 1199, 2010.
- [78] P. Jouy, a. Vasanelli, Y. Todorov, L. Sapienza, R. Colombelli, U. Gennser, and C. Sirtori, "Intersubband electroluminescent devices operating in the strong-coupling regime," *Phys. Rev. B - Condens. Matter Mater. Phys.*, vol. 82, pp. 1–11, 2010.
- [79] D. Dini, R. Köhler, A. Tredicucci, G. Biasiol, and L. Sorba, "Microcavity polariton splitting of intersubband transitions," *Phys. Rev. Lett.*, vol. 90, no. 11, p. 116401, 2003.
- [80] Y. Todorov, A. M. Andrews, I. Sagnes, R. Colombelli, P. Klang, G. Strasser, and C. Sirtori, "Strong light-matter coupling in subwavelength metal-dielectric microcavities at terahertz frequencies," *Phys. Rev. Lett.*, vol. 102, no. 18, 2009.
- [81] R. Colombelli and J. M. Manceau, "Perspectives for intersubband polariton lasers," *Phys. Rev. X*, vol. 5, no. 1, 2015.
- [82] S. Zanotto, "Intersubband polaritons in photonic crystal cavities," 2014.
- [83] S. Zanotto, R. Degl'Innocenti, L. Sorba, A. Tredicucci, and G. Biasiol, "Analysis of line shapes and strong coupling with intersubband transitions in one-dimensional metallodielectric photonic crystal slabs," *Phys. Rev. B*, vol. 85, no. 3, p. 35307, Jan. 2012.
- [84] Y. Todorov and C. Sirtori, "Intersubband polaritons in the electrical dipole gauge," *Phys. Rev. B - Condens. Matter Mater. Phys.*, vol. 85, no. 4, 2012.
- [85] W. Kohn, "Cyclotron Resonance and de Haas-van Alphen Oscillations of an Interacting Electron Gas," *Phys. Rev.*, vol. 123, no. 4, pp. 1242–1244, 1961.

- [86] L. Brey, N. F. Johnson, and B. I. Halperin, "Optical and magneto-optical absorption in parabolic quantum wells," *Phys. Rev. B*, vol. 40, no. 15, pp. 10647–10649, Nov. 1989.
- [87] M. Geiser, F. Castellano, G. Scalari, M. Beck, L. Nevou, and J. Faist, "Ultrastrong Coupling Regime and Plasmon Polaritons in Parabolic Semiconductor Quantum Wells," *Phys. Rev. Lett.*, vol. 108, no. 10, p. 106402, Mar. 2012.
- [88] P. Harrison, *Quantum Wells, Wires and Dots: Theoretical and Computational Physics of Semiconductor Nanostructures*. Wiley, 2011.
- [89] H. C. Liu and F. Capasso, *Intersubband Transitions in Quantum Wells: Physics and Device Applications I*. Academic Press, 2000.
- [90] D. Dietze, a Benz, G. Strasser, K. Unterrainer, and J. Darmo, "Terahertz meta-atoms coupled to a quantum well intersubband transition," *Opt. Express*, vol. 19, no. 14, pp. 13700–6, Jul. 2011.
- [91] a Benz, S. Campione, S. Liu, I. Montañó, J. F. Klem, a Allerman, J. R. Wendt, M. B. Sinclair, F. Capolino, and I. Brener, "Strong coupling in the sub-wavelength limit using metamaterial nanocavities," *Nat. Commun.*, vol. 4, p. 2882, 2013.
- [92] G. Scalari, C. Maissen, D. Turcinkova, D. Hagenmuller, S. De Liberato, C. Ciuti, C. Reichl, D. Schuh, W. Wegscheider, M. Beck, and J. Faist, "Ultrastrong Coupling of the Cyclotron Transition of a 2D Electron Gas to a THz Metamaterial," *Science (80-.)*, vol. 335, no. 6074, pp. 1323–1326, 2012.
- [93] Y. Todorov and C. Sirtori, "Few-Electron Ultrastrong Light-Matter Coupling in a Quantum LC Circuit," *Phys. Rev. X*, vol. 4, no. 4, p. 041031, 2014.
- [94] I. Carusotto and C. Ciuti, "Quantum fluids of light," *Rev. Mod. Phys.*, vol. 85, no. 1, pp. 299–366, 2013.
- [95] A. Wallraff, D. Schuster, A. Blais, L. Frunzio, R. Huang, J. Majer, S. Kumar, S. Girvin, and R. Schoelkopf, "Strong coupling of a single photon to a superconducting qubit using circuit quantum electrodynamics," *Nature*, vol. 431, no. 7005, pp. 162–167, 2004.
- [96] M. Malerba, T. Ongarello, B. Paulillo, J. M. Manceau, G. Beaudoin, I. Sagnes, F. De Angelis, and R. Colombelli, "Strong light-matter coupling at almost the single-resonator level with subwavelength mid-infrared antennas," *submitted*, 2016.
- [97] A. Schiffrin, T. Paasch-Colberg, N. Karpowicz, V. Apalkov, D. Gerster, S. Mühlbrandt, M. Korbman, J. Reichert, M. Schultze, S. Holzner, J. V Barth, R. Kienberger, R. Ernstorfer, V. S. Yakovlev, M. I. Stockman, and F. Krausz, "Optical-field-induced current in dielectrics," *Nature*, vol. 493, pp. 70–4, 2013.
- [98] N. H. Shen, M. Massaouti, M. Gokkavas, J. M. Manceau, E. Ozbay, M. Kafesaki, T. Koschny, S. Tzortzakis, and C. M. Soukoulis, "Optically implemented broadband blueshift switch in the terahertz regime," *Phys. Rev. Lett.*, vol. 106, no. 3, pp. 1–4, 2011.
- [99] K. Maussang, A. Brewer, J. Palomo, J.-M. Manceau, R. Colombelli, I. Sagnes, J. Mangeney, J. Tignon, and S. S. Dhillon, "Echo-Less Photoconductive Antenna Sources for High-Resolution Terahertz Time-Domain Spectroscopy."
- [100] I.-C. Ho, X. Guo, and X.-C. Zhang, "Design and performance of reflective terahertz air-biased-coherent-detection for time-domain spectroscopy," *Opt. Express*, vol. 18, no. 3, pp. 2872–2883, 2010.
- [101] N. Large, M. Abb, J. Aizpurua, and O. L. Muskens, "Photoconductively loaded plasmonic nanoantenna as building block for ultracompact optical switches," *Nano Lett.*, vol. 10, pp. 1741–1746, 2010.
- [102] K. Fan, A. C. Strikwerda, X. Zhang, and R. D. Averitt, "Three-dimensional broadband tunable terahertz metamaterials," *Phys. Rev. B*, vol. 87, no. 16, p. 161104, 2013.
- [103] N. Engheta and R. W. Ziolkowski, *Metamaterials: Physics and Engineering Explorations*.

Wiley, 2006.

- [104] D. F. Sievenpiper, J. H. Schaffner, H. Jae Song, R. Y. Loo, and G. Tagonan, "Two-Dimensional Beam Steering Using an Electrically Tunable Impedance Surface," *IEEE Trans. Antennas Propag.*, vol. 51, no. 10 I, pp. 2713–2722, 2003.
- [105] M. J. Lockyear, A. P. Hibbins, and J. R. Sambles, "Microwave surface-plasmon-like modes on thin metamaterials," *Phys. Rev. Lett.*, vol. 102, no. 7, 2009.
- [106] S. S. Oh and O. Hess, "Chiral metamaterials : enhancement and control of optical activity and circular dichroism," *Nano Converg. December*, no. December, pp. 1–29, 2015.
- [107] Z. Li, M. Mutlu, and E. Ozbay, "Chiral metamaterials: from optical activity and negative refractive index to asymmetric transmission," *J. Opt.*, vol. 15, p. 023001, 2013.
- [108] S. Zhang, Y.-S. Park, J. Li, X. Lu, W. Zhang, and X. Zhang, "Negative Refractive Index in Chiral Metamaterials," *Phys. Rev. Lett.*, vol. 102, no. 2, p. 023901, 2009.
- [109] "<http://www.judsontechnologies.com/>."
- [110] A. Rogalski, *Infrared Detectors, Second Edition*. CRC Press, 2010.
- [111] M. Buscema, J. O. Island, D. J. Groenendijk, S. I. Blanter, G. A. Steele, H. S. van der Zant, and A. Castellanos-Gomez, "Photocurrent generation with two-dimensional van der Waals semiconductors," *Chem Soc Rev*, vol. 44, no. 11, pp. 3691–3718, 2015.
- [112] H. Schneider and H. C. Liu, *Quantum well infrared photodetectors: physics and applications*. Springer, 2007.
- [113] F. H. Koppens, T. Mueller, P. Avouris, a C. Ferrari, M. S. Vitiello, and M. Polini, "Photodetectors based on graphene, other two-dimensional materials and hybrid systems," *Nat Nanotechnol*, vol. 9, no. 10, pp. 780–793, 2014.
- [114] L. Viti, J. Hu, D. Coquillat, W. Knap, A. Tredicucci, A. Politano, and M. S. Vitiello, "Black Phosphorus Terahertz Photodetectors," *Adv. Mater.*, vol. 27, no. 37, pp. 5567–5572, 2015.
- [115] J. Liu, *Photonic Devices*. Cambridge University Press, 2009.
- [116] J. C. Cao and H. C. Liu, *Terahertz Semiconductor Quantum Well Photodetectors*, vol. 84. Elsevier Inc., 2011.
- [117] H. C. Liu, C. Y. Song, A. J. Springthorpe, and J. C. Cao, "Terahertz quantum-well photodetector," vol. 4068, no. May 2013, pp. 1–4, 2004.
- [118] M. Graf, G. Scalari, D. Hofstetter, J. Faist, H. Beere, E. Linfield, D. Ritchie, and G. Davies, "Terahertz range quantum well infrared photodetector," *Appl. Phys. Lett.*, vol. 84, no. 2004, pp. 475–477, 2004.
- [119] H. Luo, H. C. Liu, C. Y. Song, and Z. R. Wasilewski, "Background-limited terahertz quantum-well photodetector," *Appl. Phys. Lett.*, vol. 86, no. May, pp. 1–3, 2005.
- [120] R. Zhang, X. G. Guo, C. Y. Song, M. Buchanan, Z. R. Wasilewski, J. C. Cao, and H. C. Liu, "Metal-grating-coupled terahertz quantum-well photodetectors," *IEEE Electron Device Lett.*, vol. 32, no. 5, pp. 659–661, 2011.
- [121] D. Palaferri, Y. Todorov, Y. N. Chen, J. Madeo, a. Vasanelli, L. H. Li, a. G. Davies, E. H. Linfield, and C. Sirtori, "Patch antenna terahertz photodetectors," *Appl. Phys. Lett.*, vol. 106, p. 161102, 2015.
- [122] P. D. Grant, S. R. Laframboise, R. Dudek, M. Graf, A. Bezinger, and H. C. Liu, "Terahertz free space communications demonstration with quantum cascade laser and quantum well photodetector," *Electron. Lett.*, vol. 45, no. 18, pp. 952–954, 2009.
- [123] M. I. Amanti, G. Scalari, R. Terazzi, M. Fischer, M. Beck, J. Faist, A. Rudra, P. Gallo, and E. Kapon, "Bound-to-continuum terahertz quantum cascade laser with a single-quantum-well phonon extraction/injection stage," *New J. Phys.*, vol. 11, 2009.

- [124] G. Xu, R. Colombelli, S. P. Khanna, A. Belarouci, X. Letartre, L. Li, E. H. Linfield, A. G. Davies, H. E. Beere, and D. A. Ritchie, "Efficient power extraction in surface-emitting semiconductor lasers using graded photonic heterostructures," *Nat. Commun.*, vol. 3, pp. 952–957, 2012.
- [125] A. Rogalski, *Infrared Detectors, Second Edition*. CRC Press, 2010.
- [126] I. Bahl, *Fundamentals of RF and Microwave Transistor Amplifiers*. Wiley, 2009.
- [127] C. Genet and T. W. Ebbesen, "Light in tiny holes," *Nature*, vol. 445, no. 7123, pp. 39–46, 2007.
- [128] A. E. Miroshnichenko, S. Flach, and Y. S. Kivshar, "Fano resonances in nanoscale structures," *Rev. Mod. Phys.*, vol. 82, no. 3, pp. 2257–2298, 2010.
- [129] a Degiron and T. W. Ebbesen, "The role of localized surface plasmon modes in the enhanced transmission of periodic subwavelength apertures," *J. Opt. A Pure Appl. Opt.*, vol. 7, no. 2, pp. S90–S96, 2005.
- [130] B. Luk'yanchuk, N. I. Zheludev, S. A. Maier, N. J. Halas, P. Nordlander, H. Giessen, and C. T. Chong, "The Fano resonance in plasmonic nanostructures and metamaterials," *Nat. Mater.*, vol. 9, no. 9, pp. 707–715, 2010.
- [131] F. J. González and G. D. Boreman, "Comparison of dipole, bowtie, spiral and log-periodic IR antennas," *Infrared Phys. Technol.*, vol. 46, pp. 418–428, 2005.
- [132] L. Vicarelli, M. S. Vitiello, D. Coquillat, A. Lombardo, a. C. Ferrari, W. Knap, M. Polini, V. Pellegrini, and A. Tredicucci, "Graphene field-effect transistors as room-temperature terahertz detectors," *Nat. Mater.*, vol. 11, no. 10, pp. 865–871, 2012.
- [133] M. T. Hill and M. C. Gather, "Advances in small lasers," *Nat. Photonics*, vol. 8, no. 12, pp. 908–918, 2014.
- [134] A. E. Siegman, *Lasers*. University Science Books, 1986.
- [135] K. Iga, "Surface-emitting laser - its birth and generation of new optoelectronics field," *IEEE J. Sel. Top. Quantum Electron.*, vol. 6, no. 6, pp. 1201–1215, 2000.
- [136] S. L. McCall, A. F. J. Levi, R. E. Slusher, S. J. Pearton, and R. A. Logan, "Whispering-gallery mode microdisk lasers," *Appl. Phys. Lett.*, vol. 60, no. 3, pp. 289–291, 1992.
- [137] H.-G. Park, S.-H. Kim, S.-H. Kwon, Y.-G. Ju, J.-K. Yang, J.-H. Baek, S.-B. Kim, and Y.-H. Lee, "Electrically driven single-cell photonic crystal laser," *Science (80-.)*, vol. 305, no. 5689, pp. 1444–7, 2004.
- [138] Y. Chassagneux, R. Colombelli, W. Maineult, S. Barbieri, H. E. Beere, D. A. Ritchie, S. P. Khanna, E. H. Linfield, and A. G. Davies, "Electrically pumped photonic-crystal terahertz lasers controlled by boundary conditions," *Nature*, vol. 457, no. 7226, pp. 174–178, 2008.
- [139] C. Manolatu and F. Rana, "Subwavelength nanopatch cavities for semiconductor plasmon lasers," *IEEE J. Quantum Electron.*, vol. 44, no. 5, pp. 435–447, 2008.
- [140] Y. Chassagneux, J. Palomo, R. Colombelli, S. Dhillon, and C. Sirtori, "Terahertz microcavity lasers with subwavelength mode volumes and thresholds in the milliamperere range Terahertz microcavity lasers with subwavelength mode volumes and thresholds in the milliamperere range," *Appl. Phys. Lett.*, vol. 90, no. 2007, p. 091113, 2012.
- [141] C. Walther, G. Scalari, M. I. Amanti, M. Beck, and J. Faist, "Microcavity laser oscillating in a circuit-based resonator," *Science*, vol. 327, no. 5972, pp. 1495–1497, 2010.
- [142] M. T. Hill, Y.-S. Oei, B. Smalbrugge, Y. Zhu, T. de Vries, P. J. van Veldhoven, F. W. M. van Otten, T. J. Eijkemans, J. P. Turkiewicz, H. de Waardt, E. J. Geluk, S.-H. Kwon, Y.-H. Lee, R. Nötzel, and M. K. Smit, "Lasing in metallic-coated nanocavities," *Nat. Photonics*, vol. 1, no. 10, pp. 589–594, 2007.
- [143] M. P. Nezhad, A. Simic, O. Bondarenko, B. Slutsky, A. Mizrahi, L. Feng, V. Lomakin, and Y. Fainman, "Room-temperature subwavelength metallo-dielectric lasers," no. April, pp. 1–5, 2010.

- [144] D. J. Bergman and M. I. Stockman, "Surface Plasmon Amplification by Stimulated Emission of Radiation: Quantum Generation of Coherent Surface Plasmons in Nanosystems," *Phys. Rev. Lett.*, vol. 90, no. 2, p. 027402, 2003.
- [145] J. B. Khurgin and G. Sun, "How small can 'Nano' be in a 'Nanolaser'?", *Nanophotonics*, vol. 1, pp. 3–8, 2012.
- [146] J. B. Khurgin and G. Sun, "Comparative analysis of spasers, vertical-cavity surface-emitting lasers and surface-plasmon-emitting diodes," *Nat. Photonics*, vol. 8, no. 6, pp. 468–473, 2014.
- [147] C. G. Montgomery, R. H. Dicke, and E. M. Purcell, *Principles of Microwave Circuits*. Institution of Engineering & Technology, 1948.
- [148] N. Jukam, S. Dhillon, Z. Y. Zhao, G. Duerr, J. Armijo, N. Sirmons, S. Hameau, S. Barbieri, P. Filloux, C. Sirtori, X. Marcadet, and J. Tignon, "Gain measurements of THz quantum cascade lasers using THz time-domain spectroscopy," *IEEE J. Sel. Top. Quantum Electron.*, vol. 14, no. 2, pp. 436–442, 2008.
- [149] Y. Chassagneux, J. Palomo, R. Colombelli, S. Barbieri, S. Dhillon, C. Sirtori, H. Beere, J. Alton, and D. Ritchie, "Low threshold THz QC lasers with thin core regions," pp. 30–31, 2007.
- [150] E. Strupiechonski, D. Grassani, D. Fowler, F. H. Julien, S. P. Khanna, L. Li, E. H. Linfield, a. G. Davies, a. B. Krysa, and R. Colombelli, "Vertical subwavelength mode confinement in terahertz and mid-infrared quantum cascade lasers," *Appl. Phys. Lett.*, vol. 98, pp. 4–6, 2011.
- [151] M. Wienold, L. Schrottke, M. Giehler, R. Hey, W. Anders, and H. T. Grahn, "Low-voltage terahertz quantum-cascade lasers based on LO-phonon-assisted interminiband transitions," *Electron. Lett.*, vol. 45, no. 20, pp. 1030–1031, 2009.
- [152] A. Daliri, A. Galehdar, W. S. T. Rowe, S. John, C. H. Wang, and K. Ghorbani, "Quality factor effect on the wireless range of microstrip patch antenna strain sensors," *Sensors (Switzerland)*, vol. 14, no. 1, pp. 595–605, 2014.